X-Ray Observations of High Redshift Active Galactic Nuclei and Galaxy Clusters

by

Timothy Waskett

A thesis submitted to the

University of Wales

for the degree of

Doctor of Philosophy

2004

ProQuest LLC
789 East Eisenhower Parkway
P.O. Box 1346
Ann Arbor, MI 48106-1346

DECLARATION

This work has not previously been accepted in substance for any degree and is not being concurrently submitted in candidature for any degree.

Signed .....

Date .....

STATEMENT 1

The work presented in this thesis is all my own work carried out under the supervision of Prof. Steve Eales with the exception of the following: I reduced all the *XMM-Newton* data in this thesis myself but did not take the data personally. The 3-h and 10-h field data were made available to me by Prof. Walter Gear but all the other *XMM* data in this thesis were obtained by me from the *XMM* public archive. The Canada-France Deep Fields catalogue used to identify the X-ray sources was made available to me by Dr. Henry McCracken. Prof. Steve Eales performed the calculation to obtain the sub-mm flux of the X-ray sources in chapter 3. The *Chandra* data used in chapter 4 was reduced by Dr. Paul Nandra and Elise Laird who subsequently provided me with the source list. The photometric redshifts calculated using the CFDF photometric redshift code were supplied by Mark Brodwin.

Signed .....

Date .....

STATEMENT 2

I hereby give consent for my thesis, if accepted, to be available for photocopying and for inter-library loan, and for the title and summary to be made available to outside organisations.

Signed .....

Date .....

ACKNOWLEDGEMENTS

There are many people who gave a me great deal of help and support throughout my PhD and I would like to express my gratitude to them here. The most important person has always been my wife, Kat, without whom I would not have had the excuse to leave the department at a reasonable time each day. Aside from that, she always found the time to keep me fairly sane, even when she had enough of her own work to deal with. As always she is the best friend I have.

On the technical side one man has made all the difference. Dr. Dave Nutter is not only the most useful person I know, for fixing problems with software and teaching me new tricks, but is also a good friend. Without his help this thesis would have been much longer coming and would not have looked nearly so good. The guy surely knows everything there is to know. I cannot express how grateful I am to him.

The rest of the terminal room crowd, and other PhD students, have helped make my PhD time a lot of fun. They are, in no particular order: Kris Wojciechowski, Haley Morgan, Hannah Loebl, Neal Potter, Douglas Haig, Ian Bacchus, Melanie Bowden, Owen Davies, David Hubber, Sarah Roberts, Dean Trolley, Edward Gomez, Diego Garcia, Catherine Vlahakis, Iain Brown, Robbie Auld, Bruce Sibthorpe and probably a few more names that temporarily escape me. They are the best reason to come into the department every day, if only for the bizarre conversations we have at coffee time, Keyball and Yetisports.

My family has always given me their unconditional, if slightly bewildered, love and support for which I thank them. In particular my parents Malcolm and Janet, and my two sisters Lou and Sue. At last I can tell them that I have a proper job.

I'd also like to thank the computer support team who have been (mostly) very efficient at solving all those little problems that crop up all the time, but which threaten to stop all PhD progress indefinitely unless dealt with.

A special note of thanks goes to Dr. Mat Page for all his scientific help over the course of my PhD; he has saved me from many a moment of confusion.

Finally I'd like to express my gratitude to my supervisor, Prof. Steve Eales, for giving me the freedom to try out new things and to investigate subjects that interested me rather than forcing me down a particular road. If he had been more pushy this thesis would probably make a lot more sense but I would not have enjoyed the work nearly so much.

This thesis is based on observations obtained with *XMM-Newton*, an ESA science mission with instruments and contributions directly funded by ESA Member States and NASA.

ABSTRACT

X-ray surveys of three Canada-France Redshift Survey (CFRS) fields using *XMM-Newton* are presented, with the aim of studying the Active Galactic Nuclei (AGN) and galaxy cluster populations in these fields. The X-ray sources detected in these surveys resolve 51% of the X-ray background (XRB) in the $0.5 - 10$ keV X-ray band.

The relation between the X-ray and sub-mm extra-galactic backgrounds is investigated using a combination of X-ray data and sub-mm data. The X-ray properties of the sub-mm sources and visa versa indicate that the XRB is dominated by accretion onto super-massive black holes, while the sub-mm background is dominated by dust-obscured star formation.

X-ray sources are identified with optical objects using the Canada-France Deep Fields (CFDF) survey, which covers the majority of two fields. The redshift distribution of the AGN shows a clear peak at $z \sim 0.7$.

The 2-point angular correlation function, $W(\theta)$, is calculated for the identified AGN but no significant clustering is detected. However, the results are consistent with X-ray selected AGN being good tracers of the normal, inactive galaxy population.

The environments of moderate luminosity AGN at $z \sim 0.5$ are investigated, using the clustering amplitude measure B_{gq} and close pair counts. When compared to a control sample of equivalent inactive galaxies no difference is found between the respective environments. Minor mergers with low mass companions is therefore the most likely mechanism by which these AGN are fuelled.

A new method for finding high redshift, optically selected, galaxy clusters is presented and is compared to X-ray selection. It is found that most optically selected clusters may have lower than expected X-ray luminosities suggesting that they are dynamically young compared to X-ray selected clusters.

Contents

List of Figures

List of Tables

Chapter 1

An Introduction to X-ray Sources

Astronomy is a vast and interesting science. What other subject can boast the entire Universe as its playground? This thesis represents but a tiny part of the huge endeavour to understand the Universe, but I hope that the reader will find it interesting nonetheless.

1.1 The Cosmic X-Ray Background - XRB

X-ray astronomy is the observational counterpart to high energy astrophysics. In astronomical terms these fields are relatively recent additions to the science because of the opacity of the Earths atmosphere to X-rays, which has, until the age of space instrumentation, made it impossible to study such things. X-rays are energetic photons that are produced by high temperature phenomena. They range in energy from roughly $0.12 - 50$ keV, or in wavelength from roughly $0.25 - 100$ Å (although the exact definition is somewhat debatable) and fill the gap between

extreme ultraviolet at lower energies and gamma rays at even higher energies.

Like light from all regions of the electromagnetic spectrum X-rays originate both from within our own Milky Way Galaxy and also from beyond - the so-called extra-galactic background radiation field. In a sense, extra-galactic astronomy is the study of this background radiation field and, with the exception of the CMB, to fully understand the origin of a particular background one must first resolve it into its constituent sources.

Figure 1.1 shows a recent compilation of data for the extra-galactic background. Each peak is dominated by different physical processes: the Cosmic Microwave Background (CMB) has the highest energy density and is made up of redshifted photons from the surface of last scattering, the echo of the big bang as it were; the Far-Infrared Background (FIB, or sometimes Cosmic IR Background, CIRB) is the result of dust obscuration, which reprocesses higher energy photons from e.g. stars into the far-IR and sub-mm regime; the optical and UV backgrounds are essentially starlight while the origin of the Gamma-Ray Background (GRB) is still something of a mystery but probably includes highly energetic forms of super-novae, amongst other possibilities.

The X-Ray Background (XRB) contains significantly less energy density than either the FIB or the optical background but it is no less important to understand, if we are to fully appreciate the complexities of the Universe. Very soon after it was discovered it was found that the XRB can be resolved into individual sources; from then on extra-galactic X-ray astronomy and high energy astrophysics took off, with a primary aim to understand the nature of these sources and to explain the origin of the XRB.

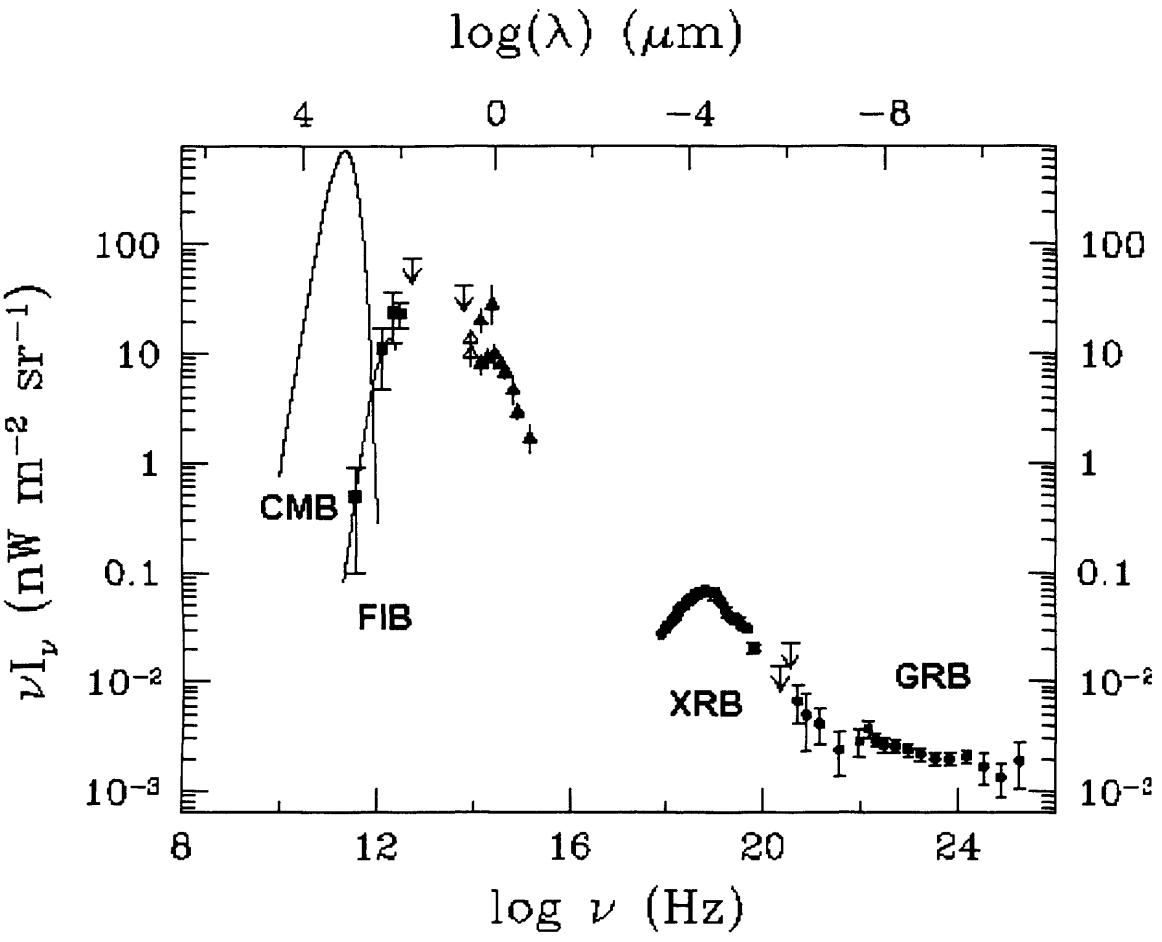

Figure 1.1: A plot of the extra-galactic background radiation field, taken from Bragaglia et al. (2000). CMB = Cosmic Microwave Background, FIB = Far-Infrared Background, XRB = X-Ray Background, GRB = Gamma-Ray Background. The optical and ultra-violet backgrounds are still somewhat uncertain in their exact form but they lie between the FIB and the XRB.

The spectrum of the XRB holds many clues as to its origin. It has a rather simple shape, significantly less complicated than the optical background, which still does not have a reliable measurement despite the relative maturity of optical astronomy. Broadly speaking the spectrum of the XRB is a bump with a peak in energy density at $\sim$ 30 keV (the XRB 'bump' in figure 1.1). In the energy range $3 - 20$ keV, the XRB can be well approximated by the following function:

$$I_\nu = AE^{-\alpha},$$

where α is the spectral index, which determines the slope of the power law model. Although the normalisation is still uncertain to within $\sim 10\%$ the spectral index has been well determined to be $\alpha \simeq 0.4$ (Comastri et al., 1995). Therefore, over this fairly limited energy range, the XRB increases slowly in energy density, since $\nu I_\nu \propto E^{1-\alpha} = E^{0.6}$ (the left hand part of the XRB 'bump' in figure 1.1). At slightly lower energies ($0.5 - 2$ keV) the XRB is well fit with another power law of spectral index $\alpha \simeq 1.0$. The current generation of X-ray telescopes detect X-rays in the energy range $\sim 0.5 - 10$ keV, and over this range the XRB is often approximated to a power law with $\alpha = 0.4$.

The remainder of this introduction gives some background to the sources that make up the XRB; the sources that form the subject of this thesis.

1.2 Active Galactic Nuclei - AGN

The vast majority of the sources that make up the XRB are point-like and it was found that almost all were associated with the central regions of galaxies.

The term Active Galactic Nucleus (AGN) is now used to describe what is, in effect, an accreting super-massive black hole (SBH) residing in the centre of a galaxy. A theoretical picture has gradually emerged from the various observations of AGN so that we now have a reasonable understanding of the mechanisms involved (e.g. Antonucci, 1993). Broadly speaking an AGN consists of the SBH itself which is fed by an optically thick accretion disc of material. Beyond this, and in the same plane, is a torus of obscuring gas and dust that causes the AGN to assume a different appearance depending on the orientation of the observer's view into the central engine. Along the axis of rotation jets of high energy plasma

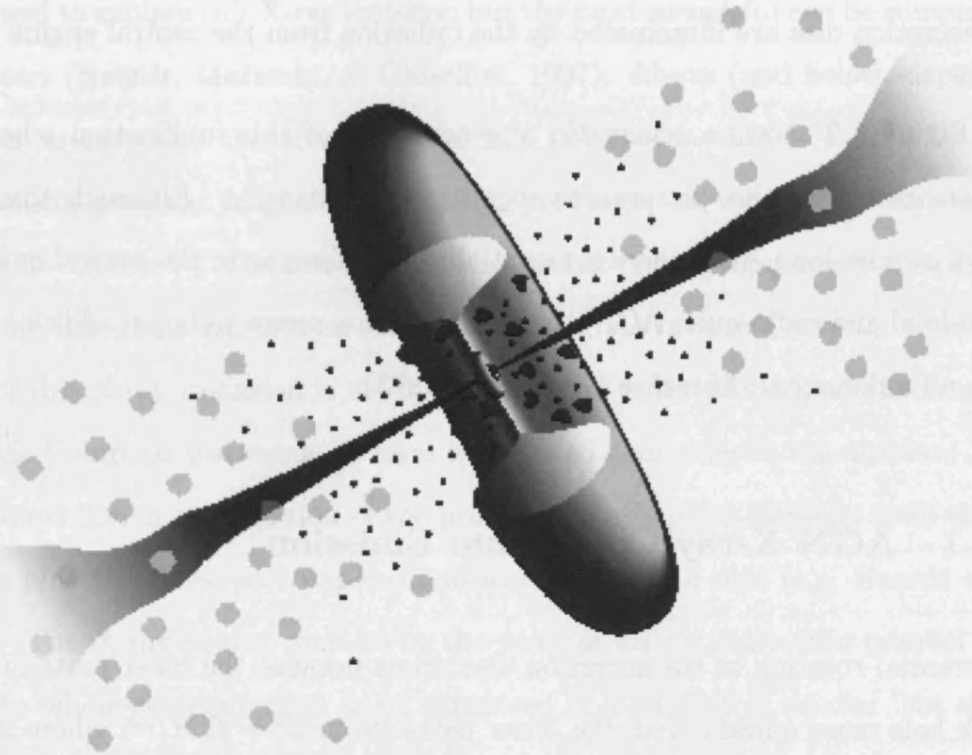

Figure 1.2: An idealised schematic representation (not to scale) of a radio-loud AGN from Urry & Padovani (1995), representing the current unification scheme that is thought to apply to essentially all AGN. The accretion disc and hot corona occupy a tiny region in the centre of this diagram, surrounded by the much larger obscuring torus. High velocity clouds orbit very close in to the central engine and so the broad emission lines produced by them are not visible when the observers' line of sight runs through the obscuring torus. The low velocity clouds that are responsible for the narrow line emission are visible even at low viewing angles. The radio jets are ejected along the rotation axis and they can travel well outside the confines of the host galaxy, where they impact with the inter-galactic medium causing radio-lobes. Radio-quiet AGN do not have such powerful radio jets and so have much less radio emission. $\sim 3/4$ of all AGN are radio-quiet.

are sometimes formed, which carry away the majority of the angular momentum lost from the in-falling accretion disc material; they can be powerful radio sources. Various other phenomena, such as broad and narrow emission line regions, arise when, respectively, high and low velocity gas clouds orbiting out of the plane of the accretion disc are illuminated by the radiation from the central engine.

Figure 1.2 shows a schematic representation of this 'unification scheme' to demonstrate how this picture fits together geometrically. Although this figure shows a radio-loud AGN there is essentially no difference in the central engines of radio-loud and radio-quiet AGN; the radio emission seems to be an addition rather than a fundamental difference (Antonucci, 1993).

1.2.1 AGN X-ray Continuum Emission

Differential rotation in the accretion disc arises because the inner parts orbit the black hole more quickly than the outer parts (from $\omega^2 = GM/r^3$, where ω is the angular velocity of an element of accretion disc at a radius r from a black hole of mass M). The resultant friction between neighbouring layers causes the material in the disc (mostly gas and some dust) to gradually lose angular momentum and so spiral in towards the central black hole with the resultant loss of potential energy converted into heat. This not only results in the ultimate consumption of the material in the disc by the black hole, adding to the black hole's mass, but also produces a characteristic accretion disc thermal spectrum. The temperature across the face of the accretion disc is a function of its radius from the black hole, the closer the hotter, and so the overall spectrum is essentially the superposition of a range of black body curves at different temperatures across the whole surface of the disc. This primary emission from the accretion disc is seen as an optical/UV

continuum.

Further to this primary emission, observations in the X-ray regime reveal other components that contribute to a typical AGN continuum. Various models have been used to explain this X-ray emission but the most successful can be summarised as follows (Haardt, Maraschi, & Ghisellini, 1997): Above (and below, depending on your orientation) the accretion disc is a hot corona that is heated by some mechanism, possibly magnetic dissipation processes, to very high temperatures ($kT = 30 - 300$ keV). The free electrons in this hot corona reprocesses the primary accretion disc radiation into an X-ray continuum via inverse Compton scattering. Part of this X-ray radiation is modified when it is reflected back off the accretion disc, via Compton scattering, to form a 'reflected component'; the ultimate X-ray emission is then a combination of the primary Comptonised emission from the hot corona plus the reflected component from the accretion disc (e.g. Haardt et al., 1997). The X-ray source may be in the form of an optically thin parallel layer over the whole accretion disc, or be composed of a number of smaller 'hot spots'. Figure 1.3 shows the continuum features typical of AGN in general, the right hand side of the plot being the most relevant to this discussion.

There is likely to be a certain amount of feedback between the hard X-ray emitting corona and the softer thermalised disc with an exchange of photons between the two. Not all the hard X-rays from the corona incident on the disc are reflected, and in fact the majority ($89 - 90\%$) is thermalised in the disc and re-emitted where it is then Comptonised again by the hot corona, and so on (Haardt et al., 1997). The reprocessed thermalised radiation is therefore thought to be responsible for the UV bump and the reprocessed reflected radiation is responsible for the Compton bump at $\sim$ 30 keV (see figure 1.3). At higher energies ($\sim$ 200 keV) an exponential cut-off causes the continuum emission to drop off rapidly. This

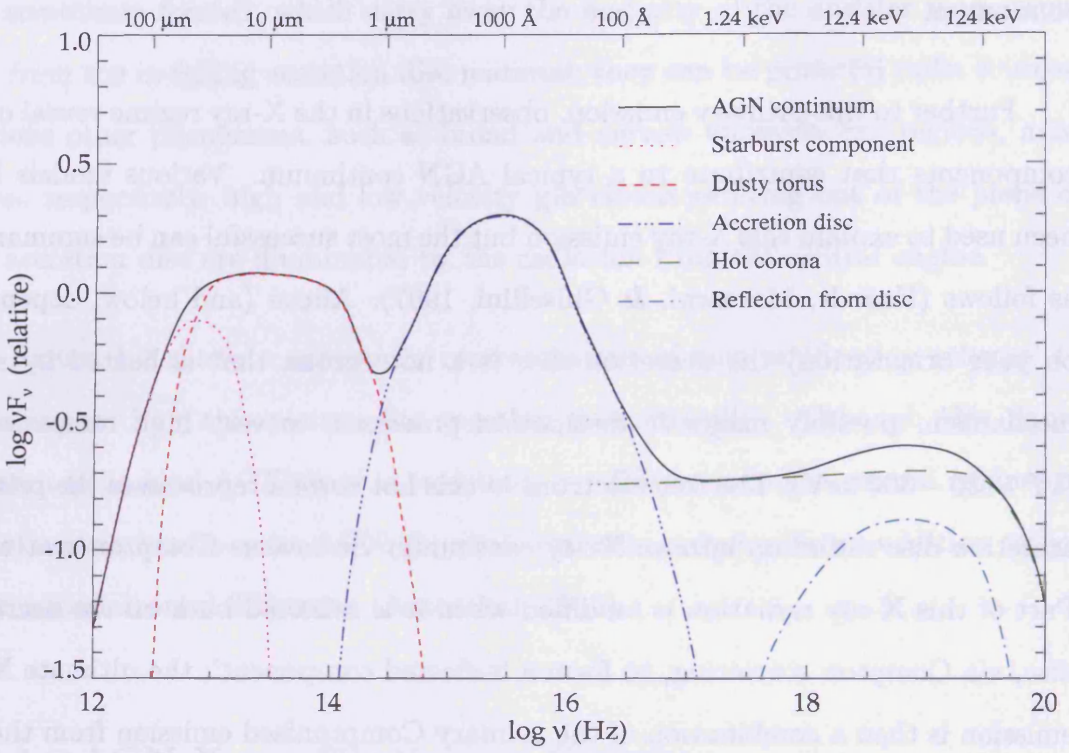

Figure 1.3: AGN continuum emission, taken from Manners (2002) and based on the mean of a sample of mainly UV excess quasars from Elvis et al. (1994).

is due to energy distribution of the Comptonising electrons: if the distribution is thermal the electrons follow a Maxwell-Boltzmann energy distribution and so the number of electrons of a given energy follows:

$$f(\epsilon) = Ae^{-\epsilon/kT},$$

where T is the temperature of the electrons. Above an energy of $\epsilon \sim kT$ the number of electrons capable of up-scattering continuum photons drops off exponentially causing the X-ray continuum to do the same. Therefore, the energy of the exponential cut-off indicates the temperature of the electrons in the hot corona.

All AGN, from Seyferts to quasars have an intrinsic underlying X-ray contin-

uum that, to first order, can be approximated by a power law with spectral index $\alpha \sim 0.8-1.0$ (see the long-dashed line in figure 1.3): a consequence of the feedback between the disc and corona. This is significantly softer than the XRB spectrum so if the XRB is composed primarily of AGN then there is a clear discrepancy between the two. However, as X-ray surveys probe deeper into the XRB and resolve more and more of it into point sources it has become clear that there is more to AGN X-ray emission than simply the accretion disc and hot corona. Obscuring material in the torus (typically neutral hydrogen gas, HI) between the AGN and an observer acts to suppress the intrinsic X-ray emission via photo-electric absorption. The low energy (soft) X-rays are absorbed more heavily than the high energy (hard) X-rays however, so what starts out as a rather soft intrinsic spectrum becomes a much harder observed spectrum. Therefore, many of the AGN that make up the bulk of the XRB actually have a significant amount of intrinsic absorption, which results in the XRB having a harder spectrum than that of a typical unabsorbed AGN (see figure 1.4 for a demonstration of this effect).

1.2.2 The Current Observational Picture

Deep exposures with the most recent and powerful X-ray observatories, *XMM-Newton* and *Chandra* (e.g Barger et al., 2003; Giacconi et al., 2002; Mainieri et al., 2002; McHardy et al., 2003; Page et al., 2003), have built on the deepest *ROSAT* X-ray surveys (e.g McHardy et al., 1998; Hasinger et al., 1998) by going deeper and to higher X-ray energies with better positional accuracy. This has opened up the study of faint X-ray sources, such as high redshift AGN, and has also revealed X-ray emission from otherwise normal galaxies at more modest redshifts (Hornschemeier et al., 2003). These surveys have now resolved the majority of the XRB in the soft

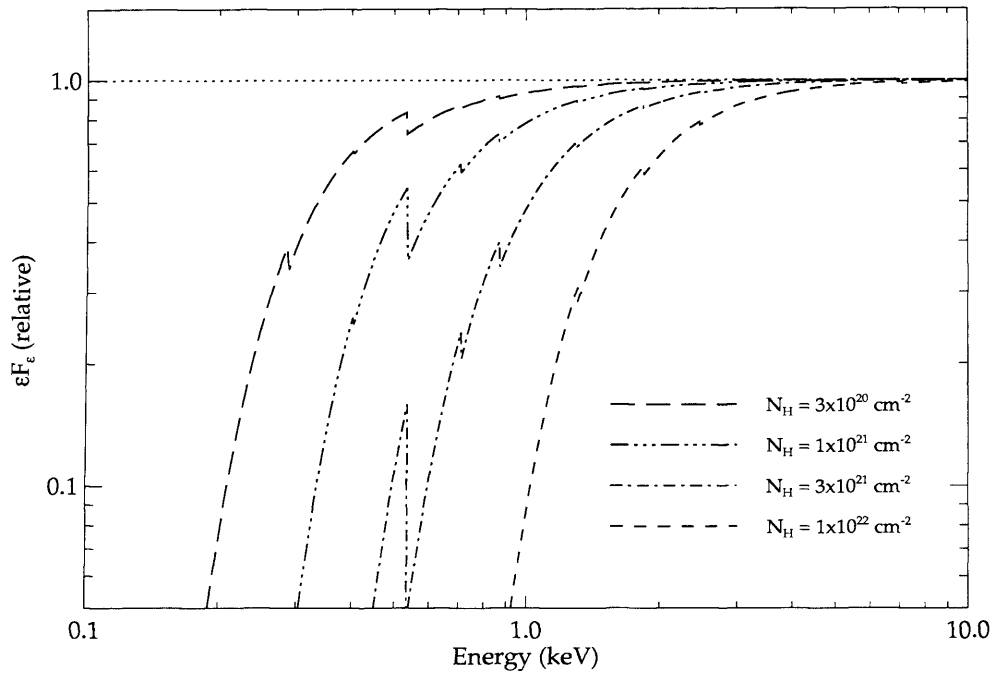

Figure 1.4: The effect of varying column densities of intervening HI on the X-ray continuum of an AGN (taken from Manners (2002)). The higher the column density of HI the higher the energy of X-rays that are 'wiped out' by the photo-electric absorption.

$(0.5 - 2$ keV) X-ray band with a small fraction left unaccounted for in the hard $(2 - 10$ keV) band (Moretti et al., 2003).

The nature of the XRB at these X-ray energies is now well on the way to being understood but there is still a small discrepancy in the hard X-ray band. The peak of the XRB lies at ~ 30 keV and the sources that dominate the $0.5 - 10$ keV band are not sufficiently hard to be the dominant sources contributing to the XRB peak. This indicates that a population of very faint sources, with very hard spectra, make up the remaining fraction of the XRB in the hard band, and would also be expected to contribute a much greater fraction to the XRB nearer its peak (Moretti et al., 2003). Such hard sources are most likely a result of extremely high obscuration.

The radiation absorbed by the obscuring material must be re-emitted at longer wavelengths and the possibility of the Far-IR/Sub-mm background being somehow connected with the XRB is discussed in many papers (e.g. Almaini, Lawrence, & Boyle, 1999). However, current X-ray/Sub-mm surveys suggest that the two backgrounds are only loosely related (e.g. Waskett et al., 2003; Alexander et al., 2003; Severgnini et al., 2000). Future instrumentation with higher energy limits are likely required to fully explain the XRB and the nature of the sources that dominate its peak.

At present though, the emphasis must be turned to those sources that we can observe easily with the current instrumentation. QSOs and type-I AGN dominate the softest X-ray energies with an increasing contribution from more obscured type-II AGN becoming important at higher energies (e.g. Gilli, Salvati, & Hasinger, 2001). Identifying the optical counterparts to these sources is crucial for a full understanding of their properties and a great deal of effort has been expended in obtaining this information (e.g. Barger et al., 2003; McHardy et al., 2003).

For example, one of the most useful quantities that can be derived for a population of sources is the luminosity function. This reveals much about the nature of a population and determining its evolution with redshift can shed light on how the population as a whole changes over time. The X-ray luminosity function (XLF) has begun to be investigated in depth by several groups (Cowie et al., 2003; Steffen et al., 2003; Ueda et al., 2003). Both Ueda et al. (2003) and Steffen et al. (2003) find that the evolution of the XLF is a function of luminosity. The population of X-ray sources with $L_X(2-10\ keV) > 3\times10^{43}$ erg s^{-1} is dominated by type-I AGN, and the number-density of these sources increases with redshift out to $z \sim 2-3$. At lower X-ray luminosities however, the fraction of type-II AGN increases rapidly with decreasing X-ray luminosity. The number-density of these sources appears to

peak at $z < 1$.

Although *Chandra* is better suited for identifying X-ray sources with optical counterparts (*XMM* has a resolution of $\sim 6''$ full width half maximum (FWHM) cf. $\sim 0.5''$ for *Chandra*), *XMM* has greater sensitivity and a larger field of view (FoV), making it better for large area surveys.

1.2.3 This Thesis

The majority of this thesis concerns the point sources detected in a medium-deep *XMM* survey composed of two separate exposures (~ 0.4 square degrees). Most of these point sources are AGN. I study the sub-mm properties of a selection of X-ray sources (chapter 3), and visa versa, and then quantify the ability of such a survey to identify X-ray sources with optical counterparts (chapter 4). I also estimate redshifts for the identified sources using photometric redshift codes. These allow a quick, and reasonably reliable, way of obtaining redshifts for objects with multi-band photometry. Although not as accurate as spectroscopy these techniques are becoming widely used as a short-cut for large surveys, where statistical properties are fairly insensitive to the accuracy of individual redshift measurements (Csabai et al., 2003; Fontana et al., 2000; Kashikawa et al., 2003; Mobasher et al., 2004). These methods can also be used on objects fainter than the spectroscopic limit, where many X-ray source counterparts reside (Alexander et al., 2001). I test two photometric redshift estimation codes on the X-ray source IDs and obtain a robust redshift distribution for those sources that could be identified reliably, while placing limits on the properties of those that could not.

In chapter 5 I analyse the clustering properties of the AGN detected in the

XMM surveys with the aim of understanding how AGN are distributed relative to the normal galaxy population. In chapter 7 I investigate the environments of moderate luminosity AGN, near the peak of the AGN redshift distribution, to see if the mechanisms by which they are fuelled are influenced by the environments of the AGN host galaxies.

The accretion history of the Universe is dominated by AGN with moderate accretion rates at $z < 1$. To fully understand the processes that lead to the production of the XRB we must understand the mechanisms that lead to this accretion. Many of the AGN in this thesis are members of that important population and so hold fundamental clues that could help explain the XRB phenomenon. If we can understand the origins and causes of accretion onto SBHs then we will be a step closer to knowing how this fits in with the rest of the Universe.

1.3 Galaxy Clusters

Chapter 6 is a slight deviation from the rest of the thesis as it does not deal with AGN but with the other population of X-ray sources that contributes to the XRB, albeit only a small fraction ($\sim 5\%$ in the soft band) - galaxy clusters.

Clusters are the end point of large scale structure formation. In the hierarchical picture of structure formation small things form first from fluctuations in the dark matter density distribution. These small over-densities, or 'dark matter halos' merge with each other to form larger conglomerations of dark matter and so on. The process continues until we are left in the present day Universe with a very clumpy distribution of matter on all different mass scales. Baryonic matter, in the form of stars and galaxies etc., is caught up in the overwhelming gravity of the

dominant dark matter so that the distribution of mass is effectively traced by the light emitted from this 'ordinary' matter.

Galaxy clusters are effectively the end point of a whole merger tree history and are the largest self gravitating systems in the Universe. With masses up to $> 10^{15}\ M_{\odot}$ the dark matter halos can encompass thousands of individual galaxies within the potential well. Along with the optically visible galaxies clusters are also permeated with a very tenuous but also extremely hot ionised gas that sits in hydrostatic equilibrium with the dark matter distribution. The mass of the gas is typically similar to that associated with the galaxies and together they make up only a small fraction ($\sim 1/10 - 1/5$) of the total mass of a cluster.

The mass distribution of dark matter halos at any given point in time can be described the Press-Schechter formalism (Press & Schechter, 1974), which effectively gives a prescription for how the clumpiness of the Universe evolves. The only assumption needed for this formalism is that an expanding cosmology is permeated with a self gravitating 'gas' that experiences no forces other than its own gravity (basically dark matter). From an initially 'grainy' matter distribution this formalism predicts how the smaller matter condensations should merge together to form the larger ones, and this eventually results in a self-similar behaviour whereby the distribution of matter has forgotten the form of the initial perturbations that caused it to start collapsing in the first place. It is very successful at reproducing the observed present day clumpiness of the mass distribution from galaxy to cluster and super-cluster scales.

However, when observing galaxy clusters the mass is not an immediately observable quantity so we need something that we can observe that can then be used to estimate the mass. Fortunately there are several ways in which we can estimate

the mass of a cluster:

- Velocity dispersion of cluster galaxies. If the galaxies that make up a cluster are in dynamical equilibrium with the underlying potential well then the total mass of the system can be estimated from their line of sight velocity dispersion, σ. For an isothermal distribution, $M_{cl} \propto \sigma^2$.

- X-ray properties. Rich clusters of galaxies produce extended X-ray emission from the hot intra-cluster gas trapped in the potential well, via thermal bremsstrahlung radiation. Assuming this gas is in hydrostatic equilibrium with the cluster potential the X-ray properties are well behaved. The emissivity of the ionised gas scales as $\epsilon \propto \rho_{gas}^2 T^{1/2}$, so the total luminosity of a cluster becomes $L_X \propto \rho_{gas}^2 R_{cl}^3 T^{1/2} \propto M_{gas} \rho_{gas} T^{1/2}$. The luminosity and temperature can be estimated from the X-ray emission and so the density can be estimated using the size of the cluster. Since X-ray luminosity is most sensitive to the gas density the majority of the emission comes from the dense core of the cluster. The distribution of gas can then be used to calculate the total mass of the cluster, within a given radius, by assuming that the gas is in hydrostatic equilibrium with the dark matter:

$$M_{cl}(\leq r) = -\frac{kT}{\mu m_p G}\left(\frac{d\ln \rho_{gas}(r)}{d\ln r} + \frac{d\ln T}{d\ln r}\right) r,$$

  where T is the temperature and μm_p is the mean particle mass of the gas.

- Gravitational lensing. Much more difficult to achieve, this technique relies on detecting background galaxies that have been gravitationally lensed by the mass of the cluster. The amount of distortion experienced by the background galaxy depends on the surface mass over-density of the cluster.

All three methods give results that are consistent with each other, giving added certainty to the mass determinations.

1.3.1 The Evolution of Cluster X-ray Properties

If we accept that the hierarchical picture of structure formation is the way in which clusters form, then they must still be forming today. As each sequential level of the hierarchy collapses then previous sub-structure is erased, leaving a central core which is essentially in quasi-equilibrium, while further out the cluster continues to grow through accumulation of in-falling matter. If a sphere were placed around the core, separating these two distinct regions, then the density within the sphere is always about 200 times the background density, whatever the epoch. Within this framework clusters should, therefore, be quite easy to understand as, at their most basic level, they are only governed by a couple of processes. Kaiser (1986) used the assumption that the thermodynamics of the intra-cluster medium (ICM) is only determined by gravitational processes and that the emission from the hot gas is pure bremsstrahlung, to predict how the X-ray properties of clusters should evolve as we look to higher redshifts. The prediction of the resultant model is that clusters are self-similar, so that the properties of one cluster can simply be appropriately scaled to predict the properties of a cluster of different mass. This is the 'self-similar' model.

According to this model the characteristic cluster quantities are predicted to scale as follows: $\rho^* \propto (1+z)^3$, $M^* \propto (1+z)^{-3}$, $R^* \propto (1+z)^{-2}$, $T^* \propto (1+z)^{-1}$, $L_X^* \propto (1+z)^{-1/2}$ (assuming that the spectrum of density fluctuation in the early Universe is a power law i.e. scale free-initial conditions, and has a spectral index $n = -1$). That is, clusters at $z > 0$ should be denser, less massive, smaller,

cooler and slightly less luminous. This means that the low redshift cluster scaling relations, predicted from assuming hydrostatic equilibrium and the virial theorem, should evolve with redshift also.

The key relations are then: $L_X \propto M\rho T^{1/2}$, $L_X \propto T_X^2(1+z)^{3/2}$ and $L_X \propto M^{4/3}(1+z)^{7/2}$. We also have the relations between the velocity dispersion of the cluster galaxies and the properties of the hot gas e.g. $T \propto \sigma^2$.

However, observations have revealed that real galaxy clusters do not follow these idealised scaling relations, so the self-similar model must be wrong to some degree. In reality, rather than following the relation $L_X \propto T_X^2$ clusters scale more like $L_X \propto T_X^3$.

The solution to this discrepancy lies in the physics missing from the self-similar model. Galaxy clusters are not simply subject to gravitational processes, such as adiabatic compression during collapse and shock heating, there is a great deal more going on. Kaiser (1991) introduced pre-heating into the self-similar model, which increases the entropy of the ICM (defined as $S = T/n^{2/3}$ where n is the fully ionised gas density) and prevent it from becoming so dense. This decreases the X-ray luminosity, especially for poorer clusters, where the extra added entropy is comparable to the self-similar entropy, and results in the much steeper $L_X - T_X$ relation.

The exact source of this extra heating during the formation of a cluster is not known but there are a number of candidates. Supernovae explosions could provide some heat but it is not enough to account for the observed relation. Heating by a central AGN is a more likely mechanism, as much more energy is available (Valageas & Silk, 1999).

A significant consequence of this pre-heating is that high redshift clusters do not produce nearly as much X-ray emission as predicted by Kaiser (1986). In the original self-similar theory the X-ray luminosity function of clusters should evolve in a positive way towards high redshift and the comoving X-ray emissivity from clusters is predicted to increase, $\epsilon \propto (1+z)^{5/2}$ (for $n = -1$), so that high redshift clusters should be very numerous and easy to find. However, this is not the case and in fact negative evolution has been observed meaning that high redshift clusters are much harder to find than initially expected.

1.3.2 The Cooling Flow Problem

Continual input of energy by a central AGN may also be the best explanation for the so-called 'cooling flow problem'. Put simply, this aspect of cluster evolution is a question of energetics. The hot gas in a cluster emits X-rays and so should cool down as the energy is carried away. The cooling rate is sensitive to the density of the gas because, as described above, the emission increases as ρ^2, so the cooling rate is fastest in the centre of the cluster. Now, if the gas in the centre of a cluster is cooling quickly i.e. the cooling time is significantly less than the Hubble time, then the hydrostatic support in the centre of a cluster decreases as the temperature drops. This results in an inflow of gas leading to an increase in the central gas density. Because the gas is now denser it will radiate more efficiently, see above, and so will cool more quickly. $t_{cool} \propto T^2$ at constant pressure so the cooler the gas gets the quicker it cools.

This runaway cooling effect should mean that all the gas in the cores of rich clusters (where the cooling time is less than the Hubble time) should continue to cool until it has accreted into a central region, usually a giant elliptical cD galaxy.

The inflow rate is given by $\dot{M}_X = (2L_{cool}\mu m)/(5kT)$ (Fabian, 1994) and can be as high as 500 $M_\odot$ yr^{-1} in some clusters. Why is it then that we do not see this extraordinary accretion rate in every cluster, and why does the gas in the cores of clusters appear to stop cooling once it reaches about 1/3 of the virial temperature? Some clusters do have cooling flows and are observed to have large in-flow rates but other clusters should be experiencing much more powerful cooling flows than they are observed to have. This is the cooling flow problem and is an outstanding problem in cluster evolution.

As mentioned at the start of this section a possible resolution of this problem could be found by assuming a continual heating of the gas in the cores of clusters by some mechanism that is capable of injecting vast quantities of energy into the ICM. Powerful AGN are the obvious candidate as the energy injection rate can easily outweigh the radiative cooling of the cluster gas. Also, the cooling flow itself may provide the necessary fuel to keep an AGN active and so a sort of feedback is set up between the cluster gas and the central AGN.

Another possibility is thermal conduction that draws energy in to the centre of the cluster from the hotter outer layers of gas to prevent the temperature in the centre dropping enough to start a significant cooling flow. However, because conduction rate increases with temperature it should become less efficient just as radiative emission is becoming more so i.e. in the cooler cores. Therefore, if an equilibrium is established between conduction and radiation it will be unstable leading inevitably to one process dominating over the other, i.e. either a cooling flow or an isothermal gas distribution. In reality most clusters experience a sort of half-way house in that they have a slightly cooler core than the bulk of the X-ray gas, with moderate in-fall rates but not a powerful cooling flow. This issue has not yet been fully resolved.

1.3.3 The Relative Evolution of X-ray/Optical Properties

There is - and needs to be - some distinction between galaxy clusters detected via X-ray means and ones discovered by optical methods. Although the original definition of galaxy clusters arose because they were first discovered in optical surveys as over-densities of galaxies, the galaxies themselves are only a symptom of the underlying phenomenon.

During the formation of a cluster the galaxies and the hot gas go down very different evolutionary paths. Therefore, a cluster detected as an over-density of optical galaxies may not necessarily be detected by X-ray methods.

When a cluster is first collapsing (or when several smaller dark matter clumps come together, in the hierarchical picture) the member galaxies to be have a high line of sight velocity dispersion due to the rapid in-fall and there is no clear separation of different galaxy types. Only once the cluster has had time to relax do the galaxies settle down into a well behaved dynamical state. The equipartition of energy between large and small galaxies eventually causes the most massive galaxies, such as giant ellipticals, to fall into the central regions of the cluster with a small velocity dispersion, while the smaller galaxies remain more widely distributed with a higher velocity dispersion.

So a cluster evolves from a very mixed up, irregular, high σ state into a more relaxed, regular, lower σ state with a clear mass-density relation. Other evolutionary effects also conspire to suppress star-formation in the galaxies with the highest environmental density (i.e. the cluster core) so what we end up with is a core of massive, red, elliptical galaxies surrounded by a halo of less-massive, blue, spiral galaxies. The more evolved a cluster becomes the lower the fraction of

spiral galaxies becomes and the more relaxed and regular it appears.

The gas, on the other hand, has yet to fully virialise with the dark matter distribution in a young cluster. The outcome of this is that although there is an over-density of optical galaxies at the position of the cluster the gas has not achieved its full potential X-ray luminosity. Only when the hot gas has become virialised and has reached the higher central density does the X-ray luminosity and temperature start to behave in the ways described in section 1.3.

The two effects of high σ and low L_X mean that dynamically young clusters do not follow the expected $L - \sigma$ relation found for local evolved clusters (e.g. Lubin, Mulchaey, & Postman, 2004). X-ray surveys are therefore most sensitive to dynamically old, evolved clusters while optical techniques can also be sensitive to the younger cluster population. At high redshift there is a higher proportion of young clusters so optically selected samples show a significant difference in the X-ray/optical relations to those found for X-ray selected samples.

1.3.4 This Thesis

The work in chapter 6 concentrates on methods for finding high redshift galaxy clusters. Because different methods for finding clusters have different selection effects I employ both X-ray and optical techniques to find clusters within my data. Comparing different methods for finding clusters is important because evolutionary effects may alter the sensitivity of a particular cluster detection method in ways that we don't yet understand. Any bias that affects one technique may be overcome by the use of another technique that doesn't suffer from the same bias.

Only once we fully understand the evolutionary processes that cause devia-

tions from our expectations can we truly characterise the selection functions of different cluster finding methods. By relying on one method alone we would risk misinterpreting our findings and missing important factors that influence our understanding of cluster evolution.

Throughout this thesis I assume an H_0 of 75 km s^{-1} Mpc^{-1} and a concordance Universe with $\Omega_M = 0.3$ and $\Omega_\Lambda = 0.7$, unless otherwise stated.

Chapter 2

XMM-Newton Data Acquisition and Reduction

2.1 Introduction

As this thesis is based on data taken by the *XMM-Newton* X-ray space telescope I will outline the data and its basic reduction in this chapter, along with the source detection procedure I used to obtain the catalogues presented in chapter 4. Other data is used at various stages throughout this thesis but I was not involved in its acquisition or reduction. Therefore, I will not present a discussion of these other data here except where it relates directly to this thesis.

2.2 *XMM-Newton* Overview

XMM-Newton is an X-ray telescope that was launched into a high altitude, long period orbit in late 1999. Ordinary optics simply can't reflect X-rays so like all X-ray telescopes *XMM* uses special mirror assemblies that comprise a series of nested grazing-incidence mirrors, which focus the X-rays onto the detectors. There are three mirror assemblies (modules) in total, each one focussing X-rays onto a primary imaging instrument. The imaging cameras are designed to detect X-rays in the range $\sim 0.15 - 15$ keV, although the range is often restricted to less than this for useful scientific analysis.

All three imaging cameras are CCD designs, two of which are identical and are essentially the same technology used to make optical CCDs. These two are the Metal Oxide Semi-conductor CCDs (MOS) and they each receive $\sim 44\%$ of the light from their respective mirror modules, the rest being diverted to Reflection Grating Spectrometers (RGS) for high resolution X-ray spectroscopy (I offer no further details on the RGS instruments here as they are irrelevant to this work apart from the reduction in the flux the two MOS instruments experience because of them). The remaining X-ray CCD is of a different design to the MOS cameras and sits in the unobstructed beam of the third and final mirror module. This CCD is of the pn design, which offers superior sensitivity over the MOS design, particularly at higher photon energies.

All three cameras observe approximately the same area of sky in each exposure and operate simultaneously, as do the two RGS instruments. In addition to the X-ray instrumentation a small optical/UV telescope, the Optical Monitor (OM), also observes part of the same field as the primary cameras and is used principally for obtaining simultaneous UV data of the X-ray sources under study. This si-

multaneous operation of all the instrumentation on *XMM* gives it a big advantage over other X-ray telescopes, for example *Chandra*, which tend to offer a suite of instrumentation of which only one can be used during any given exposure.

2.3 X-ray Data

Two main *XMM* surveys are considered in this work, X-ray surveys of the Canada-France Redshift Survey (CFRS) 3 and 14-h (also known as the Groth Strip) fields (Lilly et al., 1995b). The 14-h *XMM* data was first presented in Miyaji & Griffiths (2001).

The data for the 3-h field were taken on 17th February 2001 by *XMM-Newton* over a period of 51.5 ks, using the thin optical blocking filters and in full frame imaging mode. All three primary instruments gathered data (MOS 1, MOS 2 & PN) as well as the OM telescope. This field is centred on R.A. 03:02:38.60 Dec. +00:07:40.0.

The 14hr field data was obtained from the public archive after the proprietary period had expired, to extend the coverage of available *XMM* data for the CFRS fields. This data was first presented in Miyaji & Griffiths (2001) and later in Miyaji et al. (2003) and Miyaji et al. (2004). Of the several available exposures of this field, one was selected that most closely matched the exposure of the 3-h field. The exposure was taken over 56.1 ks, using thin filters, and is centred on R.A. 14:17:12.0 Dec. +52:24:00.0.

In addition to the two main surveys presented in this thesis a third survey is also presented, albeit in less detail because of the lack of deep optical coverage for

this field. This third field is coincident with the 10-h CFRS field and was similarly surveyed by *XMM* for 50.8 ks, using the thin filter for the PN instrument and the medium filter for the two MOS instruments. This field is centred on R.A 10:00:40.4 Dec. +25:14:20.0. I do not discuss the Optical Monitor data here, for any of the above surveys.

2.4 X-ray Data Reduction

The *XMM-Newton* raw data were processed using version 5.3 of an ensemble of tasks collectively titled the Science Analysis System (SAS). These tasks allow re-running of basic pipeline processes as well as further data reduction tasks.

2.4.1 Creating Event Files

The raw data files are labelled correspond to the different instruments on board *XMM*. PN refers to the PN instrument, M1 to the MOS1 instrument etc. Each instrument has several files, each corresponding to one of the CCD chips on the arrays that make up the detector (7 for each MOS instrument and 12 for the PN), plus a few housekeeping files. These need to be processed into a single calibrated photon event file which can then be used to create images, rate curves etc. To do this there are two tasks that need to be run.

`epproc`

`emproc`

The first creates an event file for the PN instrument and the second creates

two event files, one for each MOS instrument. In addition, they create an attitude history file which is important for many other tasks. The photon event files record the time, position and energy of each photon incident on the detectors and are the basis for all further processing. These tasks also remove hot and flickering pixels and columns which would otherwise contaminate the data.

Figure 2.1 shows an image produced by using every event in the PN event file for the 3-h field. This example illustrates how heavily contaminated the event file is before it is properly filtered.

2.4.2 Filtering the Data

Basic Filtering and image Generation

It is possible to create an image directly from the initial event files, however this will not produce useful results. Filtering of the event files is essential to obtain usable data, and so this is the next step. Non X-ray associated events such as cosmic rays create patterns on the detectors that look different from the impacting of X-rays. These events can be flagged and filtered out easily. On the other hand soft protons, produced by the sun and projected towards Earth in solar flares, produce patterns that look identical to X-rays, so these events need more careful attention.

The first part of the filtering process involves removing all the events that do not look like X-rays. This is simply a matter of screening out events from the event file that have flags indicating a non-X-ray event pattern. The event file is left containing only X-rays and soft protons. At this stage it is also prudent to

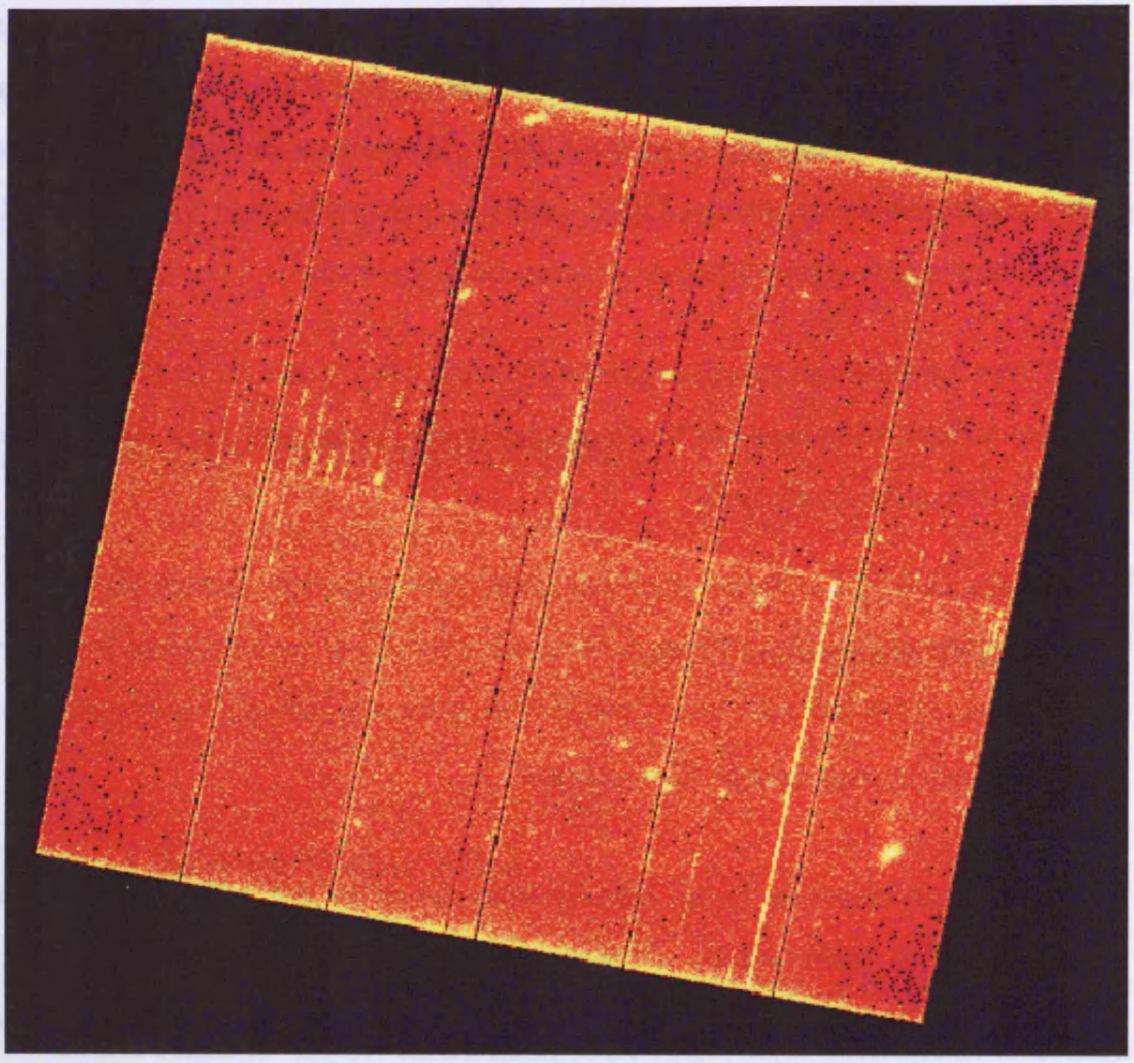

Figure 2.1: Unfiltered PN image. The arrangement of the PN CCD chips can be clearly seen in this image, which is aligned in R.A and Dec coordinates. The contrast is logarithmically scaled.

reduce the number of events in the file by retaining only those with energies in a sensible range. In this case I have chosen $0.5 - 10.0$ keV, despite the fact that the data includes a much broader range of energies ($\sim 0.15 - 15$ keV). This is mainly because the instruments operate most effectively in the mid-range but it also removes some low energy Galactic contamination. The lowest energy is also most strongly attenuated by Galactic absorption, so anything below 0.5 keV is

fairly useless for extra-galactic work.

Figure 2.2 shows the result of this filtering process on the image in figure 2.1. Events falling outside of the field of view of the mirror assembly have now been removed as have several bad columns of data. This image still contains events produced by soft proton impacts however, so the background level is still rather high.

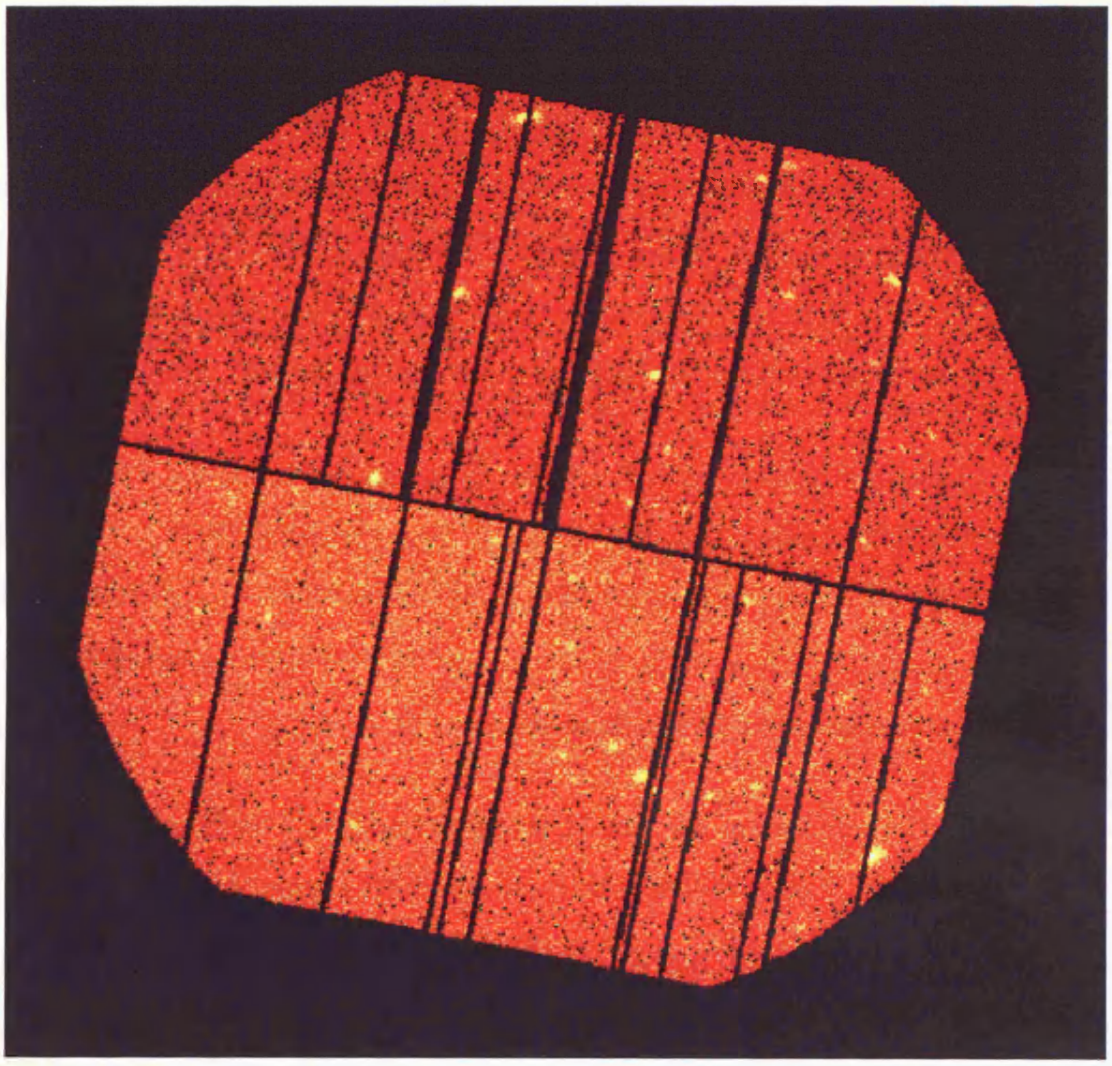

Figure 2.2: A partially filtered PN image after removal of most of the non X-ray events. The FoV of the mirror module is now apparent with the corners having been 'clipped off'. Only photons in the energy range $0.5 - 10$ keV are used to create this image.

Removing Flaring Events

An observation that experienced no flaring events will have a fairly low and constant count rate throughout the observation. Any flaring event will show up as a rapid increase in the count rate to many hundreds of counts per second, and this can lead to serious contamination of the data. For the data in this work flaring events cause a loss of $\sim$ 20% of the total observing time in the 3-h field and $\sim$ 10% for the 10hr field. The 14-h field was less affected by flares and so only $\sim$ 2% of data had to be removed.

To remove flaring events a rate curve is created from the unfiltered event list using energies greater than 10 keV. Figure 2.3 shows the rate curve produced for the 3-h field for a time bin of 50 s. The latter part of this exposure was seriously contaminated by flaring events where the count rate soared by a factor of 100.

By inspecting this rate curve a suitable threshold can be chosen, for example in figure 2.3 50 is appropriate. Then a 'good time interval' (GTI) file is created that flags all time periods as good if they have a count rate less than 50 i.e. periods not contaminated by flares. It can then be used to filter out the high count rate periods from the already partially filtered event file.

The final filtered event file should then be free of all non X-ray events and will contain only photon events within the specified energy range. All further processing can be done using this fully filtered event file. Figure 2.4 shows the final result of this filtering. The remaining noise is primarily due to the quiescent internal instrument background caused by high energy particles interacting with the structure surrounding the detectors. There is also detector noise but this is negligible and only becomes important at energies below $\sim$ 0.5 keV. Due to

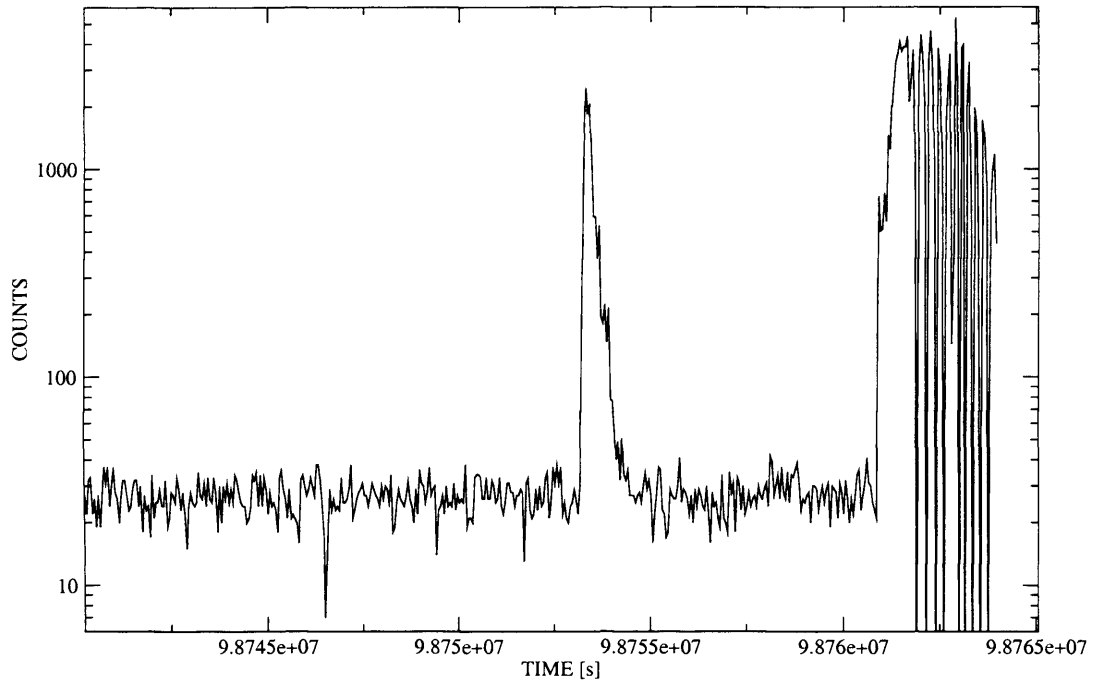

Figure 2.3: Rate curve showing the count rate as a function of time for a section of the 3-h PN exposure. Flaring events cause a rapid increase in the count rate as soft protons flood the detector, resulting in high backgrounds if these events are not screened out.

the small number of photons involved in X-ray observations additional noise is introduced by the Poissonian statistics, and ultimately this is the dominant source of error in the final measurements.

2.5 Source Detection

Detecting sources in X-ray images can be done in many ways but I use the standard method, commonly used for many *XMM* surveys. This source detection procedure is based around a two stage sliding box method combined with a maximum likelihood routine to improve the source parameters and increase the reliability of the final source list. This method is compared to other techniques by Valtchanov,

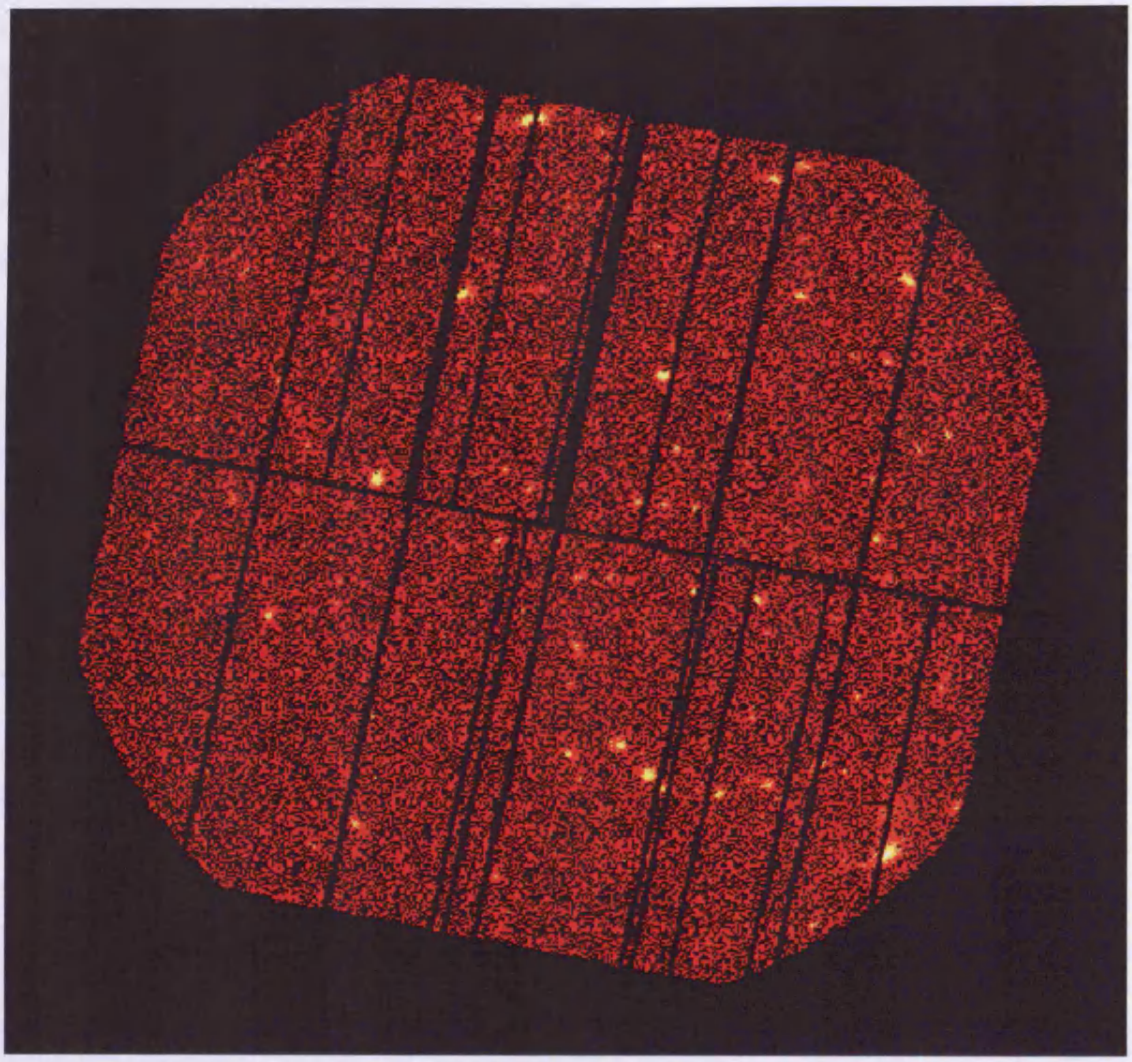

Figure 2.4: Fully filtered PN image after removal of time periods containing flaring events. The background level is now much reduced (c.f. figure 2.2) revealing fainter sources.

Pierre, & Gastaud (2001), and although not the best method for detecting extended sources it is one of the most robust and reliable ways of detecting point sources (primarily AGN), and is included in the SAS collection of tasks.

2.5.1 Energy Bands

Because X-rays are so energetic the CCDs not only measure the time and position of an incoming photon, but can also determine its energy in a crude way. Therefore it is sometimes convenient to separate the data into more than one energy band. Most authors use two or three and I keep to the canonical soft and hard bands as $0.5 - 2.0$ keV and $2.0 - 10.0$ keV respectively. In order to perform the source detection two images from each instrument must be created, so six images in total.

The low end 0.5 keV cutoff ensures that X-ray emission from the Galaxy, which is greatest below this level, is kept to a minimum. Attenuation of soft X-rays by Galactic HI is also more pronounced at energies lower than this cutoff and so this too is avoided. The high energy limit of 10 keV is set by the instrument response, which decreases rapidly at higher energies, more so for the MOS instruments than the PN instrument.

Using two X-ray bands it is possible to define a quantity called the hardness ratio, which gives an indication as to the basic spectrum of a source. For this work it is defined as:

$$HR = \frac{N(H) - N(S)}{N(H) + N(S)}$$

where $N(H)$ and $N(S)$ are the count rates observed for a source in the hard and soft bands respectively, after correction for vignetting. Higher values indicate a harder spectrum.

2.5.2 Detection Stages

Here I describe each stage involved in the detection procedure. There are many stages involved and it is highly labour intensive, but it has the advantage that if anything goes wrong part way through it won't be necessary to repeat all the previous stages. It is possible to run a chain task that will do each of the tasks one after the other, but this is less transparent and generates many intermediate files that are less easy to control. I find it more reliable to do the tasks individually so that errors can be traced more easily.

eexpmap

This is run once for each band for each instrument. It creates an exposure map for each band equal to the relative exposure time that each part of the field of view experiences. Basically it quantifies the vignetting of the telescopes which is quite significant towards the edge of the FoV (see figure 2.5).

emask

Run once for each instrument. This produces a map for each instrument that has a value one in the field of view, and zero elsewhere. Gaps between chips also have value zero. figure 2.6 shows an example.

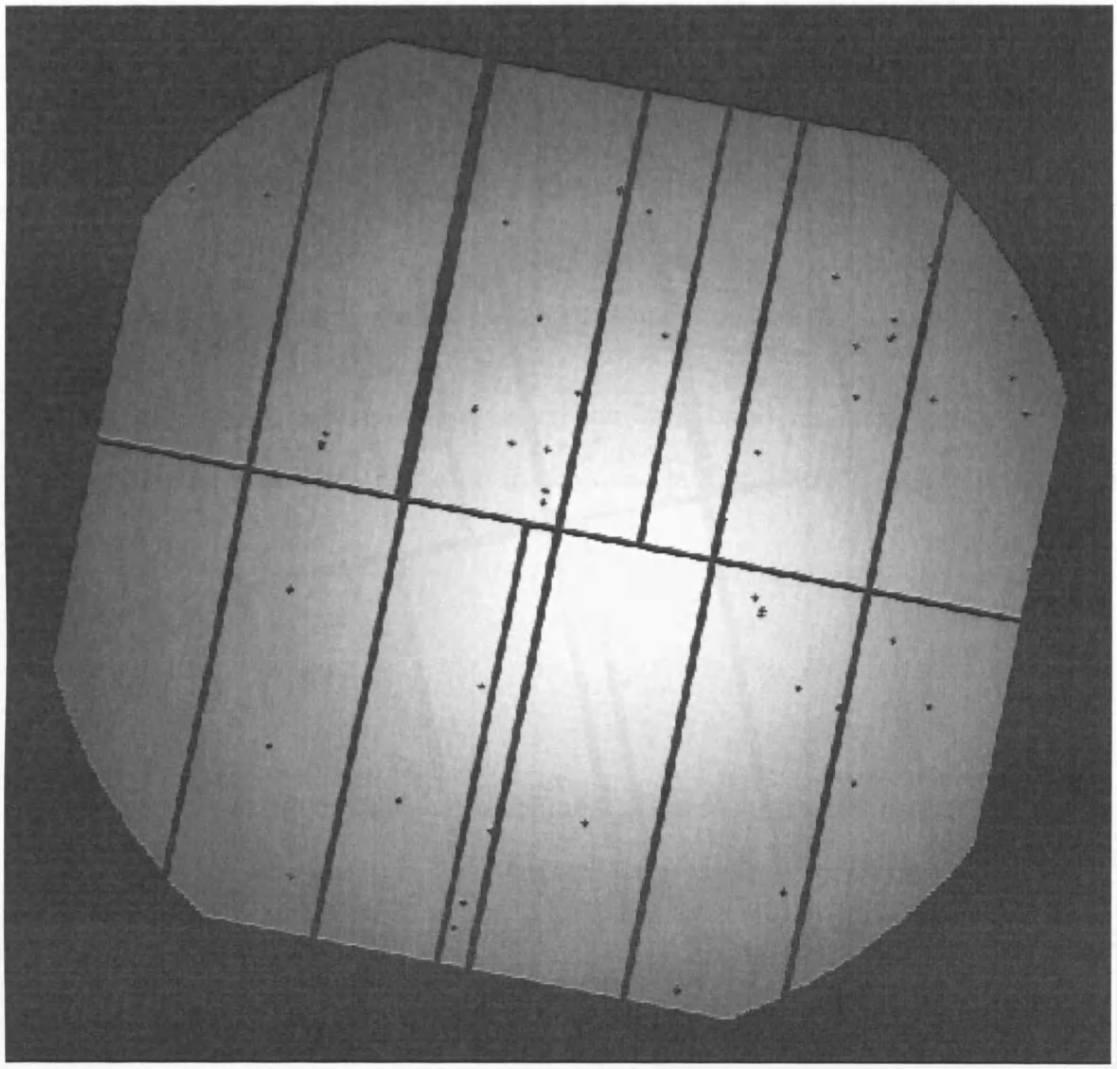

Figure 2.5: Exposure map for the 3-h PN exposure in the soft band. The grey scale is linear. The vignetting of the mirror assembly reduces the effective exposure time by a factor of three or more between the optical axis and the edge of the detector.

eboxdetect (1)

A sliding box source detection algorithm is run on the images which flags any region that exceeds a minimum likelihood limit of 10 (equivalent to about 4 σ) as a source. The likelihood limit L is defined such that $L = -\ln P$, where P is the probability of finding an excess above the local background (defined using

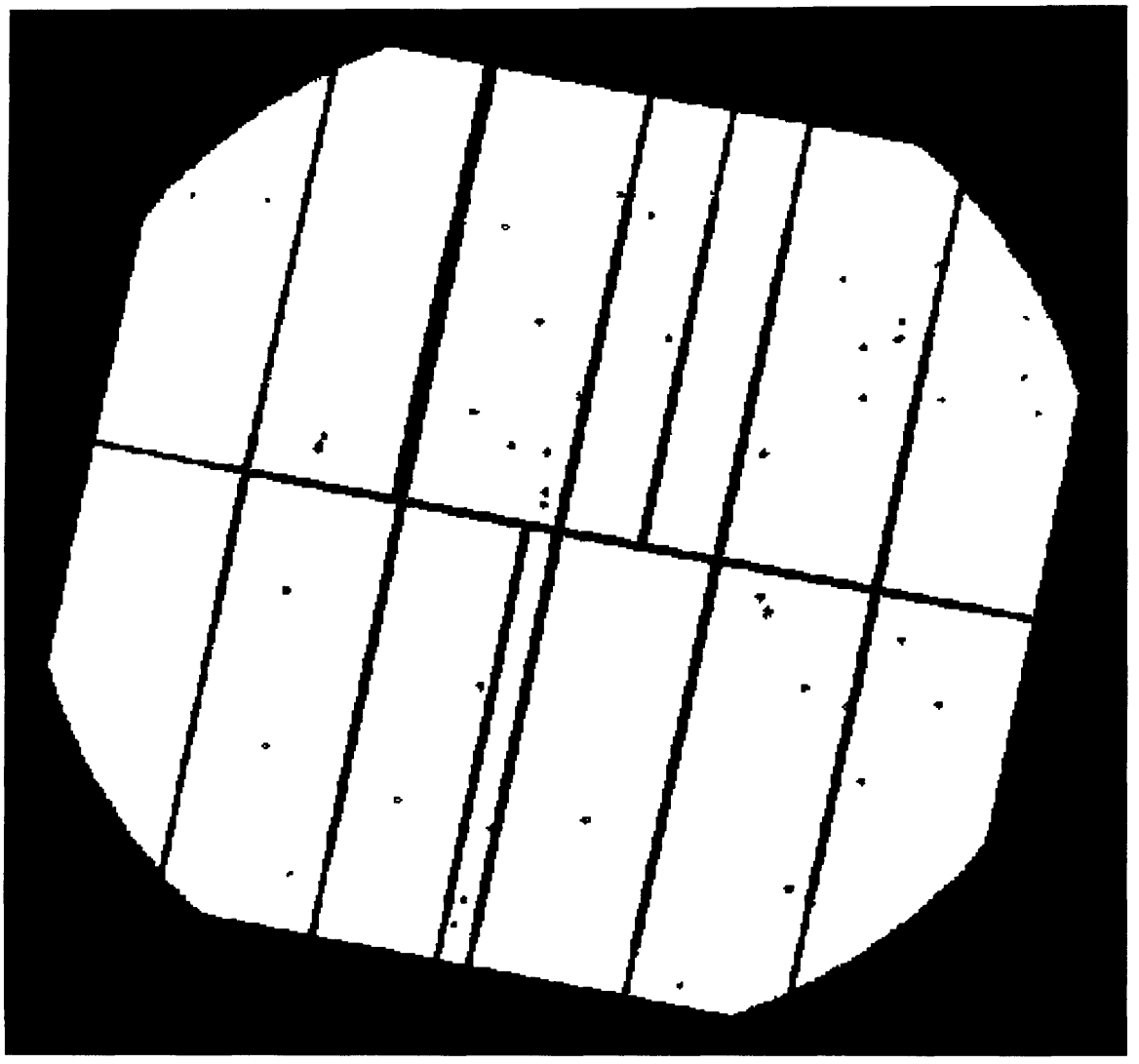

Figure 2.6: Detector mask for the 3-h PN exposure. White represents areas containing usable data for the source detection procedure.

the pixels immediately surrounding the sliding box) which is not due to a source. Essentially this statistic is the user's control over the signal-to-noise ratio that defines an acceptable source. Inevitably, selecting a low likelihood limit will cause more sources to be detected, but a tradeoff has to be made between sensitivity to faint sources and contamination of the source list by spurious detections caused by random fluctuations in the background. Typically, for the sliding box tasks, a fairly low likelihood is chosen so that the later Maximum Likelihood source detection task

(see below) has many potential sources in its input lists.

The box size is increased for successive passes (the number of which is determined by the user) so that regions of different size are all detected at this stage; extended sources, like galaxy clusters for example, will not be detected by the smallest box size (3×3 pixels) so larger sizes are required.

This routine can either be run once for each band for each instrument, on both bands simultaneously for each instrument or simultaneously on both bands of multiple instruments.

esplinemap

Run once for each band for each instrument, this task creates background maps corresponding to each of the six input images. It uses the list of flagged regions from the previous task to remove all the bright sources from the images and interpolate between the gaps to create smoothed background maps. Figure 2.7 shows an example.

eboxdetect (2)

This pass is essentially the same as the first sliding box pass but this time it employs the background maps from the esplinemap task. Because this background map is a far better model for the slowly varying fluctuations than the local one (calculated from the pixels surrounding the box), it enables fainter sources to be detected and so increases the number of sources passed to the next task.

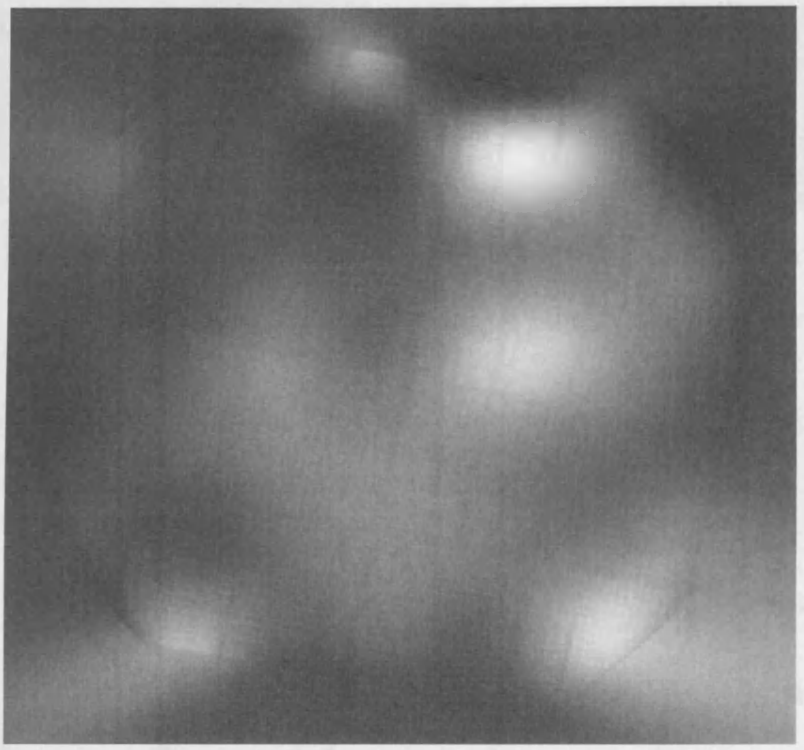

Figure 2.7: Background map for the 3-h PN soft band exposure. The grey scale is linear and shows the variation of the background across the detector.

emldetect

This task is a maximum likelihood (ML) algorithm designed to improve the reliability of the final source list. It takes the source list produced by the second sliding box task as an input list and checks each position against a model for the telescope Point Spread Function (PSF) at that position. A region is flagged as being a source if it exceeds a given threshold probability. In this case I use a higher minimum detection likelihood of 15 with the aim of minimising the number of possible spurious detections, albeit at the expense of slightly less sensitivity. However, the final source parameters are derived using data from both bands and all three instruments simultaneously, which also helps achieve maximum accuracy and further helps to minimise spurious detections from any single camera. Using all the avail-

able data also allows fainter sources to be detected that might otherwise be missed by a using a single detector. In addition, I turn on the error estimation and source extent fitting capabilities of 'emldetect' so that each source is fully parametrised. This task uses all of the exposure maps and background maps from the previous tasks so that the vignetting and local background are taken into account when calculating the parameters for the individual sources.

2.5.3 Energy Conversion Factors

The three X-ray imaging instruments on *XMM* don't measure flux directly, they detect photons, and the different instruments have different sensitivities to photons of different energies. In particular the PN instrument was designed to have a greater overall sensitivity than the two MOS instruments, especially at the higher energy range. Therefore it is necessary to use the correct conversion factor for each band and for each instrument to convert the number of detected photons for a source into a flux. There are many factors that affect the energy conversion factor (ECF): the expected spectrum of a source, the column density of neutral hydrogen that the spectrum is attenuated by and thickness of the optical blocking filter used for the given instrument. Other factors also play a more minor role but these three things are the most important.

Using the web based count rate simulator *WebPIMMS*, part of the NASA High Energy Astrophysics Science Archive Research Centre (HEASARC) web-pages, I obtained flux to counts conversion factors for *XMM* PN and MOS instruments by entering the relevant filter thickness (all thin filter 1 except for the 10-h MOS exposure which used the medium filter) and assuming an average source spectrum of a power law with a photon index $\Gamma = 1.7$ (see section 2.6). The column density of

Table 2.1: Summary table for the 3 *XMM* fields.

				PN ECF		MOS ECF	
Field	R.A. [fk5]	Dec. [fk5]	nH (cm^{-2})	Soft	Hard	Soft	Hard
3-h	03:02:38.6	+00:07:40	7.16E20	7.241	1.311	2.125	0.4534
14-h	14:17:12.0	+52:24:00	1.30E20	7.484	1.316	2.121	0.4553
10-h	10:00:40.4	+25:14:20	2.76E20	7.421	1.314	2.074	0.4506

galactic neutral hydrogen was also entered using the values from table 2.1 (obtained from the HEASARC on-line nH calculator), with no additional intrinsic absorption. The output values are those used in the source detection tasks and convert the counts per second measurement into a flux measurement in units of 10^{-11} erg cm^{-2} s^{-1} (see also table 2.1):

$$Flux = \frac{counts\ per\ second \times 10^{-11}}{ECF}\ erg\ cm^{-2}\ s^{-1}$$

The biggest source of error in these conversion factors is the assumed source spectrum. Even if a power law is assumed for every source there is a broad spread in the photon indices ($\sim 0 - 3$) so for any individual source the assumption of $\Gamma = 1.7$ is likely to be wrong on some level. However, statistically this choice is reasonable and will give fluxes correct to within $\sim 10\%$ for virtually all the sources.

2.6 Notes on X-ray Spectra

The hardness ratio, mentioned above, is in effect a crude measure of the spectrum of a source. Typically the spectrum of an AGN can be simply parametrised by a power law with just two free parameters, the normalisation and the photon index. The photon index is the slope of the power law and Γ is the typical symbol used to

represent it. Quantitatively it gives the number of photons per unit energy range.

$$\frac{dN(E)}{dE} = KE^{-\Gamma}$$

The spectral index on the other hand determines the flux (or intensity in the case of the X-ray background, since it is diffuse and not point like) as a function of energy, typically represented as α.

$$S(E) = K'E^{-\alpha}$$

One is related to the other through integration, and it can be seen that:

$$\alpha = \Gamma - 1$$

For example, the X-ray background has a photon index of 1.4 but a spectral index of 0.4. This is a downward slope towards higher energies, but the energy contained in the background actually increases with energy. This is because the background is so flat. To get the energy density in the spectrum we must multiply the intensity by the frequency. Since frequency is proportional to energy this makes the slope increase by one more i.e.

$$\nu I_\nu \propto E^{1-\alpha} \propto E^{2-\Gamma}$$

So now the exponent is > 1 and the energy density increases with energy. The turnover in the X-ray background occurs at about 30 keV, so this simple approximation is good for the energies detected by *XMM*.

The importance of this is clear when one considers that the XRB is composed

almost entirely of the integrated emission of AGN throughout the Universe. Many X-ray bright AGN have spectra with much steeper slopes than the XRB ($\Gamma \sim 2$), indicating that these sources contribute less and less to the XRB at progressively higher energies. Although these sources dominate the XRB in the soft band they constitute a negligible fraction of the background at its peak at ~ 30 keV, assuming that the spectral shape does not change significantly over this range.

2.7 Basic Results

2.7.1 3-h and 14-h Fields

In total there are 146 sources detected in the 3-h field and 154 in the 14-h field. Most are point sources. Tables 4.2 & 4.3 list the basic properties of the X-ray sources, in the two fields. Throughout this work sources labelled with 3.* refer to 3-h field sources and those labelled with 14.* refer to sources in the 14-h field.

Figures 2.8 and 2.9 show false colour images of the two main fields considered in this work, the 3-h and 14-h fields. Lowest energy X-rays are coloured red with progressively higher energy X-rays being coloured green and then blue. Sources with hard spectra therefore show up blue in these images and soft sources appear red. All the extended sources detected are in the 3-h field and the majority are concentrated in the diffuse red patch visible in the lower right hand corner of the 3-h image, surrounding a bright QSO (source 3.1 in table 4.2 & 4.4). This could be indicative of a galaxy cluster and if the QSO is part of the cluster then the cluster has a redshift of 0.641. Unfortunately because the QSO is so bright it is hard to tell if it actually lies within a cluster, or whether the diffuse emission is simply an

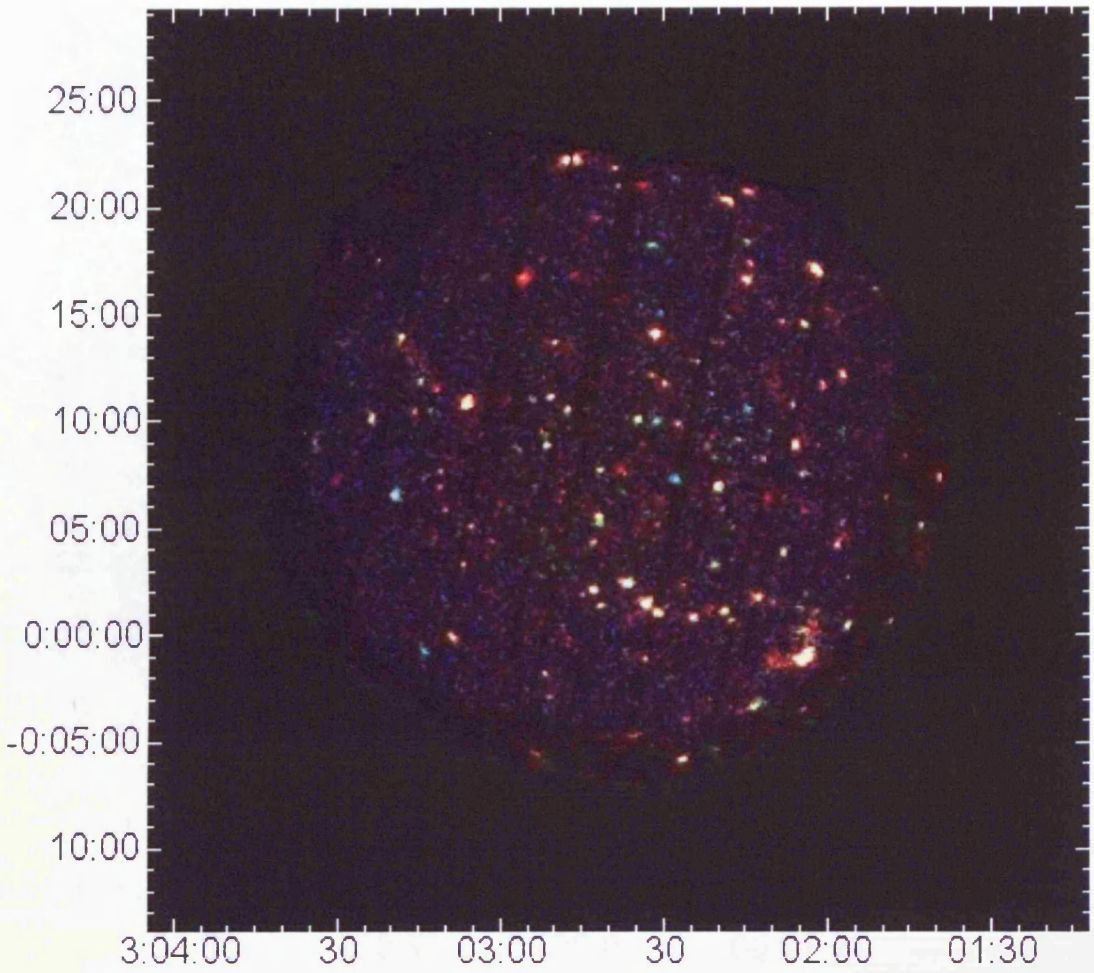

Figure 2.8: False colour X-ray image of the 3-h field. Because each *XMM* exposure gathers data from all the X-ray instruments simultaneously, this image has been constructed from data taken by all three primary cameras. The FoV of each camera covers roughly the same area of sky but with different CCD chip geometries, so mosaicing of data from the three cameras helps to fill in the gaps present in any one array (although not to the same depth of course). Soft X-rays are red ($0.5 - 1.5$ keV), medium are green ($1.5 - 3.5$ keV) and hard are blue ($3.5 - 10$ keV).

effect due to the broadening of the *XMM* point spread function towards the edge of the map. It is also unfortunate that this particular source lies off the edge of the deep optical map I use to identify the X-ray sources, and so an optical cluster search of this region is not possible at this time. Digitised Sky Survey images of this region do not show any evidence for a galaxy cluster but do show the optical counterpart for the QSO.

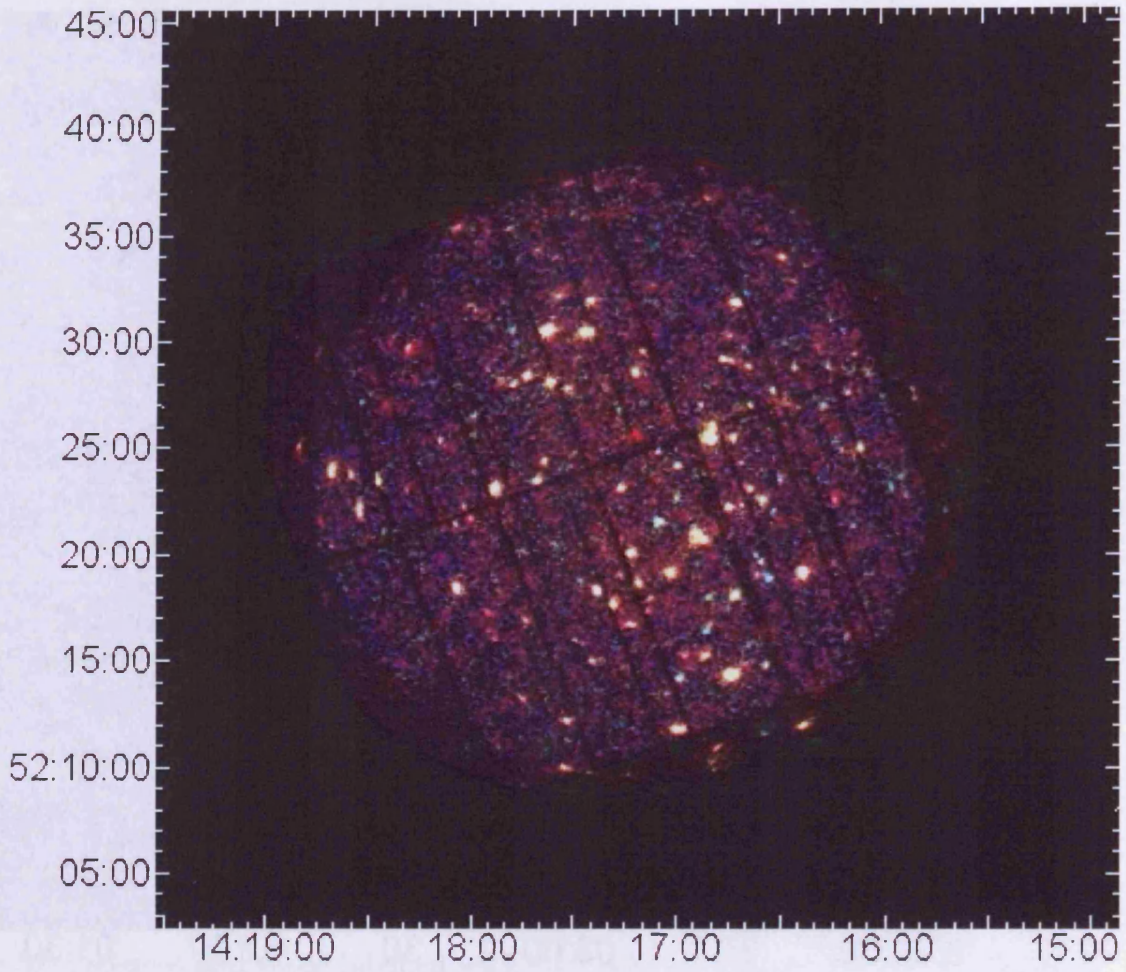

Figure 2.9: As figure 2.8 but for the 14-h field.

Figure 2.10 shows the differential source counts versus both soft and hard band flux, for all the sources detected in the two fields. These plots clearly demonstrate the effect of incompleteness at lower fluxes where the source counts drop off dramatically. This effect begins to become important at fluxes of 1.5 and 6×10^{-15} erg cm^{-2} s^{-1} for the soft and hard band sources respectively. Above these fluxes we are effectively 100% complete. This is comparable in depth to, for example, the HELLAS2XMM survey (Baldi et al., 2002), the early *XMM* Lockman Hole observations (Hasinger et al., 2001) and serendipitous *Chandra* observations (e.g. Gandhi et al., 2004), while reaching slightly deeper than the Serendipitous

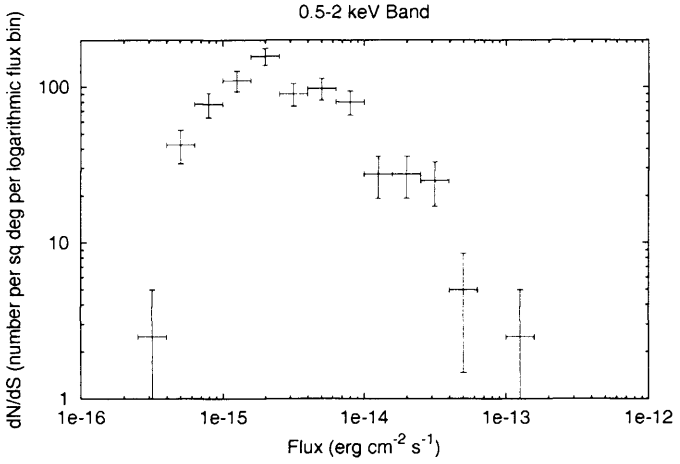

(a)

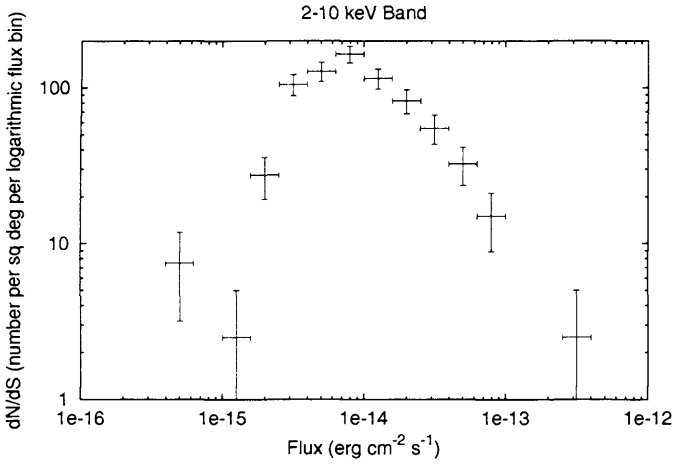

(b)

Figure 2.10: Differential source counts for the combined 3-h and 14-h field X-ray sources. Incompleteness causes the source counts to turn over at ~ 1.5 and $\sim 6 \times 10^{-15}$ erg cm^{-2} s^{-1} in the soft and hard bands respectively. Source fluxes are calculated from the source detection procedure outlined in the text. Horizontal bars indicate the logarithmic flux ranges over which the sources are tinned. Vertical error bars are the square root of the number of sources in each bin.

XMM Survey in the AXIS field (e.g Barcons et al., 2002).

2.7.2 10-h Field

Since the 10-h field does not have deep optical coverage it is not studied to the same degree as the other two fields. However, for completeness figure 2.11 shows a false colour image of this field. The most interesting feature in this field is the region of faint extended soft emission in the lower left corner. This is a suspected galaxy cluster at high redshift or a low luminosity group at low redshift. Deep optical data of this area would resolve this question.

There are 151 X-ray sources detected in this field.

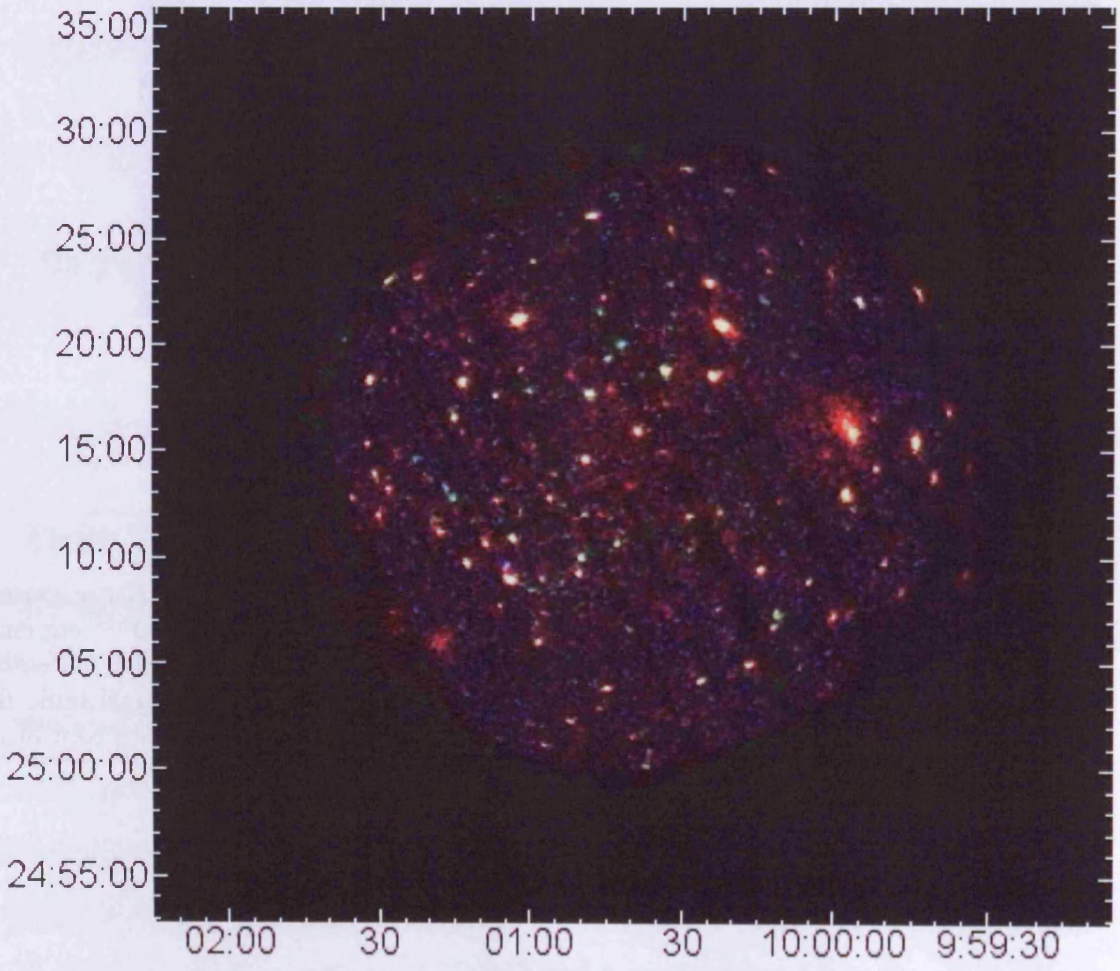

Figure 2.11: As figure 2.8 but for the 10-h field.

Chapter 3

The X-ray/Sub-mm Relation

This chapter concerns the analysis of a comparison between X-ray and sub-mm data for two regions, one in the 3-h field and one on the 14-h field, dubbed the Canada UK Deep Sub-mm Survey (CUDSS) (Webb et al., 2003a; Eales et al., 2000). Results from this work are reported in the first paper to come from my PhD (Waskett et al., 2003).

3.1 Introduction

Recent advances in sub-mm astronomy have allowed rapid progress in our understanding of the early Universe. This region of the electromagnetic spectrum has largely been opened up by the powerful instrumentation that has become available within the last decade. One of the key instruments in this field has been the sub-mm Common User Bolometer Array (SCUBA), operating primarily at 850 μm, at the Naysmith focus of the 15m James Clerk Maxwell Telescope (JCMT) on

Mauna Kea in Hawaii. Since its commission, deep surveys with SCUBA (Smail, Ivison, & Blain, 1997; Hughes et al., 1998; Barger et al., 1998; Eales et al., 1999) have resolved a significant fraction of the recently discovered far-IR and sub-mm background (Puget et al., 1996; Fixsen et al., 1998; Hauser et al., 1998), also called the Cosmic IR Background (CIRB). The importance of this becomes clear when one considers that the total integrated energy observed in the CIRB is comparable to the total integrated energy associated with the optical-UV background. Dust is very important in the interstellar medium as it absorbs optical-UV photons and re-radiates far-IR photons, thus affecting our view of the Universe. Since this is the mechanism that produces most of the CIRB, it is possible that half of the light ever emitted by stars has been reprocessed by dust. However, there is one other mechanism that could contribute to this background light and that is the absorption, by dust, of the radiation from Active Galactic Nuclei (AGN).

In the standard model of AGN the central black hole is fed by an accretion disc (e.g.. Antonucci, 1993). Around this disc lies a torus of heavily obscuring material containing large amounts of dust (e.g.. Nenkova, Ivezić, & Elitzur, 2002). If viewed close to the axis the AGN may be visible directly, in which case a Quasar or a Type-I Seyfert Galaxy is observed, with characteristic broad spectroscopic lines. Evidence for the obscuring torus comes from observations of Type-II Seyfert Galaxies, which in this model are seen edge-on. type-I emission, which would indicate the presence of an AGN, can only be indirectly observed by reflection off material above and below the torus. Direct evidence for the torus itself comes from its interaction with the nuclear radiation. The AGN heats up the torus which produces primarily mid-IR emission, but there will also be sub-mm emission from the dust. The process is much the same as in starlight re-processing, but here it is mainly UV and X-ray photons that are absorbed, and the dust tends to be hotter.

Models suggest that between 5 and 30% of the CIRB might be produced in this way (Gunn & Shanks, 1999; Almaini et al., 1999). Franceschini, Braito, & Fadda (2002) argue for the revision of this standard model, and suggest that Type-I and Type-II AGN are different populations that follow unrelated evolutionary paths, in particular at high redshifts. As deeper and more extensive X-ray/mid-IR surveys are collated this possibility will be tested more thoroughly, and a more complete picture of AGN may emerge.

The Cosmic X-ray Background (XRB) on the other hand contains much less energy than the optical or IR backgrounds ($\sim$ 1/100 *th* depending on the definition). With the advent of powerful new X-ray telescopes such as *Chandra* and *XMM-Newton*, it has become possible to resolve most of this background radiation into discrete sources (e.g. Rosati et al., 2002; Hasinger et al., 2001). The simplest form of the XRB is a power law defined as,

$$N = KE^{-\Gamma}$$

where N is the number of photons per second per cm^2 per keV, K is a normalisation constant and Γ is the photon index. This reaches a peak in energy density at $\sim$ 30 keV, and below this it has a very hard spectrum with a photon index $\Gamma = 1.4$. The most completely resolved part is the soft XRB ($0.5 - 2$ keV), which is dominated by unobscured AGN and QSOs but these sources have much steeper (i.e. $\Gamma > 1.4$) spectral shapes than the XRB and cannot explain the spectrum at harder energies. Therefore, a population of more heavily obscured AGN, with flatter spectral shapes, is likely to be involved in the production of the hard XRB. The resolution of the XRB is less complete at these higher energies, although *XMM-Newton* with its sensitivity up to energies of 10 keV, is making a major contribution here. The deepest X-ray surveys with *Chandra* and *XMM-Newton* are beginning

to reveal a population of highly obscured AGN (e.g. Hasinger et al., 2001). An obvious possibility is that these highly obscured AGN, responsible for the hard XRB, are also producing the CIRB.

The most direct way of testing this, of course, is to make X-ray observations of the sources revealed by the deep SCUBA surveys. The studies which have so far been carried out (Almaini et al., 2003; Fabian et al., 2000; Hornschemeier et al., 2000) suggest that SCUBA sources are not generally X-ray sources.

In this chapter I investigate the sub-mm/X-ray relation for objects in the 3-h and 14-h Canada France Redshift Survey fields (Lilly et al., 1995b), for which both *XMM* and SCUBA data exist.

The composite images shown in this chapter are a result of merging images from the PN and two MOS instruments together using the SAS task 'emosaic'. This task is only used in this instance to produce a clear image, and is not used for further analysis of the data, except for the statistical tests described in section 3.2.2. See figs. 3.1 and 3.2.

The majority of the work presented in this chapter concentrates on the 3-h *XMM* field and the corresponding CUDSS region which lies in the centre of the *XMM* FoV. The 14-h field is also part of CUDSS but the survey region lies towards the edge of the *XMM* FoV, and the X-ray data are therefore less reliable.

3.2 SCUBA sources

There are 27 sources detected at 850 μm in the 3-h CUDSS field, spanning a region of approximately $9' \times 6.4'$ (Webb et al., 2003a). This lies in the central part of

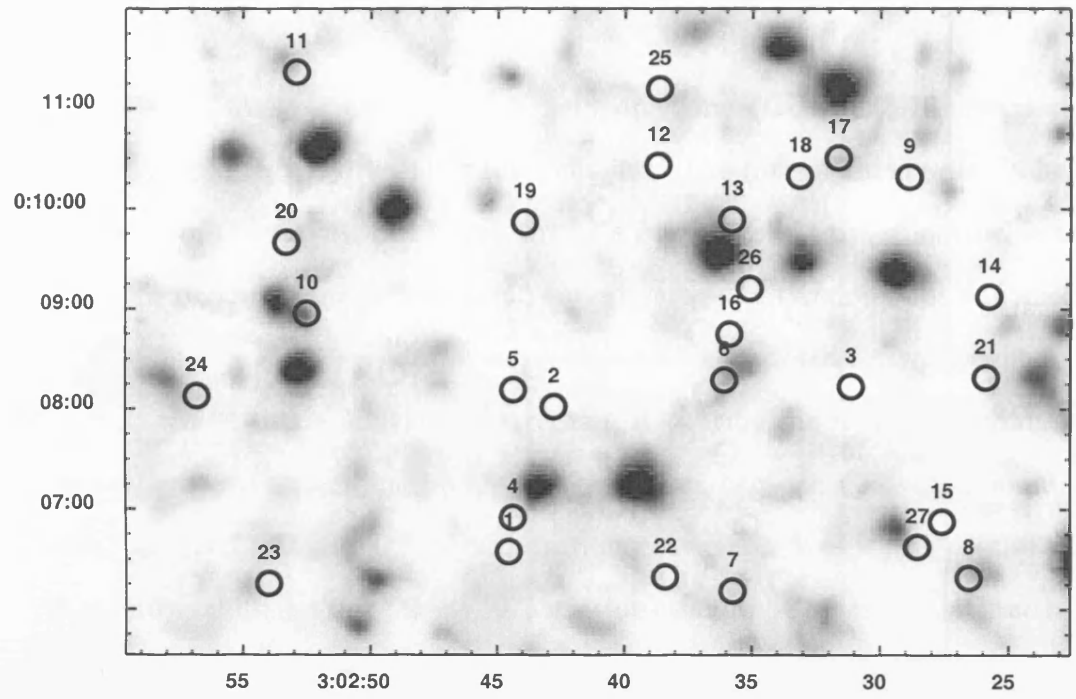

Figure 3.1: The central part of the 3-h *XMM* survey showing the 3-h CUDSS region in the soft X-ray band, for clarity. Overlayed are 14″ diameter circles at the positions of the SCUBA sources. Numbers and positions are from Webb et al. (2003a).

the *XMM-Newton* FoV which is roughly circular with a diameter of $\sim 30'$.

The 14-h CUDSS field is approximately $7.7' \times 6.4'$ (Eales et al., 2000) and is centred about $8.5'$ North-East of the *XMM* pointing axis. This map contains 23 sources.

3.2.1 X-ray properties of the SCUBA sources

The first thing to do when comparing sources in the same area but different parts of the spectrum is to see if any of them match up. An inexact match-up does not necessarily mean that two objects are unassociated, because of the error in

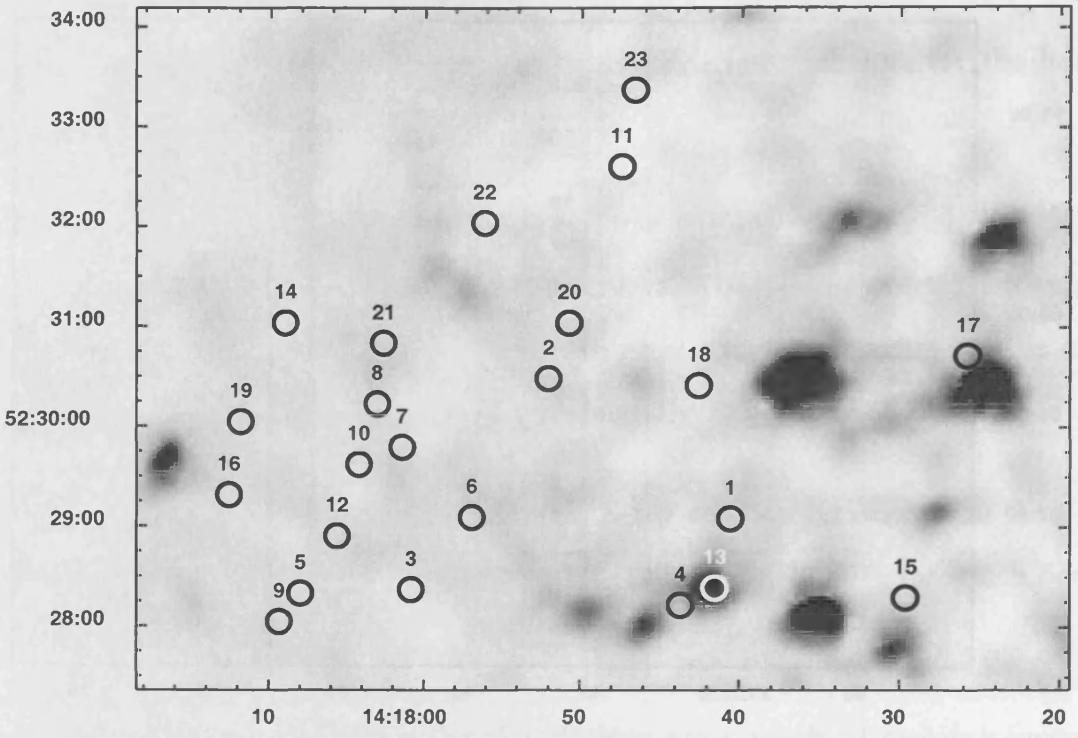

Figure 3.2: As fig 3.1 but for the North-East part of the 14-h *XMM* survey showing the 14-h CUDSS region. Numbers and positions are from Eales et al. (2000) and Webb et al. (2003b). The pattern of X-ray sources in this plot is mainly due to natural variations in number density across the sky, and the domination of two QSOs near the right edge, although the far top left may suffer slightly from the declining sensitivity of *XMM* towards the edge of its FoV.

the positional accuracy of both sets of objects, caused by the finite resolution of the instruments involved. For SCUBA the FWHM of the 850 μm beam is $\sim 14''$, whereas for *XMM* the on-axis FWHM is $\sim 6''$, which increases with larger off-axis angles. For the purposes of this work the *XMM* PSF can be considered constant, and equal to $6''$, across the area containing the 3-h SCUBA sources, as this is a small fraction of the total *XMM* FoV. As for the 14-h field, the off-axis angle of the CUDSS map means that the *XMM* PSF is not so well behaved, and further analysis less reliable. However, as an approximation the FWHM has a median value of $\sim 9''$ across the 14-h CUDSS map.

The 3-h Field

Of the 27 SCUBA sources in the 3-h field only one (CUDSS 3.10) is possibly associated with a region of faint X-ray emission. The flux of this region is below the flux limit of the survey, but it appears as a faint patch in the smoothed image, fig. 3.1. This region was picked up by an earlier version of the detection software at the thresholds used, however after re-analysis with the updated software, which has better calibration, this source is no longer detected using the same thresholds. An additional degree of uncertainty exists for this region, because it lies on a boundary between two PN CCD chips. Source detection near chip edges is less precise than in the centre of chips, so this possible associations should be regarded with extreme caution.

Given the position of the SCUBA sources the probability that there is a chance coincidence with an unrelated X-ray source within a distance r is given by Poissonian statistics as:

$$P = 1 - exp(-\pi n r^2)$$

where n is the surface density of X-ray sources.

CUDSS 3.10 lies $\sim 3.6''$ from the centre of the region of faint X-ray emission (given by the detection with the earlier version of SAS). The surface density of X-ray sources at the flux limit of this survey is $n = (5.7 \pm 0.5) \times 10^{-5}$ per square arc second, thus for this source, which is below the flux limit, $P > 0.0023$. A deeper exposure of this region would determine if this X-ray region is actually a source, and thus a significant association, or just noise.

The 14-h Field

Figure 3.2 shows the CUDSS 14-h map as viewed in soft X-rays with the SCUBA sources overlayed. CUDSS 14.13 is clearly near a significant X-ray source, and this is indeed detected by the XMM source detection software. This X-ray source has a soft band flux of $(6.7 \pm 0.51) \times 10^{-15}$ erg cm^{-2} s^{-1} and a hard band flux of $(2.2 \pm 0.25) \times 10^{-14}$ erg cm^{-2} s^{-1}, assuming a power law photon index of 1.4. The positional offset is 4.8″, and the surface density of X-ray sources brighter than the flux of this source is $n = (4.5 \pm 0.4) \times 10^{-5}$ per square arc sec. This leads to $P = (3.3 \pm 0.2) \times 10^{-3}$ for this coincidence.

Webb et al. (2003b) discuss this SCUBA source to some extent. It is identified with the optical source CFRS14.1157, which is 1.2″ from the position of my X-ray detection. This source is also detected in the radio (Eales et al., 2000) and by ISO making it an interesting source. It also has a spectroscopically measured redshift of $z = 1.15$ (Hammer et al., 1995b). The optical/NIR colours are very red, $(I-K)_{AB} = 2.6$, consistent with an irregular or spiral galaxy with high extinction, and the X-ray hardness ratio is quite high (~ -0.3) implying that this is a fairly heavily obscured object. HST imaging of this object shows a disturbed morphology (Webb et al., 2003b), suggesting the X-ray activity may be related to a possible interaction.

By taking the measured redshift for this source, and the X-ray flux in the two bands, it is possible to estimate the column density of neutral hydrogen responsible for the obscuration of the X-rays. If we assume an intrinsic photon index of $\Gamma = 2.0$ (Hasinger et al., 2001) then a column density of $N_H = 3.0 \times 10^{22}$ cm^{-2} produces the correct X-ray fluxes.

It is interesting to ask at this point whether, assuming an AGN is responsible for the X-ray emission, it can also be responsible for the sub-mm flux measured by SCUBA (through the heating of dust). By assuming that 3% of the bolometric luminosity of an unobscured AGN (optical through to X-ray) is emitted in the $0.5 - 2$ keV band (Page et al., 2001), and correcting for the intrinsic absorption, the AGN has a total luminosity of $(1.0 \pm 0.1) \times 10^{38}$ W.

The far-IR luminosity on the other hand is $(2.0 \pm 0.6) \times 10^{39}$ W, assuming a single dust temperature of $40K$ and $\beta = 1.5$. This means that the AGN is 20 times less luminous and so cannot possibly power the far-IR luminosity on its own. The majority of the far-IR luminosity must therefore be powered by star-formation, and in-fact Webb et al. (2003b) estimate a star-formation rate of 210 $M_{\odot}$ Yr^{-1} assuming that the far-IR luminosity is produced in this way. However, the far-IR luminosity is highly model dependent and can be much lower, for example a single temperature dust component of < 20 K gives a far-IR luminosity low enough to be equal to the AGN luminosity. Although this model is unlikely in light of the high inferred star formation rate which would result in at least some warm dust, and this would push up the luminosity greatly. For example, a two dust component model with 50 times as much cold dust (15 K) as warm dust (45 K) and $\beta = 2$ (e.g. Dunne & Eales, 2001) has a far-IR luminosity of $(8.6 \pm 2.7) \times 10^{38}$ W, making it 8 times as luminous as the AGN. Thus, the conclusion that this source is dominated by star-formation and not an AGN is hard to avoid.

Further evidence for the star-formation activity of AGN host galaxies can be found in the 8 mJy SCUBA survey fields (Ivison et al., 2002). The X-ray detected SCUBA sources in these fields (15%) are consistent with obscured AGN, but the AGN bolometric luminosities are not sufficient to power the far-IR luminosities, unless the X-ray emission is attenuated by Compton thick ($N_H > 10^{24}$ cm^{-2})

material. If not, star-formation is likely to be responsible instead.

Page et al. (2001) draw a similar conclusion for high redshift X-ray selected sources that have a SCUBA detection. For their sample the AGN luminosity and far-IR luminosity are more closely matched, being at most a factor of 4 different in favour of the far-IR luminosity. The main differences in this case are that the AGN in their sample are at higher redshift ($z = 1.5 - 3$) and are more luminous ($L_{AGN} > 4.36 \times 10^{12} L_{\odot}$) than CUDSS 14.13. The HI column densities in their sample are similar to CUDSS 14.13.

Whereas Page et al. (2001) target X-ray sources with SCUBA, a reverse study whereby bright SCUBA sources are observed with the *Chandra* X-ray observatory was carried out by Bautz et al. (2000). They measure the AGN/far-IR luminosity for two bright, lensed sub-mm sources at high redshift and find that the AGN is responsible for the majority of the far-IR luminosity in one and $\sim$ 40% in the other, implying that some other power source must be responsible for the deficits.

3.2.2 Statistical analysis

The fact that only one out of 50 SCUBA sources matches an X-ray source does not mean that the population as a whole is not significantly emitting X-rays. A simple way to test this is to coadd the X-ray counts associated with each SCUBA source and see if the average X-ray flux of the SCUBA sources is statistically significant. I refer to this as the coadding technique.

The CUDSS 3-h map is located in the centre of the *XMM* FoV which lies entirely in the central CCDs of the two MOS arrays. However, the PN array contains many chip boundaries in this region, and several SCUBA sources lie on

or near one of these boundaries. Therefore, to avoid possible problems caused by inconsistencies between sources, the PN data is not used in the analysis.

Due to the 14-h CUDSS map being off-axis in the *XMM* survey I consider the 3-h field to be more useful and accurate for study. However, for consistency, the 14-h field is analysed in the same way as the 3-h map, but is considered separately because of the difficulty in combining the results from the two regions in any sensible way. The following description relates to the 3-h field, with differences for the 14-h field noted where relevant.

The *XMM* optics spread out photons from a point source into several pixels in the images (the PSF). Although the pixel at the co-ordinates of the source should contain the peak of the emission, neighbouring pixels also contain information from the source. This effect is important for faint X-ray sources in particular because in some cases there may be no actual photon counts in the pixel corresponding to position of the source. Therefore, for analysis of the SCUBA sources in the X-ray images, the information from the whole PSF of *XMM* needs to be recovered and incorporated into the central pixel.

Images were accumulated in each band for the two MOS instruments and superimposed, as described at the end of section 2.4. They were then convolved with a 2D Gaussian of $FWHM = 6''$, the FWHM of the on-axis *XMM* beam ($9''$ for the 14-h field to reflect the larger, off-axis, PSF). This creates a map in which the signal in each pixel is the best possible estimate of the X-ray signal at that point. By smoothing the image with the *XMM* PSF (or a reasonable model for it in this case), the information in the central pixel contains all the information from the surrounding pixels, weighted according to how likely it is that the photons detected in those pixels came from the source. This technique for making the best

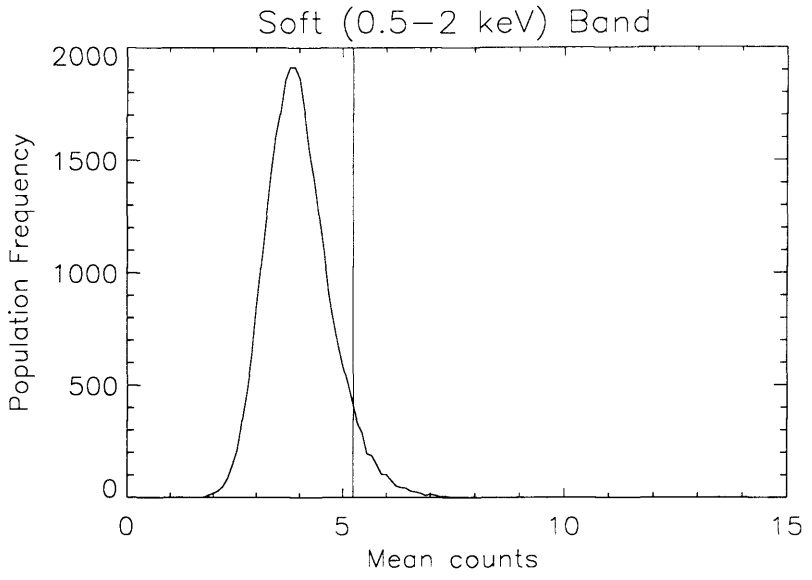

(a)

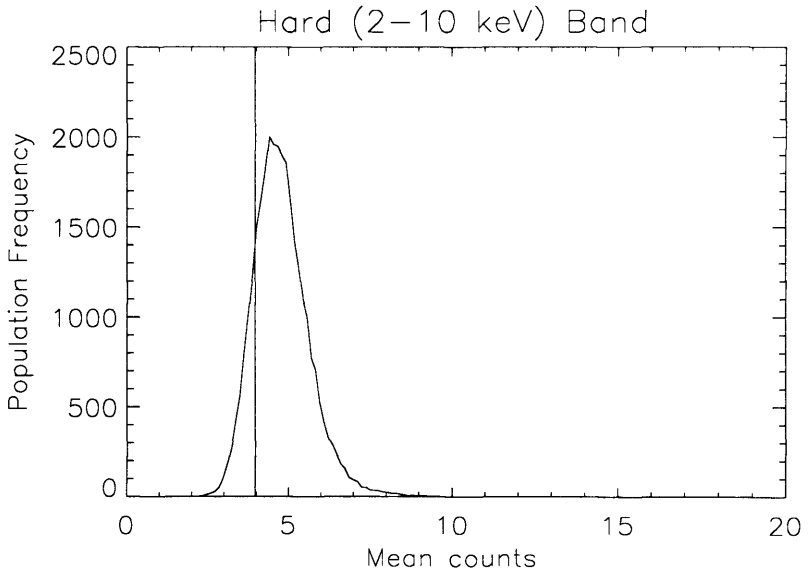

(b)

Figure 3.3: Histograms showing the distribution of mean X-ray counts associated with each source for 30,000 artificial SCUBA samples in the 3-h field. Vertical lines represent the mean counts for the real SCUBA sources. See text for details.

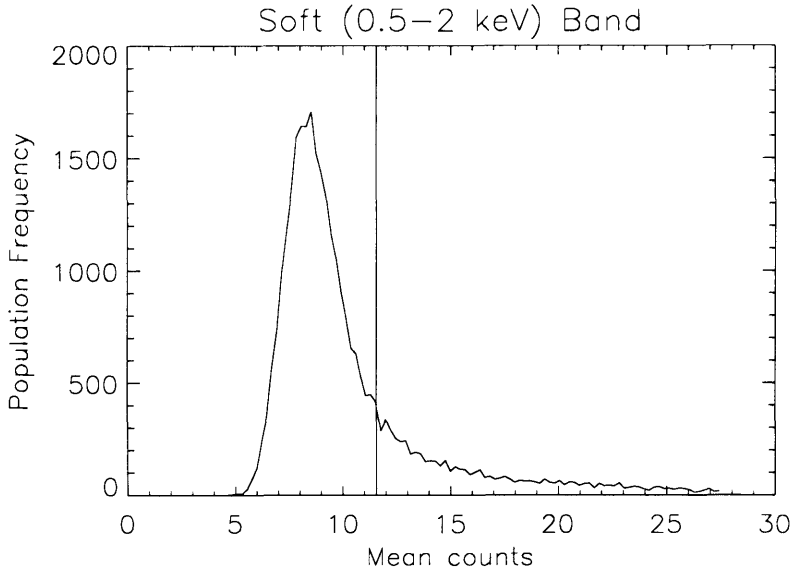

(a)

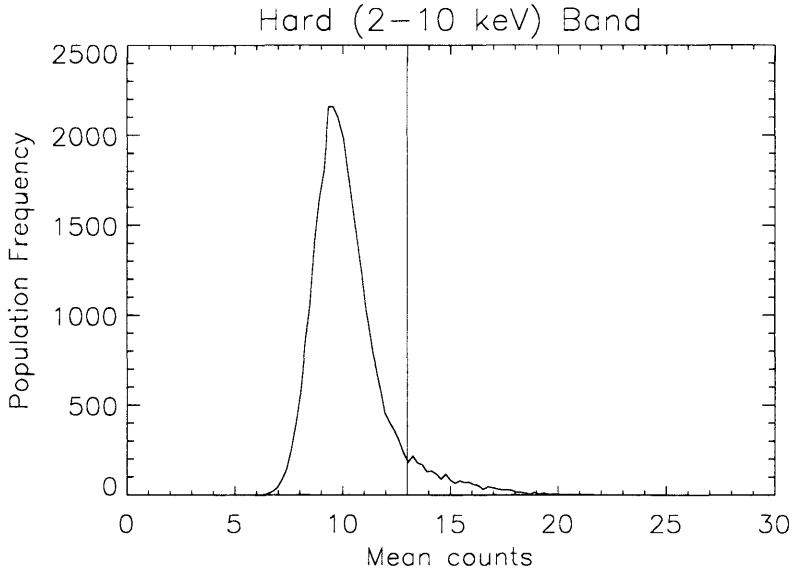

(b)

Figure 3.4: As for figures 3.3(a) & 3.3(b) but for the 14-h field. This plot highlights the higher background in this field compared to the 3-h field, a feature of the survey itself rather than the poorer response of the instrument for large off-axis angles.

estimate of the flux at a given point has been widely used in other wavebands (e.g. Phillipps & Davies, 1991; Eales et al., 2000), and is similar to the stacking technique used in the analysis of the *Chandra* Deep Fields (e.g Brandt et al., 2001).

The mean X-ray flux of the 27 SCUBA sources was determined for each energy band. To estimate the significance of the values a Monte-Carlo simulation was used. 30,000 random samples of SCUBA sources were produced at randomly selected positions within the CUDSS region, each with 27 sources. The mean X-ray flux for each sample was measured in the same way as for the real sample. The distribution of these means is shown in figs 3.3(a) and 3.3(b). The number of trial samples for which the mean equals or exceeds the observed sample mean is then calculated (See figures 3.4(a) and 3.4(b) for the 23 SCUBA sources in the 14-h field). A low number of trials exceeding the observation indicates a significantly important measurement.

Out of 30,000 random trials 2,010 equalled or exceeded the observation ($\sim$ 6.7%) for the soft band and 25,800 ($\sim$ 86.0%) for the hard band (see fig. 3.3(a) and 3.3(b)). A more restricted sample was also tested, in case some of the less secure SCUBA detections were in fact false. The 9 SCUBA sources with the highest flux produced $\sim$ 63.3% and $\sim$ 62.4% of trials that equalled or exceeded the observation, for the soft and hard bands respectively. Thus the SCUBA population is not detected, and is lost within the unresolved X-ray background. Converting the mean counts per SCUBA source into a mean flux gives a 99% upper limit estimate of 1.25×10^{-16} erg cm^{-2} s^{-1} in the soft band and 6.62×10^{-16} erg cm^{-2} s^{-1} in the hard band, the true values falling below these limits 99% of the time.

As an additional test, to take the accuracy of the SCUBA positions into account, I repeated this test by selecting the brightest X-ray pixel within a search

radius of 4″ of the given SCUBA position, instead of just taking the pixel value at that position. No significant difference was obtained, as the mean fluxes for both the randomly generated samples and the true samples increased by a similar number of X-ray counts, leading to similar significances and mean X-ray flux limits.

For the 14-h field 22.7% and 7.4% of trials equalled or exceeded the observation, in the soft and hard bands respectively (see figures 3.4(a) and 3.4(b)). The flux limits are less stringent than the 3-h field at 8.0×10^{-16} erg cm^{-2} s^{-1} in the soft band and 1.3×10^{-15} erg cm^{-2} s^{-1} in the hard band. This is likely to be a consequence of the 14-h CUDSS region being off-axis in the *XMM* survey. The vignetting of the telescope increases the flux limit towards the edge of the FoV because of the reduced effective exposure time compared to on-axis.

3.3 sub-mm properties of X-ray sources

Taking the reverse approach, the sub-mm properties of the 18(16) X-ray sources within the 3-h(14-h) SCUBA maps can be determined. The SCUBA maps are heavily confused, not only from the positive sources but also the negative side lobes produced by the chopping procedure. Therefore, the SCUBA sources not associated with X-ray sources are removed from the map, including the side lobes. This reduces the confusion from known sources, in order to better test the low level emission in the map that is unresolved but may still be real, and associated with X-ray sources. After this procedure, the weighted mean 850 μm flux of the 3-h X-ray population is found to be 0.48 ± 0.27 mJy. The 14-h field yields a mean 850 μm flux of 0.35 ± 0.28 mJy. These are not significant detections, but are tentatively

suggestive of dust emission.

These measurements are in contrast to the mean sub-mm flux of 1.69 ± 0.27 mJy obtained by Barger et al. (2001) for a sample of 136 X-ray sources selected in the $2-8$ keV band, detected in the Chandra Deep Field North. Although for a restricted sample of soft X-ray sources with $\Gamma > 1$ they find the mean sub-mm flux is much lower at 0.89 ± 0.24 mJy, consistent with my 3 σ upper limits of 0.81 and 0.84 mJy for the two fields. This is also consistent with Almaini et al. (2003) who measure a noise weighted mean of 0.89 ± 0.3 mJy for their X-ray sources. It is perhaps not surprising that Barger et al. (2001) find many X-ray sources with hard spectra ($\Gamma < 1$), for which they measure a mean sub-mm flux of 1.77 ± 0.21 mJy, since their sources are selected in a hard X-ray band. In contrast my sources are selected in the soft $0.5-2$ keV band as well as the hard $2-10$ keV band, and so there are many more sources with soft rather than hard spectra in my surveys. These soft sources dominate my sub-mm measurement which could partially explain my lower values.

An alternative explanation for the differing mean sub-mm measurements in different studies may come from the different methods used in calculating them. Not removing SCUBA sources that do not coincide with X-ray sources will result in higher residual sub-mm measurements than my method.

The mean soft X-ray flux for the X-ray sources in these two regions are $(1.8 \pm 0.1) \times 10^{-15}$ erg cm^{-2} s^{-1} for the 3-h CUDSS map and $(7.8 \pm 0.4) \times 10^{-15}$ erg cm^{-2} s^{-1} for the 14-h CUDSS map, measured in the soft band.

3.4 Discussion

3.4.1 AGN Verses Star-formation

The lack of X-ray/SCUBA coincidences suggests three main possibilities. Either the X-ray survey is not deep enough to detect the AGN that may exist within the SCUBA sources; the AGN are obscured by Compton thick material, leading to very little nuclear radiation escaping unhindered ($N_H > 10^{24-25}$ cm^{-2}); or the SCUBA sources do not contain AGN.

Redshift information on the X-ray and SCUBA populations lends support to the separate population hypothesis. Recent deep X-ray surveys (Hasinger et al., 2001; Rosati et al., 2002; Mainieri et al., 2002) have determined the redshift distribution for large fractions of their sources. With a median redshift of < 1 these surveys differ from the AGN synthesis models (Gilli et al., 2001) which predict higher peak redshifts of 1.3-2. In contrast the deep SCUBA populations have been placed at much higher redshifts, typically $z \sim 2$ or greater (Ivison et al., 2002; Chapman et al., 2003b), which would naturally explain the small overlap between the two observed populations.

Can I be sure that SCUBA sources are powered by star-formation and not by AGN? The latter is still a possibility, despite the low SCUBA/X-ray coincidence, as the AGN may be heavily obscured and as such not visible to this X-ray survey. NGC6240, for example, is known to be a starburst galaxy that also contains a heavily obscured AGN ($N_H > 2 \times 10^{24}$ cm^{-2}) (e.g Iwasawa & Comastri, 1998; Lira et al., 2002). To compare the SCUBA sources to NGC6240 I use the SED for a 'high-reddening' starburst galaxy taken from Schmitt et al. (1997). This fits the

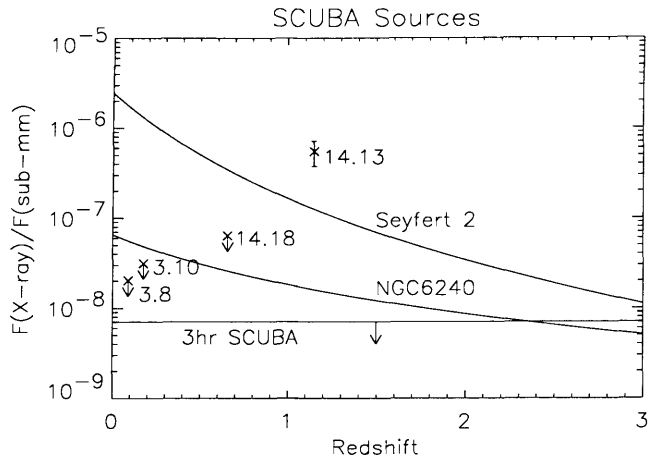

(a)

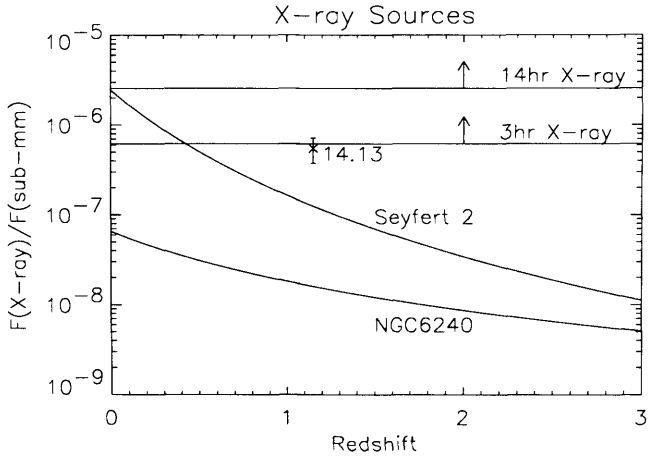

(b)

Figure 3.5: X-ray to sub-mm flux ratios for the SCUBA sources (3.5(a)) and the X-ray sources (3.5(b)). Template SEDs of NGC6240 and a Seyfert 2 Galaxy are plotted for comparison. Horizontal lines represent the ratios of the measured mean fluxes for the 3-h sub-mm sample (3.5(a)), and the X-ray samples (3.5(b)). The only definite sub-mm/X-ray coincidence is plotted in 3.5(b), and is from Eales et al. (2000) with redshift from Webb et al. (2003b). The two 3-h SCUBA sources with secure IDs and spectroscopic redshifts (Webb et al., 2003a) are plotted in 3.5(a) along with the only other 14-h SCUBA source with a secure ID and redshift (Webb et al., 2003b). The low z 3-h sources are not representative of the SCUBA population as a whole, which in general lie at higher z, and so do not necessarily have the same properties. Their optical counterparts both show merger morphology. Source labels are the CUDSS reference numbers.

measurements for NGC6420 well (Lira et al., 2002). I use this SED as a basic template, modified for an X-ray photon index of 1.4 to approximate the broad characteristics of NGC6240 (Iwasawa & Comastri, 1998). I calculate the ratio between the soft X-ray flux and the 850 μm flux in observed frame as a function of redshift, and this is plotted in fig. 3.5. I also plot the X-ray/sub-mm flux ratio for a typical Seyfert 2 galaxy with respect to redshift, using a template also taken from Schmitt et al. (1997).

The upper limit on the ratio of the mean X-ray to sub-mm flux for the SCUBA sample is consistent with the template for NGC6240 as long as the redshifts of the SCUBA sources are > 2.3. This is consistent with redshifts measured for many SCUBA sources (Ivison et al., 2002; Chapman et al., 2003b), and so I conclude that in general it is still possible that most SCUBA sources may contain Compton thick AGN like NGC6240. Almaini et al. (2003) rule out the possibility that SCUBA sources are QSOs, unless they are Compton thick and at very high redshift, and show that they are consistent with a starburst template at $z > 2$. This is in general agreement with my results. The SCUBA sources with secure identifications and spectroscopic redshifts (Webb et al., 2003a,b) are also plotted for the two fields.

A similar plot for the X-ray sources is shown in fig. 3.5(b). Note that the 14-h field has a higher mean X-ray flux because this field is dominated by several bright X-ray sources (two are known QSOs, Schade et al., 1996).

In an alternative approach I can calculate the far-IR and AGN luminosities of the ensemble of X-ray sources in the 3-h CUDSS map, as I did with CUDSS 14.13 (section 3.2.1). I use the mean SCUBA flux measurement of 0.48 mJy at 850 μm, and assume a column density of 10^{22} cm^{-2} to be representative of the X-ray sources. For any reasonable far-IR SED the AGN luminosity, from optical through

to X-ray, never exceeds the far-IR luminosity for redshifts below 2. If I require the entire sub-mm flux to be produced by the AGN then the X-ray sources must either be modestly absorbed at very high redshifts, or extremely highly absorbed and at lower redshifts. This shows that in general the bolometric luminosities of the X-ray sources in this field are probably dominated by star-formation in the same way as CUDSS 14.13 is. All of this, however, is highly speculative because of the highly model dependent nature of the far-IR luminosity calculation, and the marginal (not even 2 σ) sub-mm detection.

3.4.2 Extra-Galactic Background Radiation

The following analysis is based on the 3-h CUDSS region.

The upper limit on the average X-ray flux of the SCUBA sample also allows us to place an upper limit on the contribution the SCUBA population makes to the XRB. My sub-mm sample constitutes about 20% of the extra-galactic background at 850 μm, and so I scale my upper limit by a factor of 5 to calculate an upper limit on the contribution dust sources make to the XRB (assuming that the X-ray/sub-mm ratio is not dependent on sub-mm flux). The sample provides a maximum of 3.3% of the XRB at 0.5−2 keV, and so the population as a whole must contribute no more than 16.5% in this band. In the hard band the SCUBA sample contributes an upper limit of 6.1% to the XRB and so the population as a whole provides at most 30.7%. It is clear that sub-mm sources do not dominate the X-Ray background at low energies, but it remains to be seen if their contribution to the peak of the XRB ($\sim$ 30 keV) is more significant.

Taking the opposite approach I can estimate the contribution of AGN to the

850 μm background. The simplest way is to convert our 3 σ upper limit sub-mm flux, as measured in section 3.3, of the detected X-ray sources into a smooth background by multiplying it by the number density of X-ray sources detected by our survey. Comparing this to the intensity of the CIRB at 850 μm gives an estimate of a 2.3% contribution from AGN. Assuming the 3-h field is a typical extra galactic region and that the X-ray sources are indeed AGN then this is a little low compared with theoretical models (e.g. Almaini et al., 1999). My X-ray survey, however, only resolves about 32% of the X-ray background in the soft band (by summing the contribution of X-ray sources in this small SCUBA map area). If I assume that the background I have not resolved has the same X-ray/sub-mm ratio as my X-ray sample, then 7.2% of the sub-mm background is produced by the sources making up the X-ray background. This may be too low because the fainter X-ray sources may be more heavily obscured, and the results from the *Chandra* Deep Fields do suggest that the ratio decreases at lower X-ray flux (Barger et al., 2001). However, I have argued above that much of the sub-mm emission from X-ray sources is from dust heated by star-formation and not by AGN, and thus the estimate above is really an upper limit on the contribution of AGN to the sub-mm background. These two arguments work in opposite directions and may act to cancel each other out.

The contribution of the SCUBA sources to the X-ray background and of the X-ray sources to the sub-mm background strongly suggest the two backgrounds are disjoint, with the sub-mm background mostly produced by stellar nucleosynthesis and the X-ray background by accretion on to black-holes.

3.5 Concluding Remarks

This study adds weight to the growing body of evidence pointing to the fact that SCUBA sources may indeed contain active nuclei, but that their presence is secondary to starburst activity as a power source for their high far-IR luminosities. In some cases it is possible to view the active nucleus directly using current X-ray satellites, but there are still many SCUBA sources that show no evidence of X-ray emission. Higher and higher column densities of HI progressively wipe out X-ray emission up to higher energies, and as such are capable of putting AGN beyond detectability by current X-ray detectors sensitive only up to $\sim$ 10 keV. If this is the case for the majority of SCUBA sources then the scenario outlined above will need to be modified, as it is possible for the entire sub-mm luminosity of a SCUBA source to be powered by a very powerful but highly obscured AGN, with no need for a starburst. How common such highly obscured systems are is likely to remain uncertain until X-ray instruments become available with good spatial resolution and good sensitivity above 10 keV, in order to detect obscured AGN beyond $z = 2$, where many SCUBA sources are being identified. The deepest current X-ray surveys however (Alexander et al., 2003), suggest that the low detection rate of X-ray emission from SCUBA sources in less deep surveys is more likely to be due to low AGN luminosity rather than heavy obscuration, which would tend to support the statement at the start of this section.

Star-formation may also be the dominant source of the far-IR bolometric luminosity of galaxies containing relatively bright X-ray emitting AGN. Certainly the significant sub-mm measurements of X-ray sources in other studies indicates that this is the case. Even a modest sub-mm flux equates to a high far-IR luminosity, whatever dust SED is assumed.

I conclude that in general the two extra-galactic backgrounds are mainly produced by different processes, with the sub-mm background being predominantly produced by dust being heated by starlight, and the X-ray background being dominated by accretion onto super-massive black-holes.

Chapter 4

X-ray Source Identification

4.1 Introduction

The work in this chapter forms the basis for the second paper to come out of my PhD (Waskett et al., 2004). It primarily concerns the identification of the sources detected by *XMM* with optical objects found in the deep exposures taken as part of the Canada-France Deep Fields survey (CFDF) (McCracken et al., 2001). This is a crucial part of the analysis of the X-ray sources as it reveals the nature of the AGN host galaxies, and allows comparison of the X-ray and optical properties of those galaxies. It is also useful for separating out contamination by stars, which make up a small fraction ($5 - 10\%$) of the detected X-ray sources.

To improve on my understanding of the identification statistics I compare the IDs for a subset of the *XMM* sources with the IDs obtained using *Chandra* positions for the same sources. Since *Chandra* has superior positional accuracy this subset is used to test the ability of *XMM* to reliably identify X-ray sources.

4.2 Optical Identifications

4.2.1 XMM

After correcting the *XMM* astrometry against known bright QSOs the process of identifying the X-ray sources with optical counterparts can be carried out. This process is important for the procedures in the following sections, especially in obtaining the redshift distribution of the AGN.

Both survey fields are coincident with the Canada-France Redshift Survey (CFRS) (Hammer et al., 1995a; Lilly et al., 1995a) and the Canada-France Deep Fields survey (CFDF) (McCracken et al., 2001). The former covers a $10' \times 10'$ section in each field with spectroscopic redshifts for many of the galaxies, while the latter covers almost the entirety of both and reaches 3 magnitudes deeper ($I_{AB}(3\sigma, 3'') \sim 25.5$) albeit with no spectroscopic follow-up. I therefore use the CFDF catalogue as the basis for my identification process and extract CFRS redshifts as appropriate to monitor the accuracy of the photometric redshift determination (see section 4.4). The CFDF data were taken with the *Canada-France-Hawaii Telescope* using the UH8K mosaic camera in B, V and I, with U data supplied by either the CTIO (3-h field) or the KPNO (14-h field). Total exposure time were typically $\sim$ 5 hours for B, V and I, and $\sim$ 10 hours for U. The lengthy data reduction process is described in detail in McCracken et al. (2001). Of the 146(154) X-ray sources in the 3-h(14-h) fields 115(149) lie within the CFDF regions.

To determine the optical identifications of the X-ray sources I have used the frequentist approach of Downes et al. (1986). Since *XMM* has a positional accuracy

of $\sim 2''$ (this is a worst case situation for large off axis angles; on axis positional accuracy is more like $1.5''$), only 1% of *XMM* sources will have positions which are $> 6''$ away from the object that caused the emission. The first step in my ID procedure was thus to find all CFDF objects within $6''$ of the *XMM* position. I then calculated the following statistic for each object:

$$S = 1 - exp(-d^2 \pi n(< m))$$

where d is the offset between the *XMM* position and that of the optical object, and $n(< m)$ is the surface density of optical objects brighter than the magnitude (m) of the possible association. It may appear that this statistic gives the probability that the candidate object is a foreground or background object and is not physically related to the *XMM*. However, S is not a probability because it doesn't take into account galaxies that are fainter than the magnitude of the candidate galaxy, and that *might* have had a lower value of S. Therefore this possibility needs to be taken into account when deriving the sampling distribution of S. Downes et al. (1986) describe an analytic way to do this. The end result is a true probability value, P'. Typically a value of P' is several times higher than the equivalent S value. In all but two cases, I chose the CFDF object with the lowest value of P' as the most likely association. In these two exceptions, the galaxy with the lowest value of P' was close to $6''$ away from the *XMM* position, and I preferred the candidate with a slightly higher value of P' but which was much closer to the *XMM* position (these two IDs are confirmed by the *Chandra* X-ray positions, sources 14.15 & 14.50). Table 4.1 gives the statistics for my candidate identifications.

A consequence of this method is that because fainter objects are more numerous, they will have higher P' values than brighter objects at the same offset. Therefore, relatively optically faint objects are seldom identified with X-ray

Table 4.1: Summary of ID statistics for both *XMM* fields. P' values given are for the best ID where more than one candidate lies within the 6″ search radius.

	3-h	14-h
$P' < 0.05$	59	82
$0.05 < P' < 0.1$	16	24
$0.1 < P' < 0.2$	16	18
$0.2 < P' < 0.5$	13	16
$P' > 0.5$	12	8
Blank Field	2	1
Outside CFDF	28	5

sources, unless they are very close to the X-ray position. For example, at the optical completeness limit of $I_{AB} = 25.5$ an object at an offset of 0.8″ will have $P' = 0.15$, which is the same P' as a 20.6 magnitude object at 6″ offset.

4.2.2 The *Chandra* Training Set

I initially chose a P' value of 0.1 as being my dividing line between identifications and objects that are likely to be physically unrelated to the X-ray source. The number of spurious identifications can be estimated by simply adding up the values of P' for objects with $P' < 0.1$. This is ~ 2 in the 3-h field and ~ 3 in the 14-h field. In the two fields, 181 sources have $P' < 0.1$, which is 68% of the *XMM* sources for which there are deep CFDF images. The error rate of false associations is $5/181 \sim 3\%$.

I was able to refine my identification criteria using the fact that part of the 14-h field has also been surveyed with *Chandra* (the NE quadrant). The *Chandra* data are not the focus of this chapter but they are summarised here: The data were taken in August 2002 using the ACIS-I instrument and were reduced using the standard CIAO v2.3 data reduction software. The total good exposure time after

screening was 158 ks. Source detection was performed using the CIAO wavdetect algorithm (Freeman et al., 2002), run on images in the $0.5-8$, $0.5-2$, $2-8$ and $4-8$ keV bands, using a false source probability of 10^{-7}. Full details of the *Chandra* observations are given in Nandra et al. (2004, in preparation).

Within the *Chandra* FoV there are 63 *XMM* sources, 55 of which were also detected by *Chandra* within $10''$ of the *XMM* position. I performed a similar ID process to that employed above using these new positions, and succeeded in identifying 51 of the 55 *Chandra* sources. Two unidentified sources were also unidentified in the *XMM* analysis, and are essentially blank fields with no CFDF objects lying within $6''$ of either the *XMM* or *Chandra* position (sources 14.54 & 73). Of these 51 sources, 42 had previously been identified by *XMM*. 40 were identified as the same object by both *XMM* and *Chandra*; the remaining 2 had different IDs (sources 14.10 & 149). However, in one of these 2 cases the *Chandra* ID was the second best *XMM* ID (14.149) (the *XMM* IDs are listed in tables 4.5 & 4.7). The other 9 sources were securely identified by *Chandra* but not by XMM, so these are considered 'new' IDs (sources 14.65, 80, 85, 90, 102, 114, 115, 122, 129)

Given the expected number of spurious *XMM* IDs for the whole 14-h field (106 identified sources) is ~ 3 I would expect 1-2 spurious IDs in the subsample covered by the *Chandra* FoV. I found 2 IDs that were wrong in this sample and so feel confident that our estimate of ~ 3 spurious *XMM* IDs in this field is accurate.

I relaxed the selection criteria for the *XMM* ID candidates to see if I could find more identifications for the *XMM* sources without significantly increasing the number of false associations. By increasing the cut-off to $P' < 0.15$ a further 5 *XMM* sources within the *Chandra* FoV are identified. Four of these are judged

to be correct (14.85, 90, 102 & 114) given the *Chandra* ID and one is incorrect (14.115). Extrapolating to my entire survey, I estimate that by relaxing my P' criterion I gain 22 additional identifications, of which probably ~ 5 are inaccurate. For the rest of this work IDs with $P' < 0.15$ are considered secure.

To summarise: with this new P' threshold I identify 84 out of 115 sources in the 3-h field and 119 out of 149 sources in the 14-h field. One extra QSO lies outside the 3-h CFDF map but is coincident almost exactly with an *XMM* source and so is identified as such. An additional QSO lies on a chip boundary in the 3-h field and is assumed to be responsible for the X-ray emission detected to either side of the boundary (sources 3.7 and 19, see table 4.2 and the very top of figure 2.8, hereafter referred to as source 7), so in total 86 3-h sources are identified. In the 14-h field the *Chandra* positions succeeded in identifying an extra 4 sources (14.65, 80, 122 & 129), bringing the total number of identified sources in this field to 123. Out of the *XMM* sources within the area of the CFDF, I have identified 75% of the sources in the 3-h field and 83% of the sources in the 14-h field. Only a small part of the difference between the two fields are the *Chandra* positions that exist for some of the 14-h *XMM* sources. I expect of my 209 identifications, 10 are incorrect.

There are 4 new *Chandra* IDs and 3 IDs that were changed when *Chandra* positions were used rather than *XMM* positions (after increasing the P' limit to 0.15). These 7 sources, that were not possible to identify using *XMM* positional data but which were possible to identify using *Chandra* positions (sources 14.10, 65, 80, 115, 122, 129 & 149), give us an insight into the properties of the remaining 58 unidentified *XMM* sources. The X-ray fluxes of the unidentified XMM sources cover a large range of fluxes (see figures 4.1 and 4.2), but the median I magnitude of the new IDs is 23.6, cf. the median I magnitude for the other *XMM* IDs is 21.2

(range: 11.5 to 25.5), nearly 10 times brighter. This is a consequence of the effect described at the end of section 4.2.1. Section 4.4 describes the redshift information obtained for the IDs and it appears that these *Chandra* IDs lie, in general, at higher redshifts than most of the *XMM* IDs, which would partially explain their relative optical faintness.

4.3 X-ray to Optical Flux Ratios

A convenient way of discriminating between different classes of X-ray source is the ratio between their X-ray and optical flux. Figures 4.1 and 4.2 show the total I band magnitude (measured using a variable aperture to encompass the total flux of each object) versus the X-ray flux for all the identified sources in the 3 & 14-h fields. The X-ray flux is calculated assuming a photon index $\Gamma = 1.7$. The I band magnitude is related to the flux in this band, f_I, by $log\ f_I = -0.4 I_{AB} - 5.57$, where f_I has the units erg cm^{-2} s^{-1}. Lines of constant X-ray to optical flux are plotted for comparison. AGN tend to occupy the space between the $log(f_X/f_I) = \pm 1$ lines while quiescent galaxies mostly lie below the $log(f_X/f_I) = -2$ line, with a mixture in between.

An early use of $log(f_X/f_{opt})$ as a diagnosis tool comes from the study of X-ray sources detected in the *Einstein* Observatory Extended Medium-Sensitivity Survey (Stocke et al., 1991). The original definition uses the $0.3-3.5$ keV X-ray band and the V optical band, but more recently the R band has tended to be used for deep X-ray surveys and the X-ray bands vary from study to study. To compare my plots to those of Stocke et al. (1991) I convert my $0.5-10$ keV fluxes into $0.5-7$ keV fluxes, by assuming a photon index of 1.7, and I convert my V_{AB} and I_{AB} band

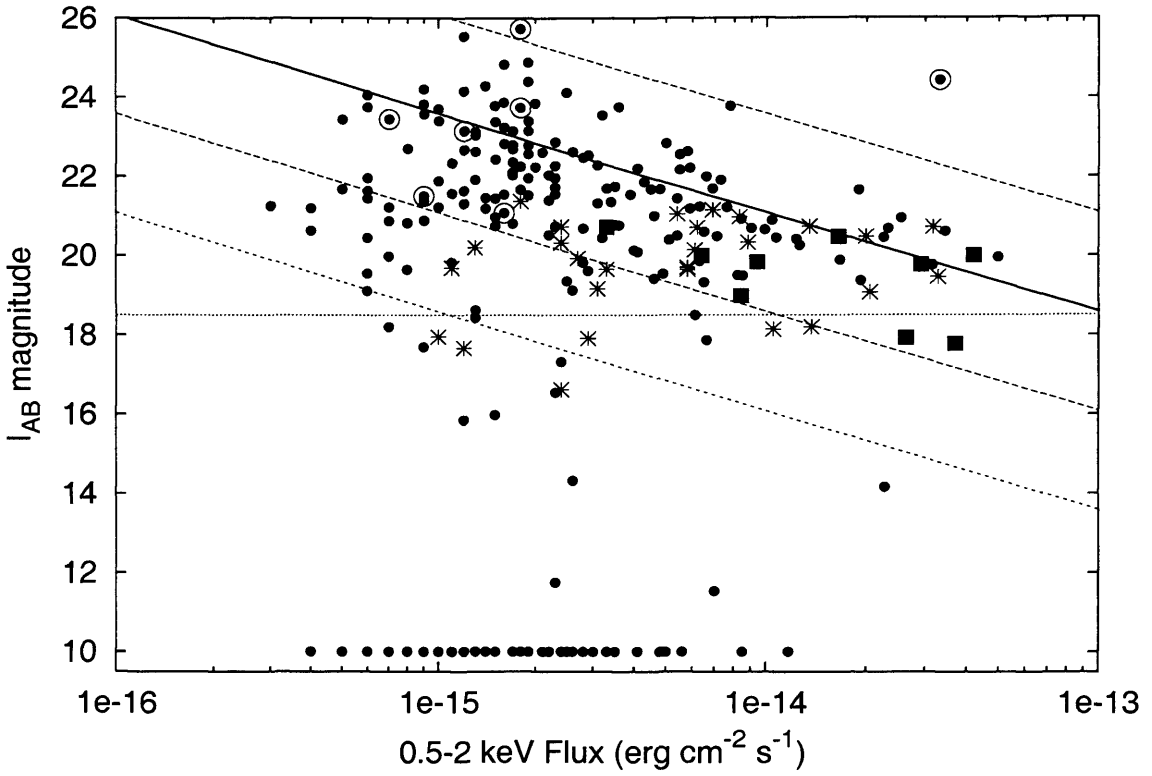

Figure 4.1: Soft X-ray to optical flux ratio for all sources detected in both the 3 and 14-h fields. Lines of constant flux ratio are plotted; solid line - $log(f_X/f_I) = 0$; longer dashed lines ± 1 and shorter dashed line -2. AGN tend to occupy the region between the dashed lines, quiescent galaxies lie mostly below the dotted line while a mixture, including starburst galaxies, occupy the region in between. The dotted line at $I_{AB} = 18.5$ shows the saturation limit of the CFDF and so magnitudes brighter than this are likely to be underestimated. Solid squares - known QSOs; asterisks - identifications with a stellar profile. Unidentified sources, within the optical coverage, are placed at $I_{AB} = 10$. The sources identified using *Chandra* positions, including the 3 with alternative *Chandra* IDs, are ringed with larger circles (sources 14.10, 65, 80, 115, 122, 129 & 149, see end of tables 4.5 & 4.7).

magnitudes to R band by using the prescription $R = I - 0.2(V - I)$ (Hornschemeier et al., 2001) and the conversions $V = V_{AB} + 0.044$ and $I = I_{AB} - 0.309$ (since I have no direct R band magnitudes). The optical flux in erg cm^{-2} s^{-1} is then $log\ f_R = -0.4R - 5.47$, for figure 4.3. This gives me an equivalent plot to those used in McHardy et al. (2003) (see figure 4.3) so that a direct comparison can be made between our two surveys. The appendix to McHardy et al. (2003) describes how their $log(f_X/f_{opt})$ plots are equivalent to those of Stocke et al. (1991), so my

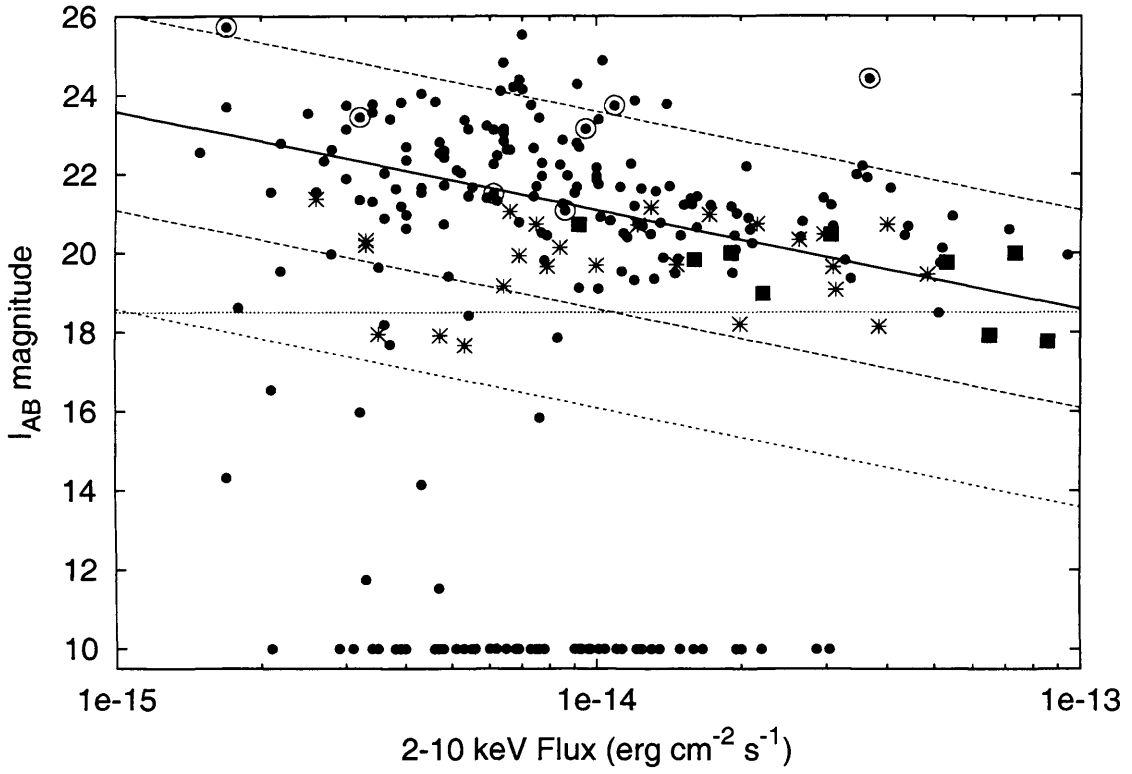

Figure 4.2: As for figure 4.1 but showing the hard X-ray to optical flux ratio.

figure 4.3 should also be close to the original definition. Comparing figures 4.1 and 4.2 with figure 4.3 shows that there is not a great deal of difference in the position of the lines of constant $log(f_X/f_{opt})$, so distinguishing between different classes of X-ray sources using figures 4.1 and 4.2 should be reliable.

Barger et al. (2002, 2003) have plotted similar diagrams for the *Chandra*-Deep Field North survey, an X-ray sample approximately ten times fainter than my own. In the *Chandra* survey the median optical apparent magnitude of X-ray sources flattens off at low X-ray fluxes, bringing the majority of sources below the AGN region on the $log(f_X/f_I)$ plot. However, at the flux limit of my survey I am still predominantly detecting AGN with only a minor contribution from quiescent galaxies. Additionally, the redshift distribution of my identified sources (see section 4.4) places the majority of the AGN in my survey at $z < 1$ which is the pe-

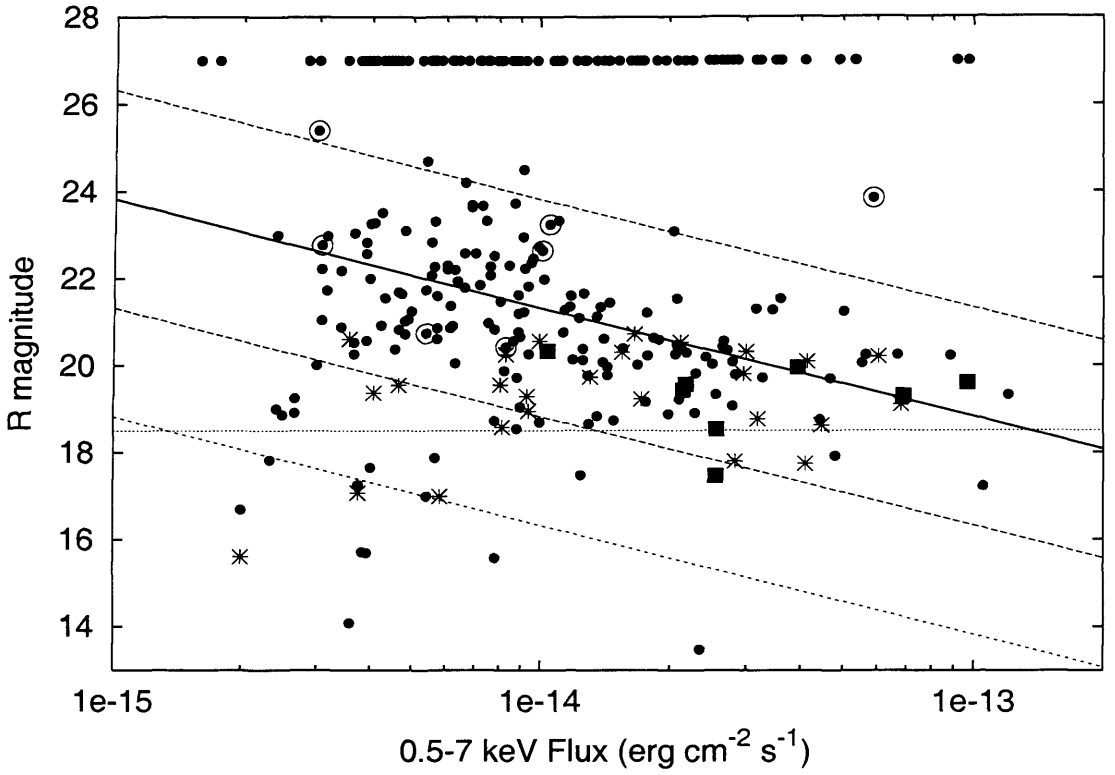

Figure 4.3: As for figure 4.1 but showing the 0.5-7 keV X-ray to R band optical flux ratio as used in McHardy et al. (2003). Unidentified sources are now plotted at $R = 27$.

riod of peak formation of super-massive blackholes with low accretion rates (Cowie et al., 2003). These two facts mean that medium-deep surveys such as mine are well placed to study this important period of growth for intermediate luminosity AGN, without the need for very deep surveys, which are able to probe much earlier times in the evolution of AGN and study the X-ray properties of more 'normal' galaxies.

In figures 4.1 and 4.2, the extra sources identified by *Chandra*, but not by *XMM*, in the 14-hr field all reside in the higher $log(f_X/f_I)$ regions. This suggests that they are AGN rather than starbursts or quiescent galaxies. Given that the *XMM* unidentified sources are in general optically fainter than the identified ones ($I_{AB} > 22$, see section 4.2.2 and end of section 4.2.1), and that their X-ray fluxes

are similar, this implies that the unidentified X-ray sources are most likely AGN too, with high f_X/f_I ratios. One interesting point to note is that source 14.10 has a different *Chandra* ID to the one given by the *XMM* position; it is the *Chandra* ID that is plotted in these figures. However, the *Chandra* ID is significantly fainter than the *XMM* ID ($I_{AB} = 24.4$ cf. 19.0) and so this source now has an extreme $log(f_X/f_I)$ value of ~ 2 (cf. ~ -0.3 for the *XMM* ID). I assume here that the *Chandra* ID is the correct one but given this extreme flux ratio it is possible that *XMM* has correctly identified this source, rather than *Chandra*. However, this source could be an example an EXO (Extreme X-ray/Optical ratio source Koekemoer et al., 2004), a possible new class of X-ray source, if the *Chandra* ID is the correct one.

In addition to the known QSOs in these fields, 27 of the identifications have stellar optical profiles. Figures 4.1 and 4.2 show that most of these lie in the AGN part of the diagram, suggesting that they are QSOs rather than stars.

4.4 Photometric Redshifts

Only a handful of the CFDF IDs have spectroscopic redshifts. Including known QSOs outside the CFRS regions there are 13(6) X-ray sources with spectroscopic redshifts in the 3-h(14-h) fields. The vast majority of the non-broad-line AGN do not have spectroscopic redshifts and so I turn to photometric techniques to estimate redshifts for these.

The optical spectra of broad line AGN (QSOs) are contaminated by light from the central engine, and so obtaining photometric redshifts for them is problematic. However, Gonzalez & Maccarone (2002) have shown that for the majority of X-ray

sources, which are non-broad line AGN, the optical spectrum is not significantly contaminated and so photometric techniques work just as well as they do with 'normal' galaxies. As long as the QSOs can be identified they shouldn't affect the rest of the sample. I therefore only use the estimated redshifts for the identifications which do *not* have a stellar profile. I use two photometric redshift estimation codes in this work, a Bayesian template fitting code called BPZ (Benítez, 2000) and a code developed specifically for the CFDF (Brodwin et al., 2003), calibrated against CFRS spectroscopic data. See section 4.8 for the details and a comparison of the two codes.

The photometry for all the IDs is listed in tables 4.6 & 4.7 and the results for both codes are shown in tables 4.4 & 4.5. Figure 4.4 shows the redshift distribution, as measured by each code, of all the reliable IDs that also have reliable redshift estimates, with a bin size of $\Delta z = 0.2$. Reliable *photometric* redshifts are defined here as unsaturated objects that have 95% ($\sim 2\sigma$) redshift confidence limits $< 0.4(1+z)$ (CFDF code) or $P_{\Delta z} > 0.9$ (BPZ code), otherwise spectroscopic redshifts are used where they exist; in total 129(120) estimates are reliable for the BPZ(CFDF) code. Despite the differences between the distributions measured by the two different codes the overall shape of the distribution is clear, with a peak at around $z = 0.7$. In both distributions nearly 60% of the objects lie in the range $0.4 \leq z < 1$. The median redshifts are significantly different however: 0.62 for BPZ and 0.79 for the CFDF code. For the rest of this work the CFDF code is assumed to be more accurate (see appendix to this chapter) and so all further quoted photometric redshifts are those given by this code.

An interesting point to note here is that the extra sources identified by *Chandra* and not by *XMM* (see end of table 4.5, sources 14.10, 65, 80, 115, 122, 129 & 149) lie, in general, at higher redshifts than the majority of the *XMM* identified sources.

If all the unidentified sources lie at higher redshifts than all of the other sources, then the median redshift of the total increases to $z \sim 1.1$.

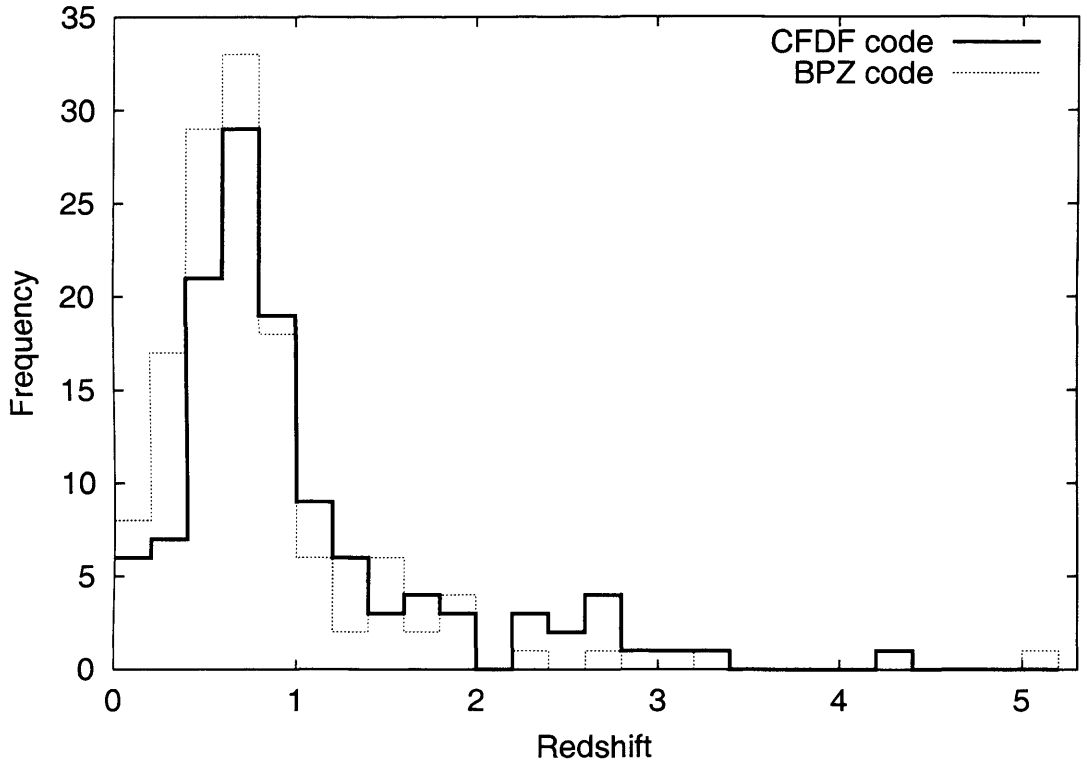

Figure 4.4: Redshift distribution of the identified X-ray sources as measured by the two different photo-z codes. Where a spectroscopic redshift exists it is used in preference to the photometric one in both histograms. All unreliable redshifts are excluded (i.e. those indicated with * or s in tables 4.4 & 4.5, and saturated objects with $I_{AB} < 18.5$). The overall shape of this distribution remains unchanged if the less reliable redshift estimates are also included; only the normalisation increases.

4.5 Absolute Magnitudes - Galaxy Types

Figure 4.5 shows the absolute I_{AB} magnitude plotted against redshift. The different symbols represent the best fitting template determined for each galaxy by the CFDF code, using six band photometry. Although the code uses 15 templates for greater accuracy each symbol here represents a small range of templates for clarity.

In general the two photo-z codes agree reasonably well as to the best fitting galaxy type.

The X-ray sources all lie in a band defined at the faint limit by the limiting magnitude of the optical data, and at the bright limit by the saturation magnitude. Objects brighter than this magnitude do not have reliable photometric redshifts and so do not appear in this plot. Aside from these selection effects there are several other trends apparent here. Apart from QSOs, in general, at lower redshifts, the bluer galaxy types occupy the region near the faint limit while progressively redder galaxies occur at brighter magnitudes (see figure 4.6). However, this trend breaks down at higher redshift where there are fewer sources, and errors in the photometry are likely to be more important. There is no clear domination of one galaxy type over any other, indicating that AGN have no preference when it comes to the morphology of their host galaxies. Nor is there any apparent preference for optical luminosity of the host galaxy, unlike the narrow absolute magnitude range preferred by the starburst galaxies detected in μ Jy radio surveys (Chapman et al., 2003a). X-ray sources occupy the whole optical luminosity range available to them in this plot. There are four apparently very luminous ellipticals at $z > 2.5$ (sources 3.32, 3.90, 3.92 & 14.31) which may be erroneous identifications. The CFDF code becomes less reliable above a redshift of 1.3 (Brodwin et al., 2003) and so it is possible that these sources actually lie at lower redshifts (in fact the BPZ code places three of these sources at $z < 1$, see tables 4.4 & 4.5, and classifies them as spirals; likely a consequence of this code using a magnitude based prior) and so are consequently of less extreme luminosity. With this in mind, high redshift sources should be viewed with some caution, in particular those source within the box in figure 4.5, which have luminosities in excess of many of the QSOs.

The extra sources identified by *Chandra* but not by *XMM* in the 14-h field

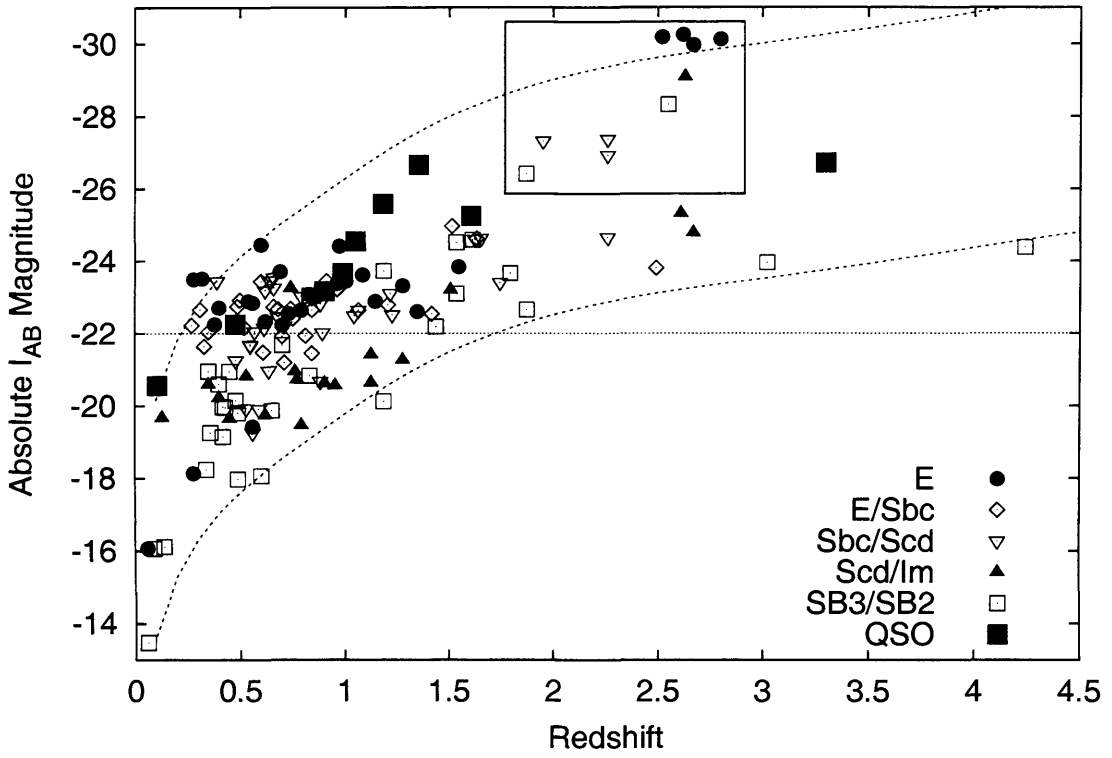

Figure 4.5: Absolute I_{AB} magnitude vs. redshift for the identified sources (148 sources after removal of stellar and saturated objects). The horizontal line is the approximate position of M_I^*. The first four galaxy types are taken from Coleman et al. (1980), although some interpolation is used to create intermediate templates, and the starburst symbol represents both the SB3 and SB2 types from Kinney et al. (1996). QSOs have been plotted using the best fit template for the K correction, in general the bluest starburst. Upper and lower curves are the approximate saturation limit and completeness limit of the optical data ($I_{AB} = 18$ and 24.5 respectively), calculated for an Scd galaxy (due to larger K corrections some ellipticals lie above the bright limit for Scd galaxies). The objects within the box have extremely high luminosities when compared to the majority of the QSOs, which indicates that they may have been given incorrect redshifts.

also cover a wide range in galaxy types. The two higher redshift sources are the bluest galaxy types while the two lowest redshift sources are the reddest types. Three of the four hug the lower luminosity limit, a consequence of their relative optical faintness.

Converting the 0.5 – 10 keV X-ray flux of the identified sources into X-ray luminosity gives us figure 4.7. Although the striking correlation here is possibly

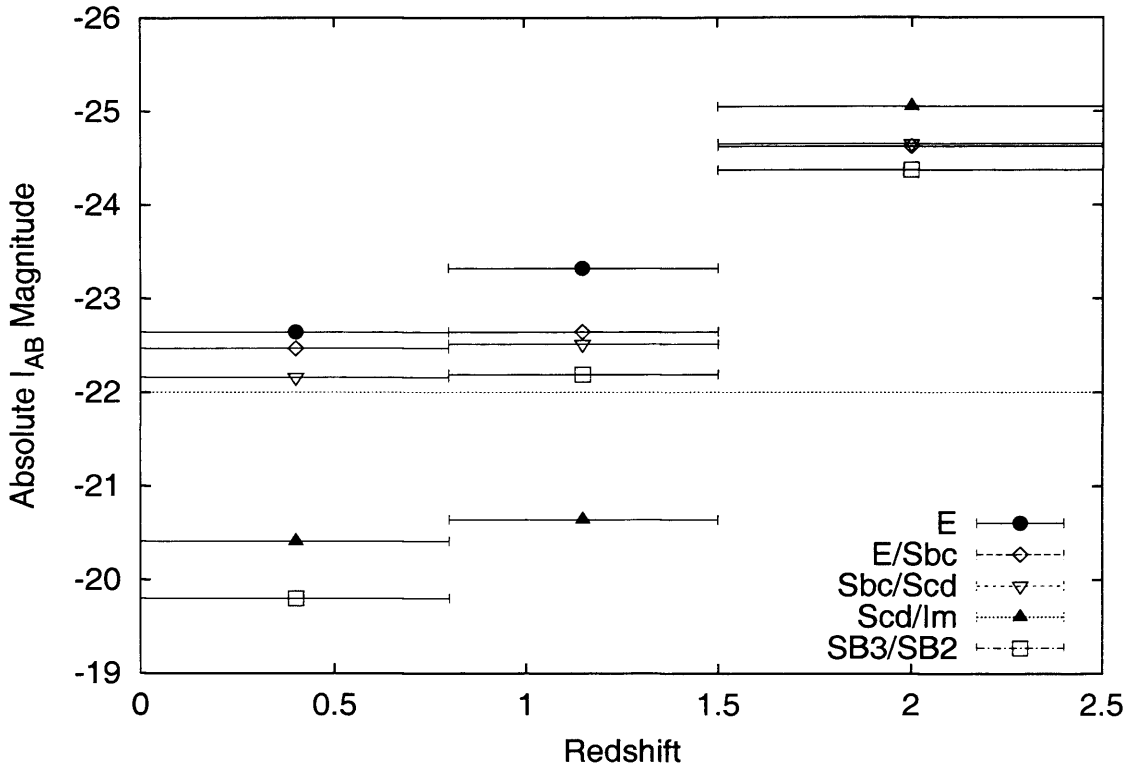

Figure 4.6: Median values for the galaxy types in figure 4.5. The highest z bin includes all sources with z > 1.5. The group of Elliptical galaxies at M ~ -30 in figure 4.5 is off the vertical scale in this plot. The horizontal line is the approximate position of M_I^*.

dominated by the same selection effects seen in figure 4.5, it is rather reminiscent of the Magorrian relation (Magorrian et al., 1998), with black-hole mass represented by X-ray luminosity and bulge mass represented by optical luminosity. Whether this correlation is real or not depends on exactly where the optically faint and saturated sources lie in this plot. I would expect optically faint sources to fall in the lower right part of this plot and the saturated sources to fall in the upper left part, effectively smearing out the correlation. However, if the optically faint sources are *not* at much higher redshifts than the identified sources (contrary to my arguments above) then both their X-ray and optical luminosities will be low, placing them amongst the sources plotted here. The very luminous ellipticals, mentioned above, also appear in this plot, slightly above the general trend, again

suggesting that they have been misclassified (as have, potentially, a group of lower luminosity ellipticals, also lying away from the trend).

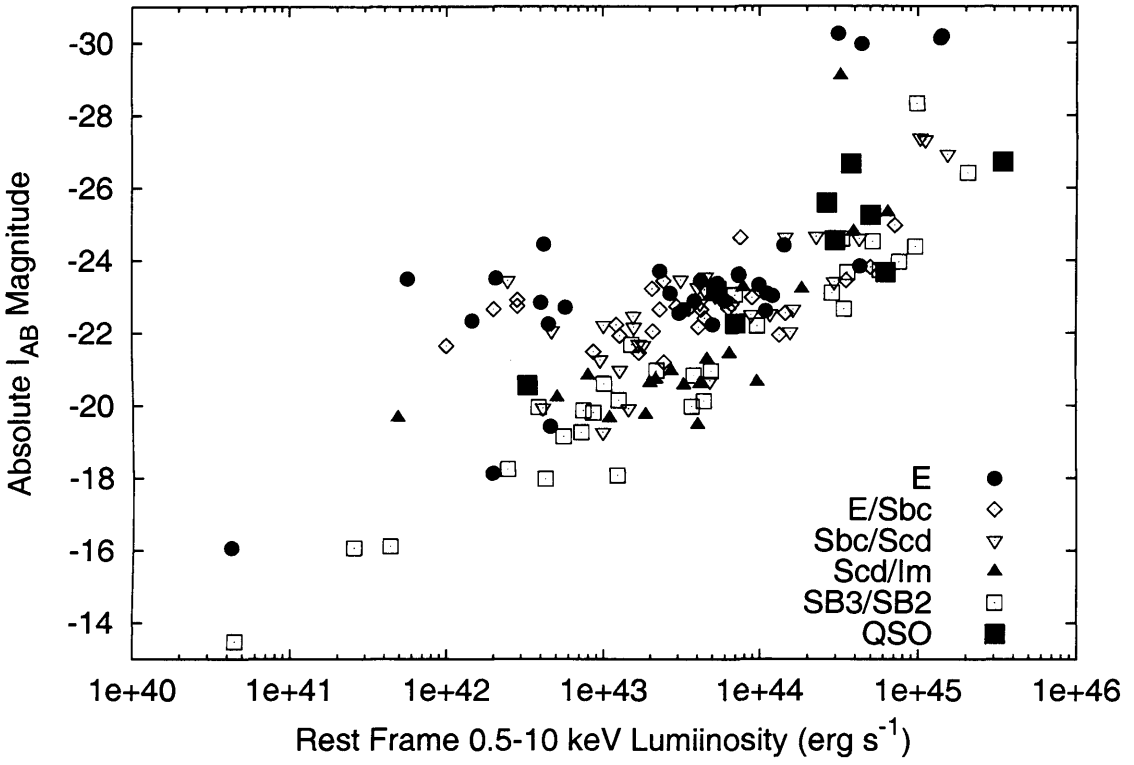

Figure 4.7: Absolute I_{AB} magnitude vs. X-ray luminosity calculated from the $0.5 - 10$ keV flux for the same sources as figure 4.5. The X-ray luminosity is K-corrected assuming an intrinsic power law slope with photon index $\Gamma = 1.7$.

Plotting these sources in a different way illustrates what type of objects contribute to the XRB. For this discussion I assume the XRB to have a spectrum of $I(E) = 11E^{-0.4}$ keV s^{-1} cm^{-2} sr^{-1} keV^{-1} (McCammon & Sanders, 1990; Fabian & Barcons, 1992), although the overall normalisation is still somewhat uncertain. Figure 4.8 shows absolute I_{AB} magnitude vs. X-ray flux with the same symbols as in figure 4.5. The 300 sources in this survey (assuming the majority of the 'stars' are misidentified QSOs) contribute $\sim 51\%$ to the XRB in the $0.5 - 10$ keV range, while the 148 sources included in these figures (i.e. the securely identified sources with redshift estimates) provide $\sim 27\%$. Of this 27%, sources brighter than M_I^*

contribute 69% while fainter sources contribute 31%. This calculation shows that the XRB is not dominated by the most optically luminous galaxies, but that a significant contribution comes from galaxies with fairly low optical luminosity.

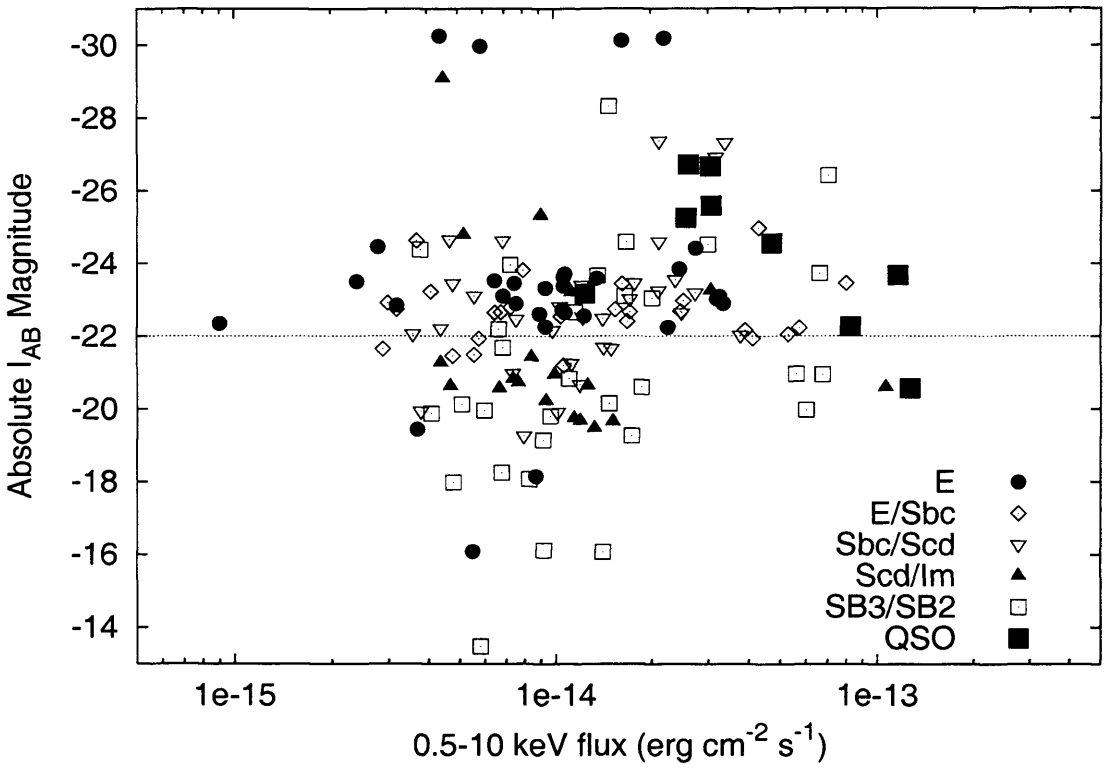

Figure 4.8: Absolute I_{AB} magnitude vs. total X-ray flux for the same sources as figure 4.5. The horizontal line is the approximate position of M_I^*.

4.6 Concluding Remarks

I have presented source catalogues for a survey, using the *XMM-Newton* X-ray telescope, of $\sim$ 0.4 square degrees of sky. I show that reliable identifications can be obtained for $\sim$ 75% of the *XMM* sources using *XMM* positions alone. Those sources that cannot be identified using *XMM* positions alone are optically fainter ($I_{AB} > 22$) than most of the identified ones, and are likely to be AGN at generally

higher redshifts. I have obtained the following results:

- The flux ratio f_X/f_{opt} of the sources in my survey show that they are predominantly AGN.
- The optical properties of the AGN span a large range of absolute magnitudes, in contrast to the result found for the starburst galaxies detected in μ Jy radio surveys, which tend to have a very narrow range of absolute magnitudes (Chapman et al., 2003a).
- AGN are found in host galaxies spanning the full range of Hubble types, with no clear preference.
- For the identified X-ray sources with good redshifts there is a strong correlation between optical and X-ray luminosity, reminiscent of the Magorrian relation between black-hole mass and bulge mass. However, this may be due to selection effects.
- The redshift distribution of the AGN shows a clear peak at $z \sim 0.7$.

The last result supports other recent studies (Barger et al., 2003) that show the peak formation of super-massive black holes occurred at relatively recent times ($z < 1$). Medium-deep X-ray surveys such as mine, which resolve a large fraction of the XRB but are still dominated by AGN, are able to probe this epoch effectively.

4.7 Catalogue

The following tables make up the full catalogue of X-ray sources. It is split into 3 sections for each of the two fields in this survey. The first tables for each field (4.2

& 4.3) contain the positions and fluxes of the X-ray sources as measured by the source detection software. The second tables (4.4 & 4.5) have the identification information for all of the good ID candidates ($P' < 0.15$) including the CFDF catalogue number, the ID position, the distance between the ID and its corresponding X-ray source, P' value and redshift information. The final tables (4.6 & 4.7) show the photometry for each good ID. The X-ray sources are ordered by total number of counts detected in the full X-ray band, greatest first. Due to vignetting this order is approximately but not exactly the same as the flux order. Source 23 in the 14-h field is detected by SCUBA at 850μm and is discussed in chapter 3 in more detail.

Table 4.2: X-ray properties of the 3-h field *XMM* sources. Sources 7 and 19 are in fact the same source split into two due to it lying on a PN chip gap (*).

[a] Flux in units of 10^{-15} erg s^{-1} cm^{-2}, based on a photon index of 1.7.
[b] Hardness ratio given by source detection procedure, one for each X-ray camera. Marked with '?' if not detected or a bad measurement.
[c] - = lies outside CFDF map; e = extended source (X-ray property); q = known QSO; s = object with a stellar profile, from $P' < 0.15$ list (q and s are optical properties).

XMM	R.A.[fk5]	Dec.[fk5]	0.5 – 2 kev[a]	2 – 10 kev[a]	0.5 – 10 kev[a]	PN HR[b]	M1 HR[b]	M2 HR[b]	Notes[c]
1	45.52820	-0.02260	119.0 ± 2.6	262.9 ± 9.7	382.9 ± 10.1	-0.4 ± 0.0	-0.4 ± 0.0	-0.4 ± 0.0	- q
2	45.78054	0.17228	33.0 ± 1.2	48.6 ± 3.8	81.7 ± 4	-0.6 ± 0.0	-0.5 ± 0.1	-0.5 ± 0.1	s
3	45.64490	0.01902	23.3 ± 1.0	44.3 ± 3.2	67.7 ± 3.4	-0.5 ± 0.0	-0.5 ± 0.1	-0.4 ± 0.1	
4	45.51813	0.27387	33.4 ± 1.5	76.3 ± 6.1	109.7 ± 6.3	-0.5 ± 0.1	-0.3 ± 0.1	-0.3 ± 0.1	-
5	45.63815	0.22543	16.5 ± 0.8	30.7 ± 2.7	47.2 ± 2.9	-0.6 ± 0.1	-0.2 ± 0.1	-0.4 ± 0.1	q
6	45.73817	0.26816	22.8 ± 1.2	4.3 ± 2.2	28.2 ± 2.6	-1.0 ± 0.0	-0.8 ± 0.1	-1.0 ± 0.4	
7	45.70564	0.35812	37.1 ± 2.3	85.8 ± 10.1	126.3 ± 10.3	-0.4 ± 0.1	1.0 ± 109.0	? ± ?	q*
8	45.58501	0.32717	20.6 ± 1.2	31.4 ± 4.2	53.6 ± 4.4	-0.5 ± 0.1	-0.6 ± 0.1	-0.6 ± 0.1	s
9	45.65876	0.03438	7.0 ± 0.5	23.0 ± 2.3	30.5 ± 2.4	-0.1 ± 0.1	-0.3 ± 0.1	-0.3 ± 0.1	q
10	45.59179	0.10849	6.4 ± 0.5	19.1 ± 2.0	26.1 ± 2	-0.2 ± 0.1	-0.5 ± 0.1	-0.1 ± 0.1	q
11	45.60998	0.00856	8.3 ± 0.6	17.2 ± 2.3	25.4 ± 2.4	-0.4 ± 0.1	-0.5 ± 0.2	-0.3 ± 0.1	s
12	45.61876	-0.10009	27.5 ± 2.0	87.8 ± 9.1	116.8 ± 9.4	? ± ?	0.0 ± 0.1	-0.3 ± 0.1	-
13	45.53363	0.14027	7.6 ± 0.6	17.3 ± 2.2	24.9 ± 2.2	-0.4 ± 0.1	-0.2 ± 0.1	-0.4 ± 0.1	
14	45.83447	0.10128	6.1 ± 0.6	51.2 ± 4.5	57.5 ± 4.5	0.3 ± 0.1	0.2 ± 0.1	0.2 ± 0.1	
15	45.68495	0.02951	5.9 ± 0.5	19.1 ± 2.1	25.2 ± 2.1	-0.2 ± 0.1	-0.1 ± 0.1	-0.4 ± 0.1	
16	45.54443	-0.02814	11.7 ± 2.0	19.5 ± 14.9	31.5 ± 15.1	-1.0 ± 0.8	-0.3 ± 0.4	-0.3 ± 0.5	e
17	45.63779	0.01183	5.0 ± 0.5	14.9 ± 2.2	20.5 ± 2.2	-0.3 ± 0.2	-0.3 ± 0.1	-0.3 ± 0.1	
18	45.51988	-0.00248	9.2 ± 2.1	24.0 ± 10.9	32.4 ± 11.1	-0.4 ± 0.3	-0.1 ± 0.3	-1.0 ± 5.0	- e
19	45.69801	0.35891	19.4 ± 2.3	42.1 ± 12.0	63.7 ± 12.2	-0.5 ± 0.1	-0.7 ± 1.0	? ± ?	q*
20	45.57067	0.26673	9.0 ± 0.7	12.5 ± 2.6	21.3 ± 2.7	-0.6 ± 0.1	-0.6 ± 0.2	-0.4 ± 0.1	
21	45.66192	0.03520	5.0 ± 0.6	15.9 ± 2.5	20.9 ± 2.6	-0.3 ± 0.1	-0.2 ± 0.2	-0.1 ± 0.3	e
22	45.79076	-0.00691	10.4 ± 0.8	20.7 ± 3.7	31.7 ± 3.8	-0.5 ± 0.1	-0.9 ± 1.1	-0.4 ± 0.1	
23	45.52267	0.00226	12.5 ± 2.4	0.0 ± 16.8	13.4 ± 17.1	-1.0 ± 0.9	-1.0 ± 0.6	-1.0 ± ?	- e
24	45.62240	0.11362	1.0 ± 0.3	30.7 ± 2.6	32.5 ± 2.8	0.8 ± 0.1	1.0 ± 0.9	0.5 ± 0.1	
25	45.58659	0.01362	6.3 ± 0.6	14.8 ± 2.3	21.1 ± 2.4	-0.3 ± 0.1	-0.4 ± 0.2	-0.4 ± 0.2	
26	45.49851	0.19432	8.2 ± 0.7	9.9 ± 2.5	18.3 ± 2.6	-0.7 ± 0.1	-0.3 ± 0.2	-0.6 ± 0.2	-
27	45.56441	-0.05964	5.8 ± 0.7	31.0 ± 4.2	38.2 ± 4.3	0.1 ± 0.1	0.0 ± 0.1	-0.3 ± 0.2	s
28	45.68096	0.08564	3.3 ± 0.3	9.2 ± 1.4	12.5 ± 1.5	-0.4 ± 0.1	-0.1 ± 0.2	-0.4 ± 0.1	q
29	45.56972	0.33413	10.7 ± 1.0	19.4 ± 4.4	30.0 ± 4.6	-0.5 ± 0.1	-0.3 ± 0.2	-0.6 ± 0.2	
30	45.65081	0.15964	2.6 ± 0.3	13.5 ± 1.6	16.3 ± 1.6	-0.1 ± 0.1	0.3 ± 0.2	-0.1 ± 0.1	
31	45.52784	0.23256	5.7 ± 0.6	11.5 ± 2.3	17.4 ± 2.4	-0.4 ± 0.1	-0.4 ± 0.1	-0.7 ± 0.2	-
32	45.85195	0.16103	6.3 ± 0.7	15.8 ± 3.3	22.0 ± 3.4	-0.5 ± 0.1	-0.1 ± 0.2	-0.2 ± 0.2	
33	45.49421	0.00261	5.5 ± 0.7	19.9 ± 3.7	26.0 ± 3.8	-0.2 ± 0.1	0.0 ± 0.2	-0.4 ± 0.2	-
34	45.56161	0.02398	8.4 ± 1.0	22.2 ± 3.2	30.7 ± 3.4	? ± ?	-0.1 ± 0.1	-0.4 ± 0.1	q
35	45.71698	0.17694	2.8 ± 0.3	7.8 ± 1.4	10.8 ± 1.4	-0.3 ± 0.1	-0.4 ± 0.2	-0.3 ± 0.2	
36	45.63178	0.18695	2.9 ± 0.3	4.7 ± 1.1	7.7 ± 1.2	-0.3 ± 0.1	-0.3 ± 0.2	-0.8 ± 0.2	

Table 4.2: (Continued)

XMM	R.A.[fk5]	Dec.[fk5]	0.5 – 2 keV	2 – 10 keV	0.5 – 10 keV	PN HR	M1 HR	M2 HR	Notes
37	45.42586	0.11565	17.2 ± 1.7	24.4 ± 4.9	41.9 ± 5.2	? ± ?	-0.6 ± 0.1	-0.5 ± 0.1	-
38	45.72033	0.13976	1.9 ± 0.2	10.1 ± 1.5	12.0 ± 1.5	0.0 ± 0.1	0.2 ± 0.2	-0.1 ± 0.3	
39	45.54256	0.05859	3.6 ± 0.4	7.3 ± 1.7	11.0 ± 1.8	-0.4 ± 0.1	-0.3 ± 0.3	-0.7 ± 0.2	
40	45.70438	0.16737	2.2 ± 0.3	7.7 ± 1.4	9.9 ± 1.5	-0.3 ± 0.2	0.0 ± 0.2	-0.2 ± 0.2	
41	45.50220	0.06396	4.1 ± 0.5	8.9 ± 2.3	13.5 ± 2.4	-0.5 ± 0.2	0.0 ± 0.2	-0.6 ± 0.2	-
42	45.81484	0.18964	3.6 ± 0.5	13.6 ± 2.7	17.2 ± 2.8	-0.4 ± 0.2	0.3 ± 0.2	0.1 ± 0.2	
43	45.66834	0.35188	6.5 ± 0.8	12.0 ± 4.4	17.8 ± 4.5	-0.5 ± 0.2	-0.9 ± 1.9	-0.1 ± 0.4	
44	45.44001	0.07892	7.8 ± 1.3	56.3 ± 8.0	64.0 ± 8.1	? ± ?	0.2 ± 0.2	0.3 ± 0.1	-
45	45.56227	0.02132	3.5 ± 0.8	6.9 ± 9.1	15.1 ± 9.3	-0.7 ± 0.3	-1.0 ± 1.1	-1.0 ± 6.0	
46	45.52792	0.11871	1.7 ± 0.4	15.2 ± 2.8	16.9 ± 2.9	0.2 ± 0.2	0.3 ± 0.3	0.4 ± 0.3	- e
47	45.63782	0.15807	1.2 ± 0.2	7.4 ± 1.3	8.7 ± 1.3	0.3 ± 0.1	-0.5 ± 0.4	0.3 ± 0.2	
48	45.51293	0.18638	3.1 ± 0.4	9.9 ± 2.1	13.0 ± 2.1	-0.4 ± 0.2	-0.1 ± 0.2	-0.1 ± 0.3	-
49	45.66427	0.12122	2.6 ± 0.3	1.7 ± 1.7	4.3 ± 1.8	-1.0 ± 0.5	-0.7 ± 0.2	-1.0 ± 1.3	
50	45.62214	0.15656	1.9 ± 0.3	4.8 ± 1.1	6.7 ± 1.1	-0.4 ± 0.2	-0.3 ± 0.2	-0.4 ± 0.3	
51	45.59428	0.04838	1.9 ± 0.3	7.7 ± 1.4	9.7 ± 1.5	-0.2 ± 0.2	-0.2 ± 0.2	0.0 ± 0.2	
52	45.82856	0.22103	7.8 ± 1.4	14.0 ± 13.4	24.5 ± 13.6	-0.6 ± 0.3	-0.7 ± 2.5	-1.0 ± 2.4	
53	45.64862	0.33865	7.0 ± 0.9	4.7 ± 5.4	12.5 ± 5.6	-1.0 ± 0.6	-0.7 ± 0.3	-0.8 ± 1.7	
54	45.68043	0.12087	1.5 ± 0.2	5.3 ± 1.1	6.7 ± 1.1	-0.2 ± 0.2	0.1 ± 0.3	-0.3 ± 0.3	
55	45.81259	-0.01701	1.1 ± 0.7	32.8 ± 4.5	33.4 ± 4.6	0.9 ± 0.5	0.7 ± 0.2	0.7 ± 0.2	
56	45.82917	0.22354	4.6 ± 0.8	19.6 ± 4.6	24.7 ± 4.7	0.2 ± 0.3	0.0 ± 0.3	-0.4 ± 0.2	
57	45.64058	0.29293	2.2 ± 0.4	13.0 ± 2.6	15.4 ± 2.6	0.2 ± 0.2	-0.4 ± 0.3	0.1 ± 0.3	
58	45.80320	0.18363	4.3 ± 0.8	10.0 ± 3.4	16.6 ± 3.5	? ± ?	-0.7 ± 0.2	-0.2 ± 0.2	
59	45.67962	0.01731	1.9 ± 0.3	6.9 ± 1.7	8.8 ± 1.7	-0.1 ± 0.2	-0.8 ± 1.8	-0.4 ± 0.3	
60	45.52756	-0.00129	3.3 ± 0.7	20.0 ± 4.0	23.5 ± 4.1	? ± ?	0.1 ± 0.2	0.0 ± 0.2	-
61	45.68508	0.06585	1.7 ± 0.3	3.4 ± 1.2	5.2 ± 1.2	-0.5 ± 0.2	-0.2 ± 0.4	-0.5 ± 0.2	
62	45.89454	0.14303	3.5 ± 0.6	16.6 ± 4.3	20.1 ± 4.3	-0.3 ± 0.2	0.3 ± 0.2	0.3 ± 0.3	
63	45.56991	0.29621	2.3 ± 0.5	11.8 ± 3.0	14.2 ± 3	-0.1 ± 0.2	-0.3 ± 0.5	0.5 ± 0.2	
64	45.72136	-0.03394	2.6 ± 0.4	9.2 ± 2.6	12.0 ± 2.6	-0.3 ± 0.2	0.3 ± 0.3	-0.4 ± 0.3	
65	45.56736	0.27904	2.4 ± 0.4	7.5 ± 2.3	10.0 ± 2.4	-0.5 ± 0.4	-0.3 ± 0.3	0.0 ± 0.2	s
66	45.56873	0.16770	0.4 ± 0.2	12.0 ± 1.7	12.4 ± 2	0.7 ± 0.2	0.8 ± 1.6	0.9 ± 1.7	
67	45.63815	0.22279	2.4 ± 0.4	3.3 ± 1.9	5.6 ± 1.9	-0.6 ± 0.2	-0.4 ± 0.5	-1.0 ± 1.5	s
68	45.65587	-0.08222	6.9 ± 1.1	18.1 ± 5.1	25.0 ± 5.3	? ± ?	-0.3 ± 0.2	-0.2 ± 0.2	-
69	45.64630	-0.02311	5.0 ± 0.7	6.4 ± 2.7	11.5 ± 2.8	0.4 ± ?	-0.6 ± 0.2	-0.5 ± 0.2	
70	45.54383	0.23489	2.3 ± 0.4	8.7 ± 2.5	11.0 ± 2.5	-0.4 ± 0.2	-0.8 ± 2.5	0.4 ± 0.3	
71	45.72891	-0.09511	8.4 ± 1.5	37.7 ± 10.6	49.0 ± 10.9	? ± ?	-1.0 ± 2.3	-0.2 ± 0.2	-
72	45.84670	0.28070	5.6 ± 1.0	28.6 ± 7.4	34.3 ± 7.5	0.0 ± 0.2	? ± ?	? ± ?	
73	45.53562	0.17127	1.8 ± 0.4	6.8 ± 1.7	8.7 ± 1.8	-0.2 ± 0.2	0.3 ± 0.3	-0.5 ± 0.4	
74	45.71404	0.21886	1.7 ± 0.3	4.0 ± 1.6	5.6 ± 1.6	-0.5 ± 0.3	-0.6 ± 3.7	-0.2 ± 0.3	
75	45.77694	0.07833	1.8 ± 0.3	6.1 ± 1.8	8.0 ± 1.8	-0.3 ± 0.3	-0.3 ± 0.3	-0.1 ± 0.2	
76	45.57649	0.14474	1.3 ± 0.2	3.3 ± 1.3	4.9 ± 1.3	-0.3 ± 0.3	-0.6 ± 0.3	-0.3 ± 0.3	s
77	45.64066	0.19351	3.4 ± 0.5	3.2 ± 1.4	6.9 ± 1.5	? ± ?	-0.7 ± 0.2	-0.7 ± 0.1	

Table 4.2: (Continued)

XMM	R.A.[fk5]	Dec.[fk5]	0.5 – 2 keV	2 – 10 keV	0.5 – 10 keV	PN HR	M1 HR	M2 HR	Notes
78	45.58110	0.00618	0.9 ± 0.3	6.7 ± 1.7	8.3 ± 1.8	0.5 ± 0.2	0.0 ± 0.5	-0.6 ± 0.2	
79	45.46302	0.00512	6.7 ± 1.1	22.7 ± 8.6	29.5 ± 8.7	? ± ?	-0.1 ± 0.2	-0.8 ± 2.0	-
80	45.61488	-0.06842	2.8 ± 0.5	7.3 ± 4.2	9.8 ± 4.2	-0.3 ± 0.3	-0.8 ± 1.9	-0.9 ± 3.4	
81	45.52730	-0.06149	4.9 ± 0.9	22.0 ± 6.0	27.0 ± 6.1	? ± ?	0.1 ± 0.2	-0.2 ± 0.3	-
82	45.78333	0.04980	1.9 ± 0.4	6.4 ± 2.1	8.5 ± 2.1	-0.4 ± 0.2	0.1 ± 0.5	-0.3 ± 0.3	
83	45.72353	0.15235	2.1 ± 0.4	4.8 ± 3.4	7.3 ± 3.5	-0.4 ± 0.3	-1.0 ± 3.0	-1.0 ± 1.7	
84	45.55161	-0.02431	2.5 ± 0.5	2.9 ± 3.3	4.5 ± 3.4	-1.0 ± 1.3	-0.3 ± 0.6	-0.7 ± 1.4	
85	45.59272	-0.09154	8.4 ± 1.8	50.3 ± 12.5	58.7 ± 12.6	? ± ?	? ± ?	0.1 ± 0.2	-
86	45.66681	0.33798	3.2 ± 0.6	7.9 ± 3.2	10.6 ± 3.4	-0.4 ± 0.3	-0.3 ± 0.4	0.9 ± 5.5	
87	45.69953	0.27041	2.3 ± 0.4	3.3 ± 2.5	6.1 ± 2.6	-0.6 ± 0.2	-1.0 ± 5.1	-1.0 ± 4.3	
88	45.68490	0.31344	2.6 ± 0.5	4.7 ± 3.4	7.5 ± 3.5	-0.5 ± 0.3	-0.2 ± 3.5	-1.0 ± 3.5	
89	45.54894	0.02047	1.6 ± 0.3	4.7 ± 2.1	6.8 ± 2.1	-0.5 ± 0.3	-0.4 ± 8.2	-0.1 ± 0.3	
90	45.55718	0.12999	1.2 ± 0.3	3.4 ± 1.4	4.4 ± 1.4	-0.3 ± 0.3	-1.0 ± 1.9	-0.1 ± 0.4	
91	45.72983	0.17491	0.9 ± 0.2	3.9 ± 1.3	4.9 ± 1.3	-0.2 ± 0.3	0.4 ± 0.3	-0.3 ± 0.4	
92	45.80042	0.10777	1.8 ± 0.3	4.3 ± 2.1	5.9 ± 2.1	-0.5 ± 0.2	-1.0 ± 4.6	0.4 ± 0.8	
93	45.46568	0.10026	5.0 ± 0.8	5.7 ± 3.2	10.7 ± 3.3	? ± ?	-0.6 ± 0.3	-0.6 ± 0.3	-
94	45.81926	0.16593	2.1 ± 0.4	3.5 ± 1.9	5.6 ± 2	-0.6 ± 0.3	-0.3 ± 0.6	-0.4 ± 0.4	
95	45.76141	0.06731	1.5 ± 0.3	3.4 ± 1.6	4.8 ± 1.6	-0.4 ± 0.3	-0.3 ± 0.4	-0.6 ± 2.5	
96	45.79959	0.11941	1.6 ± 0.4	6.4 ± 1.9	8.0 ± 2	-0.1 ± 0.2	-0.3 ± 0.4	-1.0 ± 53.4	
97	45.58760	0.09220	1.0 ± 0.2	3.7 ± 1.2	4.7 ± 1.3	-0.2 ± 0.2	0.0 ± 0.5	1.0 ± 7.2	
98	45.71675	-0.05170	2.1 ± 0.4	4.0 ± 3.3	5.8 ± 3.3	-0.4 ± 0.4	-1.0 ± 3.0	-1.0 ± 2.7	
99	45.49924	0.07987	0.8 ± 0.3	9.1 ± 2.3	10.7 ± 2.5	0.4 ± 0.2	0.4 ± 0.3	0.5 ± 5.4	-
100	45.63690	0.08009	1.0 ± 0.2	3.5 ± 1.5	4.5 ± 1.6	-1.0 ± 2.1	-0.2 ± 0.5	0.0 ± 0.3	s
101	45.59565	0.01603	2.3 ± 0.4	2.1 ± 2.0	4.7 ± 2	-0.7 ± 0.2	? ± ?	-1.0 ± 4.1	
102	45.63462	0.24155	0.5 ± 0.3	9.2 ± 1.8	9.5 ± 1.9	0.4 ± 0.3	0.7 ± 0.3	1.0 ± 2.3	
103	45.49848	-0.03838	7.4 ± 1.6	35.6 ± 9.2	43.1 ± 9.4	? ± ?	0.0 ± 0.2	? ± ?	-
104	45.87137	0.21793	1.1 ± 0.5	13.3 ± 4.4	14.8 ± 4.4	0.6 ± 0.3	0.0 ± 0.4	0.0 ± 0.4	
105	45.47482	0.25960	2.6 ± 0.5	6.1 ± 6.5	7.5 ± 6.6	-0.6 ± 3.2	0.0 ± 0.7	-0.6 ± 6.5	-
106	45.79630	0.09120	1.3 ± 0.3	5.3 ± 2.0	6.7 ± 2.1	-0.2 ± 0.3	-1.0 ± 9.5	-0.1 ± 0.4	
107	45.72928	0.35913	6.6 ± 1.6	34.6 ± 11.3	41.2 ± 11.4	0.0 ± 0.2	? ± ?	? ± ?	
108	45.45139	0.13241	5.1 ± 0.9	4.2 ± 4.7	10.3 ± 4.9	? ± ?	-0.9 ± 2.3	-0.7 ± 0.3	-
109	45.86996	0.28492	5.8 ± 1.2	6.5 ± 6.1	12.3 ± 6.2	-0.7 ± 0.3	? ± ?	? ± ?	
110	45.69288	0.02623	1.1 ± 0.2	2.7 ± 1.2	3.8 ± 1.2	-0.4 ± 0.3	-0.1 ± 0.5	-0.5 ± 0.4	
111	45.59645	0.17982	0.6 ± 0.3	5.4 ± 1.3	5.8 ± 1.5	0.2 ± 0.3	0.6 ± 4.3	1.0 ± 3.1	
112	45.65665	0.00677	1.0 ± 0.3	3.1 ± 1.4	4.2 ± 1.4	-0.5 ± 0.3	0.2 ± 0.5	-0.1 ± 0.5	
113	45.58457	0.23922	1.1 ± 0.3	7.3 ± 2.6	8.6 ± 3	-0.6 ± 3.8	0.6 ± 2.7	-0.3 ± 0.3	
114	45.55483	0.09976	1.3 ± 0.3	1.8 ± 1.9	2.8 ± 1.9	-0.8 ± 1.8	-0.4 ± 0.5	-0.7 ± 7.5	
115	45.51752	0.01396	1.5 ± 0.4	3.6 ± 3.0	5.4 ± 3.1	-0.2 ± 0.5	-0.7 ± 0.5	-1.0 ± 4.8	-
116	45.56075	-0.05668	1.1 ± 0.5	13.0 ± 4.4	14.6 ± 4.5	-0.5 ± 4.0	0.2 ± 0.5	0.3 ± 0.3	
117	45.61728	0.03348	0.9 ± 0.2	3.4 ± 1.4	4.4 ± 1.4	-0.3 ± 0.3	-1.0 ± 5.9	0.0 ± 0.3	
118	45.50826	0.24316	2.1 ± 0.5	3.3 ± 3.6	4.5 ± 3.7	-1.0 ± 1.4	-0.1 ± 0.7	-1.0 ± 6.2	-

Table 4.2: (Continued)

XMM	R.A.[fk5]	Dec.[fk5]	0.5 – 2 keV	2 – 10 keV	0.5 – 10 keV	PN HR	M1 HR	M2 HR	Notes
119	45.80754	0.16748	1.5 ± 0.4	7.4 ± 2.9	9.1 ± 3	-1.0 ± 1.9	-0.2 ± 0.4	0.3 ± 0.3	
120	45.60580	0.20410	0.6 ± 0.2	4.3 ± 1.3	5.1 ± 1.3	0.3 ± 0.3	-0.3 ± 0.4	0.3 ± 0.4	
121	45.79758	0.02470	1.9 ± 0.9	9.0 ± 2.4	10.8 ± 3.2	0.9 ± 5.2	1.0 ± 3.0	0.1 ± 0.3	
122	45.67800	-0.08221	3.7 ± 0.9	7.6 ± 4.2	11.8 ± 4.3	? ± ?	-0.6 ± 0.3	-0.1 ± 0.4	-
123	45.72555	-0.09968	4.9 ± 1.1	18.8 ± 8.8	22.4 ± 9	? ± ?	0.0 ± 0.3	-0.8 ± 6.2	-
124	45.55270	0.24894	1.1 ± 0.3	10.1 ± 4.3	11.8 ± 4.4	-0.7 ± 6.6	0.2 ± 0.3	-0.7 ± 3.2	
125	45.82172	0.20595	1.5 ± 0.4	4.0 ± 2.7	5.5 ± 2.7	-0.4 ± 0.4	-0.1 ± 0.5	-0.3 ± 8.1	
126	45.52680	0.08989	1.1 ± 0.3	3.8 ± 2.4	4.8 ± 2.5	-0.1 ± 0.4	-1.0 ± 4.4	-1.0 ± 3.7	-
127	45.65018	0.01281	1.0 ± 0.3	3.0 ± 1.6	3.7 ± 1.8	-0.3 ± 0.4	-0.7 ± 2.9	0.5 ± 8.5	
128	45.56355	0.13039	0.7 ± 0.2	4.6 ± 1.6	4.6 ± 1.8	-0.1 ± 0.3	1.0 ± 8.4	-0.3 ± 6.7	
129	45.57510	-0.06320	1.2 ± 0.4	9.3 ± 5.1	10.3 ± 5.2	-1.0 ± 8.4	-0.9 ± 3.4	0.4 ± 0.4	
130	45.68849	0.16774	1.1 ± 0.3	3.5 ± 1.6	4.7 ± 1.6	? ± ?	-0.2 ± 0.4	-0.3 ± 0.3	
131	45.82766	0.21335	2.3 ± 0.6	4.8 ± 6.2	7.6 ± 6.3	-0.5 ± 0.5	-0.7 ± 2.8	-0.9 ± 7.3	
132	45.64452	0.08960	0.6 ± 0.4	3.8 ± 1.0	4.1 ± 1.2	0.8 ± 1.9	0.1 ± 0.4	1.0 ± 5.1	
133	45.49471	0.03947	0.9 ± 0.4	7.6 ± 3.0	9.8 ± 3.7	-0.7 ± 5.7	0.4 ± 3.5	0.7 ± 0.3	-
134	45.58854	0.21877	1.0 ± 0.3	3.4 ± 1.8	3.6 ± 2	-1.0 ± 1.6	0.9 ± 4.0	0.1 ± 0.7	
135	45.76509	0.05516	2.4 ± 0.8	0.5 ± 11.5	5.1 ± 11.5	1.0 ± 8.1	-1.0 ± 0.8	? ± ?	
136	45.63073	0.01617	0.6 ± 0.2	3.9 ± 2.0	4.9 ± 2	-0.6 ± 4.4	0.5 ± 0.5	-0.4 ± 0.4	
137	45.49974	0.06919	1.7 ± 0.5	0.5 ± 8.5	1.9 ± 8.7	-0.8 ± 1.8	-1.0 ± 20.7	-1.0 ± 7.7	-
138	45.54203	0.10093	1.0 ± 0.2	1.7 ± 1.3	2.9 ± 1.3	-0.7 ± 0.3	-1.0 ± 21.4	-0.1 ± 0.6	
139	45.70756	0.10411	0.8 ± 0.2	3.5 ± 2.3	3.2 ± 3.8	-0.7 ± 2.9	0.5 ± 5.3	-1.0 ± 9.7	
140	45.70387	0.22224	0.8 ± 0.3	3.4 ± 1.4	4.2 ± 1.6	-0.1 ± 0.3	1.0 ± 11.4	0.7 ± 6.1	
141	45.87826	0.11130	2.4 ± 0.5	0.0 ± 10.5	2.4 ± 10.5	-1.0 ± 1.6	-1.0 ± 10.1	-1.0 ± 23.6	s
142	45.76965	0.00813	1.3 ± 0.3	2.8 ± 2.3	4.1 ± 2.3	-0.4 ± 0.3	-1.0 ± 7.4	1.0 ± 9.6	
143	45.71021	0.09775	0.7 ± 0.2	0.1 ± 4.7	0.9 ± 4.7	-1.0 ± 2.5	0.0 ± 8.6	-1.0 ± 3.2	
144	45.55071	0.18796	0.9 ± 0.3	3.7 ± 2.6	4.5 ± 2.7	-1.0 ± 2.7	-1.0 ± 7.0	0.0 ± 0.5	
145	45.68469	0.18870	1.2 ± 0.3	2.1 ± 1.9	3.4 ± 1.9	? ± ?	-0.5 ± 0.3	-1.0 ± 3.0	
146	45.63841	0.04271	1.8 ± 0.5	2.1 ± 1.6	2.1 ± 2.1	1.0 ± 7.4	-0.8 ± 3.7	? ± ?	

Table 4.3: X-ray properties of the 14-h field *XMM* sources.

[a] Flux in units of 10^{-15} erg s^{-1} cm^{-2}, based on a photon index of 1.7.
[b] Hardness ratio given by source detection procedure, one for each X-ray camera. Marked with '?' if not detected or a bad measurement.
[c] - = lies outside CFDF map; c = lies within *Chandra* map; d = detected by *Chandra* (c and d are X-ray properties); q = known QSO; s = object with a stellar profile, from $P' < 0.15$ list (q and s are optical properties).

XMM	R.A.[fk5]	Dec.[fk5]	$0.5-2$ kev[a]	$2-10$ kev[a]	$0.5-10$ kev[a]	PN HR[b]	M1 HR[b]	M2 HR[b]	Notes[c]
1	214.2072	52.42472	34.6 ± 0.9	71.4 ± 3.1	106.0 ± 3.2	-0.5 ± 0.0	-0.4 ± 0.0	-0.4 ± 0.0	c d
2	214.4009	52.50781	42.2 ± 1.2	73.4 ± 4.0	115.9 ± 4.1	-0.5 ± 0.0	-0.5 ± 0.0	-0.5 ± 0.0	c d q
3	214.1816	52.24290	49.9 ± 1.5	94.2 ± 5.3	144.3 ± 5.5	-0.5 ± 0.0	-0.4 ± 0.1	-0.4 ± 0.1	
4	214.3536	52.50655	29.3 ± 1.0	53.2 ± 3.5	82.6 ± 3.7	-0.5 ± 0.0	-0.4 ± 0.1	-0.5 ± 0.1	c d q
5	214.0966	52.32077	25.5 ± 1.0	54.6 ± 3.6	80.1 ± 3.8	-0.4 ± 0.0	-0.3 ± 0.1	-0.4 ± 0.1	
6	214.4645	52.38579	19.3 ± 0.8	33.7 ± 2.7	53.1 ± 2.8	-0.5 ± 0.0	-0.4 ± 0.1	-0.5 ± 0.1	c d
7	214.2442	52.20099	31.7 ± 1.3	51.6 ± 4.8	83.8 ± 5.0	-0.6 ± 0.0	-0.4 ± 0.1	-0.5 ± 0.1	
8	214.2543	52.32128	16.7 ± 0.7	13.8 ± 1.7	30.6 ± 1.8	-0.8 ± 0.0	-0.6 ± 0.1	-0.7 ± 0.1	c d
9	214.2152	52.34575	12.6 ± 0.6	21.1 ± 2.0	33.9 ± 2.1	-0.6 ± 0.1	-0.5 ± 0.1	-0.4 ± 0.1	c d
10	214.6612	52.39937	33.3 ± 1.5	36.8 ± 5.0	70.4 ± 5.2	-0.7 ± 0.1	-0.6 ± 0.1	-0.6 ± 0.1	c d
11	214.3964	52.46897	20.0 ± 1.0	29.7 ± 3.0	49.6 ± 3.1	-0.6 ± 0.1	-0.5 ± 0.1	-0.5 ± 0.1	c d s
12	214.5097	52.30940	19.0 ± 1.0	40.7 ± 4.0	60.2 ± 4.1	-0.4 ± 0.1	-0.3 ± 0.1	-0.5 ± 0.1	
13	214.1781	52.30314	10.5 ± 0.6	38.5 ± 2.9	49.1 ± 2.9	-0.2 ± 0.1	-0.2 ± 0.1	-0.1 ± 0.1	s
14	214.6272	52.36948	22.6 ± 1.1	43.6 ± 4.9	66.4 ± 5.1	-0.5 ± 0.1	-0.5 ± 0.1	-0.4 ± 0.1	c d
15	214.2042	52.43273	13.5 ± 0.8	21.6 ± 2.4	35.9 ± 2.5	-0.6 ± 0.1	-0.5 ± 0.1	-0.6 ± 0.1	c d s
16	214.3412	52.30776	8.8 ± 0.6	26.4 ± 2.3	35.4 ± 2.3	-0.3 ± 0.1	-0.2 ± 0.1	-0.3 ± 0.1	s
17	214.3007	52.33627	8.2 ± 0.5	19.2 ± 1.8	27.4 ± 1.9	-0.4 ± 0.1	-0.4 ± 0.1	-0.3 ± 0.1	c d
18	214.1757	52.52828	12.3 ± 0.7	26.6 ± 3.0	39.1 ± 3.1	-0.4 ± 0.1	-0.5 ± 0.1	-0.4 ± 0.1	c d
19	214.2232	52.35119	6.9 ± 0.5	14.2 ± 1.8	21.2 ± 1.9	-0.4 ± 0.1	-0.5 ± 0.1	-0.4 ± 0.1	c d
20	214.2950	52.47458	7.3 ± 0.5	10.0 ± 1.6	17.4 ± 1.6	-0.6 ± 0.1	-0.5 ± 0.1	-0.6 ± 0.1	c d
21	214.3224	52.29719	8.5 ± 0.6	11.0 ± 1.8	19.5 ± 1.8	-0.7 ± 0.1	-0.5 ± 0.1	-0.4 ± 0.1	
22	214.2686	52.36073	2.2 ± 0.3	29.6 ± 2.2	31.9 ± 2.2	0.5 ± 0.1	0.3 ± 0.1	0.5 ± 0.1	c d
23	214.4251	52.47281	6.5 ± 0.5	20.9 ± 2.3	27.5 ± 2.4	-0.3 ± 0.1	-0.3 ± 0.1	0.0 ± 0.1	c d
24	214.4132	52.39201	6.2 ± 0.4	12.2 ± 1.6	18.6 ± 1.7	-0.4 ± 0.1	-0.6 ± 0.1	-0.4 ± 0.1	c d s
25	214.2133	52.25739	9.9 ± 0.7	16.2 ± 2.5	26.2 ± 2.6	-0.6 ± 0.1	-0.4 ± 0.1	-0.5 ± 0.2	
26	214.0970	52.20381	31.8 ± 2.3	40.1 ± 6.9	72.4 ± 7.4	? ± ?	-0.4 ± 0.1	-0.7 ± 0.1	s
27	214.1846	52.37168	4.9 ± 0.4	11.3 ± 1.6	16.3 ± 1.6	-0.4 ± 0.1	-0.6 ± 0.1	0.0 ± 0.1	
28	214.3487	52.53102	8.4 ± 0.6	10.2 ± 2.1	18.7 ± 2.2	-0.7 ± 0.1	-0.5 ± 0.1	-0.7 ± 0.1	c d
29	214.3138	52.38644	4.5 ± 0.4	9.1 ± 1.3	13.7 ± 1.3	-0.5 ± 0.1	-0.3 ± 0.1	-0.5 ± 0.1	c d
30	214.2921	52.31357	6.6 ± 0.5	8.3 ± 1.4	14.9 ± 1.5	-0.7 ± 0.1	-0.4 ± 0.1	-0.6 ± 0.1	
31	214.1451	52.37693	4.8 ± 0.4	11.2 ± 1.5	16.3 ± 1.6	-0.4 ± 0.1	-0.1 ± 0.2	-0.5 ± 0.1	
32	214.1376	52.31719	1.3 ± 0.3	36.4 ± 2.9	37.8 ± 3.0	0.7 ± 0.1	0.6 ± 0.1	0.7 ± 0.1	
33	214.5687	52.49419	9.4 ± 0.8	16.0 ± 3.1	25.7 ± 3.2	-0.6 ± 0.1	-0.5 ± 0.1	-0.5 ± 0.2	c d q
34	214.3021	52.28148	5.4 ± 0.5	11.4 ± 1.8	16.8 ± 1.8	-0.5 ± 0.1	-0.5 ± 0.2	-0.3 ± 0.1	
35	214.1901	52.48455	5.4 ± 0.4	6.6 ± 1.5	12.0 ± 1.6	-0.7 ± 0.1	-0.7 ± 0.2	-0.5 ± 0.1	c d s
36	214.0283	52.41636	4.1 ± 0.5	20.5 ± 2.8	24.9 ± 2.8	-0.1 ± 0.2	0.0 ± 0.1	0.0 ± 0.1	

Table 4.3: (Continued)

XMM	R.A.[fk5]	Dec.[fk5]	0.5 – 2 keV	2 – 10 keV	0.5 – 10 keV	PN HR	M1 HR	M2 HR	Notes
37	214.1596	52.38541	4.6 ± 0.4	4.9 ± 1.2	9.4 ± 1.3	-0.8 ± 0.1	-0.4 ± 0.2	-0.5 ± 0.1	
38	214.3767	52.20776	8.5 ± 0.8	14.6 ± 3.2	23.8 ± 3.3	-0.5 ± 0.1	-0.2 ± 0.2	-0.7 ± 0.2	
39	214.1210	52.56232	7.1 ± 0.6	13.0 ± 2.6	20.2 ± 2.7	-0.6 ± 0.1	-0.5 ± 0.2	-0.1 ± 0.1	
40	214.6051	52.39169	5.9 ± 0.8	35.6 ± 5.2	43.0 ± 5.2	0.2 ± 0.2	-0.1 ± 0.2	-0.1 ± 0.2	c d
41	214.3783	52.17146	10.9 ± 1.2	21.2 ± 5.4	33.4 ± 5.6	-0.4 ± 0.1	? ± ?	-0.6 ± 0.2	-
42	214.1796	52.42409	3.1 ± 0.3	6.4 ± 1.3	9.8 ± 1.4	-0.7 ± 0.1	0.0 ± 0.2	-0.3 ± 0.2	s
43	214.1184	52.45146	5.4 ± 0.8	16.2 ± 4.1	22.6 ± 4.2	-0.5 ± 6.5	-0.2 ± 0.2	-0.4 ± 0.2	
44	214.2426	52.24067	1.7 ± 0.3	26.8 ± 3.1	29.0 ± 3.2	0.5 ± 0.1	0.2 ± 0.2	0.5 ± 0.2	
45	214.4047	52.40778	2.8 ± 0.3	6.2 ± 1.3	9.2 ± 1.3	-0.3 ± 0.1	-0.5 ± 0.2	-0.6 ± 0.3	c d
46	214.7010	52.41818	14.4 ± 1.6	24.4 ± 6.9	38.7 ± 7.0	-0.5 ± 0.1	? ± ?	? ± ?	-
47	214.2253	52.34484	3.2 ± 0.4	2.5 ± 1.6	5.8 ± 1.6	-0.8 ± 0.1	-0.8 ± 2.6	-1.0 ± 1.2	c
48	214.3763	52.46309	2.5 ± 0.3	6.3 ± 1.4	9.0 ± 1.4	-0.4 ± 0.2	-0.1 ± 0.2	-0.5 ± 0.2	c d
49	214.6377	52.39623	6.1 ± 0.7	8.4 ± 3.5	15.7 ± 3.6	-0.7 ± 0.1	-0.8 ± 5.8	-0.5 ± 0.3	c d s
50	214.4414	52.46650	3.1 ± 0.4	6.2 ± 1.7	9.4 ± 1.8	-0.4 ± 0.2	-0.6 ± 0.3	-0.4 ± 0.3	c d
51	214.1987	52.18685	13.7 ± 1.6	19.9 ± 5.7	33.8 ± 5.9	? ± ?	-0.5 ± 0.2	-0.6 ± 0.1	s
52	214.5115	52.58648	5.8 ± 0.7	14.7 ± 5.1	20.6 ± 5.2	-0.4 ± 0.2	-0.4 ± 0.4	-0.7 ± 1.8	c d s
53	214.3874	52.53400	3.3 ± 0.4	7.5 ± 2.0	10.7 ± 2.1	-0.4 ± 0.2	-0.4 ± 0.3	-0.4 ± 0.4	c d
54	214.2447	52.40347	1.4 ± 0.2	5.5 ± 1.2	7.0 ± 1.2	-0.2 ± 0.2	0.0 ± 0.3	-0.2 ± 0.2	c d
55	214.2692	52.41403	0.6 ± 0.2	10.1 ± 1.3	10.6 ± 1.4	0.4 ± 0.2	0.6 ± 0.2	1.0 ± 1.6	c d
56	214.2114	52.27627	0.7 ± 0.3	15.2 ± 2.2	15.1 ± 2.4	0.6 ± 0.2	0.4 ± 0.4	0.9 ± 1.6	
57	214.3476	52.25335	2.7 ± 0.4	6.9 ± 2.1	9.7 ± 2.1	-0.4 ± 0.2	-0.2 ± 0.2	-0.5 ± 0.4	s
58	214.2969	52.42765	2.9 ± 0.4	0.0 ± 3.0	2.9 ± 3.1	-1.0 ± 0.5	-1.0 ± 0.9	-1.0 ± 1.5	c d
59	214.4426	52.50866	1.2 ± 0.3	12.4 ± 2.3	13.6 ± 2.3	0.2 ± 0.2	0.6 ± 0.2	0.5 ± 0.2	c d
60	214.1415	52.24977	2.4 ± 0.4	12.4 ± 3.0	15.2 ± 3.1	-0.2 ± 0.2	-0.4 ± 5.5	0.1 ± 0.3	
61	214.1315	52.46085	1.4 ± 0.3	9.1 ± 1.8	10.5 ± 1.8	-0.2 ± 0.3	0.1 ± 0.3	0.5 ± 0.2	
62	214.2114	52.60877	5.1 ± 0.8	11.6 ± 4.3	17.2 ± 4.4	-0.3 ± 0.2	-1.0 ± 2.6	-0.5 ± 0.3	
63	214.1824	52.48355	2.0 ± 0.4	4.6 ± 1.7	6.8 ± 1.8	-0.4 ± 0.2	-0.6 ± 0.3	-0.3 ± 0.4	c
64	214.1698	52.37279	1.7 ± 0.3	3.0 ± 1.2	4.7 ± 1.2	-0.5 ± 0.2	-0.5 ± 0.3	-0.4 ± 0.3	
65	214.5303	52.42288	1.8 ± 0.3	10.9 ± 2.4	12.7 ± 2.4	0.0 ± 0.2	-1.0 ± 4.7	0.2 ± 0.2	c d
66	214.4933	52.36419	2.3 ± 0.4	4.8 ± 1.8	7.5 ± 1.9	-0.5 ± 0.2	-0.7 ± 3.4	-0.6 ± 0.3	c d
67	214.0590	52.37618	1.7 ± 0.3	9.2 ± 2.0	11.1 ± 2.1	-0.2 ± 0.2	0.4 ± 0.3	-0.3 ± 3.7	
68	214.0411	52.45896	2.8 ± 0.4	4.8 ± 2.5	7.7 ± 2.6	-0.8 ± 3.0	-0.5 ± 0.3	-0.4 ± 0.3	
69	214.1246	52.39181	0.6 ± 0.2	10.0 ± 1.7	10.7 ± 1.7	0.6 ± 0.2	0.5 ± 0.3	0.4 ± 0.3	
70	214.1510	52.32015	1.7 ± 0.3	5.1 ± 1.8	6.9 ± 1.8	-0.5 ± 0.2	-0.8 ± 4.9	0.3 ± 0.5	
71	214.4264	52.28511	2.0 ± 0.3	8.4 ± 2.8	11.3 ± 2.8	-0.9 ± 1.6	-0.3 ± 0.3	-0.1 ± 0.3	
72	214.1611	52.47949	1.4 ± 0.3	5.4 ± 1.5	6.9 ± 1.5	-0.1 ± 0.3	-0.1 ± 0.3	-0.3 ± 0.3	
73	214.1836	52.50285	1.9 ± 0.3	3.8 ± 1.6	5.5 ± 1.7	-0.4 ± 0.3	-0.4 ± 0.3	-0.7 ± 1.7	c d
74	214.0459	52.27223	2.5 ± 0.5	13.2 ± 4.1	15.6 ± 4.1	0.0 ± 0.2	-0.7 ± 5.1	-1.0 ± 3.2	
75	214.4716	52.29089	2.3 ± 0.4	8.5 ± 3.3	10.2 ± 3.3	-1.0 ± 1.4	0.0 ± 0.4	0.2 ± 0.3	
76	214.4302	52.22506	3.0 ± 0.5	5.6 ± 3.2	8.7 ± 3.2	-0.7 ± 0.3	-0.6 ± 6.4	0.1 ± 0.3	
77	214.1063	52.47881	1.7 ± 0.3	7.8 ± 2.7	9.8 ± 2.7	-0.2 ± 0.2	-0.6 ± 2.5	-0.7 ± 7.2	

Table 4.3: (Continued)

XMM	R.A.[fk5]	Dec.[fk5]	0.5 – 2 keV	2 – 10 keV	0.5 – 10 keV	PN HR	M1 HR	M2 HR	Notes
78	214.1596	52.44893	1.5 ± 0.3	3.8 ± 1.3	5.3 ± 1.3	-0.4 ± 0.3	-0.5 ± 0.3	-0.1 ± 0.3	
79	214.2379	52.25723	2.3 ± 0.4	2.6 ± 2.1	5.1 ± 2.1	-0.7 ± 0.3	-1.0 ± 3.4	-0.7 ± 0.4	
80	214.2873	52.49141	1.8 ± 0.3	1.7 ± 1.4	3.6 ± 1.4	-0.7 ± 0.2	-0.7 ± 3.7	-0.8 ± 2.6	c d
81	214.1471	52.33013	1.7 ± 0.3	3.5 ± 1.6	5.2 ± 1.6	-0.6 ± 0.3	-0.2 ± 0.3	-0.1 ± 0.5	
82	214.2095	52.30247	0.3 ± 0.3	8.5 ± 1.6	10.4 ± 2.0	0.8 ± 0.2	0.8 ± 3.0	0.7 ± 5.3	
83	214.2781	52.30188	1.8 ± 0.3	2.6 ± 1.4	4.3 ± 1.5	-0.7 ± 0.2	-1.0 ± 1.7	0.1 ± 0.4	s
84	214.2464	52.37810	0.5 ± 0.2	6.0 ± 1.2	6.3 ± 1.2	0.3 ± 0.3	0.4 ± 0.4	1.0 ± 1.9	c
85	214.5015	52.37220	1.3 ± 0.3	6.1 ± 1.8	7.6 ± 1.8	0.1 ± 0.2	-0.3 ± 0.6	-0.3 ± 0.3	c d
86	214.0653	52.47826	1.5 ± 0.3	4.8 ± 1.9	6.5 ± 1.9	-0.3 ± 0.3	0.0 ± 0.3	-0.5 ± 0.3	
87	214.2045	52.17611	4.1 ± 1.2	19.5 ± 6.6	25.2 ± 6.7	? ± ?	0.4 ± 0.3	-0.4 ± 0.2	
88	214.4562	52.46960	1.9 ± 0.3	2.2 ± 2.0	3.7 ± 2.0	-0.6 ± 0.3	-1.0 ± 1.8	-1.0 ± 2.2	c d
89	214.2181	52.44959	0.8 ± 0.2	4.0 ± 1.2	4.8 ± 1.2	0.0 ± 0.3	-0.1 ± 0.3	0.2 ± 0.5	c d
90	214.4895	52.44187	1.3 ± 0.3	6.4 ± 1.8	7.3 ± 1.9	-0.4 ± 0.3	0.9 ± 1.9	0.3 ± 0.3	c d
91	214.1310	52.36863	0.5 ± 0.3	7.6 ± 1.5	9.4 ± 1.9	0.6 ± 0.2	0.5 ± 7.2	0.9 ± 2.0	
92	214.3757	52.62069	3.1 ± 0.6	7.7 ± 4.5	10.7 ± 4.5	-0.3 ± 0.3	-0.9 ± 3.1	-1.0 ± 2.7	
93	214.4963	52.52676	2.2 ± 0.4	5.2 ± 3.0	7.4 ± 3.1	-0.4 ± 0.3	-0.5 ± 5.8	-0.5 ± 2.4	c d
94	214.0708	52.44832	1.2 ± 0.3	7.0 ± 2.2	8.3 ± 2.3	0.2 ± 0.2	-0.7 ± 7.9	-0.2 ± 0.4	
95	214.5116	52.35847	1.3 ± 0.3	5.4 ± 1.9	6.8 ± 1.9	-0.1 ± 0.3	-0.4 ± 0.4	0.3 ± 0.6	c d
96	214.1705	52.40487	0.7 ± 0.2	3.9 ± 1.2	4.6 ± 1.2	0.0 ± 0.3	0.1 ± 0.5	-0.1 ± 0.3	
97	214.6744	52.36030	3.9 ± 0.7	2.1 ± 12.2	5.8 ± 12.2	-0.7 ± 1.1	-1.0 ± 1.6	-1.0 ± 26.4	
98	214.0376	52.35566	1.1 ± 0.3	10.0 ± 2.7	11.3 ± 2.7	0.4 ± 0.2	0.0 ± 0.3	1.0 ± ?	s
99	214.5911	52.49812	2.9 ± 0.5	4.7 ± 5.3	7.0 ± 5.4	-1.0 ± 1.2	-0.2 ± 0.5	-1.0 ± 5.6	c d s
100	214.0341	52.48847	1.4 ± 0.3	6.2 ± 2.4	8.1 ± 2.4	0.2 ± 0.2	-1.0 ± 5.6	-0.5 ± 0.4	
101	214.2595	52.22814	0.9 ± 0.3	9.7 ± 2.5	10.5 ± 2.5	0.4 ± 0.3	-0.1 ± 0.4	0.8 ± 1.9	
102	214.4478	52.58621	2.6 ± 0.5	6.6 ± 4.0	9.2 ± 4.0	-0.4 ± 0.3	-1.0 ± 5.0	-1.0 ± 7.1	c d
103	214.1073	52.54482	1.7 ± 0.4	9.1 ± 4.8	11.6 ± 4.9	-0.7 ± 3.4	-0.3 ± 6.5	-0.1 ± 0.3	
104	213.9273	52.36767	4.0 ± 1.1	52.1 ± 9.6	56.1 ± 9.6	? ± ?	0.5 ± 0.1	? ± ?	
105	214.6253	52.45294	0.9 ± 0.4	15.7 ± 4.2	16.9 ± 4.2	0.5 ± 0.3	-1.0 ± 18.4	0.4 ± 0.2	c d
106	214.0632	52.51497	0.8 ± 0.4	10.7 ± 2.6	11.3 ± 2.9	0.4 ± 0.2	1.0 ± 3.0	0.8 ± 2.5	
107	214.2815	52.29163	1.2 ± 0.3	5.4 ± 1.9	6.6 ± 2.0	-0.7 ± 2.0	0.3 ± 0.3	-0.2 ± 0.3	
108	214.0504	52.41505	1.5 ± 0.3	3.2 ± 2.0	4.6 ± 2.0	-0.5 ± 0.3	-0.9 ± 6.3	-0.3 ± 0.5	
109	214.0487	52.50645	1.9 ± 0.8	10.3 ± 2.6	11.0 ± 3.1	0.9 ± 2.4	0.9 ± 3.7	-0.1 ± 0.4	
110	214.0181	52.47473	3.5 ± 0.6	10.1 ± 4.9	14.1 ± 5.0	? ± ?	-0.3 ± 0.3	-0.6 ± 1.6	
111	214.3619	52.31625	0.5 ± 0.2	5.5 ± 1.4	6.0 ± 1.4	0.3 ± 0.3	0.0 ± 0.6	0.6 ± 0.3	
112	214.4634	52.27096	1.6 ± 0.3	4.3 ± 2.7	5.6 ± 2.7	-0.2 ± 0.3	-1.0 ± 4.4	-1.0 ± 5.3	
113	214.1681	52.25050	1.2 ± 0.4	7.6 ± 3.1	9.4 ± 3.1	-0.5 ± 2.2	-0.1 ± 0.3	0.0 ± 0.4	
114	214.3635	52.48663	0.6 ± 0.2	3.0 ± 1.2	3.8 ± 1.3	0.0 ± 0.6	-0.6 ± 0.3	0.2 ± 0.4	c d
115	214.5706	52.38552	1.2 ± 0.4	9.5 ± 3.8	12.2 ± 3.9	-1.0 ± 6.7	0.1 ± 0.4	-0.3 ± 0.3	c d
116	214.5959	52.45144	2.4 ± 0.4	0.1 ± 7.7	2.4 ± 7.8	-1.0 ± 1.3	-0.6 ± 4.8	-1.0 ± 3.8	c
117	214.4119	52.57010	1.6 ± 0.3	12.0 ± 4.9	13.3 ± 4.9	-0.9 ± 3.0	-1.0 ± 2.7	0.5 ± 0.3	c d
118	214.2070	52.28177	1.4 ± 0.3	3.9 ± 2.9	4.7 ± 2.9	-1.0 ± 1.2	-1.0 ± 4.8	0.4 ± 0.6	

Table 4.3: (Continued)

XMM	R.A.[fk5]	Dec.[fk5]	0.5 – 2 keV	2 – 10 keV	0.5 – 10 keV	PN HR	M1 HR	M2 HR	Notes
119	214.4879	52.52328	1.6 ± 0.4	5.9 ± 5.4	8.0 ± 5.5	-0.6 ± 2.8	-0.2 ± 0.5	-0.9 ± 3.9	c d
120	213.9630	52.45442	3.3 ± 0.7	9.6 ± 4.1	12.9 ± 4.2	? ± ?	-0.2 ± 0.3	-0.3 ± 0.4	
121	214.1620	52.26432	0.9 ± 0.3	7.6 ± 2.3	9.0 ± 2.6	0.2 ± 0.2	0.8 ± 5.8	-0.1 ± 6.5	
122	214.4385	52.49725	0.9 ± 0.3	6.1 ± 1.8	6.5 ± 1.9	-0.1 ± 0.3	1.0 ± 3.0	1.0 ± 2.5	c d
123	214.1529	52.33322	0.4 ± 0.4	6.9 ± 1.7	6.6 ± 1.8	1.0 ± 1.3	0.1 ± 0.7	0.1 ± 5.2	
124	213.9741	52.38092	1.2 ± 0.4	9.0 ± 3.8	9.7 ± 3.8	0.4 ± 0.4	-1.0 ± 6.1	-0.7 ± 4.5	
125	214.1639	52.53553	0.0 ± 0.9	10.4 ± 2.2	10.6 ± 2.5	1.0 ± 1.1	1.0 ± 2.1	0.8 ± 3.7	
126	214.6787	52.48925	4.8 ± 0.9	6.2 ± 5.9	11.1 ± 5.9	-0.6 ± 0.3	? ± ?	? ± ?	
127	214.1453	52.19660	2.8 ± 0.9	31.0 ± 8.0	33.4 ± 8.1	? ± ?	0.5 ± 0.2	-0.8 ± 4.7	
128	214.3917	52.56346	1.5 ± 0.4	12.2 ± 5.5	14.3 ± 5.5	-0.6 ± 3.8	0.1 ± 0.3	-0.5 ± 19.1	c d
129	214.3361	52.41572	0.7 ± 0.3	3.2 ± 1.0	3.7 ± 1.1	1.0 ± 3.2	0.1 ± 0.4	0.0 ± 0.3	c d
130	214.1332	52.20545	0.0 ± 2.6	30.4 ± 7.0	30.4 ± 7.4	? ± ?	1.0 ± 1.2	1.0 ± 1.0	
131	214.3394	52.61589	1.7 ± 0.7	12.1 ± 5.3	13.1 ± 5.8	-1.0 ± 4.1	1.0 ± 4.0	0.5 ± 0.4	
132	214.0599	52.32782	0.9 ± 0.3	5.9 ± 2.6	7.4 ± 2.6	-0.8 ± 5.6	0.0 ± 0.3	-0.1 ± 0.5	
133	214.4719	52.47724	0.9 ± 0.3	3.6 ± 1.6	4.4 ± 1.6	-0.2 ± 0.4	0.2 ± 0.6	-0.1 ± 0.5	c
134	214.3511	52.16770	8.1 ± 1.8	29.7 ± 9.9	37.8 ± 10.0	? ± ?	? ± ?	-0.1 ± 0.2	-
135	214.5605	52.46918	1.7 ± 0.4	3.6 ± 4.2	5.2 ± 4.3	-1.0 ± 1.5	-0.2 ± 0.6	-1.0 ± 6.4	c d
136	214.3575	52.26699	1.3 ± 0.5	7.5 ± 2.6	7.4 ± 3.5	0.7 ± 2.7	-1.0 ± 3.8	-1.0 ± 4.5	
137	214.3925	52.34394	0.4 ± 0.2	4.0 ± 1.2	3.6 ± 1.4	0.1 ± 0.4	1.0 ± 4.4	0.7 ± 4.0	c d
138	214.4630	52.31588	0.4 ± 0.3	6.5 ± 1.7	6.8 ± 1.9	0.5 ± 0.3	1.0 ± 7.1	0.8 ± 3.1	
139	213.9797	52.39389	1.8 ± 0.6	11.3 ± 4.9	12.9 ± 5.0	0.6 ± 8.0	0.2 ± 0.3	-0.6 ± 4.9	
140	214.3676	52.26986	0.8 ± 0.3	4.0 ± 1.8	4.8 ± 1.8	-0.4 ± 0.5	0.5 ± 0.3	-0.6 ± 17.0	
141	213.9649	52.46058	3.3 ± 0.8	7.9 ± 5.1	11.2 ± 5.1	? ± ?	-0.3 ± 0.3	-1.0 ± 2.4	s
142	213.9892	52.26869	6.9 ± 1.5	13.0 ± 7.0	19.9 ± 7.1	? ± ?	? ± ?	-0.4 ± 0.2	s
143	214.4713	52.27683	1.2 ± 0.3	5.3 ± 4.0	6.5 ± 4.0	-1.0 ± 2.2	-1.0 ± 4.1	0.2 ± 0.4	s
144	214.3148	52.31950	0.6 ± 0.2	2.2 ± 1.3	3.0 ± 1.3	-0.1 ± 0.6	-1.0 ± 33.5	-0.4 ± 0.3	c
145	214.2030	52.16998	3.4 ± 1.0	21.1 ± 10.0	25.0 ± 10.1	? ± ?	-1.0 ± 6.4	0.1 ± 0.3	-
146	214.1845	52.34945	0.7 ± 0.3	3.6 ± 1.5	4.8 ± 1.6	? ± ?	0.6 ± 0.4	-0.6 ± 0.3	
147	214.5237	52.29217	0.6 ± 0.7	15.0 ± 4.1	15.5 ± 4.5	0.6 ± 7.9	0.6 ± 0.3	0.7 ± 1.7	
148	214.2881	52.45087	0.7 ± 0.3	2.8 ± 1.2	3.2 ± 1.3	1.0 ± 2.3	-1.0 ± 8.0	-0.3 ± 0.4	c
149	214.3729	52.59720	1.6 ± 0.5	8.6 ± 5.5	10.0 ± 5.5	-1.0 ± 2.2	0.3 ± 0.4	-0.2 ± 25.1	c d
150	214.3045	52.16597	5.0 ± 1.2	0.6 ± 19.9	5.6 ± 19.9	? ± ?	-0.9 ± 2.3	-1.0 ± 2.2	-
151	214.3701	52.24234	1.2 ± 0.3	7.0 ± 4.0	6.5 ± 4.6	-1.0 ± 1.9	1.0 ± 32.1	0.8 ± 2.6	
152	213.9823	52.44128	4.1 ± 0.8	5.1 ± 4.3	9.1 ± 4.4	? ± ?	-0.3 ± 13.7	-0.6 ± 0.3	
153	214.4056	52.59925	5.5 ± 1.2	10.0 ± 6.3	15.2 ± 6.4	? ± ?	? ± ?	-0.4 ± 0.3	c
154	214.1934	52.17992	5.5 ± 1.6	1.5 ± 52.9	5.7 ± 52.9	? ± ?	-1.0 ± 4.3	1.0 ± 9.0	

Table 4.4: ID properties of the 3-h field *XMM* source IDs ($P' < 0.15$). Coordinates are for the CFDF objects *not* the XMM sources; the offset is between the *XMM* source and the CFDF object; The first two photo-z columns ($UBVI$ & $UBVIK$) are BPZ estimates, * indicates that $P_{\Delta z} < 0.9$ and so may be less reliable; $UBVRIZ$ is the photo-z estimate given by the CFDF code and here * also indicates a less reliable estimate because of multiple likelihood peaks or broad errors. Note, not all IDs are included in the recent $UBVRIZ$ catalogue, so these sources do not have redshift estimates in this column. Photo-z estimates are always unreliable for QSOs (and potentially misidentified stars) and saturated objects ($I_{Tot} < 18.5$), regardless of any other reliability measure. Notes have the same meaning as in table 4.2.

XMM	CFDF	R.A.[fk5]	Dec.[fk5]	Offset($''$)	P'	z_{sp}	$UBVI$	$UBVIK$	$UBVRIZ$	Notes
1		45.52829	-0.02246			0.614				q
2	48603	45.78065	0.17224	0.4	8.63E-04		0.01		2.01	s
3	80878	45.64505	0.01880	1.0	8.64E-03		0.40		0.45 *	
5	36830	45.63823	0.22535	0.4	1.65E-03	1.048	0.30	0.20	2.22	q
6	27229	45.73788	0.26803	1.1	9.46E-05		0.36		3.09	
7	9684	45.70320	0.35877			0.107	0.08		0.38	q
8	15331	45.58520	0.32705	0.8	1.95E-03		0.04		0.51 *	s
9	78735	45.65896	0.03432	0.7	7.20E-04	1.350	0.19 *			q
10	63707	45.59203	0.10864	1.0	5.86E-03	3.300	0.27	0.02	3.27	q
11	82792	45.61012	0.00831	1.0	1.15E-02		1.42		1.53 *	s
13	56174	45.53374	0.14061	1.3	2.04E-02		0.70			
14	64790	45.83426	0.10138	0.8	1.40E-03		0.23		0.27	
15	78257	45.68516	0.02951	0.7	7.72E-03		0.83		0.84	
20	27963	45.57106	0.26679	1.4	1.65E-02		0.20 *		2.26	
22	85206	45.79066	-0.00681	0.5	3.34E-03		0.24 *		2.26	
24	62173	45.62261	0.11390	1.3	1.99E-02	0.827	0.89	0.50	0.84	
25	82594	45.58656	0.01374	0.4	1.15E-03		0.65		0.66	
27	97057	45.56393	-0.05948	1.8	1.22E-02		0.73		0.93	s
28	66925	45.68145	0.08571	1.8	2.54E-02	0.900	0.08		2.20 *	q
29	13762	45.57013	0.33375	2.0	2.57E-02		0.38 *		1.53	
32	50421	45.85220	0.16086	1.1	1.56E-02		0.62 *		2.52	
34	81425	45.56175	0.02372	1.0	2.84E-03	1.179	0.01 *		1.90	q
35	47530	45.71717	0.17676	0.9	4.31E-03		0.50	0.33	0.69	
36	44712	45.63191	0.18734	1.5	6.24E-02		0.62 *	0.57	0.77	
38	55466	45.72035	0.13982	0.2	4.51E-03		1.09		0.88	
39	72546	45.54229	0.05872	1.1	7.98E-02		0.70 *			
40	49318	45.70466	0.16711	1.4	1.38E-02	0.616	0.56 *	0.02	0.65	
42	45059	45.81494	0.18973	0.5	2.73E-03		0.64		0.68	
43	10078	45.66893	0.35175	2.2	1.32E-02		1.43 *		0.64	
45	80741	45.56205	0.02162	1.4	1.65E-02		0.58		0.55	
47	52216	45.63807	0.15850	1.8	8.93E-02	0.279	1.20	0.80	1.27	
49	60572	45.66460	0.12130	1.2	1.20E-04		0.09			
50	52676	45.62234	0.15646	0.8	2.31E-02		0.50 *	0.50	1.43	
51	74652	45.59399	0.04863	1.4	3.75E-02		0.30		0.49	
52	36802	45.82893	0.22079	1.6	1.46E-01		0.68 *		1.54	
53	13860	45.64914	0.33900	2.3	4.58E-05		0.50 *			

Table 4.4: (Continued)

XMM	CFDF	R.A.[fk5]	Dec.[fk5]	Offset(″)	P'	z_{sp}	$UBVI$	$UBVIK$	$UBVRIZ$	Notes
54	59782	45.68074	0.12068	1.3	8.66E-02		0.69 *		0.95	
55	87828	45.81205	-0.01745	2.5	2.43E-02		0.53		0.54	
56	36666	45.82932	0.22347	0.6	4.42E-03		0.62		0.74	
58	45122	45.80342	0.18356	0.8	1.48E-02		0.51		1.53	
59	80538	45.67983	0.01708	1.1	1.29E-01		1.20 *			
63	21366	45.56986	0.29604	0.6	1.27E-02		0.66		1.04	
64	91703	45.72206	-0.03394	2.5	1.49E-02		0.10		0.13	
65	25440	45.56747	0.27871	1.3	1.41E-02		0.90 *		0.58	s
66	49372	45.56873	0.16783	0.5	3.36E-03		0.67		0.73	
67	37810	45.63941	0.22227	4.9	9.66E-02		0.41	0.07	0.60	s
69	88844	45.64644	-0.02376	2.4	1.48E-01		1.40		0.62	
70	35116	45.54377	0.23455	1.2	3.18E-02		1.05 *			
74	38640	45.71437	0.21899	1.3	4.26E-02		0.81	0.61	1.21 *	
75	67892	45.77674	0.07782	2.0	7.98E-02		0.28			
76	55634	45.57798	0.14406	5.9	1.18E-01		0.49		0.74	s
77	43571	45.64063	0.19383	1.2	1.88E-02		0.33		0.70	
78	83233	45.58096	0.00613	0.5	3.55E-02		1.23 *		0.60	
82	73526	45.78326	0.04985	0.3	6.16E-03		0.41		1.12	
83	53438	45.72387	0.15191	2.0	1.00E-01		0.20	0.19	3.02	
86	12628	45.66658	0.33796	0.8	5.63E-03		0.50			
87	24270	45.69919	0.27188	5.4	2.74E-04		0.50 *			
89	80377	45.54901	0.02043	0.3	4.29E-03		0.50 *		0.34	
90	58389	45.55685	0.13042	2.0	4.34E-02		1.29 *		2.62	
91	47033	45.72989	0.17451	1.4	1.29E-01		0.56 *			
92	62211	45.80016	0.10824	1.9	5.35E-02		0.54		2.67 *	
95	69733	45.76151	0.06753	0.9	5.95E-02		0.36		0.49	
96	59281	45.79954	0.11961	0.8	9.37E-02		0.61 *		2.49	
97	65662	45.58770	0.09224	0.4	1.19E-02		0.60 *		2.26	
100	68850	45.63694	0.08147	5.0	2.08E-02		0.50		0.61	s
101	82909	45.59592	0.01589	1.1	5.08E-04		0.50		0.58	
104	37771	45.87234	0.21751	3.8	1.39E-01		1.31 *		0.48	
107	7980	45.72985	0.35936	2.2	8.13E-02		0.68 *		0.81	
109	23302	45.86985	0.28527	1.3	5.54E-02		1.15		1.22	
110	78856	45.69338	0.02593	2.1	9.30E-02		0.49		0.53	
111	47865	45.59669	0.17959	1.2	2.10E-02	0.700	0.68	0.57	0.92	
114	65984	45.55365	0.10004	4.4	2.64E-02		0.50		0.60	
117	77450	45.61742	0.03339	0.6	2.76E-02		1.40		1.27	
119	48812	45.80753	0.16814	2.4	6.34E-02		0.08		2.61	
120	41131	45.60592	0.20426	0.7	4.90E-02		0.99 *		1.18	
121	78808	45.79781	0.02463	0.9	1.28E-02		0.53		0.79	
125	40200	45.82095	0.20649	3.4	8.21E-02		0.05		0.06	

Table 4.4: (Continued)

XMM	CFDF	R.A.[fk5]	Dec.[fk5]	Offset(″)	P'	z_{sp}	$UBVI$	$UBVIK$	$UBVRIZ$	Notes
127	81880	45.65058	0.01198	3.3	1.36E-01		0.93			
131	38707	45.82809	0.21339	1.5	1.98E-02		0.62 *		0.68	
132	66439	45.64537	0.08987	3.2	1.14E-01		0.65		0.96	
138	64251	45.54188	0.10066	1.1	8.45E-02		0.90			
139	64429	45.70665	0.10415	3.3	3.35E-02	0.488	0.50	0.08	0.56	
141	62358	45.87798	0.11156	1.4	8.48E-04		0.53		0.58	s
142	82378	45.76926	0.00801	1.5	6.50E-02		1.70		0.65 *	
143	64800	45.71042	0.09711	2.4	4.66E-02	0.618	0.51		0.62	
144	46344	45.55012	0.18831	2.5	5.24E-03		0.10		2.63	

Table 4.5: As table 4.4 but for the 14-h field. All IDs are for *XMM* sources, except the last 7 sources, of which 4 are the extra *Chandra* IDs and 3 are the alternative *Chandra* IDs for sources 10, 115 & 149 (assumed to be the correct IDs in this work). The two BPZ columns have been corrected for the systematic error found in this field (see appendix). Notes have the same meaning as in table 4.3.

XMM	CFDF	R.A.[fk5]	Dec.[fk5]	Offset($''$)	P'	z_{sp}	$UBVI$	$UBVIK$	$UBVRIZ$	Notes
1	34649	214.2061	52.42517	0.7	5.05E-03		0.33		0.35	c d
2	56149	214.3996	52.50816	0.1	8.83E-05	0.985	0.12	0.01	0.35	c d q
3	32209	214.1803	52.24317	0.4	9.65E-04		1.11			
4	50800	214.3523	52.50681	0.4	8.15E-04	0.479	0.01 *	0.01	1.16 *	c d q
5	22314	214.0946	52.32109	1.4	1.85E-02		0.79		0.91	
6	62713	214.4630	52.38622	0.4	7.77E-04		0.35		0.35	c d
7	38711	214.2426	52.20126	0.6	1.81E-03		0.25 *			
8	39972	214.2527	52.32180	0.8	3.59E-03		0.60		0.74	c d
9	35492	214.2133	52.34607	1.1	8.10E-03	0.808	0.05 *		1.95	c d
10	83085	214.6597	52.39960	0.5	6.75E-04		0.01		1.87	c d
11	55542	214.3951	52.46950	0.7	3.89E-03	1.223	1.85		1.87	c d s
12	67282	214.5084	52.30996	0.8	1.15E-02		0.49 *		0.42	
13	31728	214.1765	52.30344	0.6	6.10E-04		0.01		1.70	s
14	79632	214.6257	52.36994	0.4	1.89E-03		0.01 *		1.18	c d
15	33860	214.2036	52.43290	1.8	2.66E-02		0.12		0.08	c d s
16	50250	214.3401	52.30799	0.7	3.80E-03		0.65		0.42	s
17	45743	214.2992	52.33660	0.4	7.12E-04		0.64		0.62	c d
18	31283	214.1747	52.52856	0.8	5.12E-03		0.51		0.52	c d
19	36477	214.2215	52.35098	2.2	6.43E-02	0.983	0.62 *		1.62	c d
20	44421	214.2939	52.47464	1.2	2.84E-02		0.38		0.36	c d
22	41100	214.2676	52.36100	0.8	1.04E-02		0.93		0.86	c d
23	58899	214.4242	52.47299	1.2	1.25E-02	1.148	1.02		0.97	c d
24	57017	214.4118	52.39237	0.2	4.00E-04		1.85		1.18	c d s
25	35314	214.2121	52.25785	0.5	2.88E-03		0.01			
26	21940	214.0957	52.20328	3.2	6.30E-02		0.48			s
27	32769	214.1832	52.37185	0.7	1.92E-03		0.59		0.60	
28	49914	214.3472	52.53151	0.7	5.10E-03		1.94 *		0.40	c d
29	46217	214.3125	52.38680	0.1	3.70E-04	1.263	2.35		1.79 *	c d
30	44815	214.2913	52.31384	1.3	1.88E-03		0.09		2.55	
31	27519	214.1437	52.37738	0.4	3.12E-03		0.51		2.80	
32	26960	214.1363	52.31716	1.3	3.53E-02		0.72	0.69	0.89	
33	73713	214.5675	52.49446	0.4	1.10E-03	1.603	0.05		2.01	c d q
34	45274	214.3008	52.28199	0.7	3.83E-03		1.85		1.61	
35	32509	214.1889	52.48491	0.4	1.92E-03		0.22 *		0.42	c d s
36	14765	214.0271	52.41650	0.8	1.93E-02		0.83		1.06	
37	29731	214.1584	52.38561	0.7	2.02E-03		0.38		0.38	
38	53900	214.3749	52.20760	2.1	1.40E-02		0.62	0.01	0.66	
39	25468	214.1194	52.56286	0.8	5.36E-03		0.37		0.83	
40	77228	214.6037	52.39150	1.9	7.56E-02		0.95		1.51	c d

Table 4.5: (Continued)

XMM	CFDF	R.A.[fk5]	Dec.[fk5]	Offset(″)	P'	z_{sp}	$UBVI$	$UBVIK$	$UBVRIZ$	Notes
42	32151	214.1767	52.42409	3.6	2.85E-02		0.36		0.28	s
43	24723	214.1170	52.45225	1.6	3.29E-02		0.63		0.70	
44	38323	214.2417	52.24076	1.3	1.66E-02		0.78			
45	55970	214.4036	52.40820	0.7	1.58E-02		1.85		0.42	c d
47	36040	214.2244	52.34527	1.1	7.04E-02		0.12 *		0.06 *	c
48	52588	214.3746	52.46325	1.1	9.85E-02		1.48		1.34	c d
49	84591	214.6364	52.39700	1.6	1.33E-02		0.01		1.40	c d s
50	59894	214.4394	52.46722	1.9	4.30E-02	0.432	0.37		0.40	c d
51	33949	214.1966	52.18739	1.9	4.57E-03		0.01			s
52	67406	214.5079	52.58727	5.2	7.08E-02		0.01 *		0.71 *	c d s
53	54325	214.3857	52.53404	1.3	2.91E-02		1.85		0.96	c d
55	42727	214.2680	52.41473	1.3	4.87E-03		0.27		0.40	c d
56	34951	214.2104	52.27638	1.2	1.78E-02		0.86			
57	49934	214.3463	52.25391	0.8	3.33E-03		0.12		2.16	s
58	45989	214.2957	52.42785	0.7	2.04E-03		0.36 *		0.33	c d
59	60130	214.4413	52.50891	0.4	3.08E-03	0.988	0.99		0.94	c d
61	25745	214.1299	52.46111	0.6	4.04E-02		0.46		1.41	
62	35004	214.2100	52.60917	0.3	6.49E-04		0.73		0.79	
63	31301	214.1806	52.48398	1.0	7.29E-02		0.52 *			c
64	30075	214.1682	52.37271	1.6	1.02E-01		0.65		0.90	
66	65555	214.4923	52.36456	0.7	1.09E-02		1.40		1.00	c d
67	17783	214.0571	52.37653	1.3	5.56E-02		0.27		0.83	
69	25429	214.1234	52.39243	1.0	2.24E-02		0.84		1.08	
70	28394	214.1494	52.32003	1.8	6.13E-02		0.62		1.65	
71	58275	214.4252	52.28522	1.0	2.47E-02		2.68 *		1.50	
72	29697	214.1606	52.47914	3.1	9.82E-02		0.80		0.87	
74	17208	214.0440	52.27264	1.3	5.64E-03		0.42			
75	63310	214.4709	52.29158	1.8	1.03E-01		0.51		0.59	
79	37913	214.2358	52.25765	1.7	4.18E-02		0.83	0.73		
82	34515	214.2076	52.30252	1.6	2.96E-02	0.808	0.79		0.88	
83	42599	214.2787	52.30243	4.2	1.44E-01		0.74		0.71	s
85	66214	214.5001	52.37308	1.9	1.28E-01		1.23 *		1.14	c d
86	18647	214.0640	52.47858	0.1	7.26E-04		0.68		1.06	
87	34543	214.2017	52.17736	4.6	7.54E-02		0.99			
88	61988	214.4549	52.46978	0.6	1.82E-02	0.995	0.60		1.63	c d
89	35432	214.2162	52.45008	1.2	4.98E-02		0.72		0.84	c d
90	65240	214.4877	52.44177	1.8	1.17E-01		1.48		1.20	c d
91	25734	214.1295	52.36941	1.6	1.19E-01		1.10 *		1.27	
92	52922	214.3745	52.62106	0.3	2.92E-03		0.65		0.71	
93	65969	214.4953	52.52738	1.3	3.50E-02	0.637	1.80		0.73	c d
94	19012	214.0697	52.44880	0.7	5.09E-02		0.51			

Table 4.5: (Continued)

XMM	CFDF	R.A.[fk5]	Dec.[fk5]	Offset(″)	P'	z_{sp}	$UBVI$	$UBVIK$	$UBVRIZ$	Notes
95	69197	214.5096	52.35876	1.4	3.39E-03		0.25		0.31	c d
97	85590	214.6735	52.36127	2.5	7.20E-02		1.85			
98	15693	214.0350	52.35468	5.5	7.68E-02		0.49		0.38	s
99	76245	214.5903	52.49852	1.2	1.64E-03	0.000	0.68		0.62	c d s
102	60656	214.4470	52.58607	2.2	1.15E-01		2.72		0.14	c d
103	23308	214.1060	52.54512	0.3	4.28E-03		2.59 *		1.87	
104	4623	213.9254	52.36858	2.4	2.66E-02		0.40 *		0.35	
105	79441	214.6239	52.45244	3.0	8.99E-02		0.62		0.75	c d
106	18587	214.0621	52.51536	0.7	5.01E-03		0.47		0.48	
107	42600	214.2799	52.29213	0.8	3.27E-02		1.60 *			
108	18555	214.0474	52.41673	5.9	7.10E-03		0.12		0.14	
109	16776	214.0476	52.50674	0.6	6.86E-02		0.12 *			
110	13827	214.0162	52.47423	3.2	1.23E-01		0.12		0.09 *	
111	51269	214.3606	52.31558	3.7	1.41E-01		1.62 *		0.43	
112	63545	214.4618	52.27126	0.6	6.08E-03		0.70		0.61	
113	31206	214.1667	52.25094	0.4	4.06E-05		0.01	0.02 *		
114	51372	214.3625	52.48662	1.5	1.33E-01		0.54 *		4.24	c d
115	73478	214.5699	52.38634	2.2	1.16E-01		0.91 *			c d
116	77033	214.5949	52.45225	1.8	2.36E-03		0.37		0.28	c
117	56581	214.4110	52.57036	1.0	7.78E-02		0.59		0.79	c d
118	34410	214.2061	52.28159	2.2	4.69E-02		0.70	1.61		
119	64736	214.4866	52.52333	1.1	5.82E-02		1.49		0.56	c d
127	27813	214.1439	52.19802	3.9	8.49E-02		0.62			
128	54966	214.3907	52.56351	1.3	1.55E-02	0.548	0.60		0.62	c d
132	18082	214.0588	52.32756	2.2	5.70E-02		0.57		0.53	
133	63277	214.4705	52.47736	0.8	7.63E-03		0.69 *		0.71	c
135	72587	214.5594	52.46943	0.7	1.21E-02		0.05		2.67	c d
137	54900	214.3911	52.34428	0.2	4.27E-04		0.59		0.57	c d
141	8503	213.9635	52.46123	1.1	5.18E-03		0.04		1.94	s
142	10561	213.9867	52.26863	2.8	7.00E-02		1.81			s
143	63681	214.4702	52.27698	0.9	8.23E-04		0.43		0.32	s
144	47052	214.3141	52.32068	3.3	3.14E-02		0.54		0.50	c
146	32896	214.1812	52.35056	5.0	2.51E-02		0.37		0.39	
147	69363	214.5235	52.29270	2.7	4.16E-02		0.72		0.66	
148	44072	214.2870	52.45245	4.5	6.76E-02		0.57	0.02	0.56	c
149	52691	214.3721	52.59709	2.0	8.52E-02		0.69		0.76	c d
151	51768	214.3684	52.24278	0.8	1.48E-01		1.60 *			
153	56022	214.4041	52.59928	1.2	3.45E-02		0.47		0.45	c
154	32679	214.1917	52.17971	2.1	1.08E-01		1.05 *			
65	69393	214.5297	52.42301	1.2	8.99E-02		1.74 *		1.12	new
80	43006	214.2861	52.49144	0.5	9.19E-02		3.47 *			new

Table 4.5: (Continued)

XMM	CFDF	R.A.[fk5]	Dec.[fk5]	Offset(″)	P'	z_{sp}	$UBVI$	$UBVIK$	$UBVRIZ$	Notes
122	59768	214.4391	52.49744	0.1	2.26E-04	0.873	0.81		0.84	new
129	48314	214.3331	52.41666	0.2	5.57E-03		5.06		0.56	new
10	82156	214.6581	52.39855	0.8	8.35E-02		0.81		1.18	alternate
115	73352	214.5694	52.38519	1.0	5.12E-02		1.23		1.74	alternate
149	52467	214.3699	52.59755	2.1	4.23E-02		0.52		0.54	alternate

Table 4.6: Optical properties of the 3-h field *XMM* source IDs, as extracted from the original CFDF *UBVI* catalogues, including CFRS *K* photometry where available. All magnitudes are AB and measured in a 3″ diameter aperture, except for the I_{Tot} magnitude which is the total magnitude measured using a variable aperture. This total magnitude is used as the prior in the BPZ photometric redshift code, while the 3″ aperture magnitudes and errors are used as the input catalogue.

XMM	CFDF	I_{Tot}	U	ΔU	B	ΔB	V	ΔV	I	ΔI	K	ΔK
2	48603	19.460	19.983	0.010	20.049	0.007	19.534	0.003	19.631	0.002		
3	80878	20.675	21.677	0.017	21.995	0.009	21.185	0.008	20.895	0.005		
5	36830	20.470	21.978	0.021	22.340	0.022	21.442	0.007	20.755	0.004	19.05	0.05
6	27229	14.156	19.903	0.008	18.154	0.002	16.867	0.001	15.310	0.000		
7	9684	17.771	20.683	0.012	19.184	0.004	19.143	0.002	18.295	0.001		
8	15331	19.071	20.343	0.010	19.986	0.007	19.575	0.003	19.217	0.002		
9	78735	17.924	18.909	0.005	18.654	0.003	18.481	0.002	18.082	0.001		
10	63707	19.996	24.437	0.071	21.355	0.006	20.537	0.005	20.243	0.003	19.93	0.11
11	82792	20.972	21.775	0.018	21.478	0.007	21.426	0.008	21.108	0.005		
13	56174	21.215	29.627	2.457	99.000	27.570	23.223	0.031	21.380	0.010		
14	64790	18.493	22.002	0.023	21.054	0.006	19.990	0.004	18.987	0.002		
15	78257	21.176	24.635	0.083	24.652	0.047	23.459	0.033	21.380	0.006		
20	27963	20.686	21.806	0.019	21.356	0.013	21.359	0.007	20.908	0.005		
22	85206	20.889	21.898	0.023	21.701	0.009	21.528	0.010	21.088	0.005		
24	62173	21.220	25.780	0.173	24.865	0.046	24.163	0.051	21.657	0.006	19.37	0.06
25	82594	19.855	22.962	0.032	22.517	0.002	21.828	0.010	20.235	0.003		
27	97057	19.642	24.009	0.057	23.275	0.892	22.319	0.015	19.802	0.003		
28	66925	20.720	21.672	0.018	21.363	0.009	20.983	0.007	20.921	0.005		
29	13762	20.445	21.358	0.016	21.390	0.013	20.883	0.006	20.650	0.004		
32	50421	21.233	23.055	0.041	22.879	0.020	22.585	0.015	21.478	0.006		
34	81425	18.979	19.975	0.008	20.075	0.059	19.692	0.004	19.342	0.003		
35	47530	19.822	24.001	0.063	23.050	0.025	22.176	0.010	20.150	0.003	18.36	0.02
36	44712	22.536	24.133	0.063	24.180	0.059	23.762	0.031	22.696	0.012	21.02	0.23
38	55466	23.391	25.464	0.139	25.019	0.065	24.961	0.098	23.511	0.019		
39	72546	23.751	99.000	28.170	99.000	27.570	25.951	0.289	23.821	0.026		
40	49318	20.514	23.054	0.038	22.571	0.019	22.099	0.010	20.792	0.004	19.29	0.05
42	45059	20.763	25.765	0.224	24.925	0.063	23.951	0.037	21.830	0.007		
43	10078	19.323	21.663	0.018	21.104	0.013	20.675	0.004	19.616	0.002		
45	80741	20.780	23.839	0.055	23.477	0.140	22.823	0.021	21.434	0.007		
47	52216	22.664	25.435	0.133	24.430	0.050	24.927	0.098	22.771	0.014	20.10	0.10
49	60572	14.320	16.083	0.001	14.557	0.001	14.793	0.000	15.493	0.000		
50	52676	22.568	23.042	0.033	23.851	0.029	23.267	0.025	22.692	0.012	21.42	0.34
51	74652	21.954	22.782	0.029	23.331	0.022	22.620	0.017	22.114	0.008		
52	36802	23.772	26.835	0.536	26.319	0.189	25.888	0.204	24.331	0.037		
53	13860	11.530	15.479	0.001	14.981	0.001	99.000	27.590	14.746	0.001		
54	59782	23.374	24.617	0.081	24.349	0.041	24.251	0.060	23.406	0.018		
55	87828	19.824	24.425	0.081	23.528	0.019	22.270	0.015	20.324	0.003		
56	36666	20.999	24.735	0.104	24.041	0.037	23.186	0.021	21.349	0.006		

Table 4.6: (Continued)

XMM	CFDF	I_{Tot}	U	ΔU	B	ΔB	V	ΔV	I	ΔI	K	ΔK
58	45122	21.860	22.863	0.039	23.324	0.023	22.723	0.014	22.033	0.007		
59	80538	24.392	26.114	0.243	25.317	0.090	25.949	0.289	24.239	0.041		
63	21366	22.262	24.556	0.080	24.530	0.071	23.830	0.036	22.403	0.010		
64	91703	19.122	20.783	0.012	20.188	0.005	19.729	0.003	19.446	0.002		
65	25440	20.728	21.532	0.017	21.344	0.013	21.408	0.007	20.898	0.004		
66	49372	21.192	25.338	0.140	24.816	0.088	23.528	0.034	21.415	0.007		
67	37810	20.322	25.373	0.139	23.646	0.044	22.419	0.012	20.480	0.003	20.12	0.13
69	88844	22.832	23.595	0.046	23.263	0.020	23.407	0.030	22.922	0.016		
70	35116	21.960	24.664	0.097	24.631	1.331	23.968	0.039	22.200	0.010		
74	38640	22.357	24.618	0.089	24.510	0.054	24.114	0.039	22.656	0.010	20.95	0.28
75	67892	22.248	23.899	0.057	23.631	0.025	22.927	0.023	22.529	0.011		
76	55634	20.200	25.978	0.206	23.684	0.026	22.608	0.018	20.342	0.003		
77	43571	21.352	22.790	0.031	22.784	0.029	22.190	0.012	21.620	0.006		
78	83233	24.205	25.363	0.131	24.766	0.148	25.007	0.110	24.336	0.040		
82	73526	23.148	25.158	0.126	26.119	0.130	24.355	0.064	23.421	0.019		
83	53438	22.604	24.721	0.089	24.059	0.038	22.784	0.017	22.710	0.011	22.43	0.86
86	12628	20.449	24.341	0.073	23.413	0.041	22.446	0.012	20.690	0.004		
87	24270	11.749	20.031	0.010	16.203	0.002	99.000	27.590	15.193	0.001		
89	80377	22.819	24.496	0.081	24.486	18.736	23.821	0.046	22.979	0.017		
90	58389	21.311	24.741	0.091	23.849	0.073	23.557	0.037	21.556	0.006		
91	47033	23.822	25.800	0.210	25.572	0.138	25.469	0.121	24.653	0.041		
92	62211	21.662	23.632	0.052	23.342	0.018	22.881	0.020	21.816	0.007		
95	69733	23.779	25.889	0.202	26.092	0.126	24.995	0.108	24.278	0.034		
96	59281	24.826	26.236	0.280	26.122	0.112	26.124	0.293	24.889	0.057		
97	65662	23.400	24.732	0.087	24.640	0.008	24.399	0.069	23.454	0.019		
100	68850	17.949	24.076	0.056	21.920	0.009	20.561	0.005	18.087	0.001		
101	82909	16.544	22.402	0.024	20.436	0.005	19.088	0.002	16.739	0.001		
104	37771	21.565	22.805	0.037	22.514	0.017	22.417	0.013	21.946	0.007		
107	7980	21.989	25.070	0.117	24.479	0.058	23.925	0.037	22.243	0.009		
109	23302	22.627	24.828	0.113	24.410	0.051	24.564	0.067	23.238	0.017		
110	78856	22.334	24.714	0.085	24.296	0.037	23.591	0.036	22.475	0.010		
111	47865	21.441	24.540	0.081	24.394	0.066	23.567	0.026	21.861	0.007	20.18	0.11
114	65984	18.620	25.873	0.205	23.568	10.073	22.265	0.016	20.146	0.004		
117	77450	23.573	25.057	0.105	23.730	0.026	24.465	0.068	23.684	0.024		
119	48812	21.439	23.170	0.046	22.612	0.017	22.227	0.011	21.811	0.007		
120	41131	24.048	24.726	0.087	25.891	0.187	25.285	0.110	24.489	0.038		
121	78808	21.522	26.250	0.298	25.646	0.080	24.312	0.064	21.917	0.008		
125	40200	20.967	24.508	0.097	23.062	0.022	22.261	0.012	21.182	0.006		
127	81880	21.881	25.757	0.169	25.380	0.069	24.503	0.077	22.253	0.011		
131	38707	20.740	24.036	0.072	23.331	0.025	22.722	0.016	21.151	0.005		
132	66439	21.630	25.378	0.124	24.863	0.048	23.967	0.044	22.117	0.009		

Table 4.6: (Continued)

XMM	CFDF	I_{Tot}	U	ΔU	B	ΔB	V	ΔV	I	ΔI	K	ΔK
138	64251	23.701	24.855	0.112	24.388	13.718	25.507	0.224	23.845	0.053		
139	64429	19.642	23.781	0.049	22.802	0.016	22.032	0.012	20.286	0.003	18.97	0.04
141	62358	16.623	23.468	0.046	21.494	0.007	19.967	0.003	16.775	0.001		
142	82378	22.623	23.273	0.040	22.910	0.017	22.992	0.027	22.659	0.013		
143	64800	20.872	26.405	0.294	24.800	0.048	23.495	0.031	21.154	0.005		
144	46344	17.689	19.214	0.006	18.540	0.017	18.218	0.002	17.933	0.001		

Table 4.7: As table 4.6 but for the 14-h field. All are *XMM* IDs except the 7 sources at the end, of which 4 are the extra *Chandra* IDs and 3 are the alternative *Chandra* IDs for sources 10, 115 & 149 (assumed to be the correct IDs in this work).

XMM	CFDF	I_{Tot}	U	ΔU	B	ΔB	V	ΔV	I	ΔI	K	ΔK
1	34649	20.604	22.083	0.027	21.833	0.008	20.906	0.005	20.887	0.004		
2	56149	19.996	21.011	0.011	20.814	0.004	20.206	0.003	20.146	0.002	19.25	0.04
3	32209	19.955	21.499	0.016	21.650	0.012	21.687	0.009	20.375	0.003		
4	50800	19.762	20.918	0.011	20.549	0.003	20.338	0.003	19.932	0.002	18.62	0.02
5	22314	20.940	23.925	0.052	23.580	0.023	22.796	0.014	21.181	0.005		
6	62713	19.365	22.842	0.031	21.814	0.007	20.807	0.004	19.632	0.002		
7	38711	19.756	20.889	0.012	20.609	0.007	20.529	0.005	19.986	0.003		
8	39972	19.882	21.883	0.019	21.622	0.009	21.131	0.006	20.266	0.003		
9	35492	20.252	21.836	0.019	21.512	0.008	21.141	0.006	20.690	0.004		
10	83085	19.029	19.341	0.006	19.402	0.003	19.050	0.002	19.163	0.002		
11	55542	20.473	20.462	0.008	20.817	0.004	20.640	0.003	20.601	0.003		
12	67282	21.646	22.252	0.024	22.505	0.011	21.992	0.008	21.796	0.006		
13	31728	18.139	18.673	0.004	18.484	0.002	18.340	0.002	18.266	0.001		
14	79632	20.447	20.959	0.013	21.015	0.006	20.689	0.005	20.621	0.003		
15	33860	20.732	21.866	0.025	21.598	0.007	20.993	0.005	20.804	0.004		
16	50250	20.332	21.723	0.018	21.682	0.008	21.257	0.005	20.478	0.003		
17	45743	19.500	21.927	0.018	21.665	0.008	21.000	0.005	19.891	0.003		
18	31283	20.410	24.435	0.084	23.418	0.022	22.253	0.010	20.636	0.004		
19	36477	21.688	22.600	0.027	22.926	0.017	22.378	0.012	21.862	0.008		
20	44421	21.908	22.999	0.028	23.126	0.015	22.596	0.010	22.136	0.008		
22	41100	21.396	25.205	0.094	25.809	0.110	24.060	0.029	21.727	0.007		
23	58899	20.595	23.926	0.046	23.727	0.017	22.901	0.011	20.859	0.004		
24	57017	20.704	20.950	0.013	21.264	0.005	20.971	0.005	20.825	0.004		
25	35314	20.652	21.180	0.014	21.315	0.011	20.852	0.007	20.921	0.004		
26	21940	20.717	22.460	0.025	22.138	0.015	21.508	0.008	20.834	0.004		
27	32769	19.538	23.555	0.042	22.650	0.014	21.744	0.008	20.108	0.003		
28	49914	20.917	22.668	0.024	22.217	0.008	21.850	0.007	21.115	0.005		
29	46217	21.674	22.246	0.023	22.010	0.008	21.850	0.007	21.780	0.006		
30	44815	17.858	19.017	0.005	18.405	0.002	18.075	0.001	18.030	0.001		
31	27519	21.675	23.824	0.048	23.463	0.021	22.640	0.013	21.784	0.007		
32	26960	21.913	24.136	0.057	24.395	0.036	23.511	0.021	22.285	0.009	20.05	0.17
33	73713	19.830	20.614	0.009	20.179	0.003	20.022	0.003	19.940	0.002		
34	45274	20.498	20.923	0.011	20.967	0.005	20.924	0.005	20.696	0.004		
35	32509	21.047	22.392	0.031	22.123	0.009	21.722	0.007	21.169	0.005		
36	14765	22.197	24.752	0.101	24.544	0.046	24.011	0.031	22.594	0.012		
37	29731	19.417	24.038	0.054	22.720	0.015	21.446	0.007	19.861	0.003		
38	53900	19.487	22.389	0.025	21.902	0.007	21.189	0.005	19.979	0.003	19.86	0.07
39	25468	20.480	22.216	0.029	22.049	0.010	21.215	0.006	20.781	0.004		
40	77228	22.211	24.501	0.066	24.475	0.032	23.949	0.023	22.421	0.009		
42	32151	19.166	23.495	0.052	21.318	0.006	20.295	0.003	19.284	0.002		

Table 4.7: (Continued)

XMM	CFDF	I_{Tot}	U	ΔU	B	ΔB	V	ΔV	I	ΔI	K	ΔK
43	24723	21.435	28.837	2.281	25.717	0.074	24.382	0.033	22.068	0.008		
44	38323	20.804	23.055	0.034	23.001	0.025	22.515	0.016	21.331	0.006		
45	55970	22.474	22.745	0.025	23.017	0.013	22.758	0.012	22.620	0.010		
47	36040	23.546	25.564	0.122	24.189	0.034	24.191	0.033	23.849	0.028		
48	52588	24.116	27.024	0.278	26.175	0.082	26.353	0.129	24.301	0.032		
49	84591	20.139	20.724	0.011	20.659	0.005	20.423	0.004	20.255	0.003		
50	59894	21.321	23.496	0.037	23.169	0.012	22.366	0.009	21.818	0.006		
51	33949	18.196	18.663	0.004	18.590	0.003	18.429	0.002	18.319	0.001		
52	67406	19.703	20.846	0.011	20.480	0.003	20.283	0.003	19.834	0.002		
53	54325	21.693	26.103	0.143	25.971	0.082	24.887	0.043	22.150	0.008		
55	42727	19.100	23.883	0.048	22.882	0.020	20.947	0.006	20.034	0.003		
56	34951	21.218	25.758	0.137	25.174	0.086	23.832	0.029	21.535	0.005		
57	49934	19.936	20.887	0.012	20.261	0.003	20.082	0.003	20.060	0.002		
58	45989	19.611	23.302	0.031	22.088	0.009	21.138	0.005	19.974	0.003		
59	60130	21.633	25.885	0.122	25.372	0.044	24.292	0.025	21.810	0.006		
61	25745	24.280	26.496	0.286	26.391	0.127	25.197	0.061	24.329	0.035		
62	35004	20.398	22.511	0.033	22.271	0.013	21.819	0.010	20.573	0.003		
63	31301	23.845	30.147	7.485	25.851	0.089	25.132	0.057	24.371	0.041		
64	30075	23.139	24.581	0.070	24.981	0.053	24.272	0.033	23.336	0.018		
66	65555	21.721	25.481	0.119	24.648	0.033	24.136	0.024	21.966	0.007		
67	17783	22.689	24.259	0.059	23.836	0.026	23.223	0.017	22.810	0.011		
69	25429	21.955	25.709	0.140	25.404	0.076	24.389	0.039	22.469	0.011		
70	28394	22.103	23.097	0.034	23.532	0.022	22.941	0.014	22.313	0.009		
71	58275	22.233	23.094	0.035	22.601	0.011	22.501	0.012	22.348	0.010		
72	29697	21.455	26.837	0.407	26.093	0.111	24.203	0.032	21.860	0.007		
74	17208	19.354	24.329	0.063	22.774	0.021	21.459	0.008	19.846	0.002		
75	63310	22.866	25.857	0.151	25.289	0.053	24.425	0.042	23.493	0.024		
79	37913	21.555	23.936	0.051	24.030	0.047	23.302	0.027	22.014	0.008	19.69	0.12
82	34515	21.247	23.964	0.052	23.823	0.031	23.040	0.017	21.493	0.006		
83	42599	21.367	25.007	0.077	24.604	0.049	23.383	0.020	21.519	0.007		
85	66214	23.126	26.543	0.242	26.303	0.109	26.023	0.109	23.289	0.016		
86	18647	22.427	25.258	0.134	25.485	0.067	24.289	0.031	22.761	0.011		
87	34543	20.087	25.699	0.133	25.731	0.236	23.235	0.027	20.729	0.005		
88	61988	22.784	24.803	0.068	24.672	0.028	24.003	0.021	23.073	0.013		
89	35432	22.695	26.697	0.336	25.239	0.053	24.524	0.034	22.945	0.012		
90	65240	23.037	26.297	0.165	25.458	0.054	25.545	0.065	23.760	0.022		
91	25734	23.432	27.667	0.583	27.714	0.465	26.550	0.204	23.880	0.025		
92	52922	22.283	25.644	0.113	24.669	0.031	23.915	0.021	22.517	0.010		
93	65969	22.032	24.772	0.067	23.988	0.020	23.581	0.018	22.160	0.008		
94	19012	24.151	25.458	0.176	25.879	0.087	25.063	0.053	24.410	0.037		
95	69197	18.426	22.208	0.023	21.213	0.006	19.858	0.003	18.954	0.002		

Table 4.7: (Continued)

XMM	CFDF	I_{Tot}	U	ΔU	B	ΔB	V	ΔV	I	ΔI	K	ΔK
97	85590	21.540	23.259	0.037	22.774	0.023	22.545	0.017	21.843	0.010		
98	15693	19.692	24.862	0.080	22.824	0.015	21.614	0.007	19.796	0.002		
99	76245	17.916	24.060	0.046	22.236	0.009	20.767	0.004	18.024	0.001		
102	60656	22.618	23.540	0.037	22.576	0.009	22.496	0.009	22.717	0.010		
103	23308	22.785	23.290	0.047	22.994	0.016	22.580	0.012	22.857	0.011		
104	4623	20.130	21.190	0.014	21.147	0.008	20.631	0.005	20.345	0.004		
105	79441	21.379	25.360	0.094	24.645	0.028	23.575	0.017	21.649	0.006		
106	18587	20.820	23.401	0.052	22.828	0.014	22.035	0.009	21.150	0.005		
107	42600	23.143	27.876	0.537	25.716	0.129	99.000	27.170	23.360	0.022		
108	18555	15.978	17.022	0.003	16.079	0.001	15.676	0.001	16.215	0.001		
109	16776	24.879	26.622	0.344	25.663	0.079	25.112	0.059	25.125	0.069		
110	13827	21.745	23.003	0.043	22.759	0.014	22.183	0.010	22.088	0.008		
111	51269	21.673	22.241	0.024	22.261	0.010	21.994	0.008	21.796	0.006		
112	63545	21.542	25.140	0.098	24.470	0.030	23.531	0.020	21.868	0.007		
113	31206	15.846	16.910	0.002	16.391	0.001	16.065	0.001	16.579	0.001	20.18	0.19
114	51372	23.747	99.000	28.900	99.000	27.420	25.784	0.075	23.869	0.023		
115	73478	22.561	25.482	0.117	25.137	0.048	24.550	0.033	22.797	0.011		
116	77033	17.319	22.573	0.023	21.042	0.004	19.616	0.003	18.364	0.001		
117	56581	23.864	25.303	0.089	25.247	0.042	24.655	0.033	23.882	0.023		
118	34410	21.188	23.482	0.040	23.363	0.028	22.665	0.016	21.469	0.006	16.87	0.00
119	64736	23.231	25.506	0.100	24.899	0.034	24.737	0.037	23.380	0.017		
127	27813	20.686	23.484	0.041	23.146	0.025	22.288	0.012	21.097	0.005		
128	54966	20.742	23.296	0.033	22.842	0.011	22.186	0.008	21.033	0.004		
132	18082	21.398	23.234	0.036	22.982	0.016	22.411	0.011	21.618	0.006		
133	63277	20.885	23.153	0.030	22.757	0.010	22.314	0.008	21.108	0.004		
135	72587	22.028	23.860	0.041	23.099	0.012	22.874	0.011	22.390	0.008		
137	54900	20.624	23.394	0.041	22.917	0.013	22.075	0.008	20.886	0.004		
141	8503	19.659	20.331	0.013	19.949	0.003	19.730	0.003	19.767	0.002		
142	10561	21.154	21.622	0.016	21.684	0.012	21.558	0.008	21.261	0.005		
143	63681	17.666	22.299	0.024	20.402	0.004	19.274	0.002	17.796	0.001		
144	47052	19.544	23.664	0.046	22.854	0.014	21.680	0.007	20.169	0.003		
146	32896	18.197	21.600	0.017	20.884	0.006	19.695	0.003	18.882	0.002		
147	69363	20.445	23.624	0.046	23.090	0.014	22.261	0.010	20.744	0.004		
148	44072	19.979	24.554	0.057	23.498	0.019	22.170	0.008	20.445	0.003	22.48	0.81
149	52691	22.265	24.010	0.047	23.896	0.019	23.531	0.016	22.609	0.010		
151	51768	25.536	99.000	28.900	26.481	0.115	27.660	0.421	25.322	0.071		
153	56022	22.166	23.969	0.044	23.567	0.015	22.970	0.012	22.290	0.009		
154	32679	22.549	27.366	0.471	25.803	0.206	25.213	0.098	22.626	0.014		
65	69393	23.732	25.287	0.088	24.833	0.038	24.730	0.037	24.149	0.032		
80	43006	25.724	26.615	0.193	26.385	0.135	25.412	0.071	25.712	0.122		
122	59768	21.501	25.005	0.076	24.330	0.022	23.542	0.015	21.623	0.005	19.79	0.07

Table 4.7: (Continued)

XMM	CFDF	I_{Tot}	U	ΔU	B	ΔB	V	ΔV	I	ΔI	K	ΔK
129	48314	23.447	99.000	28.900	99.000	27.420	25.069	0.052	23.600	0.022		
10	82156	24.416	25.157	0.091	25.807	0.092	25.527	0.082	24.557	0.042		
115	73352	23.150	23.228	0.036	23.918	0.022	23.843	0.020	23.190	0.014		
149	52467	21.073	24.253	0.053	23.505	0.015	22.750	0.010	21.393	0.005		

4.8 Appendix

The work in this chapter depends heavily on the reliability of the photometric redshift estimation codes I use. There are two codes whose results are presented in this work, one by Benítez (2000) which uses a Bayesian approach and template fitting technique, called BPZ; and another that is developed by Mark Brodwin specifically for the CFDF (Brodwin et al., 2003) utilising the CFRS to calibrate the template fitting. These two codes are slightly different and each have their strengths. This appendix is concerned with the reliability testing of these two codes. For a more detailed discussion of the CFDF code, and its reliability when compared against the CFRS spectroscopic sample, refer to Brodwin et al. (2003).

For reasons of timing the input to BPZ is from an older version of the CFDF catalogues than that employed for the specific CFDF code. Therefore this should be taken into account when comparing the two codes.

4.8.1 BPZ Photometric Redshift Estimation Code

This code has been tested by Gonzalez & Maccarone (2002) and Benítez (2000) and has proven to be highly successful, but I use a different filter set and photometry from these studies and so it was prudent to re-test the code for my specific needs. I outline my procedure for these tests in this appendix.

Both fields have CFRS spectroscopic measurements for over 200 objects (Hammer et al., 1995a; Lilly et al., 1995a). I searched for CFDF (McCracken et al., 2001) counterparts to all CFRS objects that were not identified to be stars or QSOs and that had good spectroscopic measurements (classification 2, 3 or 4). The U, B,

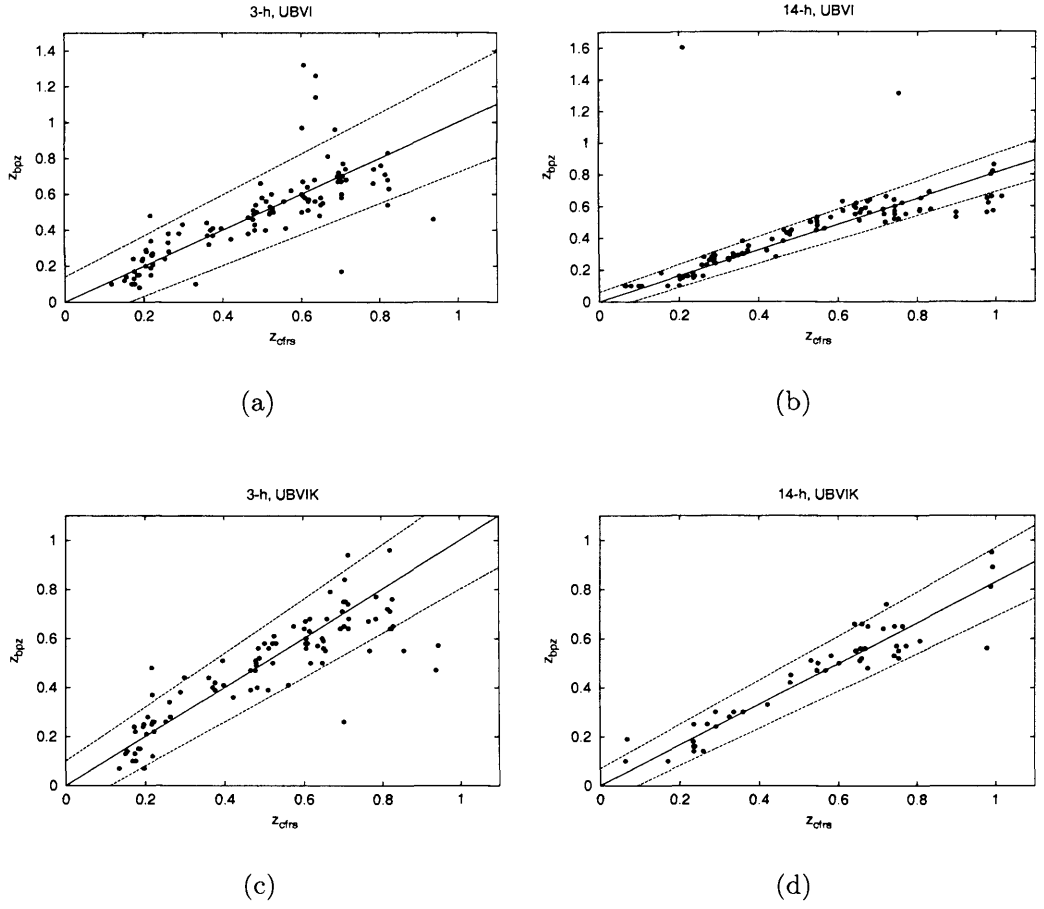

Figure 4.9: Photometric vs. spectroscopic redshift for the 3-h (fig 4.9(a), 4.9(c)) and 14-h (fig 4.9(b), 4.9(d)) fields. The best fit gradients for 14-h field are 0.81 for $UBVI$ and 0.83 for $UBVIK$. The error lines shown are of the form $\sigma(1+z)$ where $\sigma = 0.14, 0.06, 0.1, 0.07$ for the sequence of plots (for the 14-h $UBVI$ plot this error ignores the two outliers, $\sigma = 0.19$ if they are included).

V and I $3''$ aperture magnitudes and errors were extracted for these objects from the CFDF catalogues together with the K magnitude and error obtained from the CFRS catalogue. This resulted in 143 objects with $UBVI$ photometry in the 3-h field, of which 112 also had reliable K photometry, and 128 objects with $UBVI$ photometry in the 14-h field, of which 57 had reliable K band photometry.

Filter transmission curves were obtained for the CFDF $UBVI$ photometry system and the CFRS K band, adjusted as appropriate for the quantum efficiency

of the detectors and the transmission of the atmosphere. Four catalogues were prepared in total, $UBVI$ and $UBVIK$ for each field. These were run through the BPZ code using the total I band magnitude for each object as the prior (see Benítez, 2000, for a full explanation of the code).

Although the general trend is good the initial results are contaminated by a non-trivial number of catastrophic errors. Fortunately BPZ also provides a reliability estimator in the form of a probability measure which quantifies the spread of the redshift estimation likelihood (again see Benítez, 2000). By selecting only those objects with a reliability of $P_{\Delta z} > 0.95$ the majority of the outliers are eliminated. See figure 4.9 for the final plots for all four catalogues, they contain 106, 102, 98 and 48 respectively after removal of the objects with $P_{\Delta z} < 0.95$ (i.e. $15 - 25\%$ of objects removed).

Some interesting results can be seen in these plots. The most striking is that although the overall scatter of the 14-h field results are smaller than for the 3-h field the trends are significantly deviated from the expected 1:1 relationship. This is most likely caused by inaccurate U band photometry for this field, as a consequence of leakage from outside the desired passband. However, because this is a systematic effect it can be corrected for by dividing all the BPZ redshifts for the 14-h field by the gradient of the best fit line. The gradients are 0.81 and 0.83 for the $UBVI$ and $UBVIK$ catalogues respectively. A second interesting feature in the 14-h plots is the presence of a notch at a redshift 1 where BPZ tends to assign lower redshifts. This is likely to be caused by the 4000 angstrom break beginning to shift beyond the peak of the I band. It is not clear whether the addition of the K band helps here because of the smaller number of objects with K data.

Aside from the systematic effect seen in the 14-h field the results are encour-

aging. The scatter about the expected 1:1 line is comparable to or better than that found in Gonzalez & Maccarone (2002) ($\sigma = 0.14$ for the 3-h field $UBVI$). In general the addition of K data does not appear to significantly reduce the small scale scatter in redshift estimates, and so for my X-ray sources, of which the vast majority don't have K data, this method is perfectly acceptable. Having identified the systematic effect in the 14-h data this is corrected for in the main body of this work.

One point to note is the reduction in the number of significant outliers in the two plots that include the K band data. There are two effects that contribute to this. The majority of the outliers do not have K band data and so do not appear in these plots. However, of the five significant outliers in the two fields that do have K data two of the photometric redshift estimates are dramatically improved while the other three remain roughly the same. For example, of the two outliers in the 14-h field one is fixed by K data while the other is absent because it has no K data. In addition, many objects that are removed from the $UBVI$ plots because of bad $P_{\Delta z}$ values have better values after the addition of K and, where the objects are outliers, nearly half have improved redshift estimates too. This can also be seen in the larger fraction of sources that have $P_{\Delta z} > 0.95$ in the $UBVIK$ catalogues when compared to those with just $UBVI$.

In conclusion, for the most part $UBVI$ photometry is perfectly adequate in order for BPZ to produce acceptable redshift estimates. However, the addition of K band photometry improves the estimates of some outliers and increases the fraction of reliable estimates. Therefore K band data should be used where available. Having said that, for the X-ray sources in my surveys this does not appear to be the case (see figure 4.11(c)), but since only a small fraction of the sources have K data its inclusion, or not, has a marginal effect on the statistical properties of the

whole sample.

Equivalent plots for the CFDF code can be found in Brodwin et al. (2003) (their figure 2). In comparison to BPZ the CFDF code redshifts fair rather better when compared to the CFRS spectroscopic sample, with fewer outliers and a smaller scatter ($\sigma \sim 0.04$ to $I_{AB} = 22.5$, $\sigma \sim 0.06$ to $I_{AB} = 24$). There are also no systematic effects, as seen in the BPZ 14-h sample.

4.8.2 CFDF Photometric Redshift Estimation Code

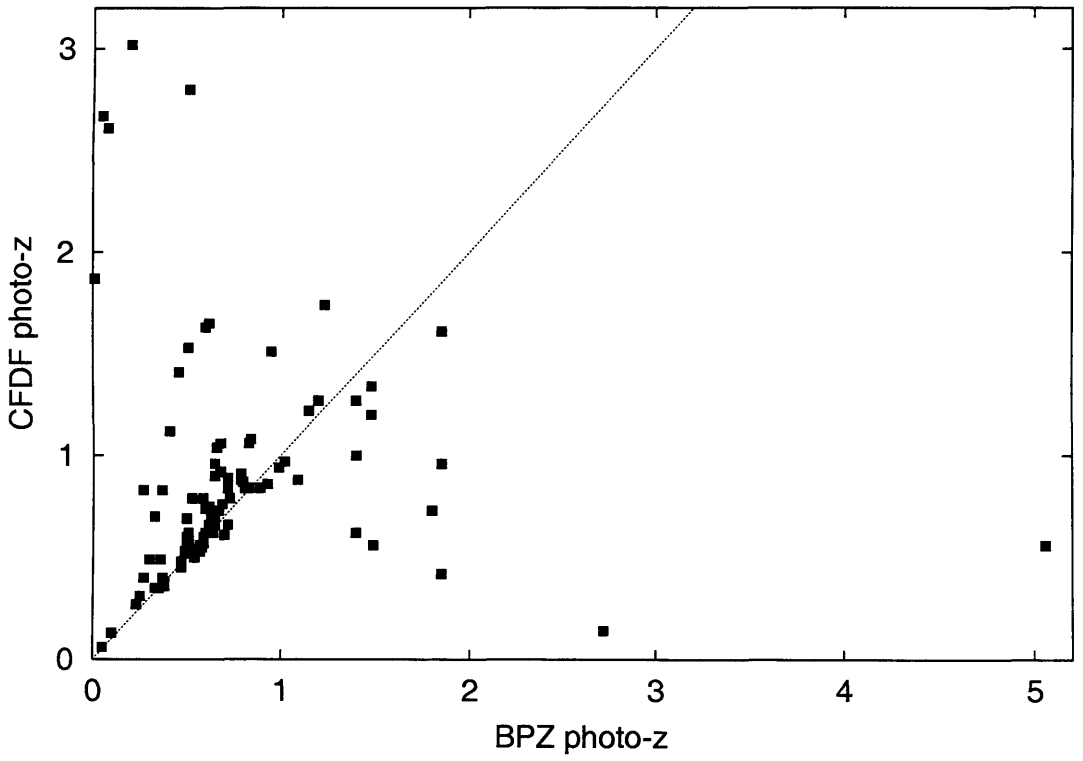

Figure 4.10: CFDF vs. BPZ photometric redshift estimates for objects that have reliable estimates from both codes (see text for details). All possible stars and known QSOs have been excluded, as have saturated objects with $I_{AB} < 18.5$.

The CFDF is currently extending beyond the original $UBVI$ survey to include additional R and Z photometry. These extra filters remove some potential red-

shift degeneracies in certain galaxy templates and so should provide more reliable photometric redshift estimates. The CFDF photometric redshift program is now underway with the full $UBVRIZ$ photometry using a code developed by Mark Brodwin (Brodwin et al., 2003, which includes a thorough analysis of its reliability). As an additional check on the original estimates I made with BPZ I obtained photometric redshifts for my identified X-ray sources from the CFDF photometric redshift program utilising these new catalogues.

Figure 4.10 shows the comparison between the redshift estimates made by the two codes for only those objects which had reliable estimates as judged by both of the in-code measures. Star like objects, known QSOs and saturated objects ($I_{AB} < 18.5$) (see catalogue tables) are excluded because photometric redshifts are unreliable for these objects. In general the agreement is good, with 79% of objects agreeing to within a factor of 1.7. The agreement is also better for $z < 1$, where the majority of objects lie (72/94 CFDF; 77/94 BPZ) and where the peak in the number density of intermediate luminosity AGN is (Cowie et al., 2003). Assuming the CFDF redshifts are correct 7/72 $z < 1$ objects are given poor redshifts by BPZ; whereas assuming the BPZ redshifts are correct 13/77 $z < 1$ objects are given poor redshifts by the CFDF code.

For the actual X-ray sources considered in this work only a handful have spectroscopically measured redshifts, with half of these being previously known QSOs. Figure 4.11 shows the results of the photometric redshift codes for all these objects. There is a clear problem in obtaining photometric redshifts for QSOs, both codes struggling to pin them down with any accuracy. However, for more optically normal AGN both BPZ and the CFDF code cope quite well for the most part. The 95% confidence limits are slightly better for the CFDF code however, and it also wins out over BPZ with fewer unreliable redshifts in my X-ray sample.

Interestingly enough the inclusion of K band data to the BPZ code does not have the same effect as I see in my tests of BPZ on the CFRS sources (above). Although the sample here is small it actually appears to have an adverse effect on the redshift estimations (figure 4.11(c)) rather than improving them as expected.

The CFDF code, being specifically designed for the objects used as IDs in this survey, seems the logical choice for obtaining redshifts for the X-ray sources. This is especially true given that it also takes full advantage of the more recent extension in the number of colours for the CFDF. This code does allow for the use of a Bayesian prior, like BPZ, although none was used in obtaining these particular results (instead the data itself is used to derive a prior for statistical analysis of the full sample). This may be seen as a slight disadvantage, since priors have been shown to be effective in reducing the number of catastrophic errors for individual galaxies (Benítez, 2000). However, the extra colour information used in the CFDF code should compensate for this to some degree, and my tests and those in Brodwin et al. (2003) show the CFDF code to be superior to BPZ in this situation.

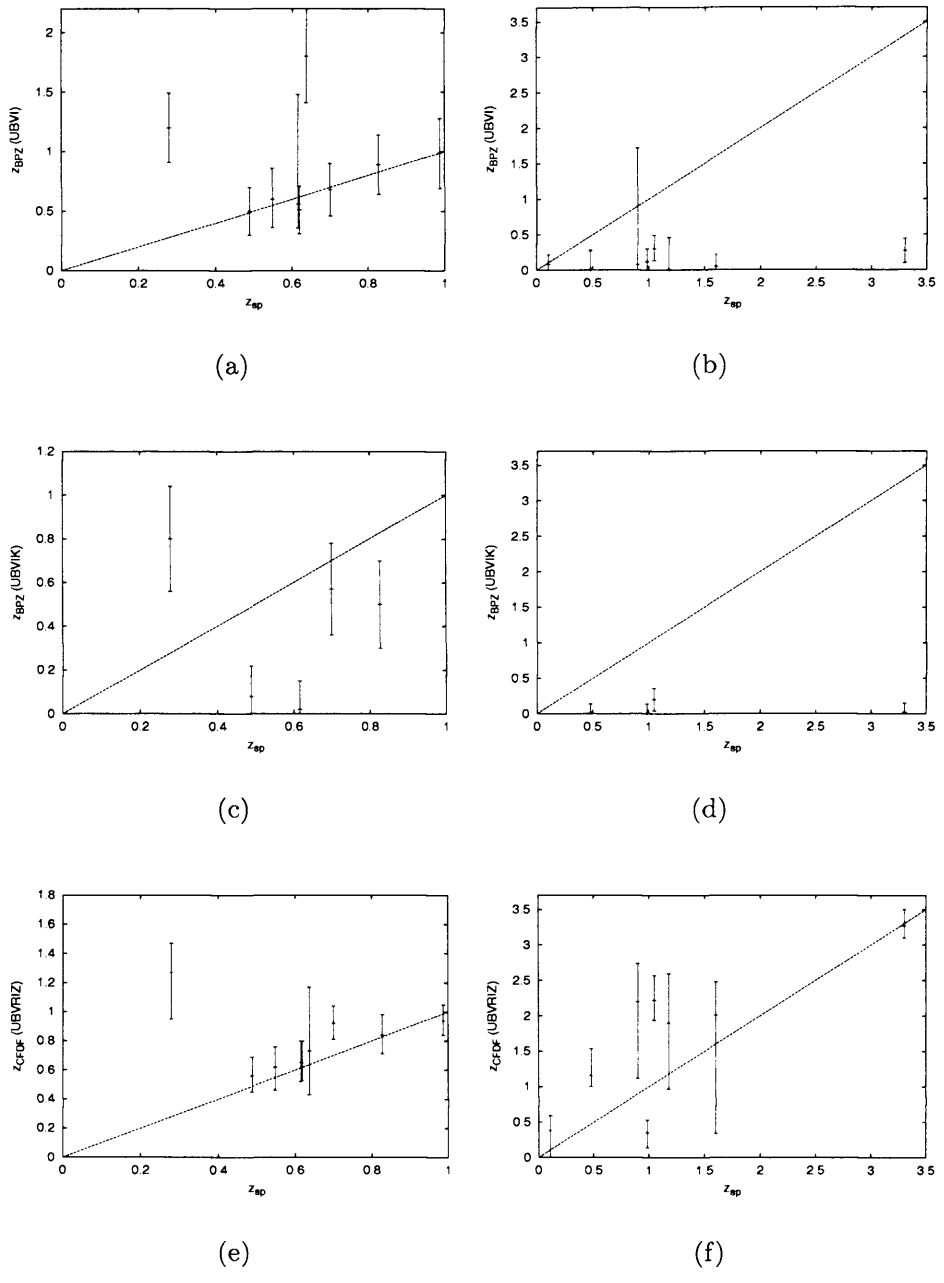

Figure 4.11: A series of plots to demonstrate the effectiveness of the two photo-z codes when compared to the handful of X-ray sources that have spectroscopic redshifts in my surveys. The left column (4.11(a), 4.11(c) & 4.11(e)) shows the results for the non-QSO X-ray sources. The right column (4.11(b), 4.11(d) & 4.11(f)) shows the results for the known QSOs. The top plots (4.11(a) & 4.11(b)) are BPZ results with $UBVI$ photometry, the middle (4.11(c) & 4.11(d)) are BPZ results for the few $UBVIK$ objects and the bottom plots (4.11(e) & 4.11(f)) show the results for the CFDF code with $UBVRIZ$ photometry. The error bars in all cases are the 95% confidence limits around the best fit redshift.

Chapter 5

Two Point Angular Correlation Function of AGN

5.1 Introduction

Measuring the clustering of galaxies has long been a useful tool in quantifying physical structure in the Universe and hence in testing theoretical models of structure formation. In particular, different cosmological models predict that the strength of the spatial clustering of galaxies will evolve in different ways over the history of the Universe; as such, measuring the clustering strength of galaxies at different redshifts is one way of distinguishing between these different cosmological models (e.g. Roche & Eales, 1999; Le Fevre et al., 1996; Brunner, Szalay, & Connolly, 2000). These measurements may also be used to test theories of galaxy formation and evolution by probing the evolution of, for example, merger rates (Roche & Eales, 1999). This treatment is not restricted to optically selected galaxies either. Every class of astrophysical source has, at some point, had some sort of clustering

analysis performed on it, from radio sources (e.g. Cress et al., 1996) to gamma ray bursts (Brainerd, 1996). Comparing the clustering properties of different classes of objects reveals whether similar, or completely different, processes are at work, resulting in the observed similarities/differences.

Although there are many different ways of quantifying clustering, correlation functions have become a common standard, both for their ease of calculation and their application to testing theories. The simplest is the two-point correlation function (Peebles, 1973) which can be expressed as an excess probability of finding two objects separated by a certain distance:

$$\delta P = N^2[1 + W(r)]\delta V_1 \delta V_2$$

where δP is the joint probability of finding one object in the volume element δV_1 and a second object in the volume element δV_2, which are separated by a physical distance r. N is the mean volume density of objects in the sample. The function $W(r)$ is the two-point correlation function that quantifies the clustering strength at any given physical scale r.

In practice, without knowing the distance of every object in a sample it is impossible to calculate this function. Often it is more convenient to calculate the *angular* correlation function, which can be achieved with simply a list of sky coordinates:

$$\delta P = N^2[1 + W(\theta)]\delta\Omega_1 \delta\Omega_2$$

where the volume elements are replaced with elements of solid angle $\delta\Omega$, separated by an angle θ. Essentially the function $W(\theta)$ is now the quantification of the physical clustering having been projected onto the flat sky, with N now representing the 2-dimensional number density. It is possible to de-convolve this projection effect by

inverting the angular correlation function via the Limber equation (Limber, 1954; Peebles, 1980) using an assumed, calculated or estimated redshift distribution for the objects in the sample. This is particularly useful for large optical surveys that may contain several hundred thousand galaxies, for which obtaining spectroscopic redshift measurements for every galaxy would be impossible.

This chapter concerns the measurement of the angular correlation function of the AGN in the 3-h and 14-h fields. This is motivated by previous studies of the clustering of AGN using *ROSAT* (Akylas, Georgantopoulos, & Plionis, 2000; Tesch et al., 2000; Vikhlinin & Forman, 1995; Carrera et al., 1998), and the fact that no equivalent studies exist using data from *XMM*. Although the surveys in this work do not have the area coverage of the *ROSAT* All Sky Survey (RASS) they do reach considerably deeper in terms of flux, so they still probe large volumes. X-ray sources may be useful tracers of large scale structure, including being an efficient way of tracing the distribution of normal galaxies (Barcons et al., 2001, 2000); so extending the clustering analysis of X-ray sources to deeper surveys is important for extending our knowledge of matter distribution to higher redshifts.

5.2 Calculating $W(\theta)$

The simplest estimation of $W(\theta)$ can be obtained by calculating the following quantity through Monte Carlo simulations:

$$W(\theta_i) = \frac{DD}{DR} - 1$$

in a given bin i, which contains the range of angular separations $\theta - \delta\theta/2$ to $\theta + \delta\theta/2$. Here, DD is the number of Data-Data pairs separated by an angle within the above

range, and DR is the number of Data-Random pairs calculated in the same way and normalised appropriately, where the random objects are distributed as described in section 5.3. Effectively, for every real object in the sample, the number of objects within an annulus of a given angular radius, and angular thickness, are counted and compared to the number of randomly paced objects within that same annulus. If there is an excess of real objects over that expected from a purely Poisson random distribution, then the above quantity will be positive. The full evaluation of $W(\theta)$ is the result of the summation of this process for every real object in the sample, in different angular bins.

This estimator works well for large samples where errors are likely to be small but the sample in this work only contains a couple of hundred objects so a more reliable estimator is used, introduced by Landy & Szalay (1993):

$$W(\theta_i) = \frac{DD - 2DR + RR}{RR}.$$

This estimator has a variance closer to that expected for Poisson noise than the earlier expression. Here RR is the number of Random-Random pairs calculated in the same way as DD and DR. If there are N_g real objects and N_r random objects in the analysis then $N_{gg}(\theta_i)$ is the number of distinct galaxy-galaxy pairs in bin i, from a possible total of $\frac{1}{2}N_g(N_g - 1)$ galaxy-galaxy pairs. Similarly $N_{gr}(\theta_i)$ is the number of galaxy-random pairs from a total of $N_g N_r$ pairs and $N_{rr}(\theta_i)$ is the number of random-random pairs from a total of $\frac{1}{2}N_r(N_r - 1)$. The quantities in the evaluation of $W(\theta)$ are normalised to the total galaxy-galaxy number such that

$$DD = N_{gg}(\theta_i), \qquad DR = \frac{N_g - 1}{2N_r} N_{gr}(\theta_i), \qquad RR = \frac{N_g(N_g - 1)}{N_r(N_r - 1)} N_{rr}(\theta_i).$$

As long as the number of random objects is very large, the error in $W(\theta_i)$ can be reduced to the Poisson error given by the number of distinct real pairs in a given bin. Hewett (1982) express this variance as:

$$[\delta W(\theta_i)]^2 = \frac{[1 + W(\theta_i)]}{N_{gg}(\theta_i)}.$$

5.3 Generating a Random Population

The random population of X-ray sources must be distributed with some care before the evaluation of the correlation function can begin. Because the optical arrangement of each *XMM* mirror module causes a significant amount of unavoidable vignetting towards the edge of the FoV, the sensitivity across each instrument is far from uniform. This variation in sensitivity needs to be taken into account when placing random sources so that the correlation function is not biased. For example, if a random population were placed on the *XMM* maps with a pure Poisson distribution with uniform large scale density, there will appear to be an excess of real X-ray sources in the centre of the FoV compared to the edges, because of the greater sensitivity there (see figure 5.1). Since the random population does not follow this trend it will result in a biasing of the correlation function, as it will appear that the AGN are clustered in the centre of the exposure. Therefore, in order to cancel any instrumental biasing, the random population needs to be placed with a varying space density (although still following a local Poisson distribution) that reflects the expected *observed* distribution of randomly distributed sources. *XMM* will naturally detect more sources in the centre of an exposure, whatever the true underlying distribution.

Table 5.1: ECF values for converting to full band flux.

Field	PN ECF	MOS ECF
3-h	3.161	0.9748
14-h	3.449	1.031

5.3.1 Sensitivity Map

SAS conveniently includes a task designed to generate sensitivity maps, called 'esensmap', which can be used to create maps for all the X-ray instruments in any user defined energy band. I generate sensitivity maps in the full band ($0.5-10$ keV) because the source detection was also performed over this range. The task takes two exposure maps and two background maps, one for the soft and one for the hard band, as input, as well as a detector map to mask unexposed areas. The output images are maps of the expected flux limit, in units of counts per second, which can be converted into a true full band flux using the ECF for the full band obtained in the same way as described in section 2.5.3. In this case the ECF values are shown in table 5.1. The PN instrument has a central flux limit approximately half that of the individual MOS instruments in both the 3-h and 14-h fields.

Figure 5.1 shows examples of sensitivity maps for the 3-h field PN and MOS1 instruments. The colour scale indicates the flux limit for each pixel in the map with the darkest regions showing the lowest flux limit, and hence greatest sensitivity. These maps do not follow exactly the same form as one would expect by considering just the exposure maps, (figure 2.5) because the local background is also taken into consideration when the task calculates the limiting flux at each point (although the exposure maps do play the most dominant role). Regions of higher background will reduce the sensitivity and hence increase the flux limit, an example of which can be seen in the upper right corner of the PN map in figures 2.5 and 5.1.

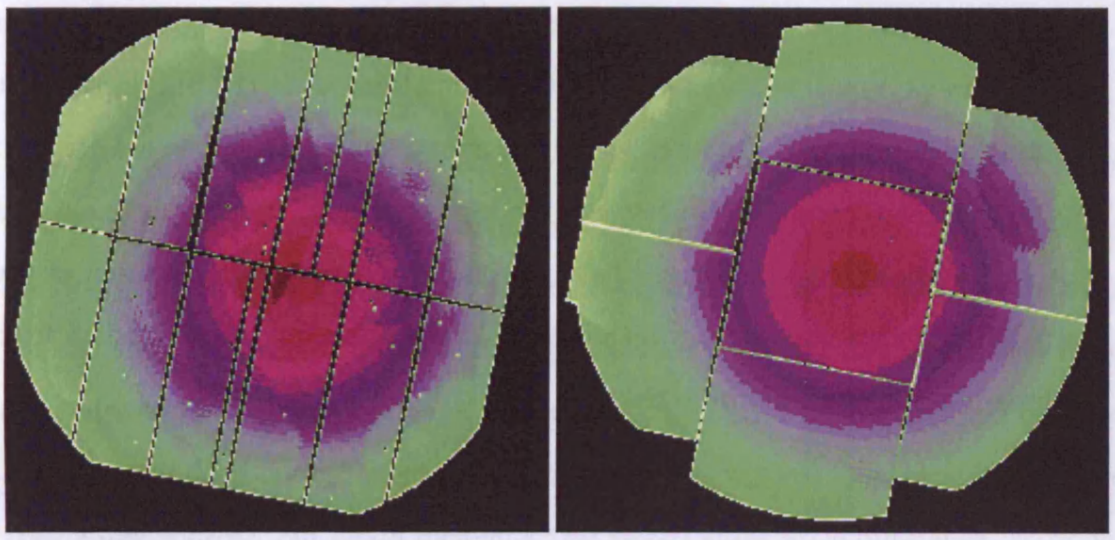

Figure 5.1: Sensitivity maps for the PN instrument (left) and MOS1 instrument (right) for the 3-h exposure.

5.3.2 X-ray Population

A random source is generated at a random position within a square map covering one of the three *XMM* instruments. Each source is also given a random flux such that a whole population of random sources will reproduce the observed number counts for real X-ray sources (e.g. Hasinger et al., 2001):

$$log\ N(>S) \propto S^{-0.8}.$$

This flux is then compared to the sensitivity map for that particular instrument at the random position to see if it would exceed the local detection limit. If it does then the source is placed in a list of detected random sources. This process is then repeated for another random source for one of the other two instruments etc.. When a total of 10^4 sources have been detected, by all three instruments combined, the list is considered complete. This process has several important effects. Firstly the sensitivity difference across each instrument is taken into account when producing

the random source list, as described above; secondly the natural difference between the instrument types is also taken into consideration, with the PN instrument detecting more sources than either MOS instrument; finally, no sources are detected outside the instrument FoV or between the gaps in the CCD chips, as one would expect. The final random list ultimately gives an accurate representation of the sampling of the true exposure, which consists of a single exposure using data from all three instruments simultaneously.

Figure 5.2 shows the same sensitivity maps as figure 5.1 with the relevant random source lists overlayed. The better sensitivity of the PN instrument is evident in this plot as is the effect of a higher effective exposure time in the centre of the FoV.

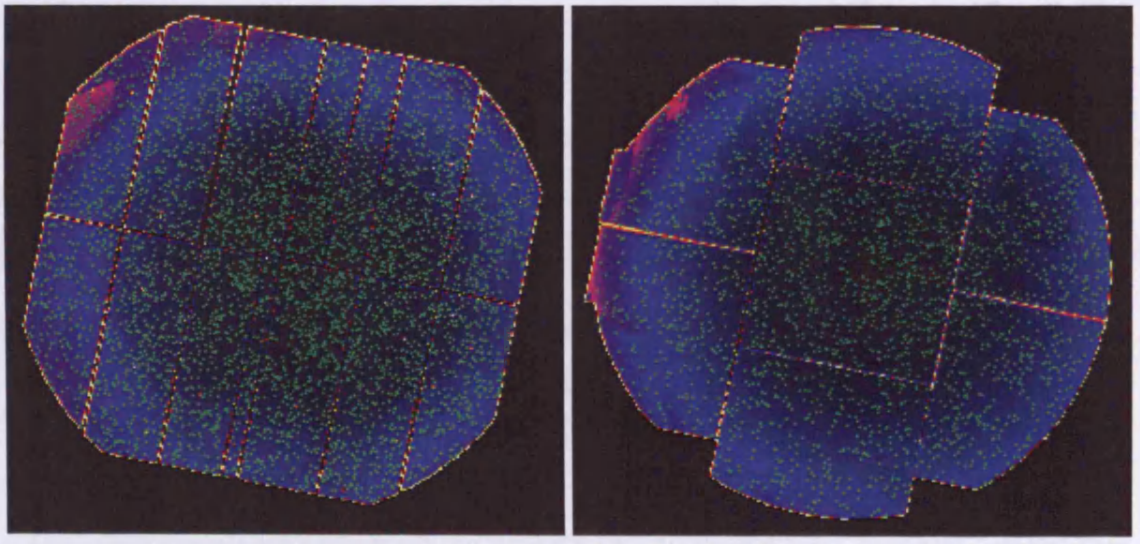

Figure 5.2: An illustration of how the randomly generated source population is distributed within the *XMM* FoV. Notice how the better sensitivity on-axis leads to a higher density of random sources. The superior sensitivity of the PN instrument can also be seen.

5.4 Results

Because the aim of this analysis is to to measure the clustering strength of AGN rather than X-ray sources in general all possible stars are removed from the source list first. In chapter 4 I argue that probably half of the sources identified as stars are actually misidentified QSOs, but as we shall see in reality this makes very little difference to the analysis. I do not consider the 10-h field in this analysis because of the lack of deep optical coverage and hence lack of optical identifications for the 10-h X-ray sources, but again including this data makes little difference.

The choice of bin size is fairly arbitrary, so initially I use logarithmically spaced bins such that $\Delta log(\theta) = 0.2$. The results for both the entire AGN sample and the brightest half are shown in figure 5.3. It is immediately obvious that there is a striking lack of any sort of clustering signal, except in the 3-h field at separations of $\sim 11''$. However, this signal is due to only three close pairs which are separated by a distance only slightly larger than the *XMM* PSF FWHM, and coupled with the complete lack of signal at any larger separations I am wary of this out-lier.

The two panels at the bottom of figure 5.3 are the results of taking error weighted means of the two individual fields, with the errors combined appropriately. However, this does not succeed in revealing any significant clustering signal.

The error bars give some indication of the number of pairs detected in each bin, so as the area of a bin increases the error bars naturally decrease until $\theta \sim 1000''$ at which point the separations are larger than half the *XMM* FoV, and so annuli around many sources lie partially off the map.

Selecting a subsample of only the brightest half of the full AGN sample ef-

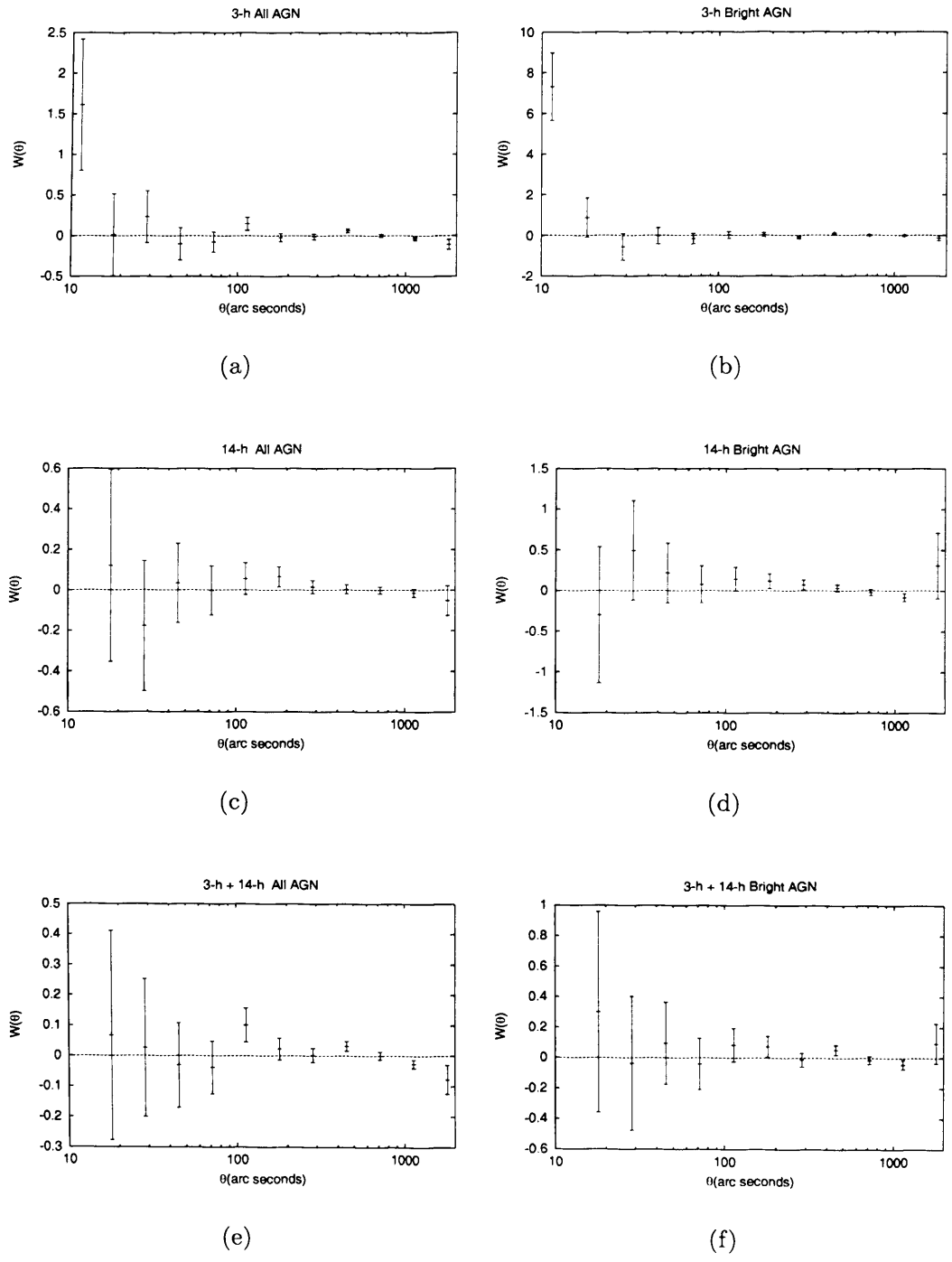

Figure 5.3: Examples of $W(\theta)$ for the AGN in the 3-h and 14-h fields. Left panels show the full AGN sample, the right panels show only the brightest half of the AGN sample. No significant clustering is detected.

fectively increases the flux limit of the survey, so making it less deep. This has the effect of reducing the uncertainty associated with projection, as in general, the brighter sources will be closer to us. Unfortunately the disadvantage of doing this is to reduce the number of sources in the sample and so increase the error bars accordingly. As can be seen from figure 5.3 no significant improvement in the clustering measurement is achieved by restricting the analysis to only the brightest half of the AGN sample.

Changing the bin sizes or using linear instead of logarithmic bins also makes no qualitative change to these figures. I also tested sub-samples of AGN with photometric redshifts within a small range of the peak in the redshift distribution (see figure 4.4) to reduce the effects of projection but again, what I gained in contrast I lost by having far fewer sources, and hence larger error bars.

5.5 Discussion

The fact that there is no significant detection of clustering in this survey does not mean that AGN do not cluster. Several effects conspire to wash out any potential signal. The most significant of these is simply the small number of sources spread over such a large range in redshift. As observed in optical measurements of the angular correlation function, the clustering strength decreases as the survey depth increases (e.g. McCracken et al., 2001), a consequence of the projection of the true correlation function onto the sky. This X-ray survey is similarly disadvantaged, being deep enough to detect AGN over a large fraction of the history of the Universe. This results in a small number of sources at any given distance, with, for example, 50 or so sources in a redshift slice of $\delta z = 0.2$ at $z = 0.7$ (see figure 4.4).

When these sources are spread over the 0.4 square degrees of the survey area it is hardly surprising that the error bars are so large.

These results are consistent with other studies of AGN clustering, using comparable numbers of sources (Carrera et al., 1998), that show no significant clustering for deep pencil beam *ROSAT* surveys, and only mildly significant clustering ($\sim 2\sigma$) for wider angle, shallower *ROSAT* surveys. A better detection of AGN clustering was found by Vikhlinin & Forman (1995); using over 250 deep *ROSAT* pointings ($\sim$ 40 square degrees) this study found a $\sim 4\sigma$ detection of clustering on scales from $25'' - 100''$. Vikhlinin & Forman (1995) conclude that AGN are spatially distributed in the same way as normal galaxies and optically selected quasars. My results are certainly consistent with this conclusion, although with only two deep pointings compared to 250, my analysis is not in a position to challenge it, even if the 10-h field were included. Figure 5.4 shows a copy of figure 5.3(f) with the best fit line from Vikhlinin & Forman (1995) for their 40 square degrees, which has a flux limit approximately an order of magnitude brighter than the sample used to create this plot. Using a parameterisation of

$$W(\theta) = \left(\frac{\theta}{\theta_0}\right)^{1-\gamma}$$

they find $\theta_0 = 10'' \pm 8''$ and $\gamma = 1.7 \pm 0.3$; this is shown by the solid line. In comparison, the best fit for the bright sample in this plot is $\theta_0 = 1.6'' \pm 2.2''$ having fixed γ at the value found for normal galaxies of 1.8, shown by the dotted line.

The *ROSAT* all sky survey also detects significant clustering of AGN in the local universe, with a correlation length in comoving coordinates of $r_0 = 6.0 \pm 1.6\ h^{-1}$ Mpc, similar to that found for normal galaxies (Brunner et al., 2000;

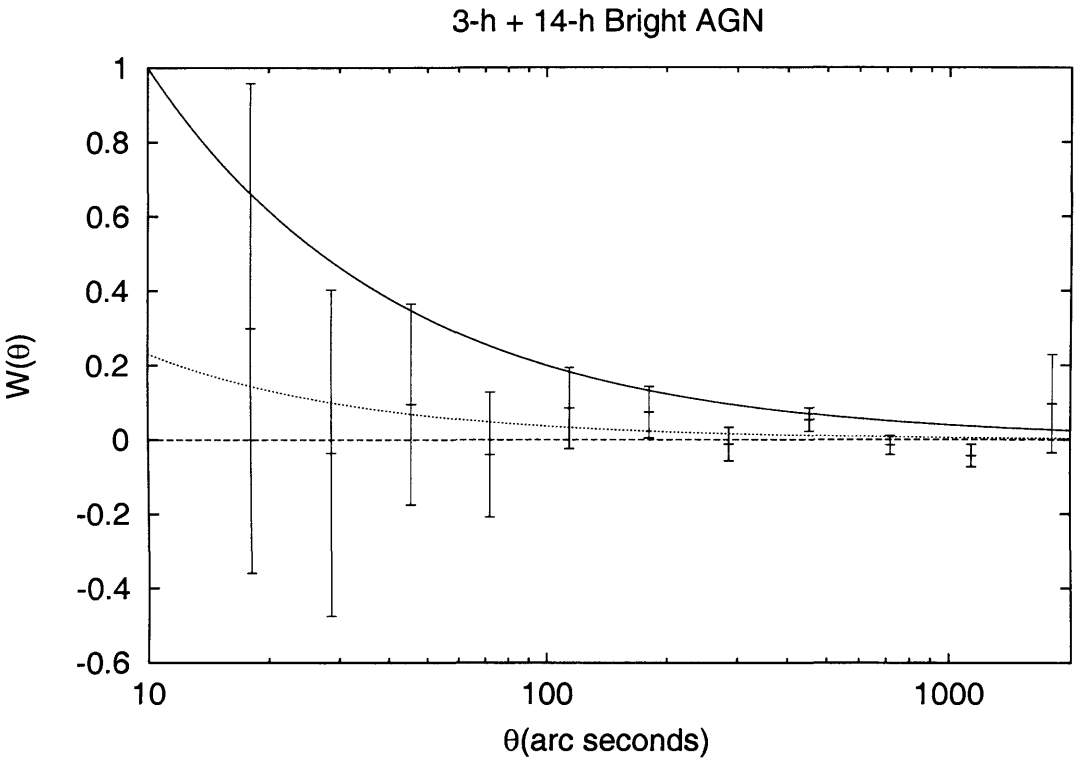

Figure 5.4: $W(\theta)$ for the total bright sample. The solid line shows the best fit results for the *ROSAT* study by Vikhlinin & Forman (1995), while the best fit for my sample is shown by the dotted line.

Loveday et al., 1995), which suggests that AGN randomly sample the normal galaxy distribution and that the two populations have similar environments. This point is something I shall address in chapter 7 in much more depth.

In an attempt to convert this physical correlation length to an appropriate angular scale length for my sample I use the Limber equation appropriate for the power law parameterisation $W(\theta) = (\theta/\theta_0)^{1-\gamma}$ (Peebles, 1980). The amplitude θ_0 can be related to the correlation length r_0 such that:

$$\xi(r,z) = \left(\frac{r}{r_0}\right)^{-\gamma} (1+z)^{-(3+\epsilon)},$$

using

$$\theta_0^{\gamma-1} = r_0^{\gamma} H_{\gamma} \left(\frac{H_0}{c}\right)^{\gamma} \left\{\int_0^{\infty} y^{5-\gamma} \phi(y)^2 \frac{[1+z(y)]^{-(3+\epsilon-\gamma)}}{F(y)} dy\right\} \left\{\int_0^{\infty} y^2 \frac{\phi(y)}{F(y)} dy\right\}^{-2}.$$

In these equations ϵ parameterises the clustering evolution of the AGN, for example $\epsilon = 0$ represents clustering that is stable in proper coordinates while $\epsilon = -1.2$ would be clustering that is constant in comoving coordinates. H_{γ} is a constant that is dependent on γ and is obtained by using the Gamma function such that:

$$H_{\gamma} = \frac{\Gamma\left(\frac{1}{2}\right) \Gamma\left(\frac{\gamma-1}{2}\right)}{\Gamma\left(\frac{\gamma}{2}\right)}.$$

For $\gamma = 1.8$ this evaluates to 3.679.

y is the angular diameter distance and is related to z by this equation:

$$y(z) = \int_0^z \frac{dz'}{\left\{[1-(\Omega_m+\Omega_\Lambda)]\,(1+z')^2 + \Omega_\Lambda + \Omega_m(1+z')^3\right\}^{0.5}}$$

which needs to be integrated numerically for non-zero cosmological constants. $\phi(y)$ is the redshift distribution of the sample converted into the y variable; in this case I assume that the redshift distribution in figure 4.4 adequately reflects the true distribution on the AGN in my sample. I also assume $H_0 = 75$ km s^{-1} Mpc^{-1}, $\Omega_m = 0.3$ and $\Omega_\Lambda = 0.7$. Making these last assumptions the function $F(y) = 1$, since

$$F(y) = \left[1 - y^2(\Omega_m + \Omega_\Lambda - 1)\right]^{0.5} = [1-0]^{0.5} = 1.$$

The detailed derivation of this specific case can be found in Peebles (1980).

Taking the value $r_0 = 6.0\ h^{-1}$ Mpc my sample should have an amplitude of $\theta_0 = 3.0''$ if $\epsilon = -1.2$, and $\theta_0 = 1.3''$ if $\epsilon = 0$. Both of these values are well within

the errors of figure 5.4 for my sample so I cannot, with any confidence, distinguish between these evolutionary paths.

The best way to obtain a reliable measure of the clustering evolution of AGN would be to perform a similar analysis to the above on a much larger sample. For example, the *XMM-Newton* Serendipitous Survey will detect many orders of magnitude more sources than my survey, with typically 50-100 sources per field and a possible 500-800 observations per year (Watson et al., 2001). With an aim to identify a significant number of the serendipitously detected AGN, this survey should be able to detect clustering in the AGN population at different redshifts, and so be able to measure the clustering evolution explicitly. This will be a natural extension of the *ROSAT* surveys of Vikhlinin & Forman (1995) and Akylas et al. (2000), being deeper than both while covering an area of sky smaller than the RASS but much larger than the 40 square degrees of the Vikhlinin & Forman (1995) study.

Chapter 6

Searching for Galaxy Clusters

So far this thesis has dealt almost entirely with the AGN detected in the two main *XMM* fields. However, galaxy clusters and groups can also be detected in X-ray surveys and appear as soft, extended X-ray emission, in contrast to AGN which are point like. This chapter details my work in detecting galaxy clusters, firstly using the X-ray data and then the optical catalogues of the CFDF maps. The CFDF work makes up the first half of this chapter, together with demonstrations of data visualisation techniques.

As an extension to the CFDF work a more refined optical cluster detection technique is described in the second half of this chapter, in relation to the *Chandra* Deep Field - South (CDF-S). This refinement is made possible by the extraordinary quality of data available for this field that allows a more precise measurement of high redshift cluster properties. This work on the CDF-S may demonstrate some fundamental limitations for the large scale X-ray cluster searches that are currently underway.

6.1 Introduction

Clusters and groups were first noticed as over-densities of galaxies on optical photographic plates. They were found to contain varying numbers of member galaxies from small associations of a few galaxies to vast collections containing many thousands. The dividing line between rich clusters and poor clusters or groups has traditionally been defined as 30 galaxies brighter than $m_3 + 2^m$ (where m_3 is the magnitude of the third brightest cluster member) within a radius of $1.5h^{-1}$ Mpc of the cluster centre (Abell, 1958). Rich clusters are then further subdivided into richness classes (R) based on the number of member galaxies that fulfil the above criteria, from $R = 0$ for the least rich (30-49 galaxies) to $R = 5$ for clusters containing more than 300 galaxies. The higher the richness number the less numerous that class becomes.

Only about 5% of all galaxies reside in rich ($R \geq 0$) clusters, but an important property is the high density of galaxies within them. The spatial density of bright galaxies within a radius of 1.5 h^{-1} Mpc of a cluster centre is $\sim$ 200 times higher than that of the field population (Dekel & Ostriker, 1999). This figure increases to $10^4 - 10^5$ for the cores of the richest and most compact clusters making mergers and tidal interaction between galaxies, among other effects, much more common. Therefore, the evolution of cluster galaxies is fundamentally different to galaxies in the field, and so galaxy clusters provide excellent opportunities for studying mechanisms that change the properties of galaxies over the history of the Universe.

Galaxy clusters are the most massive gravitationally bound objects in the Universe, but it is not the cluster member galaxies themselves that provide the majority of this mass. In fact, clusters are dominated by dark matter with the remaining *baryonic* mass dominated by the hot intra-cluster gas that sits in hy-

drostatic equilibrium with the dark matter. This hot intra-cluster gas is responsible for the extended X-ray emission (due to thermal bremsstrahlung radiation from fully ionised plasma at typically several 10^7 K) and is another very useful property of galaxy clusters (Rosati, Borgani, & Norman, 2002). Masses of clusters can be calculated by using both the gas and the galaxy population; assuming virial and hydrostatic equilibrium both the hot gas and the ensemble of galaxies will respond to the same gravitational field and both methods produce compatible results for total cluster masses. These calculations show that typical clusters have masses of $10^{14} - 10^{15}$ h^{-1} $M_{\odot}$ with the gas fraction only constituting $\sim 0.03 - 0.15$ $h^{-1.5}$ (Dekel & Ostriker, 1999) (the mass fraction associated with galaxies is typically $\sim 0.05 - 0.1$). Therefore, the dark matter is by far the most significant source of gravity, and both the gas and galaxies seem to trace the dark matter potential, and each other, reasonably well. The mass to light ratios of massive clusters approaches that of the Universe as a whole ($(M/L_B)_{cluster} = 300 \pm 100$ h $(M/L_B)_{\odot} \Rightarrow \Omega_{dynanical} \sim 0.2$) suggesting that they do not have any more dark matter associated with them beyond their own physical extent, unlike isolated galaxies.

In addition, the number and redshift distribution of galaxy clusters provides fundamental information about the cosmology of the Universe, because massive clusters are a direct probe of large scale structure formation (Press & Schechter, 1974). Therefore, the motivation to search for galaxy clusters over a wide range of redshifts is clear; both galaxy evolution and cosmology can be investigated with the same objects, as well as being prime sites for the study of dark matter.

Any single method designed to look for galaxy clusters will have associated selection effects determined by the types of observation used to carry it out; for example, finding over-densities of galaxies on the sky is prone to contamination by

chance alignments of galaxies in the same line of sight. Therefore, it is prudent to employ more than one detection method to ensure that the selection functions of each can be properly quantified. In this chapter I use two complementary sets of data for finding clusters in my fields: X-ray and optical. Where one method may be insensitive to clusters of a particular type or redshift the other method can be used to fill in the gaps.

6.2 X-ray Cluster Detection

There are many current studies employing X-ray surveys to look for galaxy clusters and groups at high redshift (e.g. Lamer et al., 2003; Refregier, Valtchanov, & Pierre, 2002; Bauer et al., 2002), all using different detection methods. However, essentially these different methods all boil down to one crucial point: that galaxy clusters are extended soft X-ray sources. This property was first noticed in observations taken with the *Uhuru* satellite (Gursky et al., 1971; Kellogg et al., 1971) which carried out the earliest X-ray sky survey (Giacconi et al., 1972). Since then X-ray telescopes have increased in throughput and sensitivity allowing more distant clusters to be detected and studied. *ROSAT* is still responsible for the largest complete X-ray cluster catalogues (Ebeling et al., 1998, 2000; Böhringer et al., 2000, 2001), but these catalogues only really stretch to modest redshifts of $z \lesssim 0.3$. With *XMM* and *Chandra* X-ray surveys are now able to detect clusters to higher redshifts ($z > 1$) than optical cluster searches, with seemingly much greater reliability. This is mainly due to the much better contrast of the cluster X-ray emission against the background, unlike the heavy contamination of high redshift clusters by field galaxies in deep of optical surveys.

In this section I attempt to evaluate various methods of detecting extended X-ray emission in my data, with the aim of finding a reliable method for studying high redshift galaxy clusters.

The canonical soft X-ray band ($0.5 - 2$ keV) has been shown to be very close to the optimum energy range for detecting clusters in *XMM* data, out to $z = 1$ (Scharf, 2002). This band maximises the signal to noise for clusters with plasma temperatures $kT \gtrsim 2$ keV while lower temperature clusters or groups would require slightly different energy ranges to achieve optimum signal to noise. However, because I am primarily interested in clusters rather than groups I use the soft band images in the following analysis.

6.2.1 Extended Sources Detected by EMLdetect

The source detection routine described in Chapter 2 is optimised for point source detection but the maximum likelihood task is also able to calculate the likelihood of a source being extended. In the source detection I performed on all three CFRS fields this capability was turned on. No extended sources were detected in the 14-h field but several were detected in the 3 and 10-h fields. This detection algorithm was found to be less than ideal for detecting extended sources by Valtchanov et al. (2001), so in order to verify the nature of the extended sources in the 3 and 10-h fields I re-analyse them using other techniques discussed by those authors. I do not repeat the work of these authors in thoroughly testing the different source detection procedures on simulated data, as my aim here is simply to show their efficacy in a few real cases.

A significant problem in detecting any astrophysical source is the presence

of noise in an image. In the case of X-ray images the background level tends to be very low, with zero count pixels being a common occurrence. However, the sources themselves may also be very faint and detecting these sources is often a case of picking significant clumps of pixels out of the noisy background. Invariably the faintest source counts in X-ray surveys are contaminated by spurious detections of regions where the background experiences a random fluctuation, causing a chance clumping of pixels. I have tried to minimise this effect in my source detection by setting the threshold for the detection probability deliberately high. As a consequence however, it is likely that I have missed many faint sources for the analysis of previous chapters. The following source detection methods, as outlined by Valtchanov et al. (2001), provide alternative ways of assessing the significance of a clump of pixels against the background.

6.2.2 Gaussian Smoothing Technique

Smoothing data has long been a useful method of enhancing features in images that are comparable to the size of the smoothing kernel. In the case of these X-ray surveys it also provides a way of evening out the rapidly fluctuating background. Although the signal to noise ratio of an isolated source is increased this comes at the expense of degraded resolution, since a source with a nearby companion will have part of its flux spread out into its neighbour and visa versa. In effect the resolution of the convolved image is a function of both the original resolution and the size of the smoothing function applied to it. For example, an image with a Gaussian PSF of width a, convolved with a second Gaussian of width b will have a final Gaussian width c such that:

$$c^2 = a^2 + b^2.$$

So this technique has its obvious limitations. Despite this it is useful for a first look analysis as it is fast and easy to perform.

I follow the method of Valtchanov et al. (2001) and convolve my *XMM* images with a Gaussian with FWHM = 12″. I tested other smoothing scales but found 12″ to be a good compromise between smoothing the background and enhancing source signal to noise for both point-like and extended emission. Heavier smoothing reduces the background noise more but at the expense of making nearby sources indistinguishable from each other. Since I am primarily concerned with source detection here, rather than full characterisation, I do not treat the different *XMM* imaging instruments separately. Instead I combine data from all three instruments before smoothing to provide the deepest possible exposures. Calculating source fluxes etc. would require a more rigorous approach, analysing data from the individual instruments to obtain specific count rates, which could then be converted into fluxes using the ECF values discussed in chapter 2.

Having smoothed an image I then perform the source detection algorithm SExtractor on it, running it through the image analysis package gaia. This is a very quick and easy way to perform source detection, most commonly used for optical data. However, with suitable input parameters it can be quite effective in detecting sources in smoothed X-ray data. The SExtractor algorithm searches for groups of joined pixels that exceed a given, user defined, threshold value and flags those regions as sources. This is similar to the sliding box method (see chapter 2), although the requirement for the pixels to be adjacent makes SExtractor less suitable for unsmoothed X-ray data. Smoothing the image helps here because it effectively fills in blank pixels, allowing the SExtractor algorithm to operate more effectively.

6.2.3 Multiresolution Wavelet Filtering Technique

An interesting method also tested by Valtchanov et al. (2001) is a filtering technique involving wavelet transforms of varying scales. It comes as part of an image analysis package called MR/1 (Starck, Murtagh, & Bijaoui, 1998). I leave the detailed description of the specific algorithm used here to Starck & Pierre (1998), who test this method on simulated X-ray data of a cluster, and use it to characterise the X-ray emission from a real cluster detected with *ROSAT*. There are many wavelet transform algorithms that can be applied to an image but the one I use here has been found to work particularly well in X-ray images, where the count rate for any given pixel is rather low (zero to several) and so have Poisson noise characteristics.

Briefly, this wavelet filtering scheme uses the *à trous* (with holes) wavelet transform algorithm, whereby an image $I(x, y)$ can be decomposed into a set of images $(\omega_1, ..., \omega_n, c_n)$, each corresponding to a different scale:

$$I(x, y) = c_n(x, y) + \sum_{j=1}^{n} \omega_j(x, y).$$

Statistical models are then applied to the wavelet coefficients $\omega_j(x, y)$ to determine if they are significant, i.e. not due to noise. Retaining the significant coefficients and then reconstructing the image essentially creates a final image free from noise, while retaining all the significant structure on every scale without degrading the final resolution. Sources within the image can then be considered as objects that are connected via significant coefficients on a number of different scales. Point sources will be primarily made up of small scales while diffuse sources will be dominated by the larger scale coefficients.

Optionally, the largest wavelet scale (representing large scale, slowly varying

structure, or a diffuse background) can be omitted from the reconstruction process leaving a uniform background level of zero. This option is particularly useful when performing photometry as the sky has effectively already been subtracted, simplifying and speeding up the calculation.

6.2.4 Results for the Lockman Hole

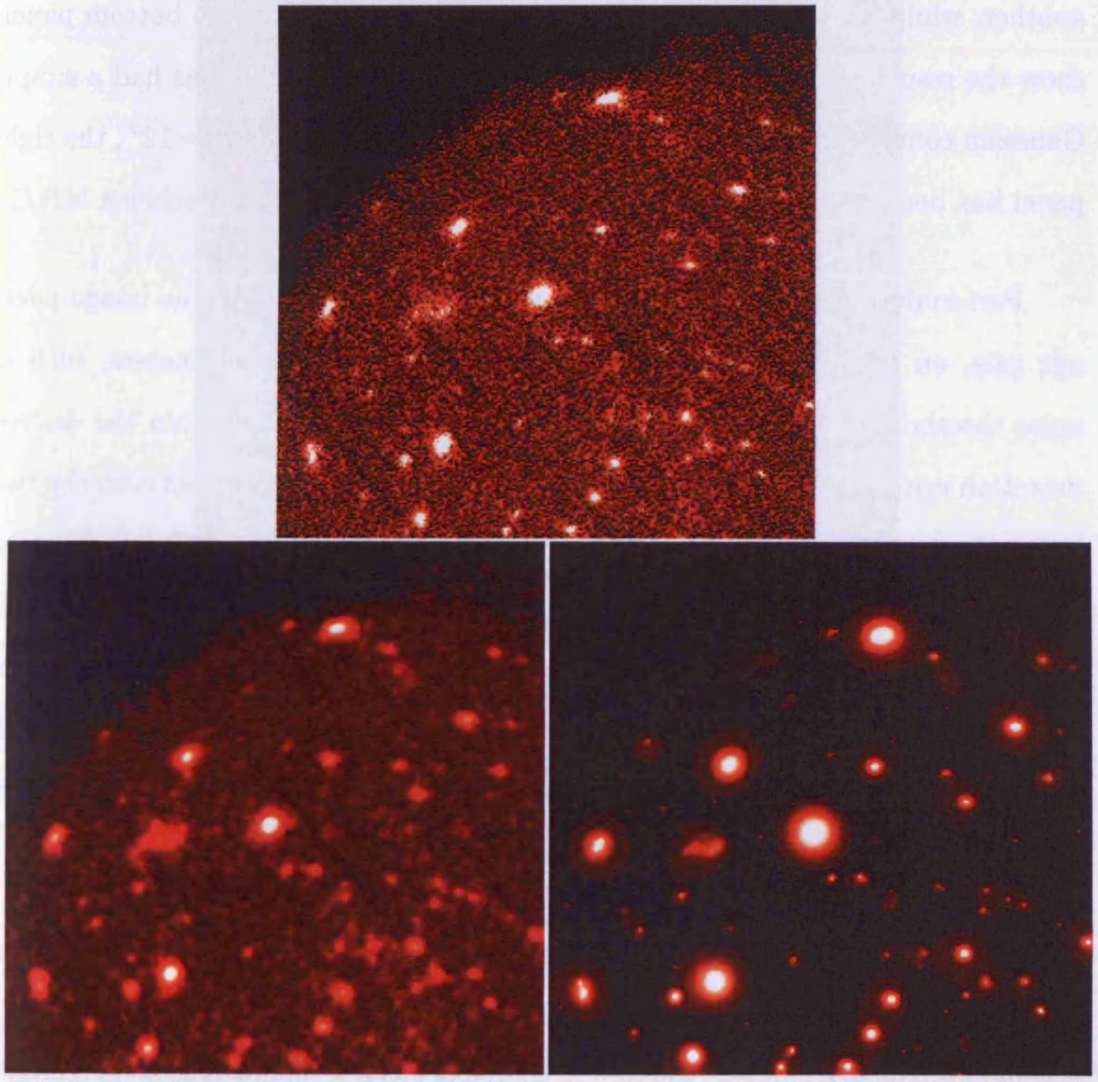

Figure 6.1: Raw data (top), simple Gaussian smoothing (bottom left) and multi-resolution wavelet filtering with the background removed (bottom right).

Figure 6.1 shows a section of the Lockman Hole *XMM* data that I obtained from the *XMM* public archive and re-reduced. The top panel shows the raw, filtered, data from all three instruments and two separate exposures combined giving a total exposure time of $\sim$ 67 ks. The pixel size in this case is $4''$. I chose this region to test the above cluster detection routines because it is known to contain a pair of high redshift clusters and a low luminosity group (Lehmann et al., 2001). The clusters are at $z = 1.263$ and appear to be interacting with one another, while the group is at a low redshift ($z = 0.074$). The two bottom panels show the result of the different image treatments: the left panel has had a simple Gaussian convolution routine performed, using a width of FWHM = $12''$, the right panel has been filtered using the multi-resolution wavelet filtering scheme MR/1.

Performing the SExtractor detection algorithm, run through the image package gaia, on both these images results in figure 6.2. Input parameters, such as noise threshold and number of joined pixels, can be tuned to obtain the desired detection criteria. The SExtractor input parameters are different between the two images here because a noise threshold level is meaningless for the MR/1 case, since only $> 4\sigma$ significant structure is present in the output image, whereas there is still a noisy background present in the Gaussian smoothed case. The detection parameters are almost infinitely tunable and so I have chosen parameters for each case such that the outputs are fairly similar here. As such, these sets of parameters may not be the optimum set for a general case, using either technique.

To determine if a source is point-like or extended the 'seeing' parameter can be entered into the SExtractor algorithm. This is then used by SExtractor to calculate a 'stellarity index' whereby a source is given a number between 0.0 (not at all star-like) an 1.0 (definitely star-like). In X-ray images the seeing quantity is fairly meaningless since there is no atmosphere through which the X-rays pass, but

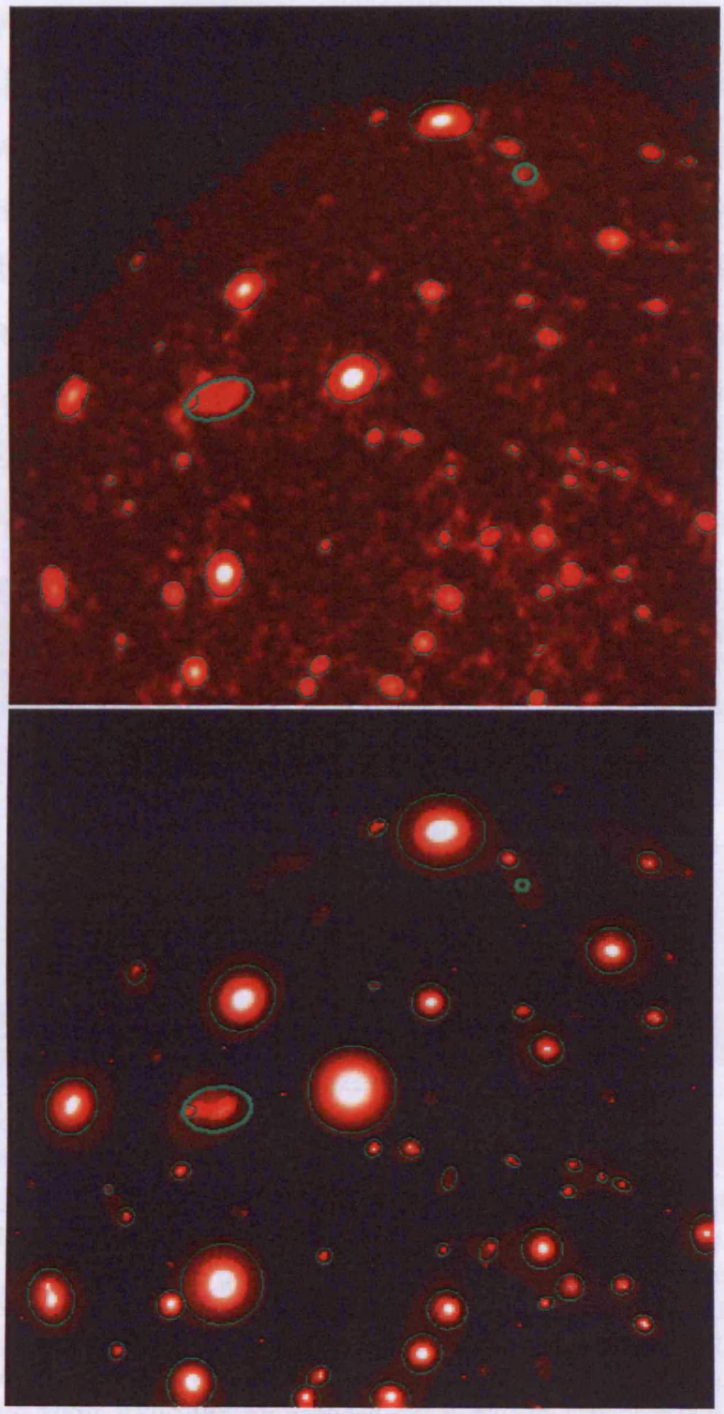

Figure 6.2: Simple Gaussian smoothing (top) and multi-resolution wavelet filtering (bottom) with sources detected by SExtractor indicated by green ellipses. Thicker ellipses show detections of the interacting clusters and the group detected by *ROSAT*.

this quantity can be taken to represent the resolution of the telescope assembly. For *XMM* the FWHM at the aim point is $\sim 6''$ so this is a good place to start, but because the PSF changes over the FOV of the telescope this quantity needs to be fine tuned until the stellarity index gives a clear distinction between point-like and extended sources. Because of the variation of the *XMM* PSF I take stellarity values close to 0.0 to mean the source is extended, while any source with an index $\gtrsim 0.1$ I assume is not significantly extended (see figure 6.3 for an example of the source separation). The plotted ellipses in figure 6.2 are isophotal limits so bright sources appear larger than faint ones, rather than being any indication of actual extent.

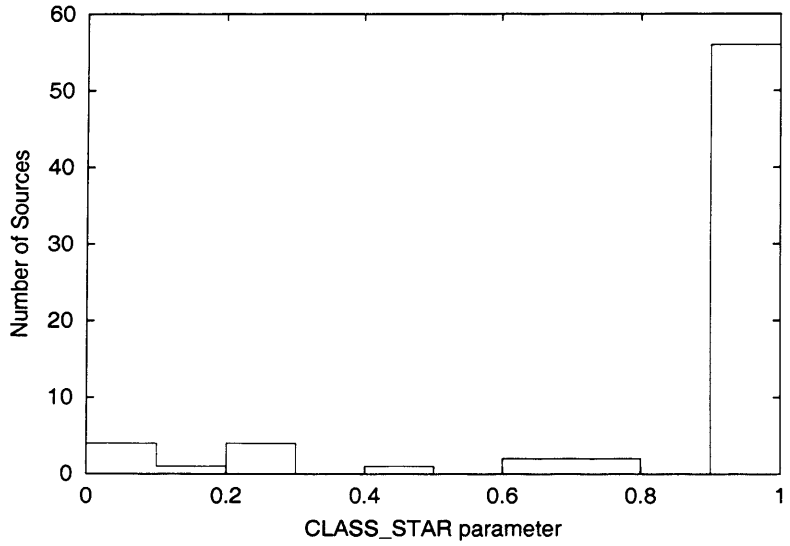

Figure 6.3: Histogram showing the distribution of stellarity index, CLASS_STAR, parameters for the sources detected in the MR/1 filtered Lockman hole *XMM* image. The interacting clusters and the group, circled with thick ellipses in figure 6.2, have CLASS_STAR values that fall in the furthest left bin. Most of the sources are point-like and so have CLASS_STAR values in the furthest right bin. Some sources have intermediate values and these sources lie primarily towards the edge of the *XMM* FoV making them hard to distinguish because of the broadening PSF.

The two sources outlined with thick ellipses are the interacting clusters and the low luminosity group previously identified by *ROSAT* (Lehmann et al., 2001).

Encouragingly, both these sources have a stellarity index close to 0.0 in both the Gaussian smoothed and MR/1 filtered images, implying that they are highly likely to be extended. The interacting clusters are clearly visible as the larger of the two highlighted sources. A certain amount of structure can also be seen in this source which I have highlighted in figure 6.4. The group is not so obvious, as it is very faint, but it is still detected by both methods, and shows some evidence for being extended. It should be noted that the stellarity index is also quite sensitive to the other detection parameters used so should not be taken to be a rigorous classification; rather it should be used as a broad guide in these cases.

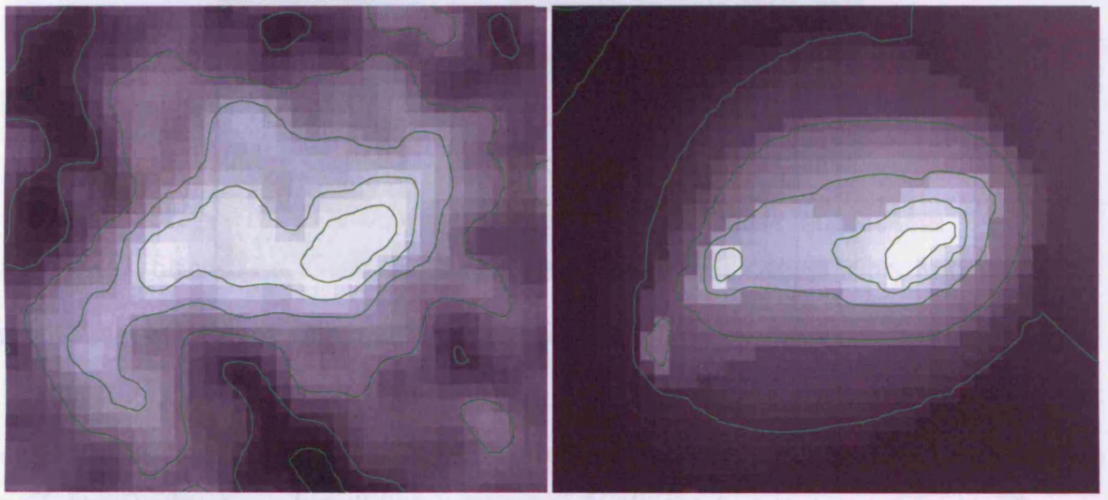

Figure 6.4: Close-up of the interacting clusters in the Lockman hole. The left panel shows the Gaussian smoothed image, the right shows the wavelet filtered image.

Returning to the interacting clusters, figure 6.4 shows a region approximately 2.5′ across, centred on the pair. The left hand panel shows the Gaussian convolved image while the right hand panel is the output of the MR/1 filtering algorithm, retaining the background. The contours illustrate two things: firstly that the Gaussian image still contains a significant quantity of noise which the MR/1 filtering has removed, and secondly the structure of the X-ray emission. In both these images the X-ray emission of both clusters is apparent, with two cores visible, particularly

in the MR/1 image. The core of the eastern cluster is detected as a separate source by SExtractor in both these cases (see figure 6.2, and is also not significantly extended. This may indicate that the eastern cluster has a compact core, although it is entirely possible that this source may in fact be an AGN embedded within the cluster core.

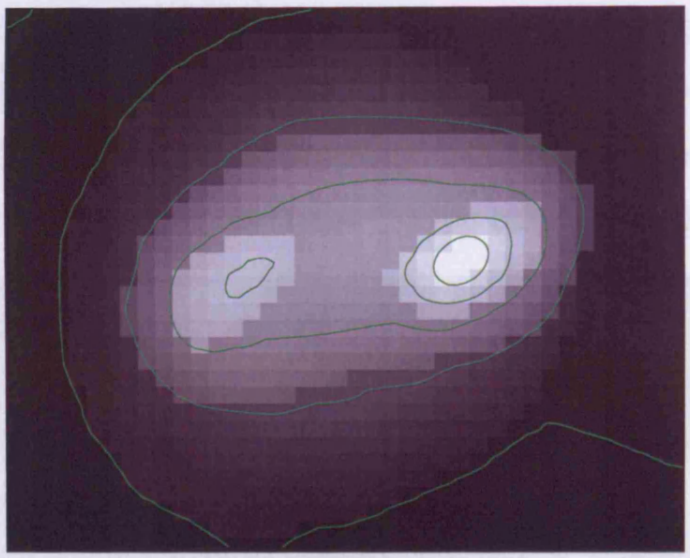

Figure 6.5: Same as right panel of figure 6.4 but using data only from MOS instruments with no chip gaps running through the source.

There also appears to be 'tail' of emission extending down to the South-East from the Eastern cluster. The exact structure of this emission is corrupted slightly by the presence of a chip boundary that bisects the 'tail' in *both* of the PN frames used in the compilation of this image. Annoyingly, despite the two exposures having different aim points different gaps fall in exactly the same place over this particular source compounding the error. The gap itself is visible as a slightly darker diagonal stripe running from the top left corner to the bottom centre in the Gaussian smoothed image in figure 6.4. The effect on the MR/1 filtered image is less obvious but it has resulted in the 'tail' being depressed slightly in the middle, making it look more like two separate sources, one of which being the possible

compact core discussed above. Reanalysing this field with MR/1 using data from only the MOS instruments for the two exposures (removing the offending PN data) results in figure 6.5. The 'tail' is now clearly absent and the Eastern core is no longer as compact. In fact, SExtractor now clearly separates the two clusters and detects both as being extended, while the group, which is still detected, is now too faint to be reliably classified as extended (due to the absence of the PN data).

This feature highlights the need for care when performing analysis on extended sources and in interpreting the results. The presence of an AGN embedded within the Eastern cluster is now less likely, and the 'tail' has been shown to be a false structure. This feature is also noted in Hashimoto et al. (2002) using the same *XMM* data for this field.

In summary, I concur with the conclusions of Valtchanov et al. (2001) that the MR/1 filtering algorithm is an excellent way of searching for, and studying, galaxy clusters. The treatment of noise in the MR/1 algorithm is self contained and is easily controlled by the user, so the detection of significant sources and structure is much more transparent than when using Gaussian smoothing. There is also the cosmetic advantage offered by MR/1, which produces recreated images free of noise; the option to remove slowly varying backgrounds also makes source photometry very simple. With this in mind I now turn to the *XMM* exposures of the CFRS fields, namely the 3, 10 and 14-h fields.

For completeness, figure 6.6 shows a VRI colour image of the Lockman Hole clusters with ROSAT contours overlayed, taken from Hashimoto et al. (2002).

Figure 6.6: Figure 1 from Hashimoto et al. (2002) showing the ROSAT contours overlayed on a VRI colour image. The cores of the two merging cluster are clearly visible in both the X-ray contours and the distribution of red galaxies. A bright lensed background galaxy is also visible near the centre of the Eastern core, which has a measured redshift of 2.57

6.2.5 Results for CFRS fields

No extended sources were detected by EMLdetect in the 14-h field so this provides a good test to see if any could be extracted using the MR/1 filtering algorithm. A sample of the 14-h field is shown in figure 6.7 with both the raw soft band data and the filtered image displayed. In this example I have elected to keep the largest wavelet scale when reconstructing the filtered image to demonstrate the difference this makes compared to removing it (see figure 6.2). Keeping the largest scale reproduces all the image characteristics present in the original, minus the noise, but removing this scale effectively removes any slowly varying background making source detection and characterisation much simpler. This example is only used as an illustration here, the source detection is run on the image without the background.

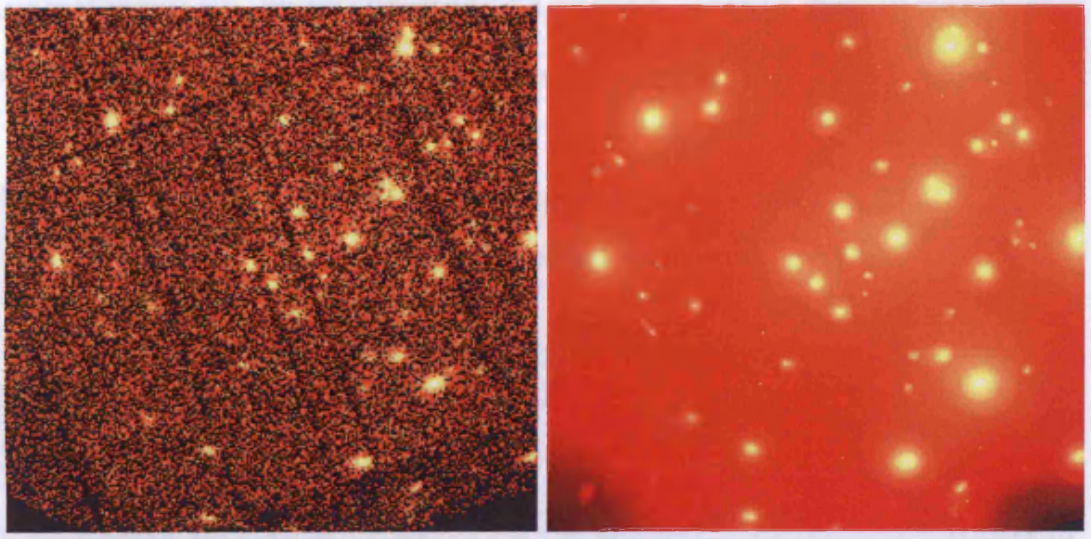

Figure 6.7: Central South section of the 14-h field. The reconstructed image retains all the wavelet scales having been filtered, including the largest scale which represents the slowly varying background.

The 10-h field is rather more interesting as the EMLdetect routine finds an extended source in the South-East of the field. Figure 6.8 shows a sample of the 10-h field containing this source along with the MR/1 filtered image, minus the background. The extended source is clearly visible in the lower left corner and SExtractor confirms that it is the most significantly extended source in this field. There is no deep optical coverage to confirm whether or not this is a cluster or group. Morphologically this region shows little to no structure and is very close to circular, indicating that this is a relaxed system.

Performing photometry on this source, using the MR/1 filtered image, gives a total number of counts of 211. This is less than the 352 counts estimated by the EMLdetect routine for this source. In contrast, the photometry for one of the point sources in this field is much closer, 100 counts with MR/1 and 90 counts with EMLdetect. Valtchanov et al. (2001) perform a flux recovery test as part of their analysis and conclude that MR/1 recovers the flux of extended sources more

accurately than EMLdetect, and both methods are comparably good at recovering flux of point sources. Therefore, I assume that the photometry on the MR/1 image is the more correct result.

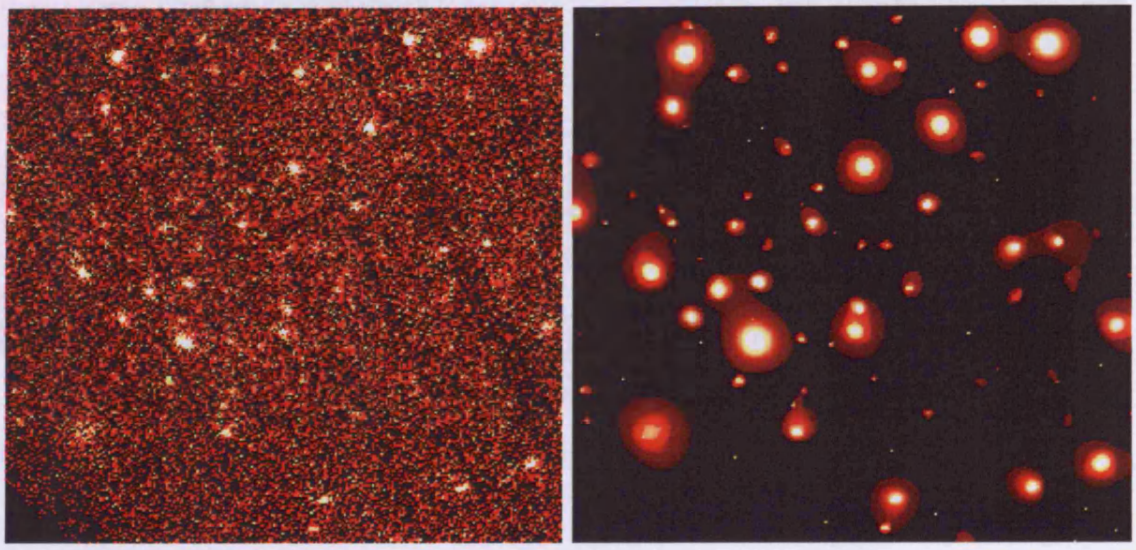

Figure 6.8: Central and South East quadrant of the 10-h field showing the MR/1 treatment of a region containing an extended X-ray source (bottom left corner of both panels, also see figure 2.11). The largest wavelet scale has not been included in the image reconstruction, effectively removing the background.

The 3-h field also contains a number of sources that are classified by EMLdetect as extended, virtually all of them surrounding the bright QSO in the South-West corner of the exposure. This region is shown in figure 6.9. The filtering treatment of this field is inconclusive, although the emission to the North of the QSO does show some evidence for extension whereas the emission to the East does not. Contamination from the bright QSO makes this very hard to interpret and again, it is unfortunate that this part of the field falls just outside the coverage of the CFDF maps. Being so close to the edge of the *XMM* exposure also complicates the situation and I am inclined to believe that the broadening of the telescope PSF has a significant effect on the appearance of this region.

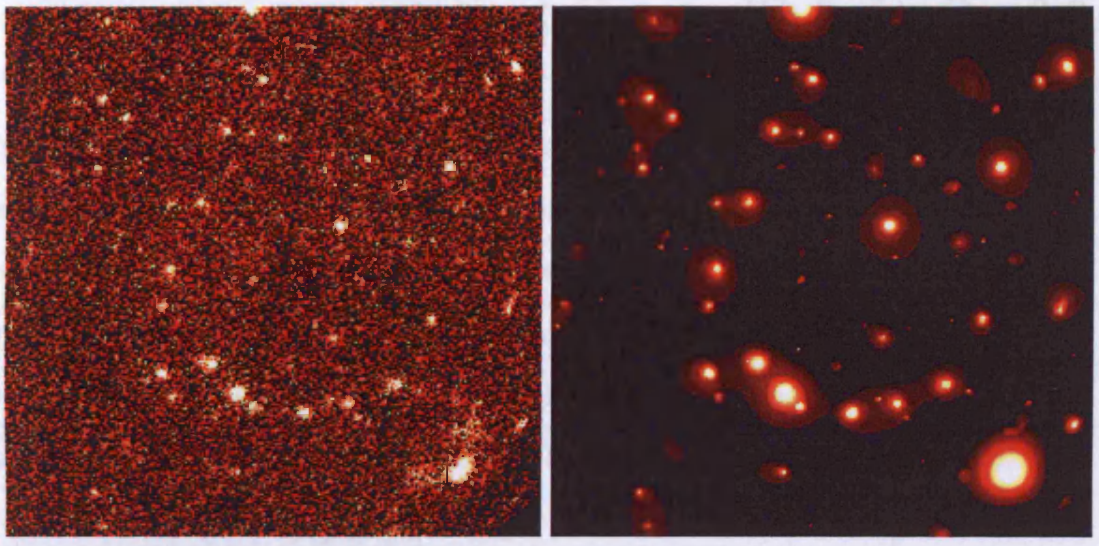

Figure 6.9: Central and South West quadrant of the 3-h field showing the region containing the bright QSO mentioned in section 2.7.1, in the lower right corner (see also figure 2.8).

6.2.6 Future Work

The MR/1 filtering method has been employed by the *XMM* Large Scale Structure (XMM-LSS) survey (Refregier et al., 2002) to search for galaxy clusters out to $z = 1$, with good success. They perform a hybrid approach to fully characterise the source parameters, by passing the source list from SExtractor to the EMLdetect task, which then tests each source against a PSF model. It would be interesting to re-run the source detection for all of my *XMM* surveys using this hybrid technique to see if the results are significantly different to the standard sliding box plus EMLdetect source detection method.

6.3 Optical Cluster Detection

As mentioned above, galaxy clusters are very obvious in the nearby Universe and can be clearly identified simply due to the high spatial density of optical galaxies compared to the field population. However, as survey depths increase so does the density of objects on the sky, leading inevitably to severe contamination by foreground objects when looking for galaxy clusters. Statistical tests can still be used to identify significant collections of galaxies (Ostrander et al., 1998) but this does not remove the possibility of chance alignments of unassociated galaxies at vastly different distances. Methods have been developed to remove foreground contamination, such as identifying the early type galaxies that tend to form the core of rich clusters, and have a well defined sequence in two band colour-magnitude diagrams. This so-called red-sequence method relies on the fact that *any* galaxy type, at a lower redshift than the cluster, will have bluer colours than the core galaxies, and so a simple colour cut can remove the vast majority of foreground galaxies for any given redshift (Gladders & Yee, 2000). The red-sequence is well defined for clusters because it is thought that all the early type galaxies that comprise the core of a cluster are formed at the same time, and evolve passively thereafter. This means that they all have similar stellar populations and so also have similar SEDs. As long as the prominent 4000 Å break is straddled by the two filters used, at the redshift of interest, then models of stellar populations can be used to calculate the position of the red-sequence on the colour-magnitude diagram.

The cluster red-sequence works well for detecting high redshift clusters but it is not well suited for studying the whole population of cluster galaxies because it only detects the early type galaxies. If one is interested in studying the Butcher-Oemler effect (Butcher & Oemler, 1978), whereby the fraction of blue galaxies

appears higher in higher redshift clusters, then late type galaxies must be detected too. Therefore, more inclusive photometric methods must be used to better sample cluster galaxy populations.

Full photometric redshift codes have been shown to work well in separating cluster members from the field when performing pointed cluster observations in several optical bands (Kodama et al., 2001; Dahlén et al., 2004). However, with the advent of large area, deep multi-band surveys, this sort of analysis is likely to be very useful for serendipitous cluster searches out to high redshifts. If near-IR bands are also included then the accuracy and range of redshifts accessible to these techniques will be even better, since at $z > 1$ the 4000 Å break can only be straddled using IR filters.

However, detecting serendipitous clusters is more complex than simply using photometric redshifts to separate cluster members from field galaxies for a known cluster. If a cluster redshift is known then simply selecting galaxies with estimated redshifts near to the cluster redshift will remove a large fraction of the field contamination. But if one doesn't know what redshift a cluster is at, or even if it exists at all, then this sort of treatment is not helpful. With this in mind I develop a fast and efficient method for detecting significant over-densities of galaxies at all redshifts, simultaneously, over an entire survey field. This will then allow more detailed analysis of individual regions to be performed using the other techniques.

6.3.1 My Algorithm

For this work I use an updated and improved version of the BPZ photometric redshift code, superior to that used in chapter 4. After fitting a best fit model

template to each galaxy, this new version also then quantifies the difference between the photometry of each input galaxy and that expected from the best fit model template. There are bound to be small differences for individual galaxies whenever there is an inexact fit to the best fit template, but if there is a systematic error in the photometry of the input catalogue then this will show up as a non-zero mean when the photometric differences are calculated for all the objects. The mean value of the differences for all the objects can then be used to apply counter offsets to the zero-points of the original photometry in the input catalogue. I repeat the tests performed in section 4.8.1, on the CFDF objects that also have spectroscopic redshifts from the CFRS, and iterate the process many times until the mean offsets are small and the comparison of the spectroscopic and photometric redshifts is noticeably improved over that in figure 4.9. Figure 6.10 demonstrates the sort of improvement that can be achieved by altering the zero-point offsets. Figure 6.10(a) is similar to figure 4.9(b) for the 14-h field but now includes all 128 objects with both CFRS redshifts and CFDF photometry, leaving in objects with less reliable photo-z's ($P_{\Delta z} < 0.95$). After altering the offsets the result is a reduction not only in the number of objects with catastrophic errors but also in the small scale scatter of the estimates around the 1:1 line (figure 6.10(b)). The systematic suppression of photo-z's observed for this field (see section 4.8.1) is now also less apparent, although there is still a worrying feature at $0.8 \lesssim z_{CFRS} \lesssim 1$ that has not been removed. There is also a reduction in the number of unreliable redshifts, from 24/128 to 9/128 with $P_{\Delta z} < 0.95$.

By using the CFDF $UBVI$ catalogues of the 3-h and 14-h fields I select a sub-catalogue of all the objects with significant detections in all four bands, and with I band magnitudes in the range $17.5 - 24$. In principle all the objects in the catalogue could be used but for the purposes of this experiment I use only the

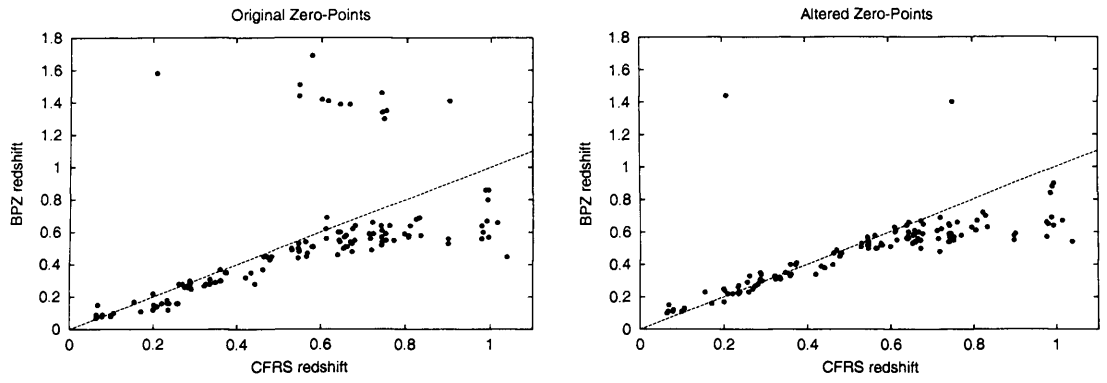

(a) (b)

Figure 6.10: Example of the effect changing zero-points on the photometric redshift estimation. The line is the 1:1 relation expected if the photometric redshifts matched the spectroscopic ones perfectly. The small scale scatter and the number of catastrophic errors is reduced but the photometric redshifts at $z \gtrsim 0.7$ are still somewhat suspect, so this should be borne in mind for the later discussions of the 14-h field.

most secure detections with good photometry measurements to reduce the photo-z computation time while also ensuring that most of the estimates are reliable. I run this restricted catalogue ($\sim$ 1/5 th of the full catalogue), with the relevant alterations to the zero-points, through BPZ and then remove the sources with $P_{\Delta z} < 0.90$ to make the final catalogue as reliable as possible (a further loss of $\sim$ 35% for the 14-h field and $\sim$ 48% for the 3-h field).

The final list of objects (10499 for the 14-h, 6826 for the 3-h field) now has a set of 3 coordinates R.A., Dec and z, which I shall abbreviate to x, y, z. I then convert the raw coordinates into a data cube array with a grid size of $\Delta_{xy} = 0.6'$ and $\Delta_z = 0.02$. To do this I effectively smooth the data by placing a 3D Gaussian at each array point and summing the contribution from each object in the list, weighted by the value of the Gaussian function at the distance between the object and the array point. So an object close to the array point will count more than a more distant object. The value at the array point can then be viewed as some sort

of measure of the local density of objects about that point. The overall redshift distribution is calculated in a similar way but without the smoothing in x and y. To obtain an over-density value the difference is taken between each array point value and the corresponding mean redshift distribution value, so that the mean for any given slice in z is then zero. This over-density value is then scaled, such that the standard deviation of values in each redshift slice is equal to 1.0. Ultimately, each coordinate within the data cube array contains a signal to noise value that gives the statistical significance of the over-density of objects at that point, relative to the mean value for the whole redshift slice. In other words, a statistic S is calculated such that:

$$S = \frac{N_c - N_b}{SD},$$

where N_c and N_b are the galaxy counts at each point, and the mean value respectively. SD is then the standard deviation of the $N_c - N_b$ array values. In this way the standard deviation of all the S values in any given redshift slice is necessarily 1.0. If an array point has a value $S = 3.0$ then it lies 3 standard deviations away from the mean value.

I choose particular smoothing lengths for the 3D Gaussian with the aim of detecting high redshift clusters. Therefore σ_{xy} is set to $1.0'$ (equivalent to ~ 0.45 Mpc at $z = 1$) and σ_z is set to 0.03 (slightly smaller than the accuracy of BPZ in the 14-h field for $0 < z < 1$), although variations of these quantities by a factor of 2 does not really change the overall results by much.

The data cube can then be loaded into an IDL program available from the IDL Astronomy User's Library called SLICER3. This is a versatile data visualisation program specifically designed to deal with data cubes. It allows the data to be sliced into planes of any orientation, so in this case slices in z are ideal. The cube

can also be rotated in all three axes so that the data can be viewed from any angle. As well as slices the program can also display the data in a number of other ways, and can also output the array values at any specified point within the cube.

6.3.2 Points to Note

A side effect of using signal to noise, rather than absolute density difference, is that the mean redshift distribution may have a profound effect on the sensitivity of this method to different richness clusters at different redshifts. For example, detecting clusters at $z = 0.9$ may in fact be easier than detecting clusters at $z = 0.6$ because the redshift distribution peaks at $z \sim 0.6$ for the CFDF catalogues. Therefore, more galaxies are required to produce an over-density of a given signal to noise than at the higher redshift, where there are far fewer galaxies in general (e.g. 10 galaxies on top of a mean of 100 is far less significant than 10 galaxies on top of a mean of 5). Of course, this effect will be balanced to a certain extent by the dimming of the galaxies in a more distant cluster, so that fewer will be detected for inclusion in the input catalogue (plus the photometric redshifts of faint galaxies are less likely to be reliable anyway). At present the selection function for this technique is not at all well defined and this is something that would need to be calculated in any future work on this data.

In this first example the smoothing lengths σ_{xy} and σ_z are constant with redshift but this is not necessarily the optimum method. The smoothing length of $1.0'$ is equivalent to different physical scales at different redshifts, so to be consistent σ_{xy} should really be a function of z to give a constant co-moving or proper distance smoothing scale at every redshift (see examples below). Also, the accuracy of photometric redshift codes tends to be a function of z too, and so σ_z

should vary as well.

For the purposes of this experiment though These details are unimportant as I am not attempting to obtain reliable science at this stage; that would require a better understanding of the selection function of this algorithm. For now I simply use this particular set of parameters to demonstrate the technique.

6.3.3 Results

Because the 14-h field seems to be generally more conducive to photometric redshift treatment than the 3-h field (see figure 4.9) I address the 14-h field here as an example. Figure 6.11 shows a SLICER3 cut through the 14-h data at $z = 0.88$, the redshift slice that contains the most significant over-density in this field. The bright blob near the bottom is a fluctuation with a peak of 6.8σ, centred on R.A. 14:16:54, Dec. 52:14:24.

This region is clearly unusual and it is possible that it is a newly discovered galaxy cluster. The redshift is also highly significant because few clusters have been found at such high redshifts. However, there is no apparent extended X-ray emission associated with this region, so it is possible that either the cluster has quite a low ICM temperature and X-ray luminosity ($kT \lesssim 2$ keV, $L_X \lesssim 10^{43}$ erg s^{-1}) or simply doesn't exist at all. If it is the first reason then this is very important as it shows that clusters with low X-ray luminosities can be detected using this method, when they would be missed by X-ray surveys. With significantly different selection functions these two methods - X-ray and photo-z - can provide complementary information on the true redshift distribution of galaxy clusters. Of course, the second possibility cannot be ruled out as a 6.8σ fluctuation can still happen through

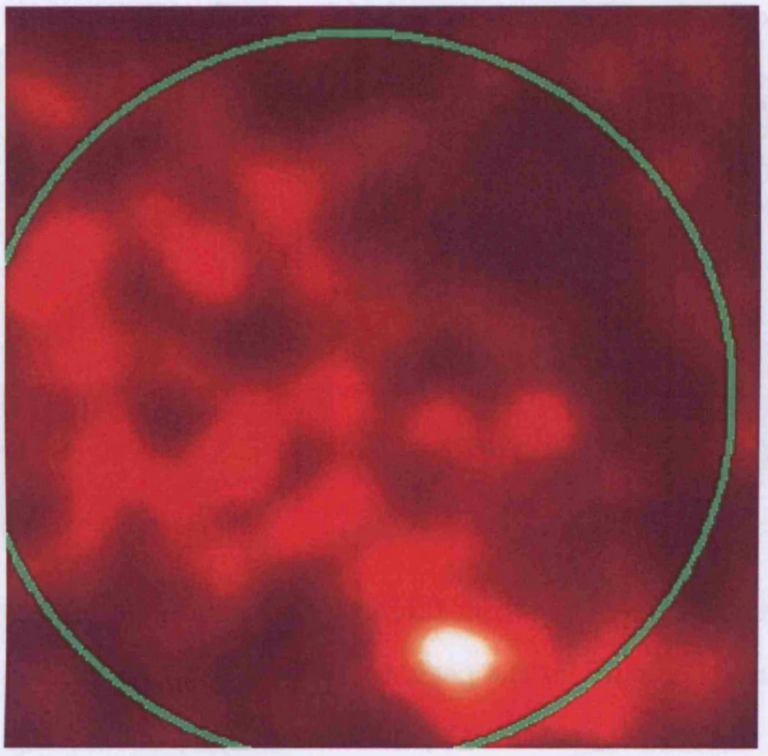

Figure 6.11: Slice through the 14-h data cube at $z \sim 0.88$. North is up and East is left. This covers approximately the same area as the *XMM* survey, the approximate extent of which is shown by the green circle, (see also figure 2.9) and is oriented in the same way.

chance, albeit highly unlikely. This region must be reevaluated when the selection function for my algorithm is fully understood.

From the peak at the centre of the region to an edge defined by a 3σ level, the region is $\sim 2.5'$ in radius (~ 1.1 Mpc at $z = 0.88$), which is fairly typical of galaxy cluster radii.

Data Visualisation

Figures 6.12 and 6.13 are special figures designed to appear in 3 dimensions when viewed in a particular way. Not everyone can achieve the desired effect but the

best method to view these images is as follows. The idea is to make your left eye see the right hand image, while your right eye sees the left hand image. By holding the page at arms length, cross your eyes, while looking at the centre of the figure, so that two images of the figure are formed and cross over to appear as two pairs of cubes. Slowly uncross your eyes until the two closest cube images overlap, leaving just three cubes. Concentrate on the central cube and slowly bring it into focus, using the edges of the cube as a guide. When the central cube is in sharp focus it should appear as if the image is in 3D with the data spread throughout the confines of the box.

If this method doesn't work an alternative is to place a finger vertically between your face and the figure on the page, to act as a focus point. Move your finger forwards or backwards, maintaining your focus on it, until only three images of the cubes are visible in the background. This will give you an idea as to where your eyes should be pointing while you refocus them to bring the central cube image into sharp focus. Eventually you should be able to remove your finger from your line of sight without losing your focus on the 3D cube image.

These figures aren't really any more than a gimmick, although it does demonstrate the speed with which a large survey area can be visually inspected for significant over-densities of galaxies. The SLICER3 program can display the data in many ways including plotting iso-surfaces around high density regions. For example, to find all the $> 3\sigma$ over-densities in the data a 3σ iso-surface can be plotted which immediately highlights the regions of interest, as is shown in figure 6.13. Each individual region can then be investigated using the technique commonly used for pointed cluster observations, using the rest of the survey to provide a suitable field subtraction.

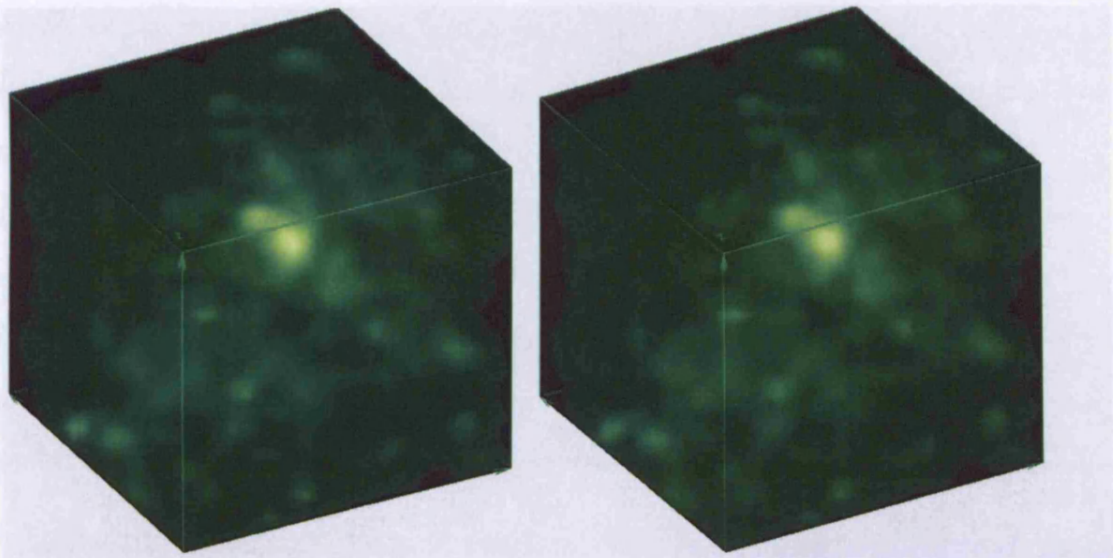

Figure 6.12: A 3D view through the 14-h data cube. The 6.8σ fluctuation is clearly visible near the top front of the cube.

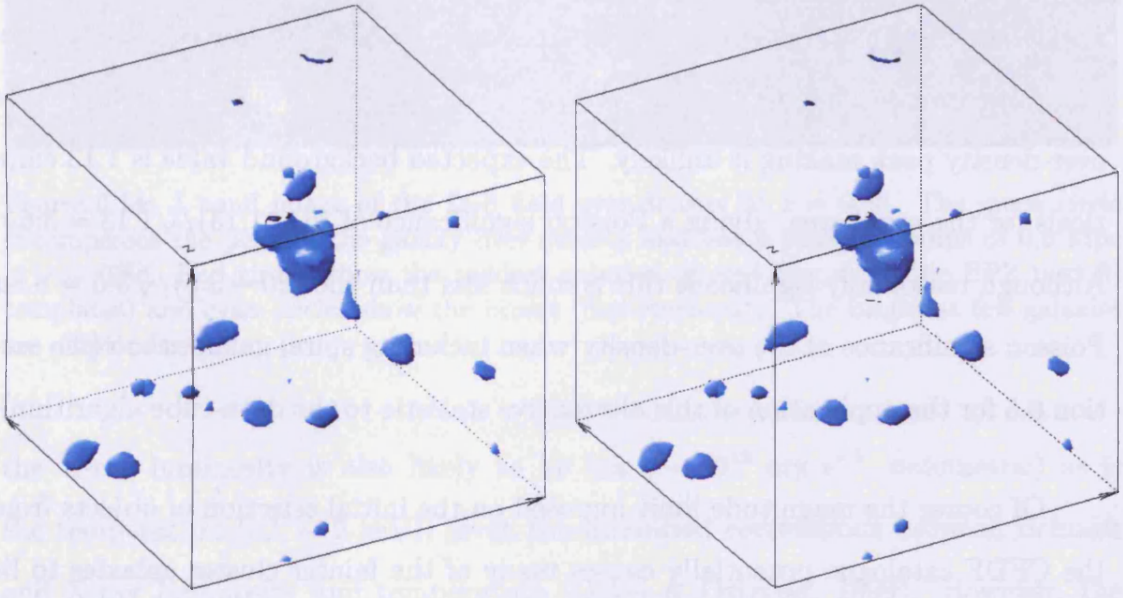

Figure 6.13: An alternative 3D view through the 14-h data cube, showing all 3σ iso-surfaces. The orientation is identical to figure 6.12.

For example, the 6.8σ fluctuation in this field is equivalent to an excess of only about 15 galaxies above the 4 or so expected for that area, calculated from the mean of the whole redshift slice. The brightest few 'cluster' galaxies are all early

types, and although there is no dominant central galaxy these brightest galaxies are within 0.25 Mpc of the peak of the over-density. The brightest galaxy has an apparent I_{AB} magnitude of 21.15, giving it an absolute magnitude of -23.54 assuming it is at $z = 0.88$ and is an elliptical (the best fit parameters given by BPZ); this is about a magnitude brighter than an L* galaxy. Figure 6.14 shows the I band image of this region showing the distribution of galaxies in the redshift range [0.78 : 0.98]. It is clearly not representative of a relaxed and spherical cluster and appears to be closer in appearance to an irregular cluster, even down to the high spiral galaxy fraction ($f_{sp} > 0.5$). This is a possible explanation for the low X-ray luminosity, as irregular clusters tend to be less X-ray bright than regular clusters.

It is possible that the Cluster Red Sequence method would successfully detect this over-density but there are only 5 elliptical galaxies within 0.5 Mpc of the over-density peak making it unlikely. The expected background value is 1.13 ellipticals for the same area, giving a Poisson significance of $(5 - 1.13)/\sqrt{1.13} = 3.6\sigma$. Although reasonably significant this is much less than the $(20 - 3.5)/\sqrt{3.5} = 8.8\sigma$ Poisson significance of the over-density when including spiral galaxies too (see section 6.5 for the application of this alternative statistic to the data-cube algorithm).

Of course the magnitude limit imposed on the initial selection of objects from the CFDF catalogue potentially causes many of the fainter cluster galaxies to be missed, so I must assume that a large fraction of the true population of this region are not detected. Even so, at least two thirds of the galaxies must have been overlooked for this 'cluster' to be classified even as high as richness 1 (see below). This is not unreasonable however, so I tentatively suggest that this region is in fact a low richness cluster. This could also help explain the lack of detectable X-ray emission associated with the region. If the cluster is low richness then

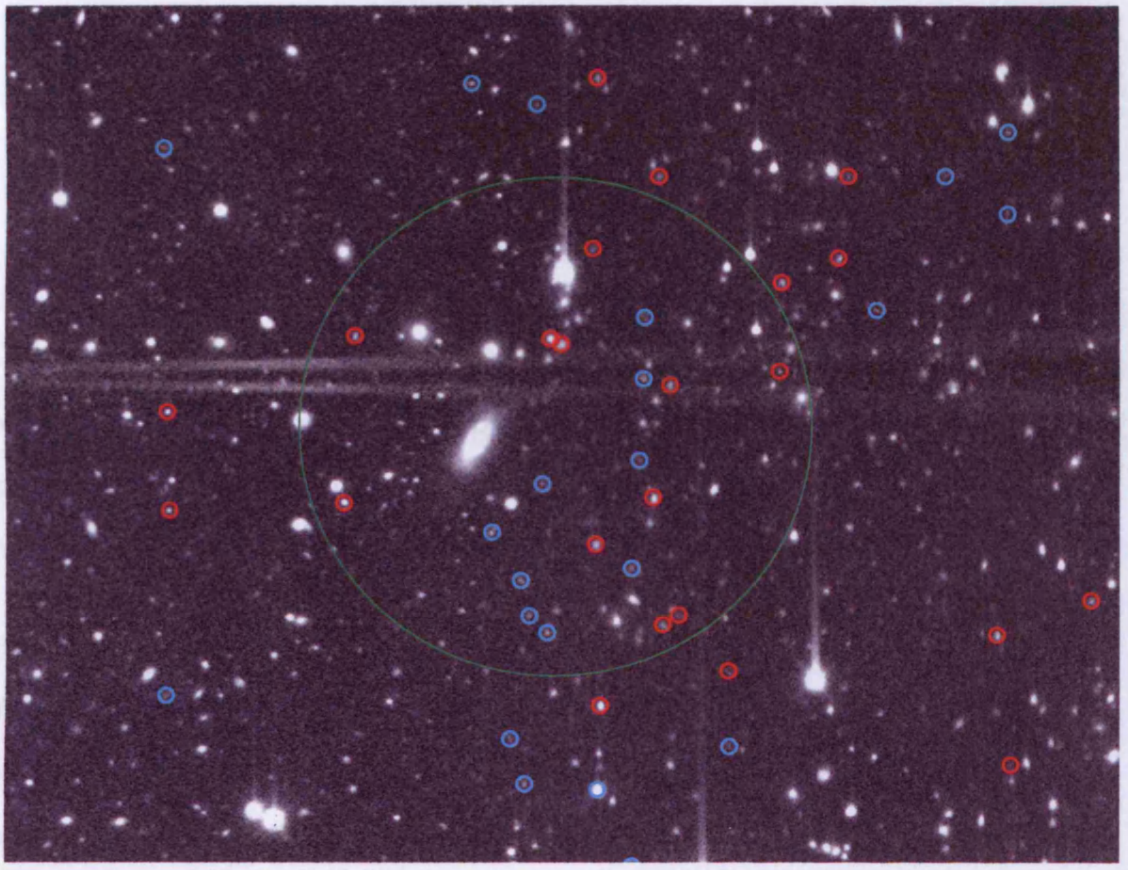

Figure 6.14: I band image of the 14-h field over-density at $z = 0.88$. The green circle encompasses the peak of the galaxy over-density and has a physical radius of 0.5 Mpc at $z = 0.88$. Red circles show the reddest galaxies (E and Sbc, from the BPZ best fit templates) and cyan circles show the bluest (Scd-starburst). The brightest few galaxies are ellipticals.

the X-ray luminosity is also likely to be low ($\sim 10^{43}$ erg s^{-1}, bolometric) as is the temperature ($kT \sim 2$ keV), given the measured correlations between richness and X-ray luminosity and temperature (Dekel & Ostriker, 1999). However, the uncertainty in the true richness of this cluster leads to even larger uncertainties in these estimates. The large K correction associated with high redshift galaxy clusters in the X-ray will cause very low temperature clusters to be missed by even deep *XMM* exposures, especially given the high off-axis position of this cluster in the *XMM* FoV ($\sim 10.5'$), so this is the most likely explanation for the lack of

detection in this case.

6.3.4 Measuring the Cluster Richness

A more rigorous measure of a clusters richness can be obtained by measuring the 2-point angular correlation function of the galaxies in the vicinity of the cluster centre, using a similar technique to that employed in chapter 5. The amplitude of the correlation function can then be equated to an Abell class, using the prescription of Yee & López-Cruz (1999) or McLure & Dunlop (2001).

Initially I separate out all objects from the reduced CFDF catalogue with photometric redshifts in the range $0.78 \leq z \leq 0.98$. This isolates the redshift slice containing the over-density and hence enhances the contrast of it against the background and foreground field galaxies. I assume that all the cluster member galaxies lie within this photometric redshift range as the errors in the redshift estimates are less than $\Delta z = 0.1$ for this field. I then calculate the amplitude of the correlation function by assuming it takes the form:

$$W_{cg}(\theta) = A_{cg}\theta^{1-\gamma}$$

and that $\gamma = 1.77$, the canonical value for the field galaxy population (Groth & Peebles, 1977). The amplitude can then be estimated directly from the data by counting the galaxies within a circle around the centre of the cluster. By integrating $w(\theta)$ out to a radius θ the following expression is obtained:

$$A_{cg} = \left[\frac{N_{tot} - N_b}{N_b}\right]\left(\frac{3-\gamma}{2}\right)\theta^{\gamma-1}$$

where N_{tot} is the total number of galaxies within the circle of radius θ and N_b is

the number of background galaxies expected to be found within the same circle. This is essentially the same as the method used in chapter 5 except now only a single circle is counted rather than a series of concentric annuli.

For this particular over-density I count galaxies out to a radius of $\theta = 1.153'$ which corresponds to a physical radius of 0.5 Mpc at $z = 0.88$ in my assumed cosmology. There are 20 galaxies in this circle with an expected background count of 3.5, calculated from the remaining survey area of $30' \times 30'$. This gives a value $A_{cg} = 6.12 \times 10^{-3} \Rightarrow \theta_0 = 4.6'$.

The value A_{cg} is the angular clustering amplitude between the cluster centre and the surrounding galaxies (equivalent to $\theta_0^{\gamma-1}$) but what we are really after is the *spatial* clustering amplitude B_{cg} $(= r_0^{\gamma})$, which gives the strength of the true 3-dimensional 2-point correlation function:

$$\xi_{cg}(r) = B_{cg} r^{-\gamma}.$$

I convert from A_{cg} to B_{cg} in the same way as Wold et al. (2000) by using the following relation:

$$B_{cg} = \frac{N_g A_{cg}}{\Phi(m_{lim}, z) I_\gamma} d_\theta^{\gamma-3}$$

where N_g is the mean surface density of galaxies per steradian, d_θ is the angular diameter distance to the cluster and $I_\gamma = 3.78$ is an integration constant. The final quantity, $\Phi(m_{lim}, z)$ is the integrated luminosity function (LF) of galaxies at the redshift of the cluster, down to some limiting magnitude defined by the survey.

$$\Phi(m_{lim}, z) = \int_{L(m_{lim},z)}^{\infty} \phi(L) dL.$$

I use the Schechter luminosity function defined in Barr et al. (2003) for the I band,

with $M_I^* = -22.65$, $\alpha = -0.89$ and $\phi^* = 0.0052$. By integrating the LF down to $I_{AB} = 24$ at $z = 0.88$ ($M_{lim} = -20.14$ for an Sbc galaxy) I obtain the value $\Phi = 0.0085$ Mpc^{-3}. The Detailed derivation of the conversion from A_{cg} to B_{cg} can be found in Longair & Seldner (1979).

The main advantage of selecting only galaxies within a redshift slice of $0.78 \leq z \leq 0.98$ is that it significantly reduces the error associated with the number of background galaxies. This is given by:

$$\frac{\Delta A_{cg}}{A_{cg}} = \frac{\Delta B_{cg}}{B_{cg}} = \frac{[(N_{tot} - N_b) + 1.3^2 N_b]^{1/2}}{N_{tot} - N_b}$$

(Yee & López-Cruz, 1999), the 1.3^2 factor coming from deviations of the field galaxy population from a true Poisson distribution (because they are clustered). Ultimately I obtain a value $B_{cg} = 237 \pm 69$ Mpc$^{1.77}$, although the error is likely to be greater than this because of the uncertainties in the true form of the LF.

Now, to convert this clustering amplitude to an equivalent Abell richness I use two calibrations. Yee & López-Cruz (1999) would class this amplitude as Abell class 0, their lower limit being $B_{cg} \sim 195$ Mpc$^{1.77}$ (after correcting for their different cosmology). McLure & Dunlop (2001) would also equate my value of B_{cg} to Abell class 0 ($146 < B_{cg} < 341$).

6.3.5 Correcting for Incompleteness

Because I perform the above analysis on only galaxies with good photometric redshifts ($P_{\Delta z} > 0.9, I_{AB} < 24$) the results will be affected by a degree of incompleteness in the catalogue. This effect is illustrated in figure 6.15. At bright magnitudes essentially all the galaxies have reliable photometric redshift estimates.

At the fainter limit, photometric errors cause many of the galaxies to have unreliable redshift estimates, and so these are lost from the reduced catalogue; at $I_{AB} = 24$ the full CFDF catalogue, which is still complete (and remains so to at least $I_{AB} = 25$), contains over twice the number of galaxies as the reduced sample. Therefore, to ensure that the results in this section are not biased it is necessary to correct the reduced sample by the incompleteness factor at any given magnitude. To do this I simply multiply the number of galaxies of a given magnitude by the ratio between the two catalogues when it is counted, in both the cluster vicinity and the background.

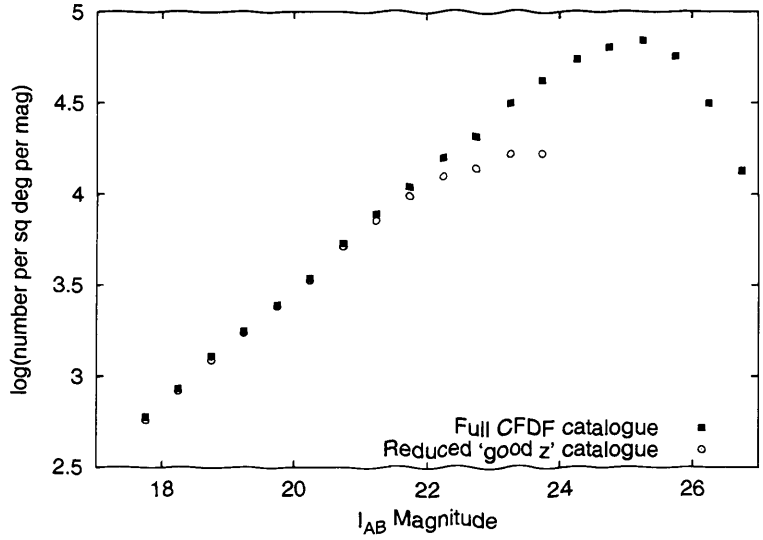

Figure 6.15: Comparison of number counts, in half magnitude bins, between the full 14-h CFDF catalogue and the reduced sample containing only $I_{AB} < 24$ galaxies with good photometric redshifts. The difference between the two catalogues shows the level of correction required by the reduced sample to account for its incompleteness.

After correcting for incompleteness the clustering amplitude increases to $B_{cg} = 368 \pm 86$ Mpc$^{1.77}$ which pushes it into the lower range of Abell Class 1 clusters under the scheme of McLure & Dunlop (2001).

This is reassuringly similar to my earlier argument and increases my confidence in the nature of this region, that it is at best a low richness cluster and hence has

low X-ray emission. Alternatively, it is possible that this over-density is actually a filament, viewed in projection and in the process of forming into a cluster, which is therefore unvirialised and will have lower X-ray emission than an equivalent virialised cluster. Objects of this type will be more common at high redshifts than in the local Universe, assuming the hierarchical merging paradigm is correct, and so it is entirely possible that this is the case here. The fact that such a region is detected by my method is encouraging as it is likely to be a very sensitive way of detecting high redshift clusters that are in the process of forming and are therefore undetectable by X-ray methods.

6.4 Discussion

At the time of writing this data-cube technique is intended to be viewed more as a visualisation demonstration, rather than for use in serious scientific application. In order to assess the usefulness of such a technique it needs to be thoroughly tested to obtain a reliable selection function. This can be done the brute force way by using simulated galaxy catalogues, and against data of real galaxy clusters and groups. It would be fairly straightforward to generate a fake survey of any size, containing a realistic number of galaxies with a suitable range of types and luminosities. Then, catalogues could be generated in any number of filters, applying appropriate photometry errors, which could then be run through a photometric redshift estimation code. By placing clusters and groups of known richness, at known redshifts throughout the artificial survey, it could be determined exactly how effective the technique is at detecting these over-densities. Parameters such as the smoothing scales σ_{xy} and σ_z could then be fine-tuned to optimise the detection of relevant structures. This technique could also allow the optimisation of a given

survey. For example, to detect clusters at $z = 2$ a UV filter is not as important as an IR filter, that much is obvious; but this technique could also tell you exactly how deep each filter should be for any given science goal. Ultimately a reliable selection function could be determined for galaxy clusters of any richness at any redshift and for any combination of photometric filters. They would also enable me to better classify the 6.8σ fluctuation in the 14-h field, as I would know how many galaxies should be detectable from a given input cluster. This would give a second check on the measurement of the Abell richness class of the cluster and would ascertain how reliable the clustering amplitude method is at estimating this quantity. Alternatively, assuming that the B_{cg} method is reliable then an analytic selection function can be determined by calculating the expected galaxy excess associated with clusters of different richness and at different redshifts. This excess can then be turned into an equivalent sigma value.

The simulations could also be used to assess whether or not it would be better to perform the algorithm on only the early type galaxies, omitting all galaxies with late type SEDs from the smoothing process. Since early type galaxies tend to populate the cores of galaxy clusters their density contrast against the field is much larger than late type galaxies. Although this situation may be less significant in higher redshift clusters, due to evolutionary processes, which would lead to an underestimation of cluster number counts at large redshift if this effect were not taken into consideration.

The biggest advantage this cluster detection technique has over any previous method is that it works better for larger surveys. Because the signal to noise value at any given point is determined from the actual data in the relevant redshift slice, the larger the area of the survey the more accurately the signal to noise values reflect reality. Since an over-density can only be measured as such when contrasted

against a well determined mean, if a survey contains a single huge over-density then it will effectively wash itself out because it will raise the mean value for the entire redshift slice it resides in. In a large survey, any individual over-density will be only a small region within a redshift slice and will not adversely affect the mean density value. Also, edge effects will be correspondingly less significant for larger surveys, since the area/circumference ratio scales with the survey size.

6.5 *Chandra* Deep Field - South

Large multi-band optical surveys are now becoming commonplace and many of them are being made publicly available. This provides an ideal extension to this work because fortunately all the really hard work - reducing and calibrating the very large and varied data sets - is accomplished prior to a survey being made public.

A prime example of this is the now public COMBO-17 data of the *Chandra* Deep Field - South (CDF-S) (Wolf et al., 2004). This superb data set comprises 17 optical filters, both broad and medium bands, which effectively create a very low resolution spectrum for each source running from 350 to 930 nm; and of course, this is ideally suited to photometric redshift treatment. In a sense a half way house between the photometric redshifts described in this work and full on spectroscopy this technique is an excellent compromise between observing time and number of objects with reliable redshifts. The photometric redshifts for the COMBO-17 data (conveniently included in the catalogue together with uncertainties and source classification amongst other parameters) are good to within 2% ($\delta z/(1+z)$) for galaxies with $R < 22$ (degrading slightly for fainter magnitudes), easily good

enough for large statistical studies.

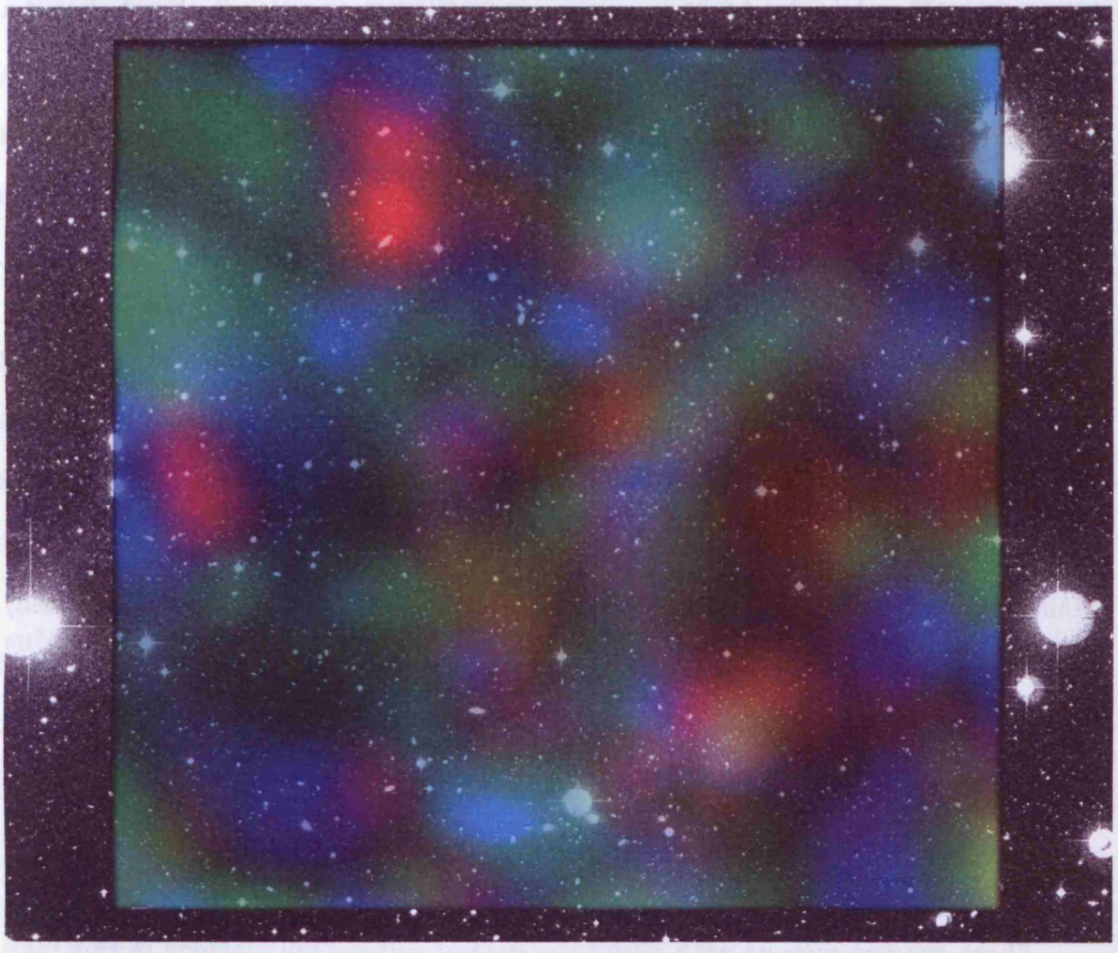

Figure 6.16: R band image of the COMBO-17 field, coincident with the *Chandra* Deep Field-South, overlayed with a colour representation of the galaxy distribution. Blue is z=[0.1:0.3], green is z=[0.3:0.6] and red is z=[0.6:0.8].

As a brief demonstration, figure 6.16 shows the R band image of the CDF-S COMBO-17 data, overlayed with a projection of smoothed galaxy density, calculated using my data cube algorithm (limited to $R < 23$). The different colours represent different redshift intervals: blue is z=[0.1:0.3], green is z=[0.3:0.6] and red is z=[0.6:0.8]. The physical smoothing length is 0.5 Mpc for red and green but 0.25 Mpc for blue (because at low z the smoothing length on the sky gets very large if kept to 0.5 Mpc). The smoothing length in redshift space is a function

that is equal to the error in redshift for a given individual galaxy (but with a minimum smoothing length of 0.01 in z, the spacing between redshift slices). i.e. if a galaxy has a redshift error of 0.02 then that particular galaxy will have a Gaussian probability function in redshift space with $\sigma_z = 0.02$. When it is counted towards a particular array point its distance from that point in both redshift and on the sky determines how much that particular galaxy counts towards that array point.

For this data cube I restrict the analysis to a square of $24.75' \times 24.75'$ (resulting in a grid of 100×100 array points separated by $0.25'$) to give a clear $2.5'$ between the edge of the smoothed map and the edge of the optical coverage. This reduces the edge effects associated with loss of galaxies in the smoothed map near the boundary (see figure 7.5 for an example of this effect in the 14-h CFDF data). With the edges removed the noise measurement within the smoothed map should also be more representative of the true galaxy distribution, and not artificially increased because of the low density values round the edge. In a sense this is a refined version of the algorithm I perform on the 14-h CFDF data.

There are two regions with very high galaxy density fluctuations in this map. They are the brightest coloured regions and both are in the top left corner. One is at $z = 0.47$ (green) the other is at $z = 0.74$ (red). Rather than show another 3D cube I elect to present the data here in this projected form to demonstrate that there are many ways to visualise data.

6.5.1 An Alternative Statistic

Because of the excellent quality of the COMBO-17 photometric redshift catalogue - significantly better than the photometric redshifts in my CFDF studies - I produce

two data cubes here using two different statistics, as a comparative test.

The first method I use is identical to that used in the CFDF study above and acts to normalise the noise in each redshift slice so that the standard deviation of all the values is equal to 1.0; I shall call the subsequent data cube values obtained using this method statistic A and, as a reminder, the value at each point can be expressed as:

$$S_A = \frac{N_c - N_b}{SD},$$

where N_c is the value at each point after the initial smoothing and N_b is the background value, or mean of all the points within each redshift slice. SD is the standard deviation of the values in each slice after having the mean value subtracted away (i.e. the standard deviation of all the numerators in the above expression for each slice).

The alternative method (statistic B) can be summarised by the following expression:

$$S_B = \frac{N_c - N_b}{\sqrt{N_b}},$$

where N_c and N_b are the same as before. The denominator in this case is effectively the Poisson noise for each redshift slice.

In general the two statistics give similar results as to the significance of a particular over-density; however, there are slight differences between the two depending on the properties of the galaxy distribution within a given slice. Figure 6.17 and table 6.1 demonstrate the differences.

Interestingly, redshift is not as big a factor as one might expect. The lines corresponding to $z = 0.20$ and $z = 0.92$ are significantly different in their slopes. Both have similar background density values (see table 6.1) so it is purely the

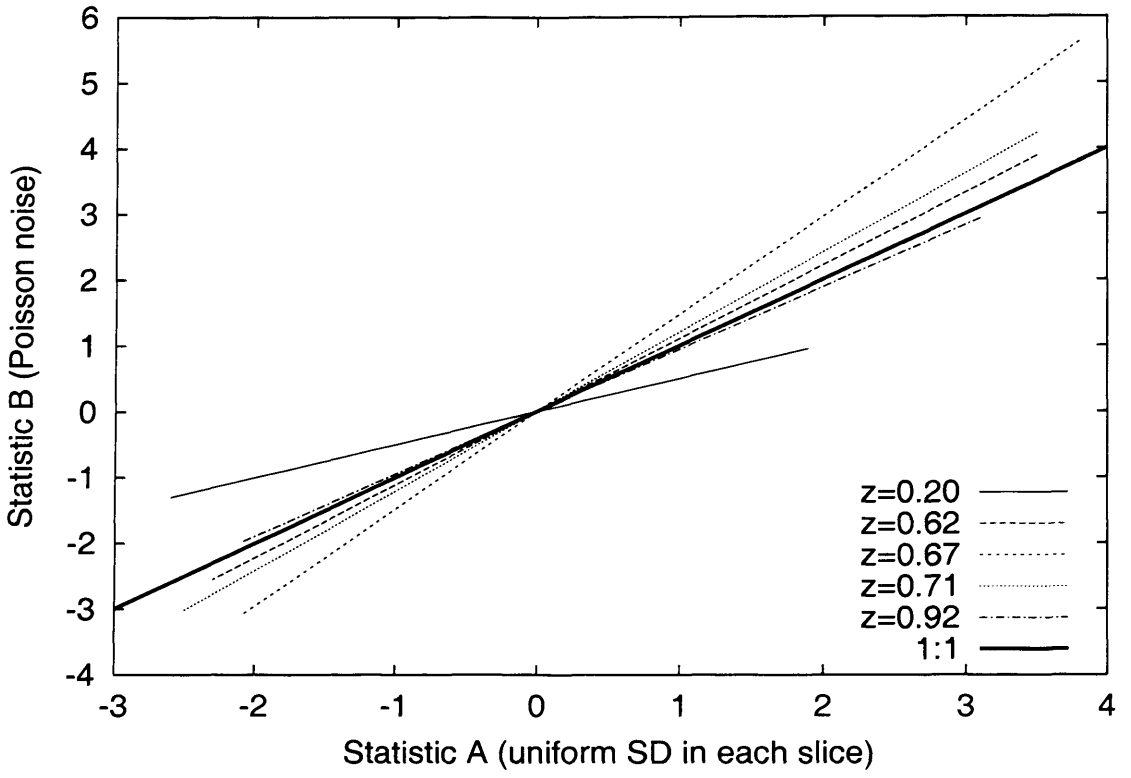

Figure 6.17: Comparison of the two statistics used to quantify structure in the data-cube technique. Identical results would follow the 1:1 line and in general the two statistics agree fairly well. Differences in the slopes of the plotted lines are the consequence of differences in the physical structure at a given redshift, rather than, for example, background galaxy counts.

clumpiness of the galaxy distribution in each slice that leads to the differences, quantified by the standard deviation of the final values in those slices. This is only partly due to the difference in redshift in this case because the smoothing length at $z = 0.2$ is over twice as large as at $z = 0.92$. However, at $z = 0.45$, for example (not plotted for clarity) the background value is again similar to that at $z = 0.92$ but the two statistics give almost identical results, as is the case at $z = 0.92$. The smoothing length does not change much between $z = 0.45$ and $z = 0.92$, so the only difference would be the actual redshift, which does not appear to affect the two statistics significantly.

Table 6.1: Relevant quantities for figure 6.17. SD refers to the standard deviation of the final statistics in the slice, for each method. SD_B effectively gives the gradient of the corresponding line in figure 6.17.

z	N_b	SD_A	SD_B
0.20	8.70	1.0	0.50
0.45	8.80	1.0	1.04
0.62	14.5	1.0	1.11
0.67	20.6	1.0	1.48
0.71	19.2	1.0	1.21
0.92	8.56	1.0	0.94

The background value also seems to be relatively unimportant. The background value at $z = 0.62$ is 64% higher than that at $z = 0.92$ but the fluctuations in galaxy density are only mildly higher, and therefore the two statistics give similar results. Also compare the two lines for $z = 0.71$ and $z = 0.67$, both have very high, and similar, background values but the differences between the two statistics are striking with $z = 0.67$ experiencing the greatest density fluctuations.

So what are the advantages and disadvantages of each statistic? Both statistics give similar answers in general and so agree qualitatively as to which regions are significantly over-dense. Things become more complex when the background level is high, however. For example, in the limit of a mean of a thousand galaxies per cell (defined by the smoothing lengths) Poisson errors will be negligible; any fluctuations in the density of galaxies will be entirely due to real structure. Statistic B would correctly identify the over-dense regions with a high significance because an over-dense region with, say, two thousand galaxies will have a significance of 63σ. Statistic A on the other hand would re-scale all the values so that the standard deviation in each slice is 1.0. If typical density fluctuations vary by a factor of two, as in the example above, then this 63σ over-density would now be given a significance of only 1σ. The final two columns in table 6.1 quantify this effect,

and it can be seen quite easily that although there are roughly the same number of galaxies at $z = 0.67$ and $z = 0.71$ there is clearly more physical structure at $z = 0.67$, as measured by the standard deviation of the statistic B values in the redshift slice. Calculating the standard deviation of values in each slice can then be considered a good way of measuring how clumpy the galaxy distribution is at any given redshift, without having to plot out a whole data cube.

In slices with low background levels the two statistics are in better agreement (apart from when the smoothing length becomes large) so there is not much to choose between the two.

The disadvantage of statistic B is that if there is a large change in the background value between different redshifts then the data cube itself will preferentially show up regions in the high background slices. Statistic A, on the other hand, produces data-cubes with a restricted dynamic range, re-normalising everything so that the structure is uniform throughout the cube.

For scientific analysis it seems that Statistic B is likely to be the more illuminating one. Although, calculating and comparing both statistics for any given survey is not complicated and will provide alternative ways of visualising the data.

6.5.2 Extended X-ray Sources Detected by *Chandra*

Because this field is coincident with a very deep *Chandra* exposure - the second deepest in existence in fact, at 1 Ms - I can directly compare the over-densities detected using my data cube algorithm with extended soft X-ray sources detected by *Chandra*.

In figure 6.18 I show the CDF-S COMBO-17 R band image again, but this time I have overlayed a multi-layered projection of three sets of iso-surface within the CDF-S data cube. Imagine figure 6.13 (but with the CDF-S cube rather than the 14-h field one) viewed from beneath with progressively lower valued iso-surfaces fading out more and more. The three surfaces correspond to 5, 4 and 3σ galaxy over-densities as measured by statistic B. Because this is a projection of all the over-densities between $z = [0.2 : 1.0]$ some lie behind others (the two blobs near source 138 are a good example, a smaller over-density is hiding behind the big one) and so a clear distinction between separate over-densities is not always possible in this figure; I shall indicate any relevant regions in the text where appropriate.

Also plotted in figure 6.18 is the position of the *Chandra* field (illustrated with green squares at the approximate positions of the deepest exposures that make up most of the 1 Ms total) and the extended X-ray objects from the catalogue, listed in table 5 of Giacconi et al. (2002). The yellow labels are the XID numbers, as published, and the radius of the circles is equal to the measured FWHM of each source (except source 645, which I have arbitrarily given a radius of $10''$ because this source, which was detected using a different technique to the others, is very low surface brightness and as such does not have a measured FWHM).

It is immediately apparent that all these 'extended' sources are still rather compact (mean FWHM= $6''$) compared to, for example, the extended source detected by *XMM* in the 10-h field (figure 6.8), which has a FWHM of $\sim 12''$. This is a consequence of *Chandras'* superior resolving power. As with *XMM* the PSF of the *Chandra* telescope module increases for larger off-axis angles; the sources included in figure 6.18 are classified as extended because their FWHM is $> 3\sigma$ larger than expected given the off-axis angle of the source. Several of the sources are clearly associated with the hot halos of individual galaxies (e.g. 116, 514) but

some, possibly most, are likely to be groups or clusters of galaxies.

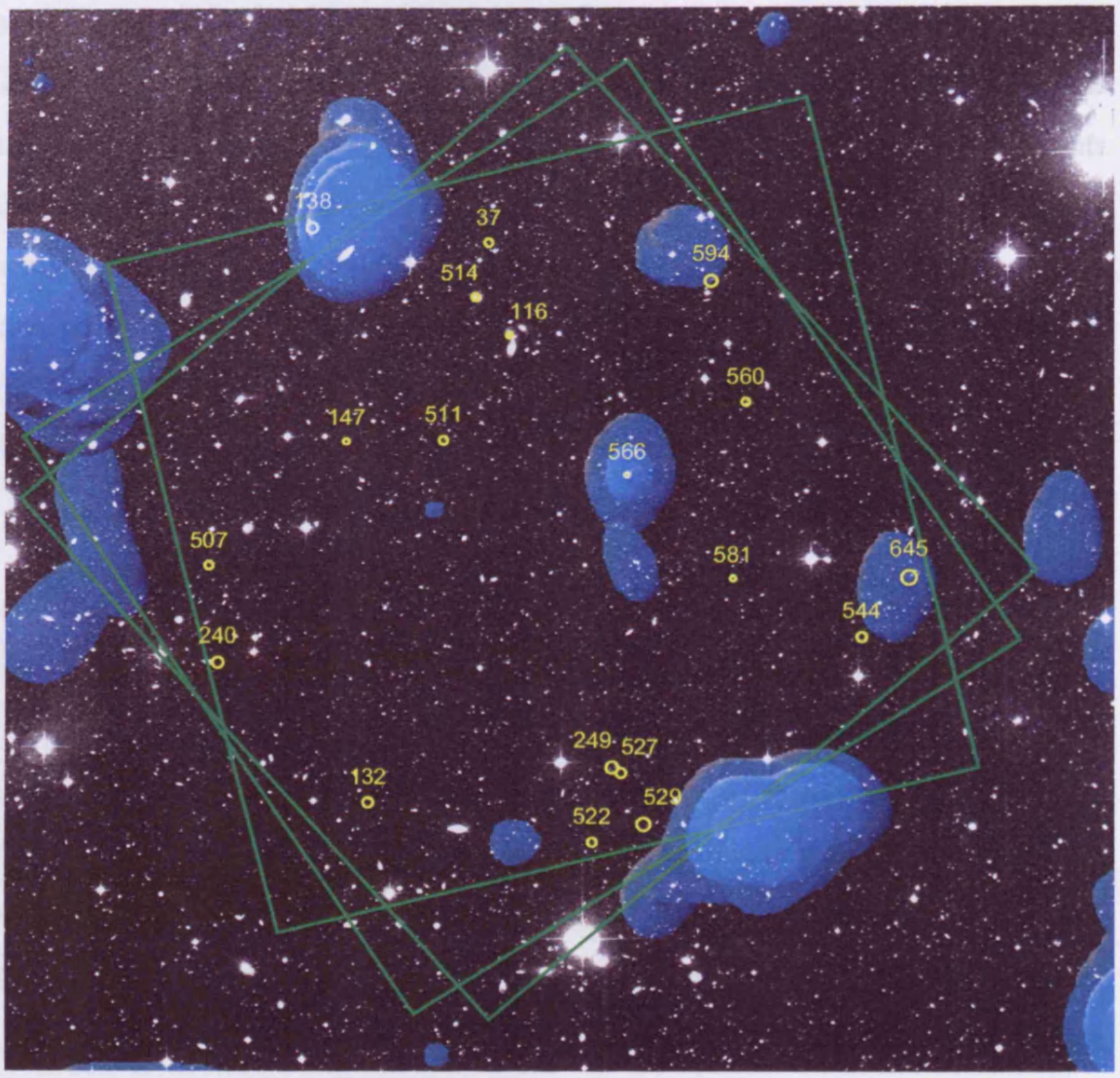

Figure 6.18: Statistic B iso-surfaces projected onto the COMBO-17 R band image of the CDF-S. The green squares show the approximate position of the *Chandra* data and the yellow circles are the extended *Chandra* sources.

Notes on Individual Sources

All further over-density values are the statistic B measurements.

Gilli et al. (2003) mention four of the extended *Chandra* sources; specifically, they relate them to a possible detection of large scale structure in this field. They claim that the X-ray source population demonstrates two clear peaks at $z = 0.67$ and $z = 0.73$, confirmed by a deep spectroscopic survey of part of the field (the K20 survey Cimatti et al., 2002).

Extended sources 560 and 645 are, they claim, identified as two galaxy groups that form part of the structure at $z = 0.67$. I agree with their assessment of source 645. Although only a marginally over-dense region ($\sim 3.7\sigma$) the area near source 645 in figure 6.18 is indeed at $z = 0.67$, although the peak of the over-density in my data cube and the X-ray source are not aligned perfectly. However, on inspection of the COMBO-17 redshifts it appears that there are two groups of galaxies at $z = 0.67$, separated by $\sim 50''$, the X-ray source being coincident with the northern core, while the density contours in my plot encompass both.

Source 560, on the other hand, is a little less clear cut. The over-density value at the position of source 560 peaks at $z = 0.58$ (with a value of $\sim 2.7\sigma$), not $z = 0.67$. The galaxy closest to source 560 has a COMBO-17 redshift of $z = 0.66$ but there are no other galaxies within $30''$ with a similar redshift. I suspect that this source has been misclassified.

Sources 594 and 566 belong to the structure at $z = 0.73$ according to Gilli et al. (2003). 594 is identified as a group and 566 is identified with a cluster. Both X-ray sources are closest to galaxies with COMBO-17 redshifts of $z = 0.76$ but the over-density to the north-east of source 594 peaks at $z = 0.43$. Although there is a slight over-density at the position of source 594 and $z \sim 0.73$ it is only very weak (1.5σ).

The cluster associated with source 566 is clearly visible in the density plot but the peak redshift I obtain is $z = 0.76$. This is quite a high significance over-density at 4.4σ, so the fact that it has been identified as a galaxy cluster (albeit at a slightly different redshift to my estimate) is encouraging. However, I suspect that the extended X-ray emission detected by *Chandra* is actually associated with the hot halo of the central cD galaxy, which is coincident with source 566, rather than the intra-cluster gas, which should be much more extended given the nature of this galaxy cluster (see below).

The only other source I am going to comment on here is number 138, which is close to the highest significance over-density in this field. Figure 6.19 shows a zoomed in portion of figure 6.18 with only the 4σ (Statistic A, this time for comparison) iso-surface plotted.

The over-density is at $z = 0.74$ and it is clearly a galaxy cluster in this R band image. Source 138 on the other hand seems to be more closely associated with a small collection of galaxies at $z \sim 1$. Unfortunately this is the limit of my data cube but there is an over-density of moderate significance (2.0σ) at the position of source 138 at $z = 1.0$. The extended X-ray emission associated with the cluster at $z = 0.74$, to the west of source 138, has likely been missed by *Chandra* because it lies so close to the edge of the various exposures, and actually falls off the edge of most (compare the positions of the green lines in this figure with the squares in figure 6.18).

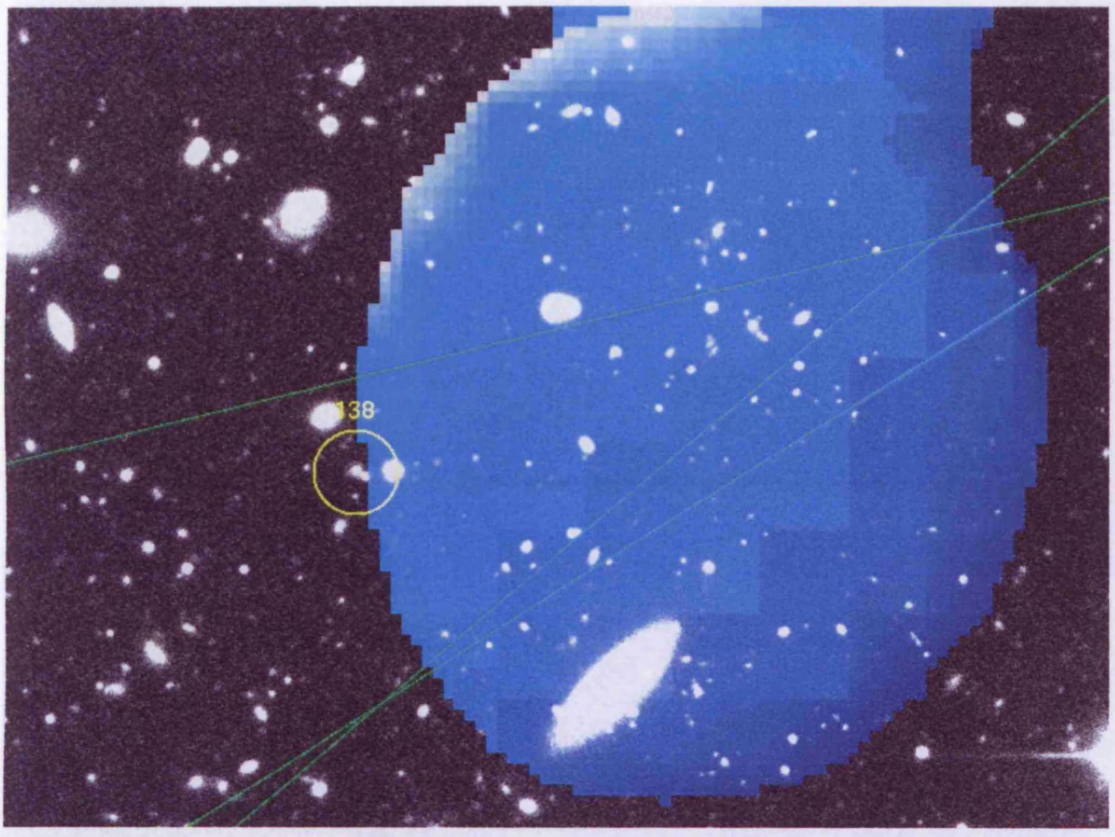

Figure 6.19: Zoomed in portion of figure 6.18 showing the most significant over-density in the CDF-S. The contour here is the 4σ iso-surface produced using statistic A.

6.5.3 XMM-Newton Data

In addition to the 1 Ms *Chandra* exposure there are also a large amount of *XMM* data for this field. In fact, there are over 500 ks of *XMM* data that is publicly available from the archive, made up of 8 separate exposures of varying lengths. This data set is extraordinarily deep for a single *XMM* field and so is invaluable for determining the X-ray properties of the over-densities detected using my data-cube technique.

I retrieved all 8 exposures from the archive and reduced and mosaicked them to form an ultimate image with an equivalent exposure time of 420 ks after removal

of flaring periods. Figure 6.20 shows the final image.

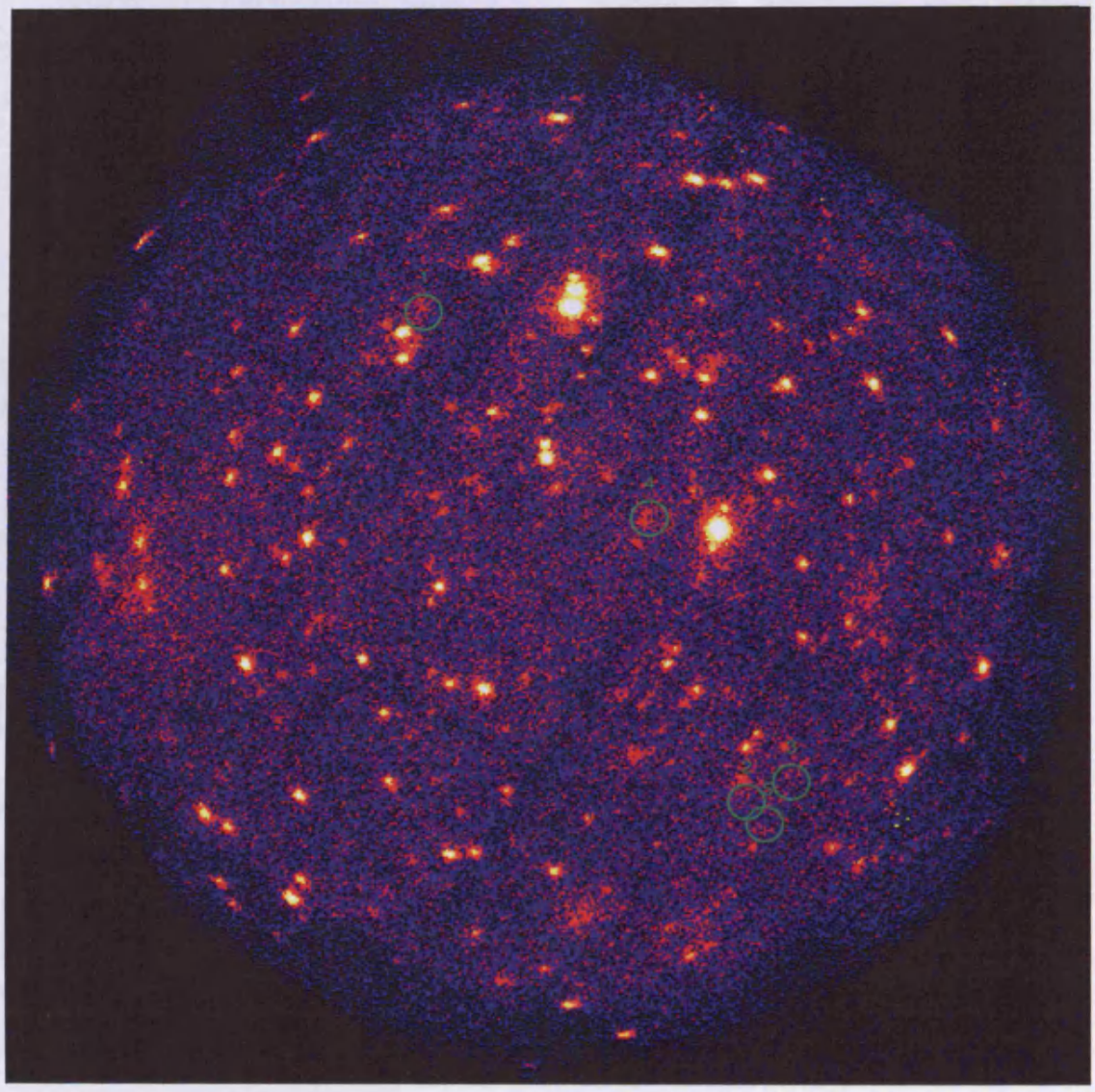

Figure 6.20: *XMM* soft band image of the CDF-S. This image is a mosaic of 8 exposure totalling $\sim$ 420 ks. The green circles indicate the five most significant ($> 4\sigma$ statistic B) galaxy over-densities detected by the data-cube algorithm that lie within $10'$ of the *XMM* exposure centre.

Also shown in figure 6.20 are the positions of the five highest significance over-densities, shown by the iso-surfaces in figure 6.18, that also have *XMM* off-axis angles $< 10'$. Regions 1 and 4 clearly have extended X-ray emission associated with then, while regions 2, 3 and 5 show some evidence for X-ray emission in their

vicinity. Region 4 is equivalent to the *Chandra* extended source 566 (see above).

Using the mosaicked MOS data (used in preference to the PN data due to the many gaps between the PN CCD chips) it is possible to measure the soft X-ray flux of regions 1 and 4, using aperture photometry. I convert photon counts into X-ray fluxes appropriate for the off-axis angle of each source. I then convert the flux into a first guess for the bolometric cluster luminosity, using K-corrections and bolometric luminosity corrections for a range of likely cluster temperatures. Using the $L_X - T_X$ relation for nearby clusters and groups (Osmond & Ponman, 2004) I use this first estimate of the cluster luminosity to estimate a more accurate temperature. Because the bolometric luminosity is only a weak function of cluster temperature this process can be iterated until a robust estimate for the luminosity is obtained (see table 6.2). Figure 6.21 shows that the temperature must be of the order of 2 keV or less for both of these clusters, even being quite conservative about the errors in the luminosity estimates.

This is a rather crude way of calculating the X-ray properties of these clusters and ideally spectral fitting should be employed to be more certain. The fact that this data is composed of 8 separate exposures complicates the issue however, and time did not permit a more thorough investigation. Although, even if I have underestimated the luminosity by a factor of two the temperature for cluster 1 is unlikely to exceed 3 keV, which is consistent with Abell class 0-1 richness.

Figure 6.22 shows the R band COMBO-17 image again, zoomed in on region 1. The contours are from the mosaicked soft band *XMM* data having been lightly smoothed to suppress low level background fluctuations. The cluster is clearly visible as both an over-density of optical galaxies and as a low surface brightness extended X-ray source. The determination of a flux for this cluster is severely

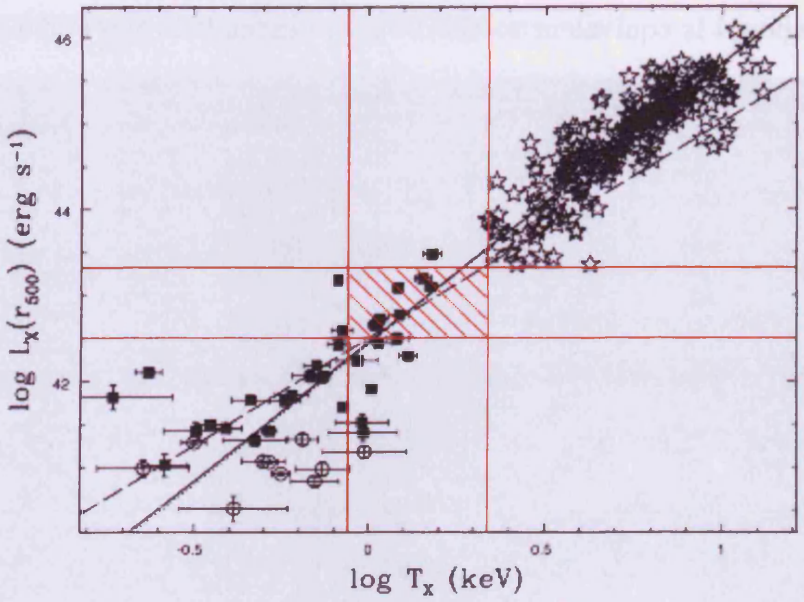

Figure 6.21: Figure 13 from Osmond & Ponman (2004) showing the $L_X - T_X$ relation for galaxy groups and clusters. Groups are shown by squares and circles, clusters by stars. The hatched rectangle shows the approximate area in which regions 1 and 4 from table 6.2 lie.

complicated by the presence of nearby X-ray bright point sources, hence the large uncertainty for this measurement in table 6.2. The core of the X-ray emission is slightly offset from the centre of the galaxy over-density, indicating that the cluster is still young and has not fully relaxed yet.

Figure 6.23 is similar to figure 6.22 but this time centred on cluster 4. The X-ray emission and the centre of the galaxy over-density peak are more closely matched than for cluster 1 but the X-ray emission itself appears less relaxed and is somewhat elongated. Again this suggests the cluster is relatively young.

Cluster 4 - *Chandra* source 566 - has a *Chandra* measured flux of only 1/4 the value I obtain from the *XMM* data. There are two possible explanations for this: either my flux measurement is wrong, or the *Chandra* flux does not take into account the full extent of the emission. The first of these possibilities is unlikely

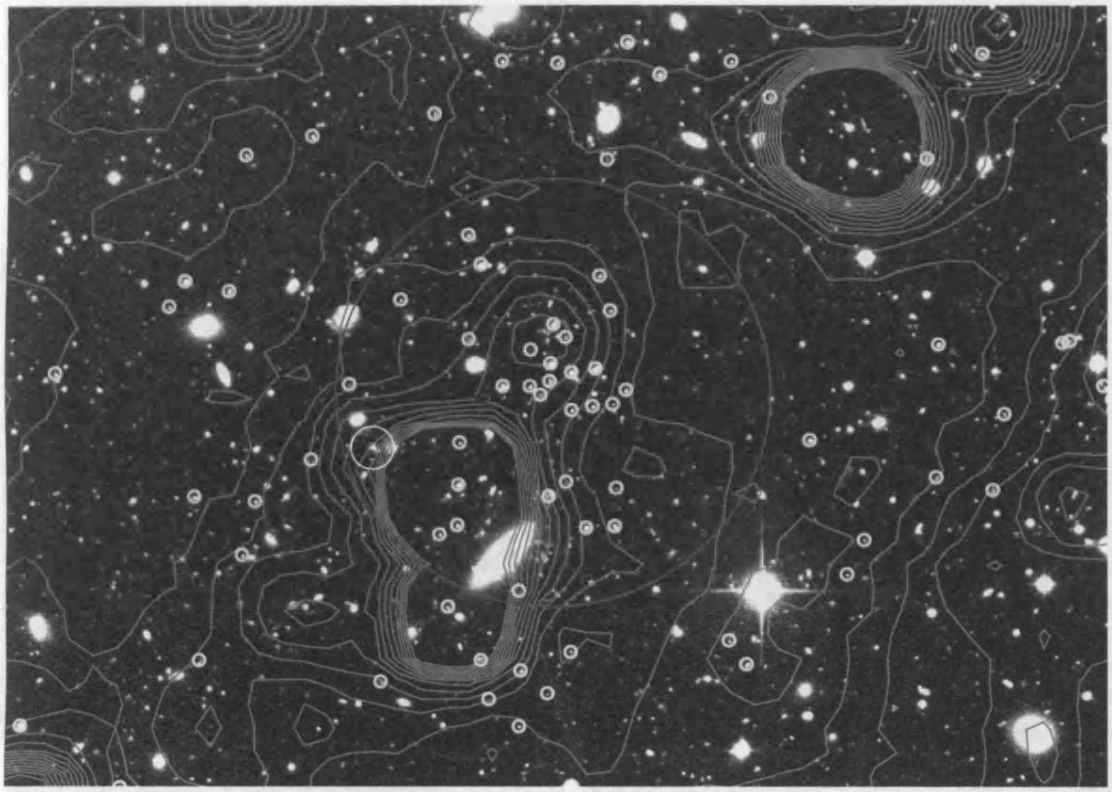

Figure 6.22: *R* band CDF-S image centred on cluster 1. The yellow circles indicate galaxies with redshifts in the range $z = [0.69 : 0.79]$, which brackets the best estimate for the redshift of the cluster, $z = 0.74$. The white circle is the extended *Chandra* source 138. The cyan contours show the soft X-ray emission from both the cluster and the nearby point sources, which are almost certainly AGN. The point sources are very bright and so only the low level X-ray contours are displayed for clarity. The green circle is 0.5 Mpc in physical radius and is centred on the peak of the galaxy over-density.

because I have checked my flux measurements for several bright point sources that appear in the *Chandra* catalogue and my measurements agree to within a few percent with the *Chandra* fluxes. The second possibility is the more likely explanation in this case and is probably a consequence of the narrow *Chandra* PSF and the way in which the source was characterised for the catalogue. Either way, the X-ray luminosity of this cluster is lower than that of cluster 1.

These two regions have X-ray properties that are consistent with low richness clusters or rich groups. The actual optical richness, on the other hand, tells a

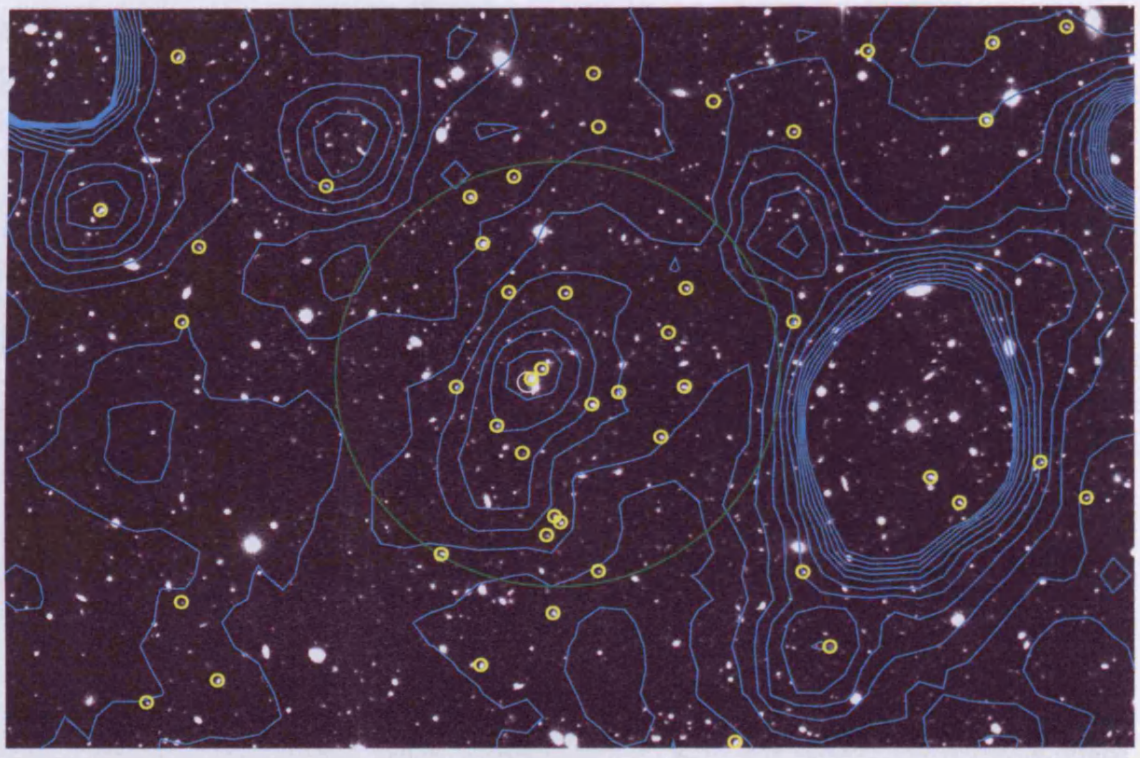

Figure 6.23: As figure 6.22 but centred on cluster 4. The galaxies indicated lie in the range $z = [0.71 : 0.81]$. The small white circle indicates the extended *Chandra* source 566.

different story.

The optical richness in table 6.2 is calculated in the same way as in section 6.3.4, but this time using R band counts down to $R = 23$ and using the following luminosity function parameters from Barr et al. (2003): $M_R^* = -22.08$, $\alpha = -0.89$ and $\phi^* = 0.0072$. The counts have not been corrected for incompleteness in this case so the values of the cluster-galaxy correlation amplitude, B_{gc}, will be minimums. Again, conversions between B_{gc} and Abell richness follow the calibration of McLure et al. (1999), after conversion to my chosen cosmology.

Because of the superior photometric redshifts of the COMBO-17 catalogue I restricted the galaxy counts to $\delta z = 0.05$ either side of the cluster redshift. Altering

Table 6.2: Properties of the over-densities shown in figure 6.20. X-ray limits are listed where it was possible to measure them reliably. The X-ray luminosity is bolometric, having been converted from the soft band flux. The X-ray temperature is an estimate based on the $L_X - T_X$ relation for nearby clusters. The X-ray Abell richness is also an estimate based on nearby clusters. B_{gc} has not been corrected for possible incompleteness. Region 4 corresponds to the *Chandra* source 566.

Cluster	z	L_X (erg s^{-1})	T_X (keV)	Abell$_X$	B_{gc} (Mpc$^{1.77}$)	Abell$_{opt}$
1	0.74	$7 \pm 4 \times 10^{42}$	~ 2	0	621 ± 161	2
2	0.68	-	-	-	415 ± 122	1
3	0.74	-	-	-	514 ± 152	1-2
4	0.76	$4.3 \pm 1.3 \times 10^{42}$	< 2	0	428 ± 151	1
5	0.61	-	-	-	184 ± 74	0

the width of this redshift band to either higher or lower values does not appreciably alter the measurements of B_{gc}, so the results are robust. One point to note here though, is that the proximity of sources 2, 3 and 5 to each other demonstrates the usefulness of the photometric redshift treatment; I have been able to remove possible contamination by the neighbouring regions when calculating the individual measurements, something I would not have been able to do without such good photometric redshifts.

It can be seen from table 6.2 that the richness calculated from the X-ray properties and that calculated from the optical properties are not in agreement for clusters 1 and 4. Add to this the fact that the measurements of B_{gc} here are minimums, since I have not corrected for incompleteness, and it appears that the optical richness is significantly greater than the X-ray properties would suggest.

6.5.4 Implications for X-ray Cluster Searches

The discrepancy between the X-ray and optical properties is intriguing at first sight because it suggests that searches for galaxy clusters using X-ray selection may be

fundamentally flawed. If the optical richness of a cluster is well linked to its mass then estimating the mass from X-ray emission alone will lead to an underestimation for many high redshift clusters. Of course, using X-ray emission to estimate the mass of a cluster requires that the gas is in hydrostatic and thermal equilibrium with the dark matter potential well. If the cluster gas has not yet virialised then the X-ray luminosity will be lower than expected because the density of gas in the core will be lower, and the X-ray temperature will be lower than expected because the virial temperature will not have been achieved. Such occurances will be more common at high redshift where there will be many more dynamically young clusters. The low X-ray luminosity of these still forming clusters will make them hard to detect in more shallow X-ray surveys.

Lower than expected X-ray emission has been observed before in other optically selected cluster samples (e.g. Donahue et al., 2001; Lubin, Oke, & Postman, 2002; Lubin et al., 2004). In some cases the X-ray luminosities of optically selected clusters at $z > 0.5$ are a factor of $3 - 40$ lower than X-ray selected clusters with equivalent velocity dispersions. Part of this effect is likely to be due to the artificially high velocity dispersions measured for the optically selected clusters. A collapsing cluster will have a high in-fall rate so the line of sight velocity dispersion σ will be higher than for an evolved cluster. However, the suppressed X-ray emission will also play a major part; the combination of the high σ and low L_X causes the discrepancy between optically and X-ray selected clusters.

These two effects combine in such a way that high redshift optical clusters do not obey the local $L_X - \sigma$ relation whereas X-ray selected clusters do. Interestingly, both optically selected and X-ray selected high redshift clusters are consistent with the same $L_X - T_X$ relation, so it is only the optical/X-ray relations that are significantly different.

So it seems that X-ray cluster searches will only detect the virialised and more evolved clusters, whereas optical searches will also find the young and unvirialised clusters.

The importance of projection effects can not be underestimated either. Although the space density of galaxy clusters is low there are still occasions when two clusters will lie in the same line of sight. Without redshifts this situation would be impossible to disentangle with either single band optical or X-ray methods. However, obtaining photometric redshifts enables the clusters to be separated, as long as they are further apart in redshift space than the accuracy of the redshift estimates. The X-ray emission on the other hand can never be disentangled though. Therefore, X-ray cluster searches can be well complemented by good multi-band optical photometry to enable situations like this to be spotted.

6.5.5 Future Work

There are a couple of aspects of this work that could do with clarification.

- Is the optical richness measure accurate?
- If it is accurate, how is it calibrated to total cluster mass?
- What are the true X-ray properties of the two clusters discussed in section 6.5.3?

The only way to resolve the first two questions would be to calibrate against known, well studied, clusters over a range of X-ray luminosities, optical richness and redshift. The clusters discussed here are relatively low mass, low richness,

low luminosity systems, however you look at them, so it would be interesting to perform a similar analysis on much more massive clusters. The third question can be resolved by thorough X-ray spectral analysis, which is something that time did not permit me to do. Although the proximity of bright point sources may make this difficult for COMBO-17 cluster 1.

If my evaluation of optical richness is wrong leading to an overestimate of the Abell class of a cluster, and if the estimated X-ray luminosities are too low then the true X-ray and optical properties of the COMBO-17 clusters will actually be more closely matched than I have suggested. However, I do not believe that the results would change enough to alter the conclusion that the clusters found using my data cube algorithm are X-ray under-luminous.

Chapter 7

The Environments of AGN

7.1 Introduction

Chapter 5 is concerned with calculating the 2-point auto-correlation function of the AGN in my two *XMM* fields. The main aim there was to determine how AGN cluster together, which indirectly also gives an indication as to the typical environments the AGN in question reside in. In this chapter I take a different approach by looking more directly at the Mpc scale environments around a selection of individual AGN in my surveys.

Studying the environments of AGN has many motivations, including providing constraints on galaxy evolution models and how well AGN trace the normal galaxy distribution. The motivation here, however, is to determine the relative importance of various possible fuelling mechanisms that could power the activity in a central engine. For example, does the Mpc scale environment of a galaxy induce the AGN phenomenon somehow, or is the region immediately surrounding the supermassive

black hole (SBH) in a galactic nucleus responsible for the onset of an AGN burst? Although discovering the exact details of the fuelling mechanism of any given AGN is beyond this study, it can certainly help to narrow down the possibilities from the vast array of theoretical models proposed thus far. By comparing the environment of AGN against a control sample of otherwise normal galaxies, differences may indicate a fundamental property of galactic nuclei that causes them to be active rather than inactive.

7.1.1 Fuelling Mechanisms

As Lake, Katz, & Moore (1998) put it, there are three distinct problems regarding the fuelling of an AGN: the first involves moving gas from the galactic scale into the central few hundred pc; secondly, the instabilities of a self gravitating disc that further compact the gas until it forms an accretion disc around the central SBH; and finally the accretion processes that enable the gas to finally be lost forever from normal space. The study of the environments of AGN aims to understand the first process, by which the fuel supply is made available to the SBH through gas transport on galactic scales. For this reason I shall ignore smaller scale processes, such as disc instabilities and galactic bars, to mention just two of the many possibilities suggested for the second fuelling mechanism.

Various mechanisms proposed in the literature make definite predictions about the nature of the environments of AGN. I briefly summarise some of those mechanisms and predictions here:

- Interactions/major mergers: This model involves two comparably sized galaxies interacting though their mutual gravitational attraction, leading to the

amalgamation of the two central SBHs with large quantities of gas being driven inwards to fuel the resulting central engine (e.g. Kauffmann & Haehnelt, 2000). The QSO produced from this will reside in a massive elliptical host, most likely in a high density environment where mergers are more common. It also correctly predicts the observed space density of QSOs that is seen to peak at $z \sim 2$. Although a successful model in predicting both the morphology and environments of very luminous QSOs (e.g. McLure et al., 1999; McLure & Dunlop, 2001) it does not explain fainter AGN that are found in spirals as well as ellipticals. If major mergers were responsible for lower luminosity AGN then many more host galaxies should be observed to have disturbed morphology or signs of recent interactions, which does not seem to be the case either (e.g. Grogin et al., 2003).

- Minor mergers: For AGN of lower than QSO luminosity, such as Seyferts, it has been proposed that mergers of small companion galaxies (SMC or smaller) may induce nuclear activity in gas rich hosts (de Robertis, Yee, & Hayhoe, 1998). This is particularly relevant to my study here as I specifically concentrate on lower luminosity AGN (see section 7.2). Predictions for this model include undisturbed hosts and no need for significantly different environments (in terms of bright galaxies) from those of comparable field galaxies. However, detecting such small companions around anything other than a nearby galaxy is problematic, so direct observations of the small companion frequency of high redshift AGN are unlikely to be made any time soon.

- Harassment: Originally proposed by Moore, Katz, & Lake (1996) to explain the morphological evolution of galaxies in rich clusters, it has also been suggested as an AGN fuelling mechanism (Lake et al., 1998). The mechanism

is instigated by the numerous high speed interactions that a relatively small disc galaxy experiences while travelling through a cluster. Rather than the cataclysmic, but relatively slow, interactions experienced by two galaxies undergoing a merger in the field, the higher speeds at which galaxies fly past one another in a cluster causes a member galaxy to be jiggled around but otherwise remain largely unchanged. Dynamical instabilities induced by this "galaxy harassment" channel gas into the central few kpc of sub-L_* galaxies, where it becomes available as fuel for an AGN. Relatively new additions to the cluster, i.e. In-falling galaxies, are more likely to have large gas reservoirs and so are more likely to host an AGN. Clearly, predictions of this mechanism include the presence of a relatively rich cluster, with the AGN either in the periphery or in the process of falling in towards the cluster. Söchting, Clowes, & Campusano (2004) present some evidence that this may be the case for low-z quasars, with nearly half of their $z < 0.3$ sample being found within $1-3\ h^{-1}$ Mpc of a cluster centre. Harassment also predicts that hosts should show slightly disturbed morphologies but not be totally disrupted.

- Cooling flows: Clusters of galaxies contain a hot intra-cluster gas that tends to be many times as massive as the cluster galaxies themselves. This provides a potentially huge reservoir of fuel for an AGN residing in a central cluster galaxy (Fabian et al., 1986), if it were to experience a radiative loss of energy and hence fall in towards the centre of the cluster - a cooling flow. Again, clear predictions can be made for this mechanism, such as the relative fraction of AGN found in clusters undergoing cooling flows. However, this mechanism can only really be applied to AGN in central cluster/group galaxies and does not fully satisfy all the observations of cluster AGN (Hall, Ellingson, & Green, 1997).

The above list is by no means exhaustive but it gives a brief example of the variety of theoretical models on offer to explain the AGN phenomenon. Of course many mechanisms proposed to fuel AGN can be equally applied to a nuclear starburst and in reality different mechanisms are likely to be more important for different classes of AGN. As always, it is a complex problem without a single simple answer.

7.1.2 Previous Work

In general, most of the previous investigations into the environments of AGN concern optically or radio selected QSOs. Radio-loud QSOs are now almost universally acknowledged to lie in over-dense regions, typically clusters of Abell 0/1 richness, across a large range in redshift (e.g. Wold et al., 2000; McLure & Dunlop, 2001; Barr et al., 2003); whereas there is still some disagreement over whether the same is true for radio-quiet QSOs. Wold et al. (2001) and McLure & Dunlop (2001) find no significant difference between the environments of matched samples of radio-loud and radio-quiet QSOs while Smith, Boyle, & Maddox (2000), amongst others, claim that radio-quiet QSOs are no more likely to be found in rich environments than non-active galaxies. However, differences between the various techniques and survey designs employed by different workers are likely to play some part in the discrepancies.

Söchting et al. (2004) employ a somewhat different technique to analysing the environments of AGN by looking at the relative positions of QSOs with respect to the large scale structure traced out by clusters and super-cluster structures in the same redshift slices. They claim that their sample of QSOs follows the large scale structure, so that QSOs are more likely to be found in the vicinity of a

cluster or in the confluence of a merging cluster system. This implies that despite not always residing in rich clusters, QSOs are nevertheless useful tracers of large scale structure. Similarly, Barr et al. (2003) claim that radio-loud QSOs can be employed as efficient tools for detecting high redshift galaxy clusters as they are often found together in the same fields; although they do warn that many of the earlier studies are likely to be biased in their calculations of QSO environmental richness because QSOs are rarely found directly in the centres of over-densities.

At lower AGN luminosities optically selected Seyfert galaxies seem much less likely to be found in rich environments. de Robertis et al. (1998) analyse a sample of Seyfert galaxies and find no significant difference between the environmental richness, or the probability of finding a close companion galaxy, compared to a matched sample of non-active galaxies. Although they do find a difference between the environments of the Seyfert 1 and Seyfert 2 sub-samples with Seyfert 1s being in poorer environments; an observation that they cannot explain in terms of the Unified Model of AGN, which predicts that there should be no difference in the environment of these two AGN classes.

In all the above cases the sample sizes have been necessarily small (typically several tens of QSOs) because of the limitations in performing large numbers of pointed observations, especially if the sample is at high redshift (see table 1 of Brown, Boyle, & Webster (2001) for a summary of a sample of studies of AGN environments). The situation at low redshifts ($z < 0.1$), however, is now somewhat alleviated by large spectroscopic surveys such as the Sloan Digital Sky Survey (SDSS) or 2df Galaxy Redshift Survey, which include many thousands of AGN. Despite this plethora of data different studies still disagree to some extent on some details of the environments of AGN. Miller et al. (2003) find essentially no change in the fraction of galaxies with an AGN, across nearly two decades in environmental

density. Of the nearly 5000 galaxies studied $\sim$ 40% showed some sign of nuclear activity, the fraction remaining constant with density. Star-forming galaxies, on the other hand, behave very differently, with a clear trend increasing towards more rarefied environments - the so called SFR-density relation. Passive galaxies, of course, are found in greater abundances in denser environments. Such a high, and constant, fraction of galaxies containing an AGN rather suggests that the fuelling mechanism for these lower luminosity objects (mostly LINERS, the most common and lowest luminosity AGN class) is a frequent occurrence, and common to a large range of environments. Major mergers therefore seem highly unlikely as a fuelling mechanism in this scenario, as do any other cluster related mechanisms, which will not be nearly common enough to produce such a high AGN fraction; although this does not preclude the possibility that rarer, high luminosity, AGN are fuelled by such mechanisms.

Kauffmann et al. (2004) also use the SDSS data to study environmental relations, including AGN fractions. They find a somewhat different result from Miller et al. (2003) in that twice as many galaxies host AGN in low density environments as in high, a trend they attribute to the fact that AGN and star-formation are related in some way. However, their classification of AGN differs to that of Miller et al. (2003), which is probably the source of this discrepancy. Kauffmann et al. (2004) only study AGN with O[III] luminosities $> 10^7\ L_{\odot}$ (total fraction $\sim$ 0.1), whereas Miller et al. (2003) are less strict, resulting in the higher overall (lower luminosity) AGN fraction.

7.1.3 Unbiased Tracers of AGN

As Miller et al. (2003) point out, different types of AGN reside in different host galaxies: radio-loud galaxies in ellipticals, Seyferts in spirals, for example, and so any tend in environmental density experienced by a particular galaxy type will necessarily result in the same trend being true for the class of AGN that resides in that host type. Since most of the AGN in the Kauffmann et al. (2004) study are type 2 Seyferts it is hardly surprising that galaxies in low density environments demonstrate a higher fraction of AGN in this case.

And herein lies the problem. Any search for AGN is likely to be biased in some way towards a particular class depending on the selection criteria. Radio selected AGN samples, for example, will preferentially select radio-loud AGN, which are clearly not the most common type of AGN and suffer from feedback with the surrounding environment, making them highly biased examples of AGN in general. Optically selected samples can also suffer from selection effects, depending on the quality of the spectroscopy and the criteria used to distinguish AGN from non-active galaxies. Miller et al. (2003) goes some way towards resolving this problem with the very large and high quality SDSS data set and by applying careful analysis to the separation of galaxies into AGN, star-forming or passive, using several emission lines.

In general, the narrow [OIII] emission line seems to be a pretty unbiased tracer of AGN activity, as it originates from beyond the obscuring torus and so is unaffected by the orientation effects that can bias other AGN emission lines. However, at higher redshifts this line becomes harder to detect in weak AGN as more of the galaxy light falls into the slit or fibre aperture, washing out the nuclear light. This problem does not affect the X-ray emission from AGN, however. X-

ray surveys are very observationally efficient at finding AGN over a wide range in redshift. Hard X-ray luminosity in particular is also a highly unbiased measure of AGN power, as the only thing that is being probed is the accretion rate of the SBH itself; the details of the exact AGN type and viewing angle are unimportant (due to the penetrating power of hard X-rays) and therefore does not bias the sample selection. The fairly tight correlation between hard X-ray and [OIII] luminosity (Xu, Livio, & Baum, 1999) indicates that the same physical process is responsible for both, namely the accreting SBH, and that hard X-rays are at least as unbiased as [OIII] when it comes to selecting AGN.

Hard X-ray emission is an excellent tracer of AGN activity because it is difficult for anything other than a SBH to generate X-ray luminosities in excess of 10^{42} erg s^{-1}. Hard X-rays are also affected far less by intrinsic absorption than soft X-rays and can penetrate large column densities of intervening neutral hydrogen (up to $\sim 10^{23}$ cm^{-2}) that would essentially completely absorb photons of energy less than 2 keV. Of course, nothing is perfect and for extremely high column densities, resulting in Compton thick obscuration ($N_H \sim 1.5 \times 10^{24}$ cm^{-2}), even hard X-rays are absorbed. But for the purposes of this study I shall ignore Compton thick AGN, with the assumption that they constitute a relatively small fraction of the total population (see Ueda et al. (2003) for a discussion of the Compton thick contribution).

With a large catalogue of X-ray selected AGN, also covered by deep optical data, my *XMM* surveys are ideally suited to the study of AGN environments. Aside from the benefits offered by X-ray selection, the addition of photometric redshifts gives a further advantage over studies that rely on a single optical filter for their galaxy counts. Although the final sample analysed here is not large (see section 7.2), the principles described in the rest of this chapter can be easily

extended to much larger samples; something that is becoming increasingly possible as data from more large area, deep surveys are made publicly available.

7.2 Selection of AGN Sample

The selection of the AGN sample requires careful consideration, in order to avoid uncertainties leading from degeneracies in redshift and luminosity, for example. In any flux limited survey, such as my *XMM* surveys, an inevitable correlation arises between redshift and luminosity; at low redshift the survey does not sample large volumes and so only the most numerous, low luminosity objects are detected; at high redshift, large volumes are sampled but only the most luminous objects are bright enough to be detected. Therefore, if I wish to study potential correlations between clustering amplitude and luminosity, or clustering amplitude and redshift, then I must select my sample accordingly so that the trends associated with one effect are not confused with those caused by the other.

Because of the nature of my *XMM* surveys it is impossible to select a sample of similarly luminous AGN over a range of redshifts, to study the redshift evolution of the clustering amplitude. Therefore, I concentrate on the relation between clustering amplitude and luminosity at constant redshift, which is more suitable for my surveys.

To be able to reduce the error introduced by uncertain background and foreground number counts, as well as reducing uncertainties in luminosity, I require the best possible photometric redshift estimates for both the AGN and the surrounding field galaxies. Therefore, I restrict this analysis to only the 14-h field, which has more accurate photometric redshifts than the 3-h field (see also section 6.3.1). The

photometric redshifts are also most accurate for $z < 0.6$, so to maximise the number of sources in my sample (because the redshift distribution peaks at $z \sim 0.7$), while maintaining a narrow enough range to minimise redshift/luminosity correlations, I select sources in the range $0.4 \leq z \leq 0.6$.

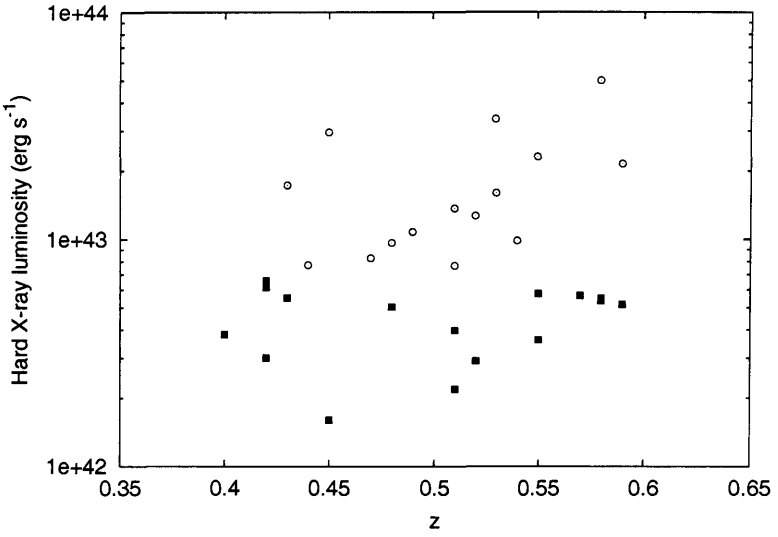

Figure 7.1: Luminosity vs. redshift for the 31 AGN in my environment sample. The full sample is split into two sub-samples divided by luminosity: Filled squares, low luminosity (16 objects); open circles, high luminosity (15 objects).

Figure 7.1 shows the final sample of 31 AGN plotted with hard X-ray luminosity versus redshift. I split the full sample into two sub-samples, based on luminosity, to test for any redshift/luminosity correlation; 16 sources are in the low luminosity sample, 15 are in the high luminosity sample. A Kolmogorov-Smirnov (K-S) test on the redshift distribution of the two sub-samples returns a statistic $P = 0.652$, which implies that there is a probability $S = 0.348$ ($S = 1 - P$, where P is the standard statistic returned from a K-S test) that the two samples are *not* drawn from the same population (both have a median $z = 0.51$), so I have satisfied my condition of minimising any redshift/luminosity correlation. Figure 7.2 demonstrates that for the redshift range I consider here I am analysing AGN that populate the break in the hard X-ray luminosity function. This is important because the break in any

luminosity function with a shallow faint end slope ($\alpha < 1$) constitutes the peak in luminosity density. Therefore, sources near the break effectively contribute more to the luminosity density of the population than either lower or higher luminosity sources. In a sense, they represent the 'average' sources in a population.

All but one of the 31 sources in this sample lie above the $log(f_X/f_I) = -1$ line in figure 4.2 (source 14.144 lies just below), confirming that they are highly likely to be AGN rather than starburst galaxies. Starbursts also typically have upper limits on their hard X-ray luminosities of $\sim 10^{41}$ erg s^{-1}, safely below the lower limit for my AGN sample.

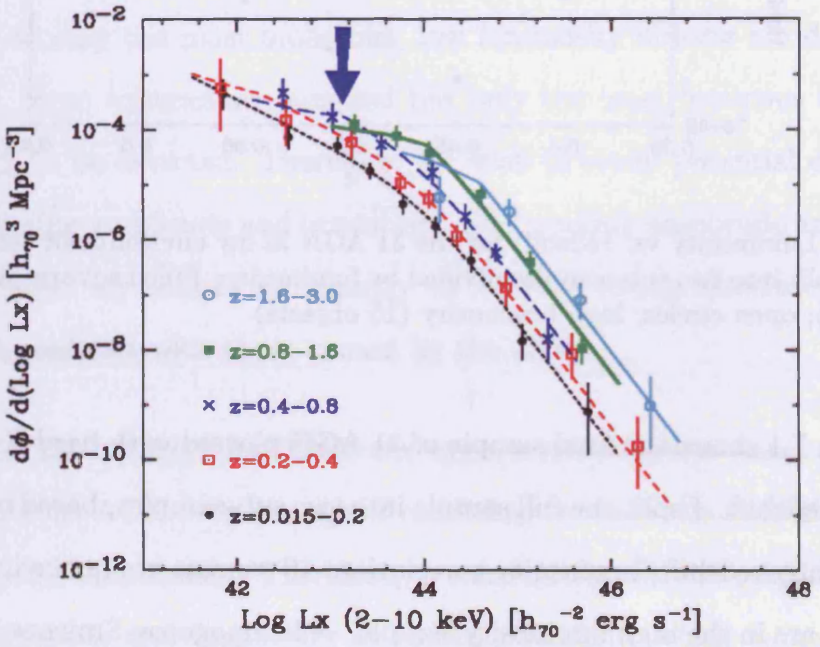

Figure 7.2: Hard X-ray luminosity function, from Ueda et al. (2003). The blue arrow indicates the 'knee' of the luminosity function for the redshift range encompassing my AGN sample. Sources near the break in any luminosity function contribute the greatest amount to luminosity density and so are important to study. The AGN in my sample straddle the break, within about one decade in luminosity, and so are well representative of the 'average' AGN.

7.3 Calculation of B_{gq}

The measurement of the clustering amplitude is essentially identical to the method used in Chapter 6 for the over-density at $z = 0.88$, with one minor difference. To summarise: the number of galaxies within 0.5 Mpc and $dz \leq 0.1$ of each AGN are counted (discounting the AGN itself) and compared to the number expected for the background, as calculated from the total number of galaxies in the same redshift range for the whole CFDF catalogue. The main difference between this study and that of chapter 6 is that here only galaxies with $I_{AB} < 23$ are counted, rather than the limit $I_{AB} < 24$ as used in chapter 6. The reason for this is that a compromise must be reached between counting galaxies to too bright a limit, resulting in low counting statistics, and counting to too faint a limit, which causes large uncertainties resulting from a high background count. A suitable range of $M^* + 1$ to $M^* + 3$ has been suggested by Yee & López-Cruz (1999) to optimise the calculation of B_{gq}, however, I can afford to go slightly deeper because I use photometric redshift cuts to improve the contrast of the AGN regions against the background counts. Using the luminosity function from Barr et al. (2003) ($M_I^* = -22.65$, $\alpha = -0.89$ and $\phi^* = 0.0052$), I reach $M^* + 3.9$ at $z = 0.4$ and $M^* + 2.8$ at $z = 0.6$ using a limit of $I_{AB} < 23$ (for a Sbc galaxy template). It is prudent to note here that varying the magnitude limit by ± 1 does not appreciably change the results, which suggests that the shape of the assumed LF is indeed suitable for this analysis. Choosing a limiting magnitude of $I_{AB} < 23$ also reduces the effect of incompleteness in the reduced, good photometric redshift, CFDF catalogue.

7.3.1 Control Sample

A big advantage that the CFDF catalogue has over other similar studies of AGN environments is that it is a contiguous patch of sky, with many field galaxies from which to get a reliable estimate of background galaxy counts. A further advantage is afforded by the availability of a large number of galaxies that can be used as a control sample against which the AGN sample can be compared. For this study I use all galaxies in a $15' \times 15'$ square in the centre of the CFDF map (to avoid edge effects), in the redshift range $z = [0.4 : 0.6]$ and with magnitudes $I_{AB} < 23$, as the control sample. I calculate B_{gg} for the resulting 820 galaxies in exactly the same way as I calculate B_{gq} for the AGN sample. A second control sample is extracted from the first, as an additional check, so that the distribution of I_{AB} magnitudes matches that of the AGN sample more closely (final K-S result of $P = 0.871$ for the 297 galaxies, rather than $P = 0.011$ for the full control sample). This second sample has a higher proportion of brighter galaxies than the full control sample and was selected by randomly removing fainter galaxies until it resembled the AGN sample I_{AB} distribution. This reduced control sample also follows the redshift distribution of the AGN sample more closely too, with $P = 0.932$ c.f. $P = 0.187$ for the full control sample. For the rest of the discussion this reduced sample will be referred to as the 'well matched control sample'.

7.3.2 Correction for Incompleteness

I correct for incompleteness in the reduced CFDF catalogue in the same way as in section 6.3.5; that is, any difference between the reduced (good photo-z) and full catalogue is corrected for by multiplying the number of galaxies of a given magnitude by the required factor to bring the number up to that expected from the

full catalogue. At most this difference is a factor of 1.5 for magnitudes in the range $I_{AB} = [22.5 : 23]$. Both the counts around the AGN and the background counts are corrected for in the same way. In general, correcting for incompleteness enhances both under and over-densities but as long as the control sample is analysed in an identical fashion to the AGN sample then the details of the correction should not adversely affect the results. In fact the same is true for the exact details of the assumed LF; as long as the control samples use the same LF as the AGN sample then the absolute measure of clustering amplitude is unimportant, it is the *relative* clustering amplitudes that reveal the important facts.

7.4 Results

Table 7.1 shows the results for both A_{gq} and B_{gq} for the AGN sample. Figure 7.3 shows these same results plotted with B_{gq} vs. hard X-ray luminosity. Additionally, the mean values for the two AGN sub-samples and the field galaxy sample are also plotted and are tabulated in table 7.2

Notice how the well matched control sample has a slightly higher clustering amplitude than the full control sample, due primarily to the higher proportion of relatively brighter galaxies in the matched sample. However, the difference between the environments of the two control samples is not really significant and does not make any qualitative difference to the final results.

Table 7.1: Results of the clustering amplitude for the 31 AGN in the range $0.4 \leq z \leq 0.6$. Luminosity is measured in the hard X-ray band ($2 - 10$ keV). Low and high luminosity sub-samples are divided by the horizontal line.

XID	z (BPZ)	Luminosity (erg s^{-1})	A_{gq}	B_{gq} (Mpc$^{1.77}$)	ΔB
94	0.40	0.381E+43	0.200E-03	32.8	69.0
37	0.42	0.301E+43	0.713E-03	117.4	75.1
106	0.42	0.657E+43	0.691E-04	11.4	68.0
153	0.42	0.614E+43	-.286E-03	-47.0	63.7
75	0.43	0.553E+43	0.106E-02	176.9	79.5
144	0.45	0.160E+43	0.459E-03	81.7	76.4
132	0.48	0.550E+43	0.194E-02	400.0	100.8
137	0.51	0.504E+43	-.735E-04	-15.4	77.3
88	0.51	0.398E+43	0.609E-04	12.7	79.3
148	0.52	0.219E+43	-.129E-03	-26.7	76.5
64	0.55	0.292E+43	0.594E-04	12.2	80.0
86	0.55	0.517E+43	-.965E-03	-197.9	62.3
112	0.57	0.361E+43	0.174E-03	35.0	81.6
118	0.58	0.577E+43	0.595E-03	117.9	87.7
89	0.58	0.566E+43	-.109E-04	-2.2	78.6
133	0.59	0.536E+43	0.440E-03	85.3	85.1
18	0.43	0.173E+44	-.268E-03	-44.7	64.4
31	0.44	0.771E+43	0.370E-03	63.6	73.5
12	0.45	0.296E+44	0.731E-03	130.1	79.6
28	0.47	0.827E+43	0.255E-04	5.1	75.5
27	0.48	0.965E+43	0.353E-03	72.8	81.6
117	0.49	0.108E+44	0.206E-03	43.0	80.5
92	0.51	0.765E+43	0.647E-03	135.3	87.6
8	0.51	0.137E+44	0.665E-03	138.9	87.8
128	0.52	0.127E+44	-.343E-04	-7.1	78.0
38	0.53	0.160E+44	0.134E-04	2.8	78.3
127	0.53	0.339E+44	0.410E-03	84.0	84.1
149	0.54	0.987E+43	0.456E-03	93.5	85.3
17	0.55	0.231E+44	0.629E-03	129.0	88.4
32	0.58	0.500E+44	0.327E-03	64.8	83.8
147	0.59	0.215E+44	0.533E-03	103.5	86.4

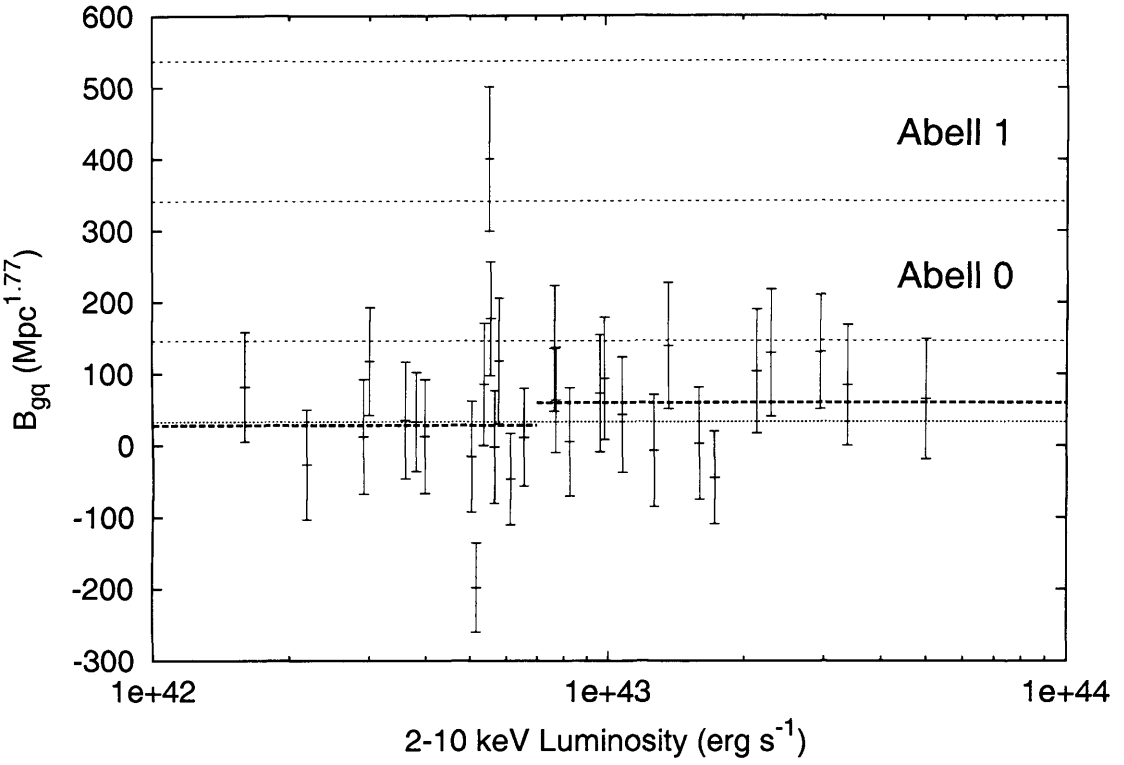

Figure 7.3: Clustering amplitude of galaxies in the vicinity of 31 AGN in the 14-h field (see tables 7.1 and 7.2). The thin dotted line at $B_{gq} \sim 35$ Mpc$^{1.77}$ is the mean value for 820 field galaxies, drawn from the same redshift range as the AGN sample and analysed in an identical fashion. The thicker, short-dashed lines show the mean values for the two sub-samples of AGN: left, low luminosity; right, high luminosity. Regions corresponding to Abell richness classes 0 and 1 are delineated by the dotted lines at 146, 341 and 537 Mpc$^{1.77}$; class 2 lies above the top line (values taken from McLure & Dunlop (2001) and re-scaled to match my chosen cosmology).

7.4.1 Kolmogorov-Smirnov Tests

The first thing that is obvious from these results is that the AGN sample is not significantly different from that of either control sample. To formalise this I perform K-S tests on each of the sample pairs listed in table 7.3. As table 7.3 shows the AGN sample is *indistinguishable* from the field galaxy population, in both its full control and well matched control forms.

The very slight hint of a correlation between AGN luminosity and environment,

Table 7.2: Results for the clustering amplitude B_{gq} in $\mathrm{Mpc}^{1.77}$.

Sample	Weighted mean	Median	Straight mean
820 control galaxies	36.6 ± 2.7	44.9	53.3
297 well matched control	42.9 ± 4.5	54.5	61.0
All 31 AGN	42.5 ± 14.0	63.6	58.3
16 low luminosity AGN	28.1 ± 19.0	22.8	49.6
15 high luminosity AGN	59.7 ± 20.7	72.8	67.6

Table 7.3: K-S tests to determine if the clustering amplitudes for the AGN are drawn from a different population to the field control samples. Here P is the standard statistic returned from a K-S test and $P = 1 - S$, where S is the probability that the two samples are not drawn from the same population. In all cases the null hypothesis, that the AGN and field samples are drawn from the same population, cannot be rejected (requires $P < 0.05$, for the null hypothesis to be rejected at the 5% level).

Samples		P
Full control	All AGN	0.703
Full control	Low AGN	0.713
Full control	High AGN	0.292
Matched control	All AGN	0.427
Matched control	Low AGN	0.592
Matched control	High AGN	0.412
Low AGN	High AGN	0.216
Matched control	Full control	0.862

when the AGN sample is split into sub-samples, is not significant at all. These results are consistent with all the various samples being drawn from the same parent population.

7.5 Close Companions

So it seems from the clustering amplitude analysis that the Mpc scale environments of moderate luminosity AGN are essentially the same as those of non-active galaxies. In this section I investigate the possibility that tidal interactions with nearby

galaxies are important as fuelling mechanisms for these AGN. Again, I compare the AGN sample to the two control samples described in section 7.3.1.

For this analysis I extend the magnitude range of the search to $I_{AB} < 24$, so one magnitude fainter than the clustering amplitude analysis i.e. $M^* + 4.9$ at $z = 0.4$ and $M^* + 3.8$ at $z = 0.6$ (similar to the SMC and LMC). I also neglect the effects of completion here because I am making a direct comparison between samples that should be affected in an identical way, and therefore an absolute measure is unnecessary. Other than that the only difference between this and the clustering amplitude analysis is the radius within which galaxies are counted.

Table 7.4 shows the number of galaxies found within a given radius of galaxies in the AGN and control samples. It is clear that the environments of AGN host galaxies are very similar to those of inactive galaxies on all the scales investigated here.

Breaking the two smallest scales down further, figure 7.4 shows the distribution of the frequency of different numbers of companion galaxies. At these scales the number of companion galaxies is small but the AGN sample has essentially the same distribution as that of the well matched control sample, and the same is true of the larger scales.

So this appears to support the conclusions of de Robertis et al. (1998), in that the likelihood of finding a companion galaxy with $R < -17.5$ within 50 kpc of a Seyfert galaxy is not statistically different from that for an inactive galaxy. AGN with sub-quasar luminosities have essentially identical environments - from 30 kpc up to 0.5 Mpc - to those of 'normal', inactive galaxies.

Table 7.4: Mean number of companion galaxies for the various samples, counted within different radii ($dz \leq 0.1$, $I_{AB} < 24$). Errors are Poisson uncertainties. The AGN sample and control samples are all remarkably similar from 30 kpc to 0.5 Mpc

	Counting Radius (kpc)				
Sample	30	50	100	250	500
Full control	0.14 ± 0.01	0.43 ± 0.02	1.61 ± 0.04	9.85 ± 0.11	38.3 ± 0.2
Well matched	0.14 ± 0.02	0.47 ± 0.04	1.79 ± 0.08	10.2 ± 0.19	40.2 ± 0.4
All AGN	0.07 ± 0.05	0.35 ± 0.11	1.45 ± 0.22	9.65 ± 0.56	39.5 ± 1.1
Low AGN	0.00 ± 0.00	0.19 ± 0.11	1.44 ± 0.30	8.56 ± 0.73	38.0 ± 1.5
High AGN	0.13 ± 0.09	0.53 ± 0.19	1.47 ± 0.31	10.8 ± 0.85	41.1 ± 1.7

7.6 Discussion

7.6.1 Implications for AGN Fuelling Mechanisms

My sample of AGN is not particularly large and so the uncertainties may hide any significant difference that really does exist between the environments of active and non-active galaxies. However, on the basis of my results I can draw some conclusions as to how the AGN in my sample are likely to be fuelled.

The typical environments of my AGN sample are no different to those of inactive galaxies in general. Aside from one example, all the AGN are found in sub-cluster richness regions, in contrast to the studies of high luminosity AGN, such as radio-loud QSOs. Therefore, any fuelling mechanism requiring the presence or proximity of a rich cluster is unlikely to be important for fuelling lower luminosity AGN. Harassment (Lake et al., 1998), for example, may be an efficient method of transporting gas into the central 500 pc of a gas rich galaxy but it requires that galaxy to be situated in the outskirts of a rich cluster. This is clearly not the case for the vast majority of AGN, which exist far from the influence of clusters and, in a purely numerical sense, harassment is simply not capable of causing up to 40%

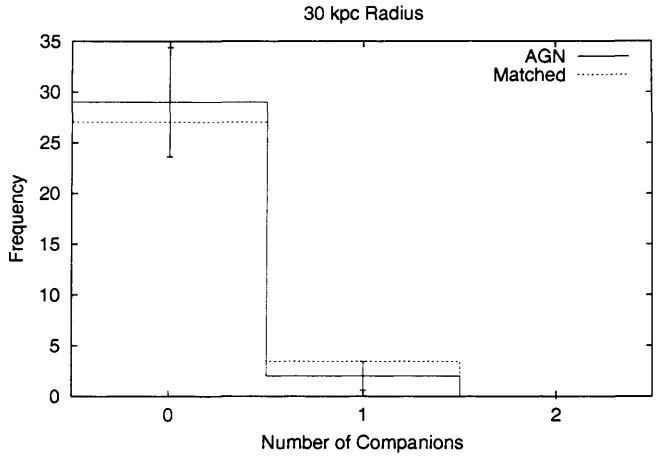

(a)

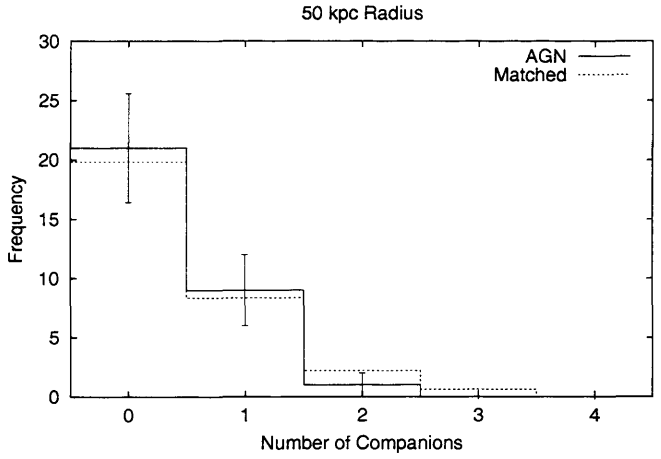

(b)

Figure 7.4: Histograms of the number of companion galaxies found within 30 kpc (7.4(a)) and 50 kpc (7.4(b)) of the galaxies in the AGN sample. The well matched control sample (scaled to match the AGN sample) is shown for comparison as the dashed histograms. Error bars on the AGN sample are Poisson uncertainties. An AGN host is no more or less likely to have a close companion than an inactive galaxy.

of all galaxies to be active at any given time (Miller et al., 2003).

As mentioned earlier, major mergers seem equally unlikely as a fuelling mechanism for the lowest luminosity AGN, especially given the high fraction of galaxies

that contain one; and even for the AGN in my sample, which are typically more luminous and therefore [$\sim$ 10 to 40 times] less common than those in Miller et al. (2003), this mechanism appears to be unimportant. Although I haven't performed any asymmetry analysis on the host galaxies of my AGN sample (to look for signs of recent major mergers or tidal interactions), Grogin et al. (2003) find that the AGN in the CDF-S (roughly comparable to the luminosities of the AGN in my sample) are no more asymmetric than the field galaxy population, suggesting that they are not under the influence of a recent merger or tidal interaction. Grogin et al. (2003) also investigate the near neighbour frequency of both the active and non-active galaxies in that field and essentially confirm my result, that there is no significant difference between the two populations. de Robertis et al. (1998) also confirm both these results for Seyfert galaxies, which typically have hard X-ray luminosities in the range of my AGN sample.

But could I be missing really close companions in my near neighbour analysis and therefore be making an inaccurate statement as to the similarity of the active and non-active samples? My close companion search is limited to $I_{AB} < 24$ (the median magnitude for the AGN sample is $I_{AB} = 21.1$ so they are brighter than most of the potential companion galaxies) and at this faint magnitude limit incompleteness accounts for the loss of over half the galaxies from the reduced CFDF catalogue, which I use in this analysis. Conceivably, most of these losses could be the nearest companions of brighter galaxies. At close proximity the photometry of a faint galaxy could be contaminated by light from its brighter neighbour, leading to an unreliable photometric redshift and its subsequent rejection from the catalogue. Therefore, if one sample in the analysis has a real excess of close, faint companions relative to another sample, then this difference will be suppressed by the preferential loss of those close companions from the catalogue. However, I

believe this possible observational bias is not present in this case for the following reason:

The CFDF photometry is measured inside a 3″ diameter aperture, which equates to a physical radius of $\sim$ 9 kpc at $z = 0.6$ (roughly the visible extent of L^* galaxies); for the photometry of a companion galaxy to be significantly affected by the light from another, brighter galaxy it would have to be less than twice this sort of distance from it, say 20 kpc to be safe. This radius equates to 45% of the area inside my smallest counting radius, which, assuming the surface density of galaxies is uniform, would result in a $\sim$ 7% probability of finding a companion within 20 kpc. Reducing the counting radius for the well matched control sample to 20 kpc I find a companion probability of 6.5%; so it does not appear that I am preferentially losing faint galaxies from the catalogue that are near other galaxies. Also, at this level of probability it would require a much larger AGN sample to be able to detect a significant deviation from the control sample (at 20 kpc the companion probability is 3.2% for the AGN sample, i.e. 1 out of 31). So I assume that this possible loss of very close companions is not responsible for the similarity between my samples on the 30 kpc scale. For the 50 kpc counting radius and above this effect should be negligible and so the observed similarity of the AGN and control samples should be real.

So that leaves the leading contender for low luminosity AGN fuelling as minor mergers. In much the same way as a major merger or interaction disrupts the eventual AGN host galaxy, the accretion of a small satellite galaxy will have the same effect but on a smaller scale and without the extreme deformation of the host disc (e.g. Walker, Mihos, & Hernquist, 1996; Hernquist & Mihos, 1995). And since satellite galaxies are very much more numerous than massive galaxies such minor mergers will be correspondingly much more common than major ones. If the

accretion of a satellite is onto a gas rich host then the satellite need only provide the impetus to send the gas in towards the awaiting central engine. A gas poor elliptical galaxy, on the other hand, requires the satellite to also provide the fuel necessary for the nuclear activity. In the former case the structure of the host galaxy seems in itself to be an important factor in determining whether the gas supply is used in a nuclear starburst or accretion onto a SBH (Hernquist & Mihos, 1995; Mihos & Hernquist, 1994), or maybe some combination. If minor mergers are common occurrences, which they undoubtedly are relative to major ones, then they are likely to be an important mechanism for the fuelling of AGN, with the differences between AGN classes being determined by the properties of the host galaxy.

7.6.2 The Richest Environments in the 14-h Field

The AGN with the richest environment in my sample is 14.132. This AGN is actually centred on the peak of an over-density (see figure 7.5), which is equivalent to Abell 1 richness according to the McLure & Dunlop (2001) calibration. However, it is clearly not a relaxed system with features extending to the north and west in the density plot shown in figure 7.5. The over-density actually peaks at $z = 0.44$ rather than the redshift of the AGN, $z = 0.48$. However, this is within the typical redshift errors for this field so the AGN is still likely to be physically associated with the over-density.

Interestingly, this region is not significantly over-dense with respect to the rest of the slice; the peak is only just more than 2σ away from the mean density (using statistic A). The main reason for this is discussed in section 6.5.1. This particular redshift slice contains a lot of large scale structure, which has caused the relative

over-density measurement for any given region to be rescaled downwards. Hence this over-density is of similar Abell richness to the one discussed in section 6.3.3 but is of far lower significance, as measured by this statistic. This point highlights the need for the calculation of a robust selection function, which would relate Abell richness to an equivalent sigma level for any given redshift and, to a certain extent, the two Abell 1 regions discussed thus far represent two points in that function.

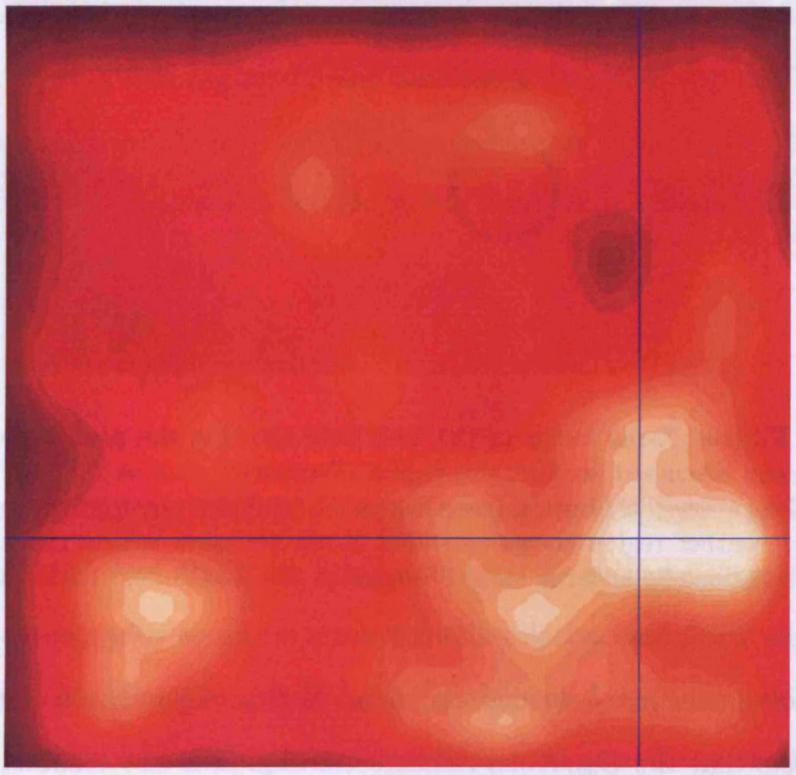

Figure 7.5: A slice through the 14-h data cube at $z = 0.48$ shows the galaxy distribution around X-ray source 14.132, the AGN with the highest environmental density in my study; its position is indicated by the blue cross-hairs. This AGN occupies the peak of an over-density corresponding to Abell class 1 richness, but is also part of a much larger structure suggesting that this may be a cluster in the process of forming.

Returning to the environment of 14.132, an Abell 1 region should be easily detectable by the *XMM* survey at $z = 0.48$. Figure 7.6 shows the MR/1 filtered *XMM* data encompassing both of the Abell 1 regions reported in this work. Aside from the emission from 14.132 at the centre of the northern region, there is no

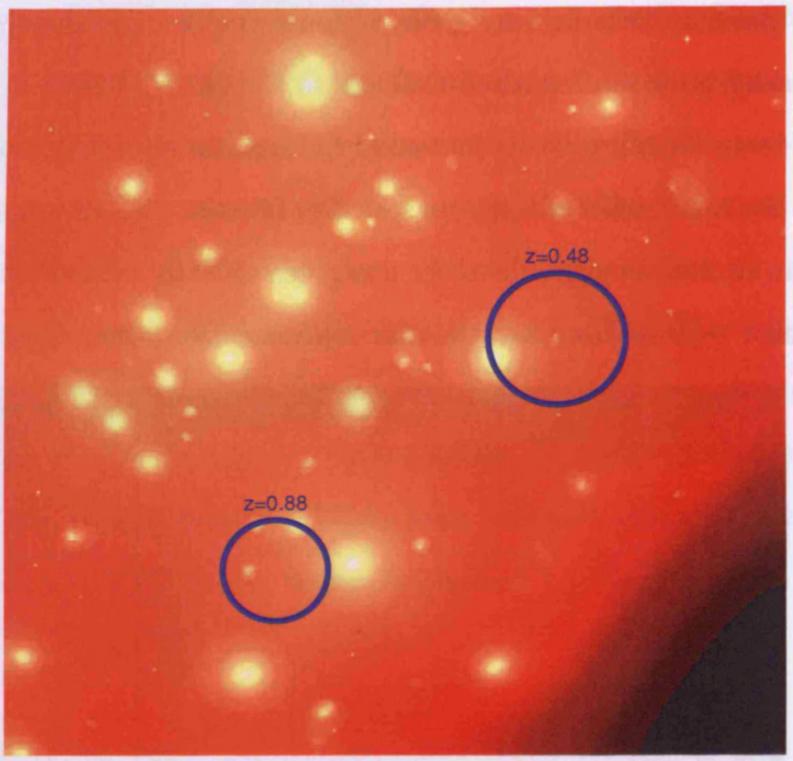

Figure 7.6: Filtered X-ray image of the 14-h field showing the positions of both of the Abell 1 regions discussed so far: the region discovered at $z = 0.88$ as a $> 6\sigma$ over-density in the galaxy distribution (see chapter 6), and the environment of AGN 14.132 at $z = 0.48$. Neither region shows extended X-ray emission within the 0.5 Mpc radius circles. Both regions lie at large off-axis angles in the *XMM* field ($> 10'$).

indication of cluster like extended emission. At first sight this is quite concerning as it suggests that the B_{gq}/Abell richness conversion is not reliable. Either that, or my calculation of B_{gq} is suspect. Other possibilities could explain this however. As with the region discussed in section 6.3.3, this over-density is at a large off-axis angle ($\sim 10.8'$) in the *XMM* FoV. At angles of $> 10'$ the sensitivity of *XMM* reduces rapidly and the PSF broadens considerably, making the distinction between point like and extended sources more problematic. It is entirely possible that source 14.132 is not an AGN at all and is in fact the emission from the core of a galaxy cluster, and it just happens to have been identified with a galaxy near the cluster centre, by the identification procedure described in chapter 4. Alter-

natively, the identification process is accurate and there really is no detectable extended X-ray emission because the cluster is still forming and is not virialised or relaxed (as evidenced by the galaxy distribution shown in figure 7.5). As such, the X-ray emission would not be as luminous as for a virialised cluster of equivalent richness, and so would have escaped detection. This argument was used in section 6.3.5 for the non-X-ray-detection of the other region in figure 7.6; however, having two such objects in a relatively small patch of sky is unlikely (although not impossible), making this argument less convincing for either region. I suspect the most reasonable explanation is the incorrect conversion from B_{gq} to Abell richness, which would have consequences for the work described in chapter 6.

7.7 Future Work

The work in this chapter is closely related to that in chapters 5 and 6, all three being possible with essentially the same data sets. As such, a natural extension to almost this entire thesis could be achieved with relative ease using any number of the very large, multi-wavelength surveys (combining deep X-ray and multi-band optical data) that are becoming increasingly common now; many of which are also publicly available.

In chapter 6 I mentioned the COMBO-17 data of the CDF-S field, which is now public and has been reduced to a ready made catalogue containing 63,501 objects, including photometric redshifts and uncertainties for a large fraction of them. Combining this catalogue with that from the deep *Chandra* X-ray survey of the same field is an ideal way of extending the work in this chapter. Although covering a smaller area than my *XMM* exposures the CDF-S is significantly deeper,

and so AGN of lower luminosity than my sample could be analysed at the same redshift. Alternatively, a similar luminosity sample to mine could be selected at a higher redshift. This opens up the possibility of studying the evolution in the environmental properties of AGN. The improved redshifts would also allow a far more accurate measurement of the AGN environments. Specifically, a significant reduction in the width of the redshift slice around the AGN would be possible, which would then reduce the uncertainty in the clustering amplitude measurement because of the lower background counts.

In addition to going to higher redshift using deeper data, a low redshift AGN sample could be selected from the vast XMM-LSS data, which will ultimately cover 64 square degrees with $\sim 10-20$ ks *XMM* data and deep multi-band optical data. This will enable the identification of relatively low redshift AGN with reasonable photometric redshifts.

Further sub-division of the X-ray selected AGN into different classes (based on their best fitting optical templates for example) would help to determine if the environmental properties of AGN of fixed luminosity are strongly correlated with the host galaxy properties, as has been suggested (Miller et al., 2003).

Chapter 8

Summary and Conclusions

8.1 Thesis Summary

The work in this thesis is fairly wide-ranging and so the individual chapters are quite self contained. Each chapter has its own conclusions but I summarise the main important points of the thesis here in an attempt to bring the individual chapters together into a coherent whole.

This thesis can be summarised as follows:

- Medium-deep X-ray surveys of the 3, 10 and 14-h Canada-France Redshift Survey (CFRS) fields using *XMM-Newton* are presented, with the aim of studying the Active Galactic Nuclei (AGN) and galaxy cluster populations in these fields. The X-ray sources detected in these surveys resolve 51% of the X-ray background (XRB) in the $0.5 - 10$ keV X-ray band.

- The relation between the X-ray and sub-mm extra-galactic backgrounds is

investigated using a combination of the *XMM* data and sub-mm data taken using the SCUBA camera on the JCMT sub-mm telescope, operating at 850μm. The X-ray properties of the sub-mm sources and the sub-mm properties of the X-ray sources indicate that the XRB is dominated by accretion onto super-massive black holes, while the sub-mm background is dominated by dust-obscured star formation. Sources detected by SCUBA do not appear to be the result of heating by an AGN and are more likely to be powered by star-formation.

- The X-ray sources in the 3 and 14-h fields are identified with optical objects, where possible, using the deep multi-band Canada-France Deep Fields (CFDF) survey, which covers the majority of these two fields. The 10-h field does not have deep optical coverage. The optical properties of the AGN host galaxies are wide ranging, indicating that X-ray selected AGN are not confined to a particular galaxy type or host optical luminosity. The redshift distribution of the X-ray selected AGN (determined using photometric redshift estimates) shows a clear peak at $z \sim 0.7$.

- The 2-point angular correlation function, $W(\theta)$, is calculated for the AGN identified in the 3 and 14-h fields but no significant clustering is detected. However, the results are consistent with X-ray selected AGN being good tracers of the normal, inactive galaxy population.

- The environments of galaxies hosting moderate luminosity AGN at $z \sim 0.5$ are investigated using the clustering amplitude measure B_{gq} and close pair counts. When compared to a control sample of equivalent inactive galaxies no difference is found between the respective environments. This suggests that environmental properties on the $30 - 500$ kpc scale have no influence on the presence of nuclear activity in a galaxy. Minor mergers with low mass

companions is therefore the most likely mechanism by which these AGN are fuelled.

- A new method for finding high redshift, optically selected, galaxy clusters is presented and is compared to X-ray selection. It is found that most optically selected clusters may have lower than expected X-ray luminosities, suggesting that they are dynamically young compared to X-ray selected clusters. This may have important implications for current X-ray cluster searches, which will miss these unvirialised clusters.

8.2 Concluding Remarks

The most important point that this thesis demonstrates is that deep X-ray and optical surveys of the same fields are an extremely powerful combination. As more large format instruments become available, over the coming decade, the number of wide-angle deep optical surveys will multiply. The sheer quantity of data that will become available in public archives is staggering and to not take full advantage of it would be a shame. The future of X-ray astronomy rests with *Constellation X* and *XEUS* but since both of these missions will have smaller fields of view than even *Chandra* future large X-ray surveys will need to be constructed from many mosaicked fields. This shouldn't be too much of a problem however, as the increase in sensitivity of these missions over *XMM* and *Chandra* should mean that large areas will still be achievable relatively quickly. They will also have the advantage of a broader spectral range, reaching right up into the peak of the XRB at 30 keV. This will enable the selection of very heavily obscured AGN, the ones most likely to be responsible for the majority of the XRB energy density.

But these missions are many years away so we must take full advantage of the current instrumentation while it is still operational. The XMM-LSS survey is likely to be the largest area joint X-ray and optical survey for many years to come. At 64 square degrees, when complete, it will contain hundreds of (luminous) galaxy clusters and many thousands of AGN at $z < 1$. Unfortunately the relatively shallow nature of the *XMM* exposures (10-20 ks) means that the lowest luminosity sources will only be visible at low redshift. However, it can provide the benchmark against which deeper surveys with future X-ray missions can be compared.

I hope that the work presented in this thesis has demonstrated the variety of science that can be investigated using this combination of data. And there is still a great deal more that I did not investigate, such as the evolution of the X-ray luminosity function and using the AGN population to test models of the XRB production; all of which would have been interesting to explore if time had permitted.

It's a big sky up there, and it's not going anywhere fast.

Bibliography

Abell G. O., The Distribution of Rich Clusters of Galaxies., 1958, ApJS, 3, 211

Akylas A., Georgantopoulos I., Plionis M., The angular correlation function of the ROSAT All-Sky Survey Bright Source Catalogue, 2000, MNRAS, 318, 1036

Alexander D. M., Bauer F. E., Brandt W. N., Hornschemeier A. E., Vignali C., Garmire G. P., Schneider D. P., Chartas G., Gallagher S. C., The Chandra Deep Field North Survey. XIV. X-Ray-Detected Obscured AGNs and Starburst Galaxies in the Bright Submillimeter Source Population, 2003, AJ, 125, 383

Alexander D. M., Brandt W. N., Hornschemeier A. E., Garmire G. P., Schneider D. P., Bauer F. E., Griffiths R. E., The Chandra Deep Field North Survey. VI. The Nature of the Optically Faint X-Ray Source Population, 2001, AJ, 122, 2156

Almaini O., Lawrence A., Boyle B. J., The AGN contribution to deep submillimetre surveys and the far-infrared background, 1999, MNRAS, 305, L59

Almaini O., Scott S. E., Dunlop J. S., Manners J. C., Willott C. J., Lawrence A., Ivison R. J., Johnson O., Blain A. W., Peacock J. A., Oliver S. J., Fox M. J., Mann R. G., Pérez-Fournon I., González-Solares E., Rowan-Robinson M., Serjeant S., Cabrera-Guerra F., Hughes D. H., The coincidence and angular clustering of Chandra and SCUBA sources, 2003, MNRAS, 338, 303

Antonucci R., Unified models for active galactic nuclei and quasars, 1993, ARA&A, 31, 473

Böhringer H., Schuecker P., Guzzo L., Collins C. A., Voges W., Schindler S., Neumann D. M., Cruddace R. G., De Grandi S., Chincarini G., Edge A. C., MacGillivray H. T., Shaver P., The ROSAT-ESO flux limited X-ray (REFLEX) galaxy cluster survey. I. The construction of the cluster sample, 2001, A&A, 369, 826

Böhringer H., Voges W., Huchra J. P., McLean B., Giacconi R., Rosati P., Burg R., Mader J., Schuecker P., Simiç D., Komossa S., Reiprich T. H., Retzlaff J., Trümper J., The Northern ROSAT All-Sky (NORAS) Galaxy Cluster Survey. I. X-Ray Properties of Clusters Detected as Extended X-Ray Sources, 2000, ApJS, 129, 435

Baldi A., Molendi S., Comastri A., Fiore F., Matt G., Vignali C., The HELLAS2XMM Survey. I. The X-Ray Data and the logN-logS Relation, 2002, ApJ, 564, 190

Barcons X., Carrera F. J., Ceballos M. T., Mateos S., 2000, in Large Scale Structure in the X-ray Universe, Proceedings of the 20-22 September 1999 Workshop, Santorini, Greece, eds. Plionis, M. & Georgantopoulos, I., Atlantisciences, Paris, France, p.205, p. 205

Barcons X., Carrera F. J., Ceballos M. T., Mateos S., 2001, in AIP Conf. Proc. 599: X-ray Astronomy: Stellar Endpoints, AGN, and the Diffuse X-ray Background, p. 3

Barcons X. et al., The XMM-Newton serendipitous survey . II. First results from the AXIS high galactic latitude medium sensitivity survey, 2002, A&A, 382, 522

Barger A. J., Cowie L. L., Brandt W. N., Capak P., Garmire G. P., Hornschemeier A. E., Steffen A. T., Wehner E. H., X-Ray, Optical, and Infrared Imaging and Spectral Properties of the 1 Ms Chandra Deep Field North Sources, 2002, AJ, 124, 1839

Barger A. J., Cowie L. L., Capak P., Alexander D. M., Bauer F. E., Fernandez E., Brandt W. N., Garmire G. P., Hornschemeier A. E., Optical and Infrared Properties of the 2 Ms Chandra Deep Field North X-Ray Sources, 2003, AJ, 126, 632

Barger A. J., Cowie L. L., Sanders D. B., Fulton E., Taniguchi Y., Sato Y., Kawara K., Okuda H., Submillimetre-wavelength detection of dusty star-forming galaxies at high redshift., 1998, Nature, 394, 248

Barger A. J., Cowie L. L., Steffen A. T., Hornschemeier A. E., Brandt W. N., Garmire G. P., Submillimeter Properties of the 1 Ms Chandra Deep Field-North X-Ray Sample, 2001, ApJ, 560, L23

Barr J. M., Bremer M. N., Baker J. C., Lehnert M. D., The cluster environments of radio-loud quasars at $0.6 < z < 1.1$, 2003, MNRAS, 346, 229

Bauer F. E., Alexander D. M., Brandt W. N., Hornschemeier A. E., Miyaji T., Garmire G. P., Schneider D. P., Bautz M. W., Chartas G., Griffiths R. E., Sargent W. L. W., The Chandra Deep Field North Survey. IX. Extended X-Ray Sources, 2002, AJ, 123, 1163

Bautz M. W., Malm M. R., Baganoff F. K., Ricker G. R., Canizares C. R., Brandt W. N., Hornschemeier A. E., Garmire G. P., Detection of X-Ray Emission from Gravitationally Lensed Submillimeter Sources in the Field of Abell 370, 2000, ApJ, 543, L119

Benítez N., Bayesian Photometric Redshift Estimation, 2000, ApJ, 536, 571

Bragaglia A., Pozzetti L., Ciliegi P., Osservatorio Astronomico di Bologna Annual Report 2000, http://www.bo.astro.it/report00/node53.html

Brainerd J. J., The Superiority of the Two-Point Correlation Function over the Nearest Neighbor Analysis as a Test for Gamma-Ray Burst Repetition, 1996, ApJ, 473, 974

Brandt W. N., Alexander D. M., Hornschemeier A. E., Garmire G. P., Schneider D. P., Barger A. J., Bauer F. E., Broos P. S., Cowie L. L., Townsley L. K., Burrows D. N., Chartas G., Feigelson E. D., Griffiths R. E., Nousek J. A., Sargent W. L. W., The Chandra Deep Field North Survey. V. 1 Ms Source Catalogs, 2001, AJ, 122, 2810

Brodwin M., Lilly S. J., Porciani C., McCracken H. J., Le Fevre O., Foucaud S., Crampton D., Mellier Y., The Canada-France Deep Fields III: Photometric Redshift Distribution to I(AB) = 24, 2003, ApJ, preprint, astro-ph/0310038

Brown M. J. I., Boyle B. J., Webster R. L., The Clustering of AGNs and Galaxies at Intermediate Redshift, 2001, AJ, 122, 26

Brunner R. J., Szalay A. S., Connolly A. J., Evolution in the Clustering of Galaxies for $Z < 1.0$, 2000, ApJ, 541, 527

Butcher H., Oemler A., The evolution of galaxies in clusters. I - ISIT photometry of C1 0024+1654 and 3C 295, 1978, ApJ, 219, 18

Carrera F. J., Barcons X., Fabian A. C., Hasinger G., Mason K. O., McMahon R. G., Mittaz J. P. D., Page M. J., Clustering of X-ray selected active galactic nuclei, 1998, MNRAS, 299, 229

Chapman S. C., Barger A. J., Cowie L. L., Scott D., Borys C., Capak P., Fomalont E. B., Lewis G. F., Richards E. A., Steffen A. T., Wilson G., Yun M., The Properties of Microjansky Radio Sources in the Hubble Deep Field-North, SSA 13, and SSA 22 Fields, 2003a, ApJ, 585, 57

Chapman S. C., Blain A. W., Ivison R. J., Smail I. R., A median redshift of 2.4 for galaxies bright at submillimetre wavelengths, 2003b, Nature, 422, 695

Cimatti A., Daddi E., Mignoli M., Pozzetti L., Renzini A., Zamorani G., Broadhurst T., Fontana A., Saracco P., Poli F., Cristiani S., D'Odorico S., Giallongo E., Gilmozzi R., Menci N., The K20 survey. I. Disentangling old and dusty star-forming galaxies in the ERO population, 2002, A&A, 381, L68

Coleman G. D., Wu C.-C., Weedman D. W., Colors and magnitudes predicted for high redshift galaxies, 1980, ApJS, 43, 393

Comastri A., Setti G., Zamorani G., Hasinger G., The contribution of AGNs to the X-ray background., 1995, A&A, 296, 1

Cowie L. L., Barger A. J., Bautz M. W., Brandt W. N., Garmire G. P., The Redshift Evolution of the 2-8 keV X-Ray Luminosity Function, 2003, ApJ, 584, L57

Cress C. M., Helfand D. J., Becker R. H., Gregg M. D., White R. L., The Angular Two-Point Correlation Function for the FIRST Radio Survey, 1996, ApJ, 473, 7

Csabai I., Budavári T., Connolly A. J., Szalay A. S., Győry Z., Benítez N., Annis J., Brinkmann J., Eisenstein D., Fukugita M., Gunn J., Kent S., Lupton R., Nichol R. C., Stoughton C., The Application of Photometric Redshifts to the SDSS Early Data Release, 2003, AJ, 125, 580

Dahlén T., Fransson C., Östlin G., Näslund M., The galaxy population of intermediate-redshift clusters, 2004, MNRAS, 350, 253

de Robertis M. M., Yee H. K. C., Hayhoe K., A CCD Study of the Environment of Seyfert Galaxies. II. Testing the Interaction Hypothesis, 1998, ApJ, 496, 93

Dekel A., Ostriker J. P., ed, 1999, Formation of structure in the universe

Donahue M., Mack J., Scharf C., Lee P., Postman M., Rosati P., Dickinson M., Voit G. M., Stocke J. T., Distant Cluster Hunting: A Comparison Between the Optical and X-Ray Luminosity Functions from an Optical/X-Ray Joint Survey, 2001, ApJ, 552, L93

Downes A. J. B., Peacock J. A., Savage A., Carrie D. R., The Parkes selected regions - Powerful radio galaxies and quasars at high redshifts, 1986, MNRAS, 218, 31

Dunne L., Eales S. A., The SCUBA Local Universe Galaxy Survey - II. 450-μm data: evidence for cold dust in bright IRAS galaxies, 2001, MNRAS, 327, 697

Eales S., Lilly S., Gear W., Dunne L., Bond J. R., Hammer F., Le Fèvre O., Crampton D., The Canada-UK Deep Submillimeter Survey: First Submillimeter Images, the Source Counts, and Resolution of the Background, 1999, ApJ, 515, 518

Eales S., Lilly S., Webb T., Dunne L., Gear W., Clements D., Yun M., The Canada-UK Deep Submillimeter Survey. IV. The Survey of the 14 Hour Field, 2000, AJ, 120, 2244

Ebeling H., Edge A. C., Allen S. W., Crawford C. S., Fabian A. C., Huchra J. P., The ROSAT Brightest Cluster Sample - IV. The extended sample, 2000, MNRAS, 318, 333

Ebeling H., Edge A. C., Bohringer H., Allen S. W., Crawford C. S., Fabian A. C., Voges W., Huchra J. P., The ROSAT Brightest Cluster Sample - I. The compilation of the sample and the cluster log N-log S distribution, 1998, MNRAS, 301, 881

Elvis M., Wilkes B. J., McDowell J. C., Green R. F., Bechtold J., Willner S. P., Oey M. S., Polomski E., Cutri R., Atlas of quasar energy distributions, 1994, ApJS, 95, 1

Fabian A. C., Cooling Flows in Clusters of Galaxies, 1994, ARA&A, 32, 277

Fabian A. C., Arnaud K. A., Nulsen P. E. J., Mushotzky R. F., The detection of distant cooling flows and the formation of dark matter, 1986, ApJ, 305, 9

Fabian A. C., Barcons X., The origin of the X-ray background, 1992, ARA&A, 30, 429

Fabian A. C., Smail I., Iwasawa K., Allen S. W., Blain A. W., Crawford C. S., Ettori S., Ivison R. J., Johnstone R. M., Kneib J.-P., Wilman R. J., Testing the connection between the X-ray and submillimetre source populations using Chandra, 2000, MNRAS, 315, L8

Fixsen D. J., Dwek E., Mather J. C., Bennett C. L., Shafer R. A., The Spectrum of the Extragalactic Far-Infrared Background from the COBE FIRAS Observations, 1998, ApJ, 508, 123

Fontana A., D'Odorico S., Poli F., Giallongo E., Arnouts S., Cristiani S., Moorwood A., Saracco P., Photometric Redshifts and Selection of High-Redshift Galaxies in the NTT and Hubble Deep Fields, 2000, AJ, 120, 2206

Franceschini A., Braito V., Fadda D., Origin of the X-ray background and AGN unification: new perspectives, 2002, MNRAS, 335, L51

Freeman P. E., Kashyap V., Rosner R., Lamb D. Q., A Wavelet-Based Algorithm for the Spatial Analysis of Poisson Data, 2002, ApJS, 138, 185

Gandhi P., Crawford C. S., Fabian A. C., Johnstone R. M., Powerful, obscured active galactic nuclei among X-ray hard, optically dim serendipitous Chandra sources, 2004, MNRAS, 348, 529

Giacconi R., Murray S., Gursky H., Kellogg E., Schreier E., Tananbaum H., The UHURU catalog of X-ray souces., 1972, ApJ, 178, 281

Giacconi R., Zirm A., Wang J., Rosati P., Nonino M., Tozzi P., Gilli R., Mainieri V., Hasinger G., Kewley L., Bergeron J., Borgani S., Gilmozzi R., Grogin N., Koekemoer A., Schreier E., Zheng W., Norman C., Chandra Deep Field South: The 1 Ms Catalog, 2002, ApJS, 139, 369

Gilli R., Cimatti A., Daddi E., Hasinger G., Rosati P., Szokoly G., Tozzi P., Bergeron J., Borgani S., Giacconi R., Kewley L., Mainieri V., Mignoli M., Nonino M., Norman C., Wang J., Zamorani G., Zheng W., Zirm A., Tracing the Large-Scale Structure in the Chandra Deep Field South, 2003, ApJ, 592, 721

Gilli R., Salvati M., Hasinger G., Testing current synthesis models of the X-ray background, 2001, A&A, 366, 407

Gladders M. D., Yee H. K. C., A New Method For Galaxy Cluster Detection. I. The Algorithm, 2000, AJ, 120, 2148

Gonzalez A. H., Maccarone T. J., A Test of Photometric Redshifts for X-Ray-selected Sources, 2002, ApJ, 581, 155

Grogin N. A., Koekemoer A. M., Schreier E. J., Bergeron J., Giacconi R., Hasinger G., Kewley L., Norman C., Rosati P., Tozzi P., Zirm A., Hubble Space Telescope Imaging in the Chandra Deep Field-South. III. Quantitative Morphology of the 1 Million Second Chandra Counterparts and Comparison with the Field Population, 2003, ApJ, 595, 685

Groth E. J., Peebles P. J. E., Statistical analysis of catalogs of extragalactic objects. VII - Two- and three-point correlation functions for the high-resolution Shane-Wirtanen catalog of galaxies, 1977, ApJ, 217, 385

Gunn K. F., Shanks T., Implications of an Obscured AGN Model for the X-ray Background at Sub-mm and Far Infra-Red Wavelengths, 1999, MNRAS, preprint, astro-ph/9909089

Gursky H., Kellogg E., Murray S., Leong C., Tananbaum H., Giacconi R., A Strong X-Ray Source in the Coma Cluster Observed by UHURU, 1971, ApJ, 167, L81

Haardt F., Maraschi L., Ghisellini G., X-Ray Variability and Correlations in the Two-Phase Disk-Corona Model for Seyfert Galaxies, 1997, ApJ, 476, 620

Hall P. B., Ellingson E., Green R. F., X-Ray Emission from the Host Clusters of Powerful AGN, 1997, AJ, 113, 1179

Hammer F., Crampton D., Le Fevre O., Lilly S. J., The Canada-France Redshift Survey. IV. Spectroscopic Selection Effects and 0300+00 Field Spectroscopic Data, 1995a, ApJ, 455, 88

Hammer F., Crampton D., Lilly S. J., Le Fevre O., Kenet T., The Canada-France Redshift Survey - VII. optical counterparts of microjansky radio sources, 1995b, MNRAS, 276, 1085

Hashimoto Y., Hasinger G., Arnaud M., Rosati P., Miyaji T., XMM-Newton observation of a distant X-ray selected cluster of galaxies at z=1.26 with possible cluster interaction, 2002, A&A, 381, 841

Hasinger G. et al., XMM-Newton observation of the Lockman Hole. I. The X-ray data, 2001, A&A, 365, L45

Hasinger G., Burg R., Giacconi R., Schmidt M., Trumper J., Zamorani G., The ROSAT Deep Survey. I. X-ray sources in the Lockman Field, 1998, A&A, 329, 482

Hauser M. G., Arendt R. G., Kelsall T., Dwek E., Odegard N., Weiland J. L., Freudenreich H. T., Reach W. T., Silverberg R. F., Moseley S. H., Pei Y. C., Lubin P., Mather J. C., Shafer R. A., Smoot G. F., Weiss R., Wilkinson D. T., Wright E. L., The COBE Diffuse Infrared Background Experiment Search for the Cosmic Infrared Background. I. Limits and Detections, 1998, ApJ, 508, 25

Hernquist L., Mihos J. C., Excitation of Activity in Galaxies by Minor Mergers, 1995, ApJ, 448, 41

Hewett P. C., The estimation of galaxy angular correlation functions, 1982, MNRAS, 201, 867

Hornschemeier A. E., Bauer F. E., Alexander D. M., Brandt W. N., Sargent W. L. W., Vignali C., Garmire G. P., Schneider D. P., The weak outnumbering the mighty: normal galaxies in deep Chandra surveys, 2003, Astronomische Nachrichten, 324, 12

Hornschemeier A. E., Brandt W. N., Garmire G. P., Schneider D. P., Barger A. J., Broos P. S., Cowie L. L., Townsley L. K., Bautz M. W., Burrows D. N., Chartas G., Feigelson E. D., Griffiths R. E., Lumb D., Nousek J. A., Ramsey L. W., Sargent W. L. W., The Chandra Deep Survey of the Hubble Deep Field-North Area. II. Results from the Caltech Faint Field Galaxy Redshift Survey Area, 2001, ApJ, 554, 742

Hornschemeier A. E., Brandt W. N., Garmire G. P., Schneider D. P., Broos P. S., Townsley L. K., Bautz M. W., Burrows D. N., Chartas G., Feigelson E. D., Griffiths R., Lumb D., Nousek J. A., Sargent W. L. W., X-Ray Sources in the Hubble Deep Field Detected by Chandra, 2000, ApJ, 541, 49

Hughes D. H., Serjeant S., Dunlop J., Rowan-Robinson M., Blain A., Mann R. G., Ivison R., Peacock J., Efstathiou A., Gear W., Oliver S., Lawrence A., Longair M., Goldschmidt P., Jenness T., High-redshift star formation in the Hubble Deep Field revealed by a submillimetre-wavelength survey., 1998, Nature, 394, 241

Ivison R. J., Greve T. R., Smail I., Dunlop J. S., Roche N. D., Scott S. E., Page M. J., Stevens J. A., Almaini O., Blain A. W., Willott C. J., Fox M. J., Gilbank D. G., Serjeant S., Hughes D. H., Deep radio imaging of the SCUBA 8-mJy survey fields: submillimetre source identifications and redshift distribution, 2002, MNRAS, 337, 1

Iwasawa K., Comastri A., ASCA spectroscopy of the luminous infrared galaxy NGC 6240: X-ray emission from a starburst and a buried active nucleus, 1998, MNRAS, 297, 1219

Kaiser N., Evolution and clustering of rich clusters, 1986, MNRAS, 222, 323

Kaiser N., Evolution of clusters of galaxies, 1991, ApJ, 383, 104

Kashikawa N., Takata T., Ohyama Y., Yoshida M., Maihara T., Iwamuro F., Motohara K., Totani T., Nagashima M., Shimasaku K., Furusawa H., Ouchi M., Yagi M., Okamura S., Iye M., Sasaki T., Kosugi G., Aoki K., Nakata F., Subaru Deep Survey. III. Evolution of Rest-Frame Luminosity Functions Based on the Photometric Redshifts for a K'-Band-Selected Galaxy Sample, 2003, AJ, 125, 53

Kauffmann G., Haehnelt M., A unified model for the evolution of galaxies and quasars, 2000, MNRAS, 311, 576

Kauffmann G., White S. D. M., Heckman T. M., Menard B., Brinchmann J., Charlot S., Tremonti C., Brinkmann J., The Environmental Dependence of the Relations between Stellar Mass, Structure, Star Formation and Nuclear Activity in Galaxies, 2004, MNRAS, preprint, astro-ph/0402030

Kellogg E., Gursky H., Leong C., Schreier E., Tananbaum H., Giacconi R., X-Ray Observations of the Virgo Cluster, NGC 5128, and 3c 273 from the UHURU Satellite, 1971, ApJ, 165, L49

Kinney A. L., Calzetti D., Bohlin R. C., McQuade K., Storchi-Bergmann T., Schmitt H. R., Template Ultraviolet to Near-Infrared Spectra of Star-forming Galaxies and Their Application to K-Corrections, 1996, ApJ, 467, 38

Kodama T., Smail I., Nakata F., Okamura S., Bower R. G., The Transformation of Galaxies within the Large-Scale Structure around a z=0.41 Cluster, 2001, ApJ, 562, L9

Koekemoer A. M., Alexander D. M., Bauer F. E., Bergeron J., Brandt W. N., Chatzichristou E., Cristiani S., Fall S. M., Grogin N. A., Livio M., Mainieri V., Moustakas L. A., Padovani P., Rosati P., Schreier E. J., Urry C. M., A Possible New Population of Sources with Extreme X-Ray/Optical Ratios, 2004, ApJ, 600, L123

Lake G., Katz N., Moore B., The Formation of Quasars in Low-Luminosity Hosts via Galaxy Harassment, 1998, ApJ, 495, 152

Lamer G., Schwope A., Elvis M., Burke D., Watson M. G., The XMM-Newton SSC serendipitous cluster survey, 2003, Astronomische Nachrichten, 324, 156

Landy S. D., Szalay A. S., Bias and variance of angular correlation functions, 1993, ApJ, 412, 64

Le Fevre O., Hudon D., Lilly S. J., Crampton D., Hammer F., Tresse L., The Canada-France Redshift Survey. VIII. Evolution of the Clustering of Galaxies from Z approximately 1, 1996, ApJ, 461, 534

Lehmann I., Hasinger G., Schmidt M., Giacconi R., Trümper J., Zamorani G., Gunn J. E., Pozzetti L., Schneider D. P., Stanke T., Szokoly G., Thompson D., Wilson G., The ROSAT Deep Survey. VI. X-ray sources and Optical identifications of the Ultra Deep Survey, 2001, A&A, 371, 833

Lilly S. J., Hammer F., Le Fevre O., Crampton D., The Canada-France Redshift Survey. III. "Single Emission-Line" Objects, Analysis of Repeat Observations, and Spectroscopic Identifications in the 1415+52 and 2215+00 Fields, 1995a, ApJ, 455, 75

Lilly S. J., Le Fevre O., Crampton D., Hammer F., Tresse L., The Canada-France Redshift Survey. I. Introduction to the Survey, Photometric Catalogs, and Surface Brightness Selection Effects, 1995b, ApJ, 455, 50

Limber D. N., The Analysis of Counts of the Extragalactic Nebulae in Terms of a Fluctuating Density Field. II., 1954, ApJ, 119, 655

Lira P., Ward M. J., Zezas A., Murray S. S., Chandra HRC and HST observations of NGC 6240: resolving the active galactic nucleus and starburst, 2002, MNRAS, 333, 709

Longair M. S., Seldner M., The clustering of galaxies about extragalactic radio sources, 1979, MNRAS, 189, 433

Loveday J., Maddox S. J., Efstathiou G., Peterson B. A., The Stromlo-APM redshift survey. 2: Variation of galaxy clustering with morphology and luminosity, 1995, ApJ, 442, 457

Lubin L. M., Mulchaey J. S., Postman M., The First Detailed X-Ray Observations of High-Redshift, Optically Selected Clusters: XMM-Newton Results for Cl 1324+3011 at z = 0.76 and Cl 1604+4304 at z = 0.90, 2004, ApJ, 601, L9

Lubin L. M., Oke J. B., Postman M., Evidence for Cluster Evolution from an Improved Measurement of the Velocity Dispersion and Morphological Fraction of Cluster 1324+3011 at z=0.76, 2002, AJ, 124, 1905

Magorrian J., Tremaine S., Richstone D., Bender R., Bower G., Dressler A., Faber S. M., Gebhardt K., Green R., Grillmair C., Kormendy J., Lauer T., The Demography of Massive Dark Objects in Galaxy Centers, 1998, AJ, 115, 2285

Mainieri V., Bergeron J., Hasinger G., Lehmann I., Rosati P., Schmidt M., Szokoly G., Della Ceca R., XMM-Newton observation of the Lockman Hole. II. Spectral analysis, 2002, A&A, 393, 425

Manners J. C., 2002, PhD thesis - Obscuration and X-ray Variability of Active Galactic Nuclei.

McCammon D., Sanders W. T., The soft X-ray background and its origins, 1990, ARA&A, 28, 657

McCracken H. J., Le Fèvre O., Brodwin M., Foucaud S., Lilly S. J., Crampton D., Mellier Y., The Canada-France deep fields survey$, 2001, A&A, 376, 756

McHardy I. M., Gunn K. F., Newsam A. M., Mason K. O., Page M. J., Takata T., Sekiguchi K., Sasseen T., Cordova F., Jones L. R., Loaring N., A medium-deep Chandra and Subaru survey of the 13-h XMM/ROSAT deep survey area, 2003, MNRAS, 342, 802

McHardy I. M., Jones L. R., Merrifield M. R., Mason K. O., Newsam A. M., Abraham R. G., Dalton G. B., Carrera F., Smith P. J., Rowan-Robinson M., Wegner G. A., Ponman T. J., Lehto H. J., Branduardi-Raymont G., Luppino G. A., Efstathiou G., Allan D. J., Quenby J. J., The origin of the cosmic soft X-ray background - optical identification of an extremely deep ROSAT survey, 1998, MNRAS, 295, 641

McLure R. J., Dunlop J. S., The cluster environments of powerful radio-loud and radio-quiet active galactic nuclei, 2001, MNRAS, 321, 515

McLure R. J., Kukula M. J., Dunlop J. S., Baum S. A., O'Dea C. P., Hughes D. H., A comparative HST imaging study of the host galaxies of radio-quiet quasars, radio-loud quasars and radio galaxies - I, 1999, MNRAS, 308, 377

Mihos J. C., Hernquist L., Triggering of starbursts in galaxies by minor mergers, 1994, ApJ, 425, L13

Miller C. J., Nichol R. C., Gómez P. L., Hopkins A. M., Bernardi M., The Environment of Active Galactic Nuclei in the Sloan Digital Sky Survey, 2003, ApJ, 597, 142

Miyaji T., Griffiths R. E., 2001, in Clusters of Galaxies and the High Redshift Universe Observed in X-rays

Miyaji T., Griffiths R. E., Lumb D., Sarajedini V., Siddiqui H., XMM-Newton view of the Hubble Deep Field-North and Groth-Westphal strip regions, 2003, Astronomische Nachrichten, 324, 24

Miyaji T., Sarajedini V., Griffiths R. E., Yamada T., Schurch M., Cristobal-Hornillos D., Motohara K., Multiwavelength Properties of the X-ray Sources in the Groth-Westphal Strip Field, 2004, AJ, preprint, astro-ph/0402617

Mobasher B. et al., Photometric Redshifts for Galaxies in the GOODS Southern Field, 2004, ApJ, 600, L167

Moore B., Katz N., Lake G., On the Destruction and Overmerging of Dark Halos in Dissipationless N-Body Simulations, 1996, ApJ, 457, 455

Moretti A., Campana S., Lazzati D., Tagliaferri G., The Resolved Fraction of the Cosmic X-Ray Background, 2003, ApJ, 588, 696

Nenkova M., Ivezić Ž., Elitzur M., Dust Emission from Active Galactic Nuclei, 2002, ApJ, 570, L9

Osmond J. P. F., Ponman T. J., The GEMS project: X-ray analysis and statistical properties of the group sample, 2004, MNRAS, 350, 1511

Ostrander E. J., Nichol R. C., Ratnatunga K. U., Griffiths R. E., The Hubble Space Telescope Medium Deep Survey Cluster Sample: Methodology and Data, 1998, AJ, 116, 2644

Page M. J., McHardy I. M., Gunn K. F., Loaring N. S., Mason K. O., Sasseen T., Newsam A., Ware A., Kennea J., Sekiguchi K., Takata T., X-ray and optical properties of X-ray sources in the 13hr XMM-Newton/Chandra deep survey, 2003, Astronomische Nachrichten, 324, 101

Page M. J., Stevens J. A., Mittaz J. P. D., Carrera F. J., Submillimeter Evidence for the Coeval Growth of Massive Black Holes and Galaxy Bulges, 2001, Science, 294, 2516

Peebles P. J. E., Statistical Analysis of Catalogs of Extragalactic Objects. I. Theory, 1973, ApJ, 185, 413

Peebles P. J. E., 1980, The large-scale structure of the universe. Research supported by the National Science Foundation. Princeton, N.J., Princeton University Press, 1980. 435 p.

Phillipps S., Davies J., A cross-correlation method for surface photometry, 1991, MNRAS, 251, 105

Press W. H., Schechter P., Formation of Galaxies and Clusters of Galaxies by Self-Similar Gravitational Condensation, 1974, ApJ, 187, 425

Puget J.-L., Abergel A., Bernard J.-P., Boulanger F., Burton W. B., Desert F.-X., Hartmann D., Tentative detection of a cosmic far-infrared background with COBE., 1996, A&A, 308, L5

Refregier A., Valtchanov I., Pierre M., Cosmology with galaxy clusters in the XMM large-scale structure survey, 2002, A&A, 390, 1

Roche N., Eales S. A., The angular correlation function and hierarchical moments of ~70000 faint galaxies to R=23.5, 1999, MNRAS, 307, 703

Rosati P., Borgani S., Norman C., The Evolution of X-ray Clusters of Galaxies, 2002, ARA&A, 40, 539

Rosati P., Tozzi P., Giacconi R., Gilli R., Hasinger G., Kewley L., Mainieri V., Nonino M., Norman C., Szokoly G., Wang J. X., Zirm A., Bergeron J., Borgani S., Gilmozzi R., Grogin N., Koekemoer A., Schreier E., Zheng W., The Chandra Deep Field-South: The 1 Million Second Exposure, 2002, ApJ, 566, 667

Söchting I. K., Clowes R. G., Campusano L. E., Relation of radio-quiet quasars to galaxy clusters at $z < 0.3$, 2004, MNRAS, 347, 1241

Schade D., Crampton D., Hammer F., Le Fevre O., Lilly S. J., Canada-France Redshift Survey - X. The quasar sample, 1996, MNRAS, 278, 95

Scharf C., Optimal Chandra and XMM-Newton Bandpasses for Detecting Low-Temperature Groups and Clusters of Galaxies, 2002, ApJ, 572, 157

Schmitt H. R., Kinney A. L., Calzetti D., Storchi Bergmann T., The Spectral Energy Distribution of Normal, Starburst, and Active Galaxies., 1997, AJ, 114, 592

Severgnini P., Maiolino R., Salvati M., Axon D., Cimatti A., Fiore F., Gilli R., La Franca F., Marconi A., Matt G., Risaliti G., Vignali C., Sub-mm and X-ray background: Two unrelated phenomena?, 2000, A&A, 360, 457

Smail I., Ivison R. J., Blain A. W., A Deep Sub-millimeter Survey of Lensing Clusters: A New Window on Galaxy Formation and Evolution, 1997, ApJ, 490, L5

Smith R. J., Boyle B. J., Maddox S. J., The environments of intermediate-redshift QSOs: $0.3 < z < 0.7$, 2000, MNRAS, 313, 252

Starck J.-L., Murtagh F., Bijaoui A., 1998, Image processing and data analysis. The multiscale approach. Image processing and data analysis. The multiscale approach, Publisher: Cambridge, UK: Cambridge University Press, 1998, ISBN: 0521590841

Starck J.-L., Pierre M., Structure detection in low intensity X-ray images, 1998, A&AS, 128, 397

Steffen A. T., Barger A. J., Cowie L. L., Mushotzky R. F., Yang Y., The Changing Active Galactic Nucleus Population, 2003, ApJ, 596, L23

Stocke J. T., Morris S. L., Gioia I. M., Maccacaro T., Schild R., Wolter A., Fleming T. A., Henry J. P., The Einstein Observatory Extended Medium-Sensitivity Survey. II - The optical identifications, 1991, ApJS, 76, 813

Tesch F., Carrera F. J., Engels D., Hu J., Ledoux C., Ugryumov A., Valls-Gabaud D., Voges W., Wei J., 2000, in Large Scale Structure in the X-ray Universe, Proceedings of the 20-22 September 1999 Workshop, Santorini, Greece, eds. Plionis, M. & Georgantopoulos, I., Atlantisciences, Paris, France, p.407, p. 407

Ueda Y., Akiyama M., Ohta K., Miyaji T., Cosmological Evolution of the Hard X-Ray Active Galactic Nucleus Luminosity Function and the Origin of the Hard X-Ray Background, 2003, ApJ, 598, 886

Urry C. M., Padovani P., Unified Schemes for Radio-Loud Active Galactic Nuclei, 1995, PASP, 107, 803

Valageas P., Silk J., The entropy history of the universe, 1999, A&A, 350, 725

Valtchanov I., Pierre M., Gastaud R., Comparison of source detection procedures for XMM-Newton images, 2001, A&A, 370, 689

Vikhlinin A., Forman W., Detection of the Angular Correlation of Faint X-Ray Sources, 1995, ApJ, 455, L109

Walker I. R., Mihos J. C., Hernquist L., Quantifying the Fragility of Galactic Disks in Minor Mergers, 1996, ApJ, 460, 121

Waskett T. J., Eales S. A., Gear W. K., McCracken H. J., Brodwin M., Nandra K., Laird E. S., Lilly S., XMM-Newton surveys of the Canada-France Redshift Survey fields - II. The X-ray catalogues, the properties of the host galaxies and the redshift distribution, 2004, MNRAS, 350, 785

Waskett T. J., Eales S. A., Gear W. K., Puchnarewicz E. M., Lilly S., Flores H., Webb T., Clements D., Stevens J. A., Thuan T. X., XMM-Newton surveys of the Canada-France Redshift Survey fields - I. The submillimetre/X-ray relation, 2003, MNRAS, 341, 1217

Watson M. G. et al., The XMM-Newton Serendipitous Survey. I. The role of XMM-Newton Survey Science Centre, 2001, A&A, 365, L51

Webb T. M., Eales S. A., Lilly S. J., Clements D. L., Dunne L., Gear W. K., Ivison R. J., Flores H., Yun M., The Canada-UK Deep Submillimeter Survey. VI. The 3 Hour Field, 2003a, ApJ, 587, 41

Webb T. M. A., Lilly S. J., Clements D. L., Eales S., Yun M., Brodwin M., Dunne L., Gear W. K., The Canada-UK Deep Submillimeter Survey. VII. Optical and Near-Infrared Identifications for the 14 Hour Field, 2003b, ApJ, 597, 680

Wold M., Lacy M., Lilje P. B., Serjeant S., Clustering of galaxies around radio quasars at $0.5 \leq z \leq 0.8$, 2000, MNRAS, 316, 267

Wold M., Lacy M., Lilje P. B., Serjeant S., Radio-quiet quasar environments at $0.5\leq = z\leq = 0.8$, 2001, MNRAS, 323, 231

Wolf C., Meisenheimer K., Kleinheinrich M., Borch A., Dye S., Gray M., Wisotzki L., Bell E. F., Rix H.-W., Cimatti A., Hasinger G., Szokoly G., A catalogue of the Chandra Deep Field South with multi-colour classification and photometric redshifts from COMBO-17, 2004, A&A, 421, 913

Xu C., Livio M., Baum S., Radio-loud and Radio-quiet Active Galactic Nuclei, 1999, AJ, 118, 1169

Yee H. K. C., López-Cruz O., A Quantitative Measure of the Richness of Galaxy Clusters, 1999, AJ, 117, 1985